THE UNIVERSITY *of* EDINBURGH

Charithea Charalambous

A Temperature Swing Adsorption Process for Carbon Dioxide Capture, Purification, and Compression Directly from Atmospheric Air

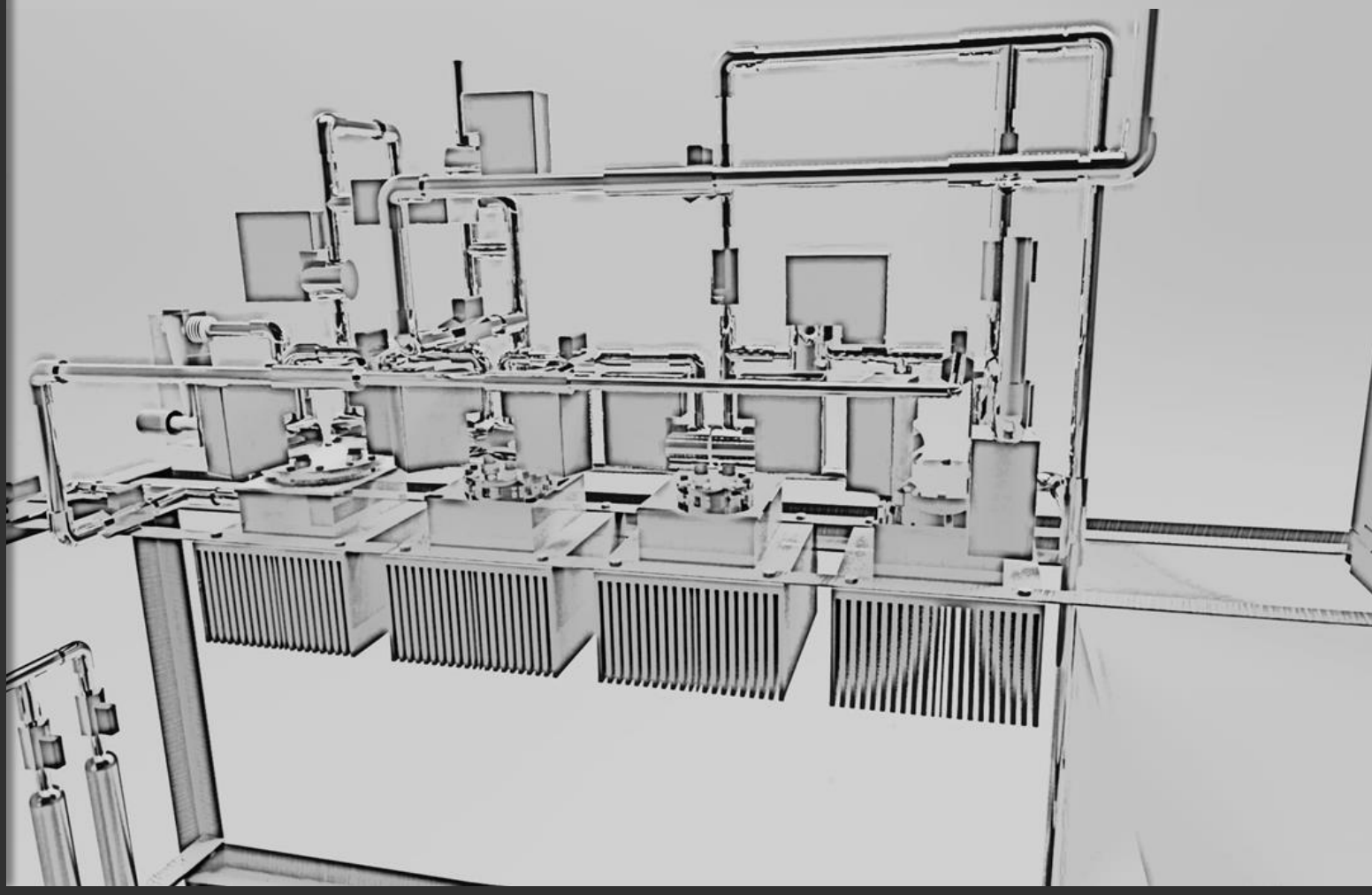

for the degree of Doctor of Philosophy

September, 2018

A Temperature Swing Adsorption Process for Carbon Dioxide Capture, Purification and Compression Directly from Atmospheric Air

Charithea Charalambous

For the degree of Doctor of Philosophy
at The University of Edinburgh
September, 2018

Charithea Charalambous

A Temperature Swing Adsorption Process for Carbon Dioxide Capture, Purification and Compression Directly from Atmospheric Air

For the degree of Doctor of Philosophy at The University of Edinburgh, September 2018

Reviewers: Prof. Joeri Denayer and Dr Hyungwoong Ahn

Supervisors: Dr Giulio Santori and Dr Maria-Chiara Ferrari

The University of Edinburgh

Carbon Capture Research Group

Institute for Materials and Processes

School of Engineering

Mayfield Rd, The King's Buildings, Sanderson Building

EH9 3JL Edinburgh

Declaration

I declare that I have completed this thesis and the work described herein solely, except where explicitly stated in the text. The novel work presented here has been conducted under the guidance of Dr. Giulio Santori at the Institute for Materials and Processes in the School of Engineering of the University of Edinburgh. The present thesis has not been submitted for any degree of professional qualification except for the one specified in the front page.

Edinburgh, 30 January 2018

Charithea Charalambous

”

Τῶν δ᾽ ὡς λόγου μόνου συμπεραινομένων μὴ εἴη ἐπαύρασθαι, τῶν δὲ ὡς ἔργου ἐνδείξιος· σφαλερὴ γὰρ καὶ εὔπταιστος ἡ μετ᾽ ἀδολεσχίης ἰσχύρισις.

[Conclusion which are merely verbal cannot bear fruit, only those based on demonstrated facts.]

— **Hippocrates**
Precepts I-II

Lay Summary

Earth's climate changes. Natural causes alone cannot explain all of these changes. It is unequivocal that human activities are contributing greatly to the global warming of the climate system, mainly by releasing billions of tons of heat-trapping gasses into the atmosphere every year. It is not a coincidence that recent relentless rise in carbon dioxide (CO_2) concentration shows a remarkably constant relationship with fossil fuel burning. About 80% of the total CO_2 emissions worldwide are generated during the combustion of fossil fuels and their use is predicted to be ever-increasing for the next few decades. This underscores the fact that humans have a great capacity to change the climate and the planet.

To date, the main international climate change agreement 'United Nations Framework Convention on Climate Change' has been ratified by 197 countries as a way to limit global temperature increases, climate change, and their consequences. Countries and nations ratified the Kyoto Protocol in 1997 and the Paris agreement in 2015 and thus are enforced to submit their strategies for significant reductions of their CO_2 emissions before 2020, in preparation of the Paris agreement. In order to remain below 2 °C, in accordance with the Paris agreement, both the First Assessment Report by the Intergovernmental Panel of Climate Change, along with many reports and studies, are considering the use of global negative emission technologies (NETs) in the second half of this century.

The capture of CO_2 directly from atmospheric air, known also as direct air capture (DAC), is a NET that has be considered by many scientists and researchers as a strategy to mitigate global warming. Although the DAC cost and energy requirements are currently prohibitive, to further understand the limitations of this technology and to bring both the cost and the energy requirements to more affordable levels competitive to other greenhouse gas removal actions research and development is needed. In this work, a temperature swing adsorption process to remove carbon dioxide from the atmosphere and to compress and purify it to levels compatible with long-term geological storage is proposed.

Abstract

Many reports, scientific papers, patents, and scientific news investigate the feasibility and affordability of direct carbon dioxide capture from the atmospheric air (DAC). Since carbon dioxide (CO_2) is extremely diluted in the atmosphere, large volumes of air have to be handled to capture comparable amounts of CO_2. Therefore, both the energy consumption and the plant size are expected to be 'prohibitive'. On the other hand, some analyses have shown that DAC is feasible and can become affordable with essential research and development. DAC has been regarded as an optional bridging or a transitional technology for mitigating CO_2 emissions in the medium-term. Priorities include investing in renewable and low-carbon technologies, efficiency and integration of energy systems, and realisation of additional environmental benefits. A heavy reliance on negative emission technologies (NETs), and consequently DAC, may be extremely risky as NETs interact with a number of societal challenges, i.e. food, land, water and energy security. Although, "...capturing carbon from thin air may turn out to be our last line of defence, if climate change is as bad as the climate scientists say, and if humanity fails to take the cheaper and more sensible option that may still be available today" MacKay (2009). Certainly, more research is necessary to bring down both cost and energy requirements for DAC.

This work firstly predicts the adsorption equilibrium behaviour of a novel temperature swing adsorption process, which captures carbon dioxide directly from the air, concentrates, and purifies it at levels compatible to geological storage. The process consists of an adsorption air contactor, a compression and purification train, which is a series of packed beds reduced in size and connected in-line for the compression and purification purposes, and a final storage bed. The in-line beds undergo subsequent adsorption and desorption states. The final desorbed stream is stored in a storage bed. This cyclic process is repeated for a number of times imposed by the required purity and pressure in the final bed. The process is been thermodynamically verified and optimised.

Since, the overall performance of this process does not only depend on the design of the process cycle and operating conditions but also on the chosen adsorbent material, further optimisation of the adsorptive and physical properties of the solid adsorbent is investigated. Thus, the optimal parameters of the potentially used porous materials is identified. Continuing the research on different adsorbent materials, an experimental investigation on the equilibrium properties of two competitive adsorbents is also performed.

Besides the thermodynamic analysis, a dynamic model is presented for the investigation of the mass and heat transfer and its influence on the adsorption rate and consequently on the overall process performance. Since the initial stream is very dilute, it is expected that the adsorption rate will be low compared to other temperature swing processes and the capture rate will be affected by the heat transfer.

Finally, the design and development of an experimental laboratory-scale apparatus is presented and analysed. Future design improvements are also discussed.

Περίληψη

Πολλές αναφορές/εκθέσεις, επιστημονικά άρθρα, πατέντες και επιστημονικές ειδήσεις ερευνούν την σποπιμότητα και οικονομική προσιτότητα της δέσμευσης διοξειδίου του άνθρακα απευθείας από τον ατμοσφαιρικό αέρα, γνωστή και ως απευθείας ατμοσφαιρική δέσμευση (ΑΑΔ). Δεδομένου του ότι το διοξείδιο του άνθρακα είναι εξαιρετικά αραιωμένο στην ατμόσφαιρα, μεγάλος όγκος αέρα πρέπει να υποστεί επεξεργασία προκειμένου να δεσμεφθούν αξιοσημείωτα ποσά διοξειδίου του άνθρακα. Επομένως, τόσο η κατανάλωση ενέργειας όσο και το μέγεθος της εγκατάστασης αναμένονται να είναι απαγορευτικά. Από την άλλη πλευρά, ορισμένες αναλύσεις έδειξαν ότι η ΑΑΔ είναι εφικτή και μπορεί να γίνει οικονομικά προσιτή με την απαραίτητη έρευνα και ανάπτυξη. Η ΑΑΔ θεωρήθηκε ως προαιρετική γεφύρωση ή μεταβατική τεχνολογία για την μείωση των εκπομπών διοξειδίου του άνθρακα μεσοπρόθεσμα. Οι προτεραιότητες περιλαμβάνουν επενδύσεις σε τεχνολογίες ανανεώσιμων πηγών ενέργειας και χαμηλών εκπομπών διοξειδίου του άνθρακα, αποδοτικότητα και ολοκλήρωση των ενεργειακών συστημάτων και πραγματοποίηση πρόσθετων περιβαλλοντικών οφελών. Μια ισχυρή εξάρτηση από τις τεχνολογίες που σκοπέυουν στην μείωση (και όχι μόνο στην σταθεροποίηση) εκπομπών διοξειρίου του άνθρακα, γνωστές και ως τεχνολογίες αρνητικών εκπομπών (ΤΑΕ), μπορεί να είναι εξαιρετικά επικίνδυνη, καθώς οι ΤΑΕ αλληλεπιδρούν με μια σειρά κοινωνικών προκλήσεων, όπως είναι η ασφάλεια των τροφίμων, του νερού και της ενέργειας. Παρόλα αυτά "...η δέσμευση διοξειδίου του άνθρακα από τον αέρα μπορεί να αποδειχθεί ως η τελευταία γραμμή άμυνάς μας, εάν η αλλαγή του κλίματος είναι τόσο άσχημη όσο λένε οι επιστήμονες περιβάλλοντος και κλιματικών αλλαγών και αν η ανθρωπότητα αποτύχει να εφαρμόσει τη φθηνότερη και πιο λογική επιλογή που μπορεί ακόμα να γίνει διαθέσιμη σήμερα" MacKay (2009). Βεβαίως, περισσότερη έρευνα απαιτείται ούτως ώστε να μειωθούν τόσο οι απαιτήσεις κόστους όσο και ενέργειας.

Αρχικά, αυτή η έρευνα προβλέπει τη συμπεριφορά μιας νέας φυσικής διαδικασίας προσρόφησης σε κατάσταση ισορροπίας η οποία λειτουργεί μέσω ταλάντευσης της θερμοκρασίας. Η μέθοδος συλλαμβάνει διοξείδιο του άνθρακα (CO_2) απευθείας από τον ατμοσφαιρικό αέρα, το συμπιέζει και το καθαρίζει σε επίπεδα συμβατά με τα απαιτούμενα για την αποθήκευση CO_2. Η διαδικασία αυτή βασίζονται στην προτεινόμενη προσρρόφηση CO_2 μέσα στους πόρους ενός κατάλληλου για αυτή την μέθοδο στερεού υλικού. Η διαδικασία συμπεριλαμβάνει έναν επαφέα αέρα για την προσρόφηση CO_2 μέσα στους πορους του στερεού υλικού που χρησιμοποιείται, ένα σύμπλεγμα συμπίεσης και καθαρισμού, το οποίο περιλαμβάνεται από μία σειρά συσκευασμένων στηλών/κιβωτίων μειωμένων σε μέγεθος και συνδεδεμένων σε σειρά για σκοπούς συμπίεσης και καθαρισμού του CO_2, και μιας τελικής στήλης αποθήκευσης. Οι στήλες υφίστανται μεταγενέστερες καταστάσεις απορρόφησης και εκρόφησης σε σειρά, που σκοπό έχουν να καθαρίσουν και να συμπιέσουν το CO_2. Η τελική αποδεσμευμένη από το εσωτερικό του πορώδες υλικού ροή φυλάσσεται σε μια τελική στήλη αποθήκευσης. Αυτή η κυκλική διαδοχική διαδικασία επαναλαμβάνεται για αρκετές φορές οι οποίες επιβάλλονται από το απαιτούμενο ποσοστό καθαρότητας και συμπίεσης στην τελική στήλη. Η διαδικασία έχει ελεγχθεί και βελτιστοποιηθεί θερμοδυναμικά.

Δεδομένου του ότι η συνολική απόδοση αυτής της διαδικασίας δεν εξαρτάται μόνο από τον σχεδιασμό του κύκλου διεργασίας και των συνθηκών λειτουργίας της αλλά και από το επιλεγμένο προσροφητικό πορώδες υλικό, η βελτιστοποίηση των προσροφητικών και φυσικών ιδιοτήτων του στερεού υλικού έχει διερευνηθεί περαιτέρω. Με αυτό τον τρόπο, οι βέλτιστες παράμετροι των ενδεχομένως χρησιμοποιούμενων πορώδες στερεών υλικών μπορούν να αναγνωριστούν. Συνεχίζοντας την έρευνα για διάφορα στερεά υλικά, μια πειραματική έρευνα διεξήχθη σχετικά με τις ιδιότητες προσρρόφησης διαφόρων αερίων μέσα στους πόρους δύο υλικών σε κατάσταση ισορροπίας.

Εκτός από τη θερμοδυναμική ανάλυση, η παρούσα μελέτη παρουσιάζει ένα δυναμικό μοντέλο για τη διερεύνηση της μεταφοράς μάζας και θερμότητας και την επίδρασή της στον ρυθμό απορρόφησης και κατά συνέπεια στη συνολική απόδοση της διεργασίας. Εφόσον η αρχική ροή είναι πολύ αραιωμένη, ο ρυθμός προσρόφησης αναμένεται ότι θα είναι χαμηλός σε σύγκριση με άλλες διεργασίες ταλάντευσης της θερμοκρασίας και ο ρυθμός σύλληψης αναμένεται ότι θα επηρεαστεί από τη μεταφορά θερμότητας.

Τέλος, ο σχεδιασμός και η ανάπτυξη μιας πειραματικής συσκευής, σε εργαστηριακή κλίμακα, παρουσιάζονται και αναλύονται. Επιπρόσθετα, μελλοντικές βελτιώσεις στο σχεδιασμό του πειραματικού συστήματος έχουν συζητηθεί.

Acknowledgements

First, I would like to thank Dr Giulio Santori for giving me a chance to work on such a novel and challenging topic, for supervising my doctoral thesis, for his lasting support in every aspect of my work and his unwavering enthusiasm.

I am also grateful to Prof. Stefano Brandani for his fruitful supervision and critical reviews during my doctoral study and for granting me the opportunity to perform a part of this thesis study in UFB, Fortaleza, Brazil. Here, I would like to extend my gratitude to Prof. Celio L. Cavalcante Jr., Dr Moises Bastos-Neto, and Dr Enrique Vilarrasa-Garcia of UFB for providing me the tools and the best resources to perform the gravimetric experiments of this study.

I would like to extend my thanks to Dr Maria-Chiara Ferrari for his critical revision during my first and third year annual reports and interviews and most importantly for acting as my second supervisor in this study. I am also grateful to Dr. Daniel Friedrich for providing me with the CySim software package license used for the dynamic model development.

An important part of this research was financially supported by EU project on Atmospheric Carbon Capture (ACCA, grant agreement no. 630863) and EU IRSES (grant no. 295156), the Offshore Gas Separation Project (OFFGAS), which are gratefully acknowledged.

I wish to extend my thanks to all the members of the carbon capture group. My special thanks go to Eleni, Alessio, Nick, Elsa, Mauro, Arran, Bruno, and Roberto for providing a great working ambience every day and for being great group mates during my doctoral study. Moreover, I would like to thank Eleni and Shreenath for their friendly and fruitful help relevant to my experimental studies in UoE.

Four years passed by fast in Edinburgh with good friends that I was lucky to find. I gained willpower and support from my IMP friends; my special friends Amanda and Sofia, but also Antonia, Dimitris, Rohan, Eva, Ares, Nelly, and many others for walking an incredibly exciting path together throughout the last years. I wish also to thank Enzo, Pedro, Paulo, Leolincoln, and Romulo for their friendship and help during my 3-month internship in Brazil.

I would like to extend my acknowledgements to the most warm-hearted person, James, for everything he did. He walked me through the difficult times and always gave me strength to carry on. Much of this would not be possible without him in my life.

Finally, I am eternally grateful to my family: my parents, Kyriaki and Soteris; my siblings, Penelope, George, and Andrea; and my grandparents, George, Charithea, and Andreas. Without their ongoing help, this work could not be accomplish on time. A special thank to my younger sister Andrea who spent two years living with me in Edinburgh. Her company, care, and unconditional love meant a lot to me. It does not matter how far (geographically) my family is, they were all always here for me with their support, encouragement, confidence, caring, and love. I dedicate this work to them.

Contents

1 Net-Zero Emissions in the Post-Paris Agreement Era: Scientific, Technological and Societal Challenges

> *We shall need a substantially new way of thinking if humanity is to survive.*
>
> **— Albert Einstein**
> (1954)

1.1 Global Warming of the Climate System

Multiple lines of evidence show changes in Earth's climate over the past century. Natural causes alone cannot explain all of these changes. It is unequivocal that human activities are contributing greatly to the global warming of the climate system, mainly by releasing billions of tons of heat-trapping gases, known as greenhouse gases (GHGs), into the atmosphere every year (Stern, 2006). Among all the human-induced climate drivers, carbon dioxide (CO_2) has the highest radiative forcing[1], is far more abundant in the atmosphere and remains there for longer than other GHGs (Le Treut et al., 2007). Today's CO_2 levels surpassed 400 parts per million (ppm) (NASA, 2017) for the first time in recorded history. It is not a coincidence that recent relentless rise in CO_2 concentration, since the beginning of the industrial era in 1750, shows a remarkably constant relationship with fossil fuel burning (NASA, 2011). About 80% of the total CO_2 emissions worldwide are generated during the combustion of fossil fuels. Their use is predicted to be ever-increasing for the next few decades enforcing the climate change, global warming, and their consequences (Sumida et al., 2012).

It has been shown that the effect of population, economic growth, industrial development, and CO_2 emissions are strongly related to the world's energy consumption (Saidi and Hammami, 2015). Figure 1.1 illustrates the world's historical and projected energy consumption by energy source for the years 1990 to 2040. It is predicted that the world's energy demands will increase and so will the world's CO_2 emissions (EIA, 2017). Looking ahead into the future, if fossil fuel burning continues at a business-as-usual rate, humanity will exhaust its reserves over the next few centuries. According to the outcomes of Scripps Institute of Oceanography, CO_2 will continue to rise to levels in the order of 1500 ppm (see Figure 1.2) (Scripps Institution of Oceanography, 2017). The atmosphere would then not return to pre-industrial levels even tens of thousands of years into the future[2] unless serious efforts

[1] *Positive radiative forcing* values of GHGs increase the Earth's energy balance by absorbing infrared radiation and re-emitting it back to the Earth's surface. Thus, GHGs result in an increase in Earth's energy budget and ultimately lead to warming.

[2] About 80 percent of the today's CO_2 emissions will be removed within a few centuries, but the remaining 20 percent will still exist in the atmosphere for several hundreds of thousand years (Inman, 2008).

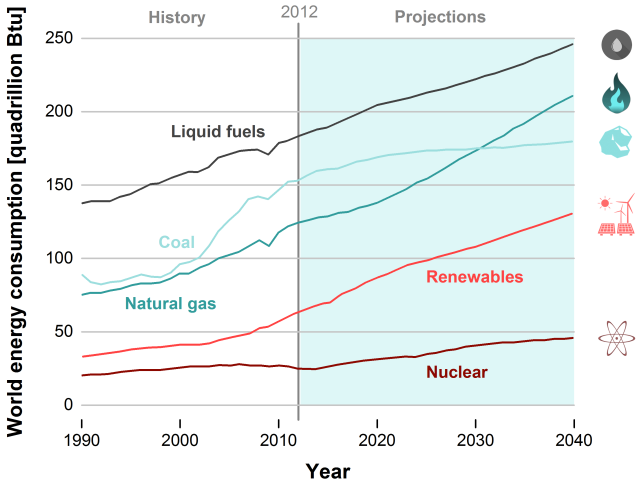

Figure 1.1. Total world energy consumption by energy source, 1990 to 2040.

Data is available online at EIA (2017).

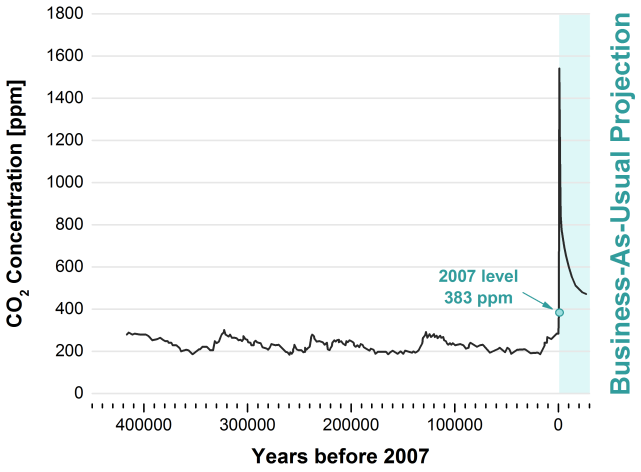

Figure 1.2. The relentless rise of carbon dioxide. 420 000 years record of carbon dioxide concentration and projection based on a business-as-usual trajectory scenario.

Analysis of air bubbles trapped in an Antarctic ice core extending back at least 400 000 years documents the Earth's changing carbon dioxide concentration (Lüthi et al., 2008).

Data is available online at http://scrippsco2.ucsd.edu/, CO_2 Program at Scripps Institute of Oceanography.

are made to reduce the dependence on fossil fuels. Figure 1.2 not only conveys the scientific measurements, but it also underscores the fact that humans have a great capacity to change the climate and the planet.

Since 1992, in the Rio Earth Summit (Keating, 1993), the need to redirect international and national plans and policies to ensure that all economic decisions fully took into account any environmental impact was recognised among all members of the United Nations (United Nations, 2012). The main international climate change agreement adopted there was the United Nations Framework Convention on Climate Change (UNFCCC). To date, it has been ratified by 197 countries as a way for nations and countries to work together to limit global temperature increases, climate change and their impacts. Two issues related to the UNFCCC are: *(i)* the Doha amendment to the Kyoto Protocol and *(ii)* the Paris agreement. The

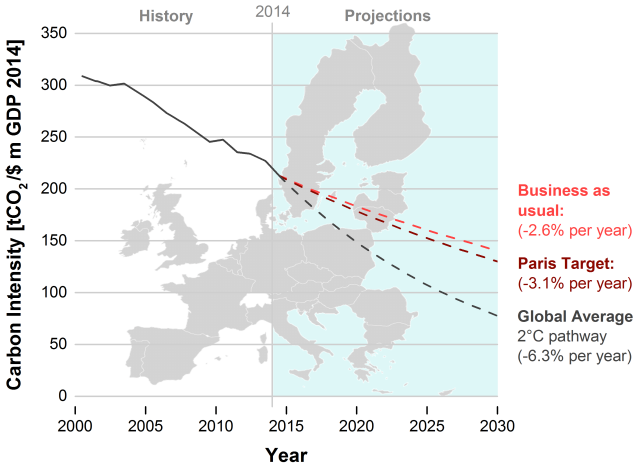

Figure 1.3. The EU's target of 40% CO_2 emissions reduction by 2030. Data is available in the PwC (2015) report.

UNFCCC countries ratified the Kyoto Protocol in 1997. The second commitment period of the Kyoto Protocol began on January 2013 and will end in 2020, under which the participating countries have committed to reducing emissions by at least 18% below 1990 levels. The United States has never signed up to the Kyoto Protocol and Canada, Russia, Japan, and New Zealand are not taking part in the second commitment period. The Paris agreement enters into force in 2020 and presents a balanced outcome with an action plan to limit global warming 'well below' 2 °C above pre-industrial levels and to pursue efforts to limit it to 1.5 °C.

In adopting the Kyoto Protocol, Europe's main key targets for 2020 are: *(i)* 20% cut in GHG emissions compared to 1990, *(ii)* 20% of total energy consumption from renewable energy, and *(iii)* 20% increase in energy efficiency (European Commission, 2017). As stated in the PwC (2015) report, the EU will need to decarbonise at 3.1% per year to reach a long-term goal of 40% reduction by 2030, which is close to the EU's business-as-usual rate as illustrated in Figure 1.3. However, the EU's Paris target brings down the emissions pathway to the long-term EU target of 80%–95% by 2050, which requires average annual decarbonisation of 6.3% (PwC, 2015). Likewise, the UK's current long-term target is a reduction in GHG emissions of at least 80% by the year 2050, relative to 1990 levels, which is consistent with the 2 °C target.

In preparation of the Paris agreement, many studies have been guided to address the required reduction of the global CO_2 emissions in order to meet the Paris targets (Friedlingstein et al., 2014; Meinshausen et al., 2015; Rogelj et al., 2015; NewClimate Institute et al., 2016; Rogelj et al., 2016; Pye et al., 2017; UKCCC, 2017). Changes in the CO_2 concentration have been predicted by employing high complexity models which consider: *(i)* the CO_2 emissions from fossil and industrial sources, *(ii)* the directly human-induced CO_2 emissions from or removals to the terrestrial biosphere, *(iii)* the contribution from oxidised methane of fossil fuel origin, *(iv)* the flux due to ocean carbon uptake, and *(v)* the net carbon uptake or release by the terrestrial biosphere due to CO_2 fertilisation and climate feedbacks (Meinshausen et al., 2011; IPCC, 2015). The Fifth Assessment Report (AR5) by the Intergovernmental Panel on Climate Change (IPCC) considers the application of global negative emissions technologies (NETs) in the second half of this century in order to obtain atmospheric concentration

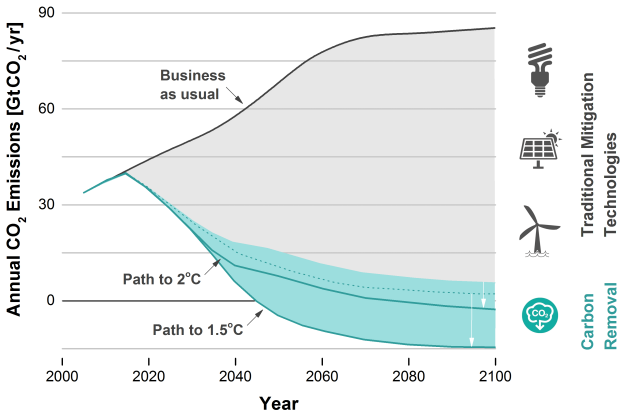

Figure 1.4. How to keep global warming below 1.5 °C or 2 °C.

Source: Mercator Research Institute on Global Commons and Climate Change.

levels of 430–480 ppm CO_2 equivalent (CO_2eq)[3] in 2100 (Fuss et al., 2014). Results have shown that in order to stay below 2 °C, CO_2 emissions will need to reach net zero by the 2050s-70s and to stay close to 1.5 °C, CO_2 emissions will need to reach net zero by the 2040s. These two paths/ global scenarios are illustrated in Figure 1.4. However, it its important to note here that the climate models employed for the predicted data are not that accurate in comparison to the short-term weather forecasts, which are based on physics that we understand reasonable well. On the other hand, slight errors in initial conditions make a forecast beyond two weeks nearly impossible.

1.2 A Boost to Keep Warming Well Below 2 °C

According to the UK Committee on Climate Change (UKCCC), significant reductions in emissions from power, heating, and transport, where zero-carbon options already exist, can be achieved. These measures among others include economy-wide improvements to efficiency, the decarbonisation of electricity, and the scaling up to markets for zero-emission vehicles and heating. Figure 1.5 provides guidance on what can be done in each sector to meet the stringency of the 1.5–2 °C limit. A report by NewClimate Institute et al. (2016) stated that a sustainable growth of renewables and other zero- and low-carbon power until 2025 is fundamental in order to reach 100% by 2050. In addition, while industrial production is expected to grow significantly, industrial emissions need to be reduced by well over 50% by 2050. Sectors like cement, ammonia, and petrochemicals need to maximise material efficiency to reduce primary material production. Other important steps include the reduction of current coal-fired power plants by at least 30% by 2025 and 65% by 2030. Efforts are needed to decarbonise the entire road transport sector. Zero-emission vehicles would have to constitute 100% of newly sold vehicles worldwide before 2035. Those measures require a particular far-reaching investment and global contribution. Therefore, their implementation seems to be unrealistic in such restricted time limits. Then, the impact on the world's economy will be immense and the shape of the energy sector will change fundamentally.

[3]Carbon dioxide equivalent is a term for describing different greenhouse gases in a common unit. For any quantity and type of GHG, CO_2eq signifies the amount of CO_2, which would have the equivalent global warming impact.

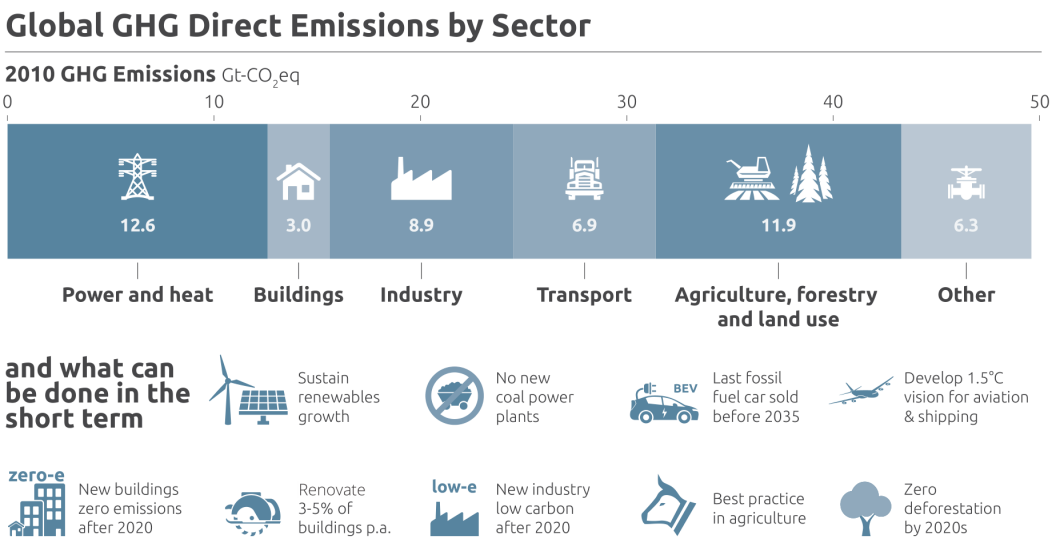

Figure 1.5. Short-term steps to limit warming to 1.5 °C.

Source: NewClimate Institute et al. (2016).
Data available at: IPCC (2015).

More challenging sectors, i.e. agriculture, aviation, and industry, are not expected to reach zero emissions on that timescale and a combination of NETs will be needed (Chichilnisky et al., 2009; Ranjan and Herzog, 2011; IPCC, 2014; Gummer et al., 2016). NETs involve: *(i)* bioenergy (energy from biomass) with carbon capture and storage (BECCS) (Creutzig et al., 2015), *(ii)* direct air capture of CO_2 from ambient air (DAC) and storage (Socolow et al., 2011), *(iii)* enhanced weathering of minerals (EW) (Schuiling and Krijgsman, 2006), *(iv)* afforestation and reforestation (AR) (Arora and Montenegro, 2011; Canadell and Raupach, 2008), *(v)* manipulation of carbon uptake by the ocean, either biologically (Joos et al., 1991) or chemically (Kheshgi, 1995), *(vi)* altered agricultural practices (Powlson et al., 2014), and *(vii)* converting biomass to recalcitrant biochar for use as a soil amendment (Woolf et al., 2010). The potential risks and opportunities afforded by all mitigation options have been studied by Smith et al. (2016). The authors stated that priorities include investing in renewable and low-carbon technologies, efficiency and the integration of energy systems, and the realisation of additional environmental benefits. A heavy reliance on NETs is extremely risky as NETs interact with a number of societal challenges, i.e. food, water and energy security, and thereby sustainable development (Smith et al., 2016). NETs in conjunction with carbon capture and storage (CCS) may be optional bridging or transitional technologies in the medium term, after 2050 (GEA and IIASA, 2012). As Schaeffer et al. (2015) declared, delayed actions to reduce GHGs emissions significantly increase the possibility of a near- and a long-term warming, shifting us far away from the 2 °C pathway. If NETs are necessary, research and development (R&D) is urgent to make these technological approaches available in the medium term. In this respect, a thorough knowledge of each NET approach is also essential in order to determine the best suited proposition to tackle climate change.

NETs vary dramatically in terms of their requirements for land, GHG emissions removed or emitted, water and nutrient use, energy produced or demanded, biophysical climate impacts (represented by surface albedo) and cost Smith et al. (2016). Table 1.1 compares the different NETs in terms of the resource implications focused on the scenario giving a

2100 atmospheric CO_2 concentration in the range of 430–480 ppm, which is consistent with a 2 °C target and is considered to be 3.3 Gt C yr^{-1} (Kriegler et al., 2015; Riahi et al., 2015). It can be seen that the EW requires large land for spreading and/or burying and the potential for carbon removal is lower than for other NETs. Even through afforestation and reforestration (AR) is relatively inexpensive compared to other NETs, the impacts on radiative forcing and consequently on water vapour content could limit effectiveness (Smith et al., 2016). Competition for land is also a potential issue, as it is for BECCS. BECCS may also be limited by nutrient demand or by increased water use, particularly if feed-stocks are irrigated and when the additional water required for CCS is considered (Smith et al., 2016). Even though the DAC cost and energy requirements are currently prohibitive, air capture is the only technological option available today able to remove the massive amount of released CO_2 from the atmosphere.

Bearing in mind the above observations, BECCS has cost that is much more reasonable and could be used to offset certain emissions (Ranjan and Herzog, 2011). However, large land requirements may limit the amount of offsets available such that DAC may play an important role in controlling CO_2 emissions. As MacKay (2009) was written:

> "...capturing carbon from thin air may turn out to be our last line of defence, if climate change is as bad as the climate scientists say, and if humanity fails to take the cheaper and more sensible options that may still be available today."

Only once all the possibilities of preventing and reducing CO_2 emissions have been exhausted will the method become essential. Eventually, the dependence on fossil fuel will end and the world will be powered by renewables. Nevertheless, as this energy utopia lies many decades in the future, by the time we arrive there, we will be burdened with an atmosphere laden with excess CO_2. As we will experience a whole series of global climates as CO_2 undergoes its rise, a consensus will likely be reached that the abnormal atmospheric CO_2 content has to be reduced. At this stage, DAC as the only present technological option able to remove massive amounts of CO_2 from the atmosphere and eventually from the oceans will become essential. R&D can help in further understanding the limitations of this technology and in bringing both the cost and the energy requirements to more affordable levels competitive with other greenhouse gas removals (GGRs).

1.3 Feasibility and Affordability of Air Capture

The method of capturing CO_2 from ambient air indicates the separation of a fairly inert and dilute component from a large volume of gas mixture (Lackner, 2009), which challenges researchers to design and deploy such a system able to efficiently capture CO_2 over nitrogen, oxygen, and argon (Keith et al., 2006). Even though the feasibility of this technology has already been proved through several lab-scale prototypes, which will be extensively discussed later in Chapter 2, its feasibility will be examined here prior to the proof of the concept.

There are several technological factors that make air capture more challenging than carbon dioxide separation from more concentrated sources, such as flue gas streams. Generally, these factors are: *(i)* the higher thermodynamic barrier due to the lower CO_2 concentration in air, at approximately 400 ppm, and *(ii)* the energy and the cost of the material to drive the air through an air capture device containing the absorbing or adsorbing material (Keith, 2009). Ever since DAC has been studied as a technology to tackle climate change, many

Table 1.1. Global impacts of NETs for the average needed global C removals per year in 2100 in 2 °C — consistent scenarios (430–480 ppm).

NET	Global C removal [Gt Ceq yr^{-1} in 2100]	Mean (max.) land requirement [Mha in 2100]	Estimated energy requirement [EJ yr^{-1} in 2100]	Mean (max.) water requirement [km^3 yr^{-1} in 2100]	Nutrient impact [kt N yr^{-1} in 2100]	Albedo impact in 2100	Investment needs (BECCS for electricity/ biofuel) [US$ yr^{-1} in 2050]
BECCS	3.3 [b]	380–700	−170	720	Variable	Variable	138 billion/ 123 billion
DAC	3.3	Very low (unless solar PV is used for energy)	156	10–300 [c]	None	None	>>BECCS [d]
EW [a]	0.2 (1.0)	2 (10)	46	0.3 (1.5)	None	None	>BECCS
AR [a]	1.1 (3.3)	320 (970)	Very low	370 (1,040)	2.2 (16.8)	Negative, or reduced GHG benefit where not negative	<<BECCS

[a] NETs with lower maximum potential than the BECCS emissions requirement of 3.3 Gt Ceq per year in 2100; mean (maximum) potentials.
[b] Results from recent studies show that BECCS deployment of around 3.3 Gt C yr^{-1} is observed for scenarios consistent with the <2 °C target (Kriegler et al., 2015; Riahi et al., 2015).
[c] Strongly dependent on different DAC technologies.
[d] Recent estimates of the total costs of DAC technologies are $1.600–2.080 per t Ceq (Chen and Tavoni, 2013).

Source: Smith et al. (2016).

researchers tried to address efficient ways to eliminate these two factors and make DAC affordable. Here, the energy and cost requirements of DAC are also discussed.

1.3.1 Feasibility. Routes to Air Capture.

An air revitalisation unit has already been developed in several space programmes for CO_2 separation from air in an enclosed atmosphere for the life support of the crew. The space carbon dioxide removal assembly (CDRA) system, used in International Space Station (ISS), employs adsorbent materials able to provide continuous CO_2 removal from the cabin atmosphere regenerating them successively by outdoor space vacuum. CDRA is a regenerative system whose principal operation utilises 4-Bed Molecular Sieve; two beds in each oxygen regeneration unit (ORU), which contains a desiccant bed and a CO_2 sorbent bed (ElSherif and Knox, 2005). The first two beds are packed with silica gel and zeolite 13X and are used to remove water that would otherwise interfere with carbon dioxide removal in the downstream zeolite 5A beds (Mattox et al., 2013). Similar system cannot be used on the earth because of its: *(i)* high energy requirements, *(ii)* unaffordable costs, and *(iii)* necessity for keeping nearly pure CO_2 on earth stored and compressed.

More recently, Lee et al. (2015) developed a system to maintain suitable indoor air quality based on electric swing adsorption (ESA) that splits the air into two portions: waste gas for removal, and recovery air for recycling back into the living space. The electrical energy requirement for treating air containing 3000 ppm CO_2 is in the range of 57.8 kJ m^{-3} of air under 20 °C selected temperature swing (Lee et al., 2015), which is equivalent to 456 kJ $molCO_2^{-1}$. However, such a system cannot be used for the purpose of this study, as CO_2 is required to be captured from an extremely dilute mixture of approximately 400 ppm and the electrical energy use is expected to be unprofitable.

It is required that an air capture device should have the following characteristics:

(i) DAC should be able to produce a stream of CO_2 from ambient air at a purity greater than 95% to allow CO_2 long-term geological storage (Brandani, 2012). In order to achieve this goal, this process is expected to include a section for CO_2 separation from air and a section for CO_2 concentration to high purity (Brandani, 2012). Climate change mitigation requires not only that CO_2 be separated from air on a much larger scale, but also that CO_2 be sequestered for millennia. The case of geological sequestration requires CO_2 to be concentrated from its ambient levels to high purity, >95% (Markewitz et al., 2012), as well as compressed to typically 73.8 bar supercritical pressure (Goos et al., 2011) to be efficiently transported and stored in geological formations (House et al., 2011).

(ii) Capturing CO_2 directly from atmospheric air requires the processing of an extremely large volume of air, far greater than other traditional CCS technologies, in order to capture comparable amounts of CO_2. This fact has significant implications on energy consumption and the required plant size. Consequently, pre-processing of air, such as drying, heating, cooling, or pressurising is expected to be unprofitable and should not be implemented in DAC (Lackner et al., 2012). This rules out technologies typically used for small-scale air capture such as membrane separation, where large pressure gradients and multiple passes are required to achieve a high-purity CO_2 stream (Brunetti et al., 2010), and cryogenic separation, where cooling and compression are required. In addition, the use of solids, such as zeolite, activated carbon, and alumina-

based molecular sieves, which are adversely affected by moisture and low adsorption capacities at ambient conditions, should be avoided (Boot-Handford et al., 2014).

(iii) In addition, DAC also requires energy to drive fans that suck in the air and channel it through the capture unit. Due to the pressure drop across the unit, the fan has to provide the air at an initial pressure, which requires more energy. Unless this energy comes from carbon-free sources, the net yield of CO_2 captured is rather poor.

(iv) Carbon dioxide in the air is so diluted that we would need a sorbent that can provide strong bonds with CO_2. What's more, this binding agent also needs to be easy to recycle and to facilitate thousands of cycles. Whilst both capture processes require energy to regenerate the sorbent, the energy demand scales proportionally to the mass of CO_2 captured as opposed to the volume of air processed.

There are several examples in the literature attesting that adsorbent processes are best suited for gas separation applications, especially for the removal of trace gas impurities from a gas mixture (Drioli and Barbieri, 2011) aiming to achieve extremely high purities, as high as 99.999% (Joss et al., 2015). For instance, the separation and concentration of carbon dioxide dilute gas from atmospheric air (Diagne et al., 1996) or the high enrichment and recovery of dilute hydrocarbons (Mc Intyre et al., 2002) have already been studied and developed by applying dual refluxed pressure swing adsorption (PSA). In addition, the removal of dilute organic contaminants, solvent vapours, or odour forming compounds from air or other industrial gases are frequently achieved by selectively adsorbing the impurity at near ambient temperature using packed activated carbon beds (Sircar et al., 1996). For instance, the removal of traces of mercury vapour from air with a concentration of 1 to 2 ppm(v) by temperature swing adsorption (TSA) can currently be reduced to less than 1 ppb(v) (Wankat, 1986; Otani et al., 1986; Vidic and Siler, 2001).

Classical CO_2 adsorbents have been primarily evaluated for the separation of moderately dilute CO_2 (<12%) from gas mixtures, such as flue gases, and not for the separation of extremely low CO_2 partial pressures as found in ambient air (Choi et al., 2011c). This constraint is significant since it cuts down the list of potential adsorbents for the air separation of CO_2, where CO_2 occurs to the extent of 400 ppm in atmospheric air. The selection of the proper adsorbent is a critical step in adsorption applications mostly because sorbents affect the overall process performance and economics (Choi et al., 2009b). It is not straightforward to choose the most promising adsorbent a priori, as there is no single, ideal adsorbent. Industrial processes frequently use zeolite 13X for the removal of CO_2 impurity during air pre-purification due to the high capacity and the steep nature of the CO_2 isotherm on zeolite 13X at low partial pressures making it ideal candidate for TSA applications (Rege et al., 2000). Indeed, according to Choi et al. (2009b), physisorbents such as activated carbons and zeolites exhibit competitive CO_2 adsorption capacities near ambient temperature and display excellent regenerability. However, physisorbents are typically hindered by the moisture resulting in the necessity of pre-treatment steps prior to adsorption (Choi et al., 2009b; Choi et al., 2011c; Rege et al., 2000).

The CO_2 separation from an extremely dilute stream have been proved to be feasible. Extracting gigatonnes of CO_2 from the atmosphere, therefore, requires CO_2 to be compressed and purified to levels imposed by CO_2 geological storage. Although the energy cost to separate CO_2 is expected to be significantly high, concentration and compression steps

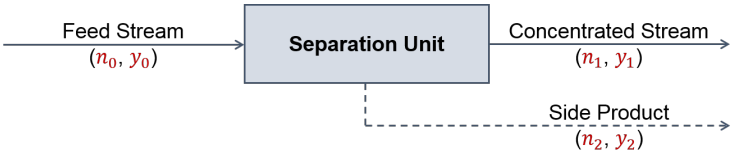

Figure 1.6. A schematic representation of a binary stream that enters the 'black box' ideal separation unit, where work is required to separate the pure in targeted component stream and the side product stream.

increase further the energy and cost of the process. In the following subsection, the energy use and process economics are addressed.

1.3.2 Value Function and Thermodynamic minimum work

For the DAC process evaluation, it is necessary to provide an estimation of the required energy costs since they have a major impact on the overall process economics (Brandani, 2012). One approach is to determine the process efficiency, which is defined as the ratio of the thermodynamic minimum work of separation (W_{min}) to the actual energy required by the process. This has been studied by House et al. (2011). Another approach is to assume a hypothetical idealised separation process, an 'ideal cascade' of ideal separation stages, providing an estimate of what it might be possible to achieve in an optimally designed separation process (Pratt, Henry R. C., 1967). As described by Ruthven (2014), this can be evaluated by the separative work, which is derived by the 'value function'.

It is postulated that a value function can be defined such that an increase in value over a theoretical stage is proportional to the energy input (δU), which is proportional to the total feed rate (F) (Ruthven, 2014). $\delta U/F$ is assumed proportional to the difference in the 'value functions' $V(y)$ of the outlet and inlet streams weighted according to their flow rates as

$$\delta U/F = \theta\, V(y_1) + (1-\theta)\, V(y_2) - V(y_0). \tag{1.1}$$

Here, θ refers to the fraction of the feed to the stage that flows in the 'forward' direction, F is the molar feed rate, and y is the molar fraction of the 'targeted trace' (dilute) component in each stream as depicted in Figure 1.6.

The separative work as a function of feed and product stream compositions provides an estimate of the lower limit of the actual work of separation while the thermodynamic minimum work is simply the negative of the free energy of mixing (Ruthven, 2014). The expression for the dimensionless theoretical minimum work, W_{min}, for separating a binary mixture into two product steams as illustrated in Figure 1.6 where all the streams consist of ideal mixtures at constant temperature and pressure, is reduced to the difference between the total Gibbs Free Energies (G) of the product streams and the feed stream (Brandani, 2012) and is governed by

$$\begin{aligned} -W_{\text{min}} &= \frac{\Delta G}{RT} \\ &= n_1\ (y_1 \ln y_1 + (1-y_1)\ln(1-y_1)) + n_2\ (y_2 \ln y_2 + (1-y_2)\ln(1-y_2)) \\ &\quad - n_0\ (y_0 \ln y_0 + (1-y_0)\ln(1-y_0))\,, \end{aligned} \tag{1.2}$$

where n refers to the moles in each stream (0: feed, 1: concentrated stream, 2: side product), y is the molar fraction of the 'targeted trace' (dilute) component in each stream, R is the ideal gas constant, and T denotes the temperature.

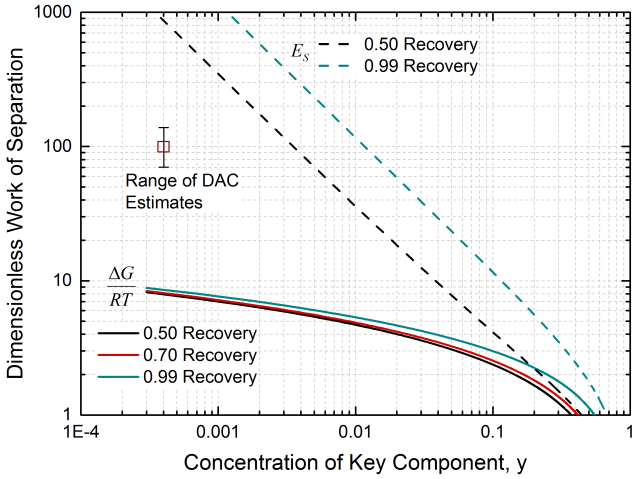

Figure 1.7. A comparison of the thermodynamic minimum work of separation $W_{\min}$ and the value function E_{s} required for separating a binary mixture considering 95% purity and 0.5, 0.7, and 0.99 recovery of the trace component.

Note that the separation factor 'a' for the calculation of the value function $V(y)$ was set to 100, as described by Ruthven (2014).

In the value function model the corresponding expression for the dimensionless minimum separative work is given by

$$E_{\mathrm{s}} = \left[n_1\, V(y_1) + n_2\, V(y_2) - n_0\, V(y_0)\right]/4, \tag{1.3}$$

where $V(y)$ is the 'Value Function' as developed by Ruthven (2014) as

$$V(y) = (2\,y - 1)\,\ln\left(\frac{a\,y}{1-y}\right). \tag{1.4}$$

Here, a is the only free design variable and is directly related to the fractional recovery. The recovery ratio is the amount of trace component captured divided by the amount of trace component in the inlet stream, which is defined as

$$Rec = \frac{n_1\,y_1}{n_0\,y_0}. \tag{1.5}$$

A comparison between the value function and the theoretical minimum work required to separate a stream of 400 ppm trace gas (y_0=4×10^{-4}) into one stream of highly concentrated trace component (at 95% purity where y_1=0.95) and a second stream of pure side product is illustrated in Figure 1.7.

High recoveries (∼0.99) can be selected also for extremely dilute streams which require, according to Eq. 1.5, lower inlet flow of gas that drops the size of the units resulting in lower capital cost. Although, as a relatively pure product is extracted from a very low concentration feed, the actual work of separation is expected to be greater than the thermodynamic minimum (Brandani, 2012; Ruthven, 2014). The minimum energy requirement estimated from cascade theory is substantially greater than the thermodynamic minimum work of separation, which significantly increases at very low feed concentration. Since no practical experience exists separating dilute gas mixtures consuming an amount of energy proximal to the ideal free energy of mixing (House et al., 2011; Zhao et al., 2017), considerations based on the separative work may reveal the intrinsic energy intensity of dilute gas separation processes (Brandani, 2012; Ruthven, 2014).

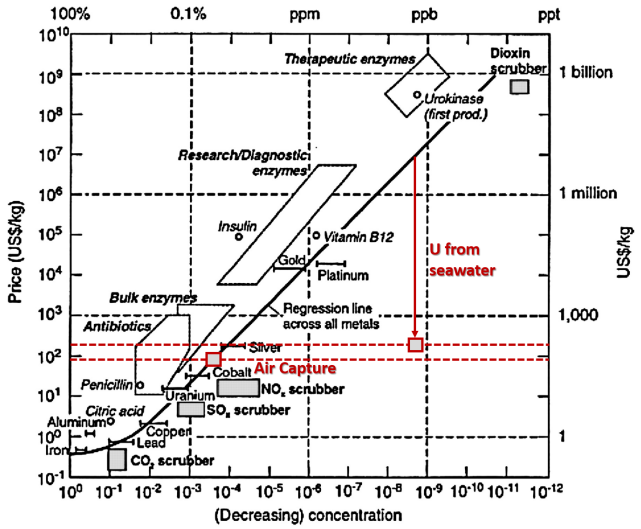

Figure 1.8. A Sherwood plot showing the relationship between the concentration of a target material in a feed stream and the cost of removing the target material.

Source: Dahmus and Gutowski (2007)

For the case of air capture, the theoretical minimum work of CO_2 separation is around 20 kJ mol$CO_2{}^{-1}$, where the minimum separative work (for 50% recovery) increases by two orders of magnitude to around 2 MJ mol^{-1} of CO_2 captured. By considering the value function approach, constrains on recovery are imposed by economic considerations. This becomes obvious for the case of 99% recovery where the minimum separative work becomes around 8 MJ mol^{-1} of captured CO_2.

1.3.3 Capital and Operating Costs

Sherwood plot, Figure 1.8, an empirical relationship between the market price for separating a substance and its initial concentration in the dilute mixture, may lead one to observe that such a process will unlikely succeed due to unaffordable cost requirements to separate dilute mixtures, which scale in proportion to the initial trace gas concentration (Dahmus and Gutowski, 2007; House et al., 2011). However, mismatches of cost estimates on novel technologies and continuous drops of prices due to development, mass production, and learning by doing suggest that Sherwood plot can be "broken" (Lackner et al., 2012). There are examples that show that the Sherwood plot can be broken, such as the extraction of uranium from seawater (see Figure 1.8), which exists at 3 parts per billion (ppb) and costs around \$300 kgU^{-1} (Schneider and Sachde, 2013). An accurate estimate today of future costs is simply impossible; not surprisingly, cost estimates of novel technologies have often been wrong (Lackner et al., 2012).

A relationship between the capital cost (size of the system) and the operating cost (mainly energy requirements) using the cascade method has been studied from Ruthven (2014). He found that the separative work decreases monotonically with the concentration of the trace species in the side production stream, y_2. In other words, low process recoveries will lead to lower operating cost and higher feed rates. Higher feed rates are proportional to the size of the system and will then require larger volumes that increase the capital cost of the system.

Table 1.2. Specifications and performance of air capture.

Property	Requirement	Reference
Solar energy available [a]	4.7–8.1 MJ m^{-2} day^{-1}	Santori et al., 2012
Minimum required purity	95%	Markewitz et al., 2012
Maximum level of impurities	y_{H_2O}<0.05%; $y_{N_2}+y_{O_2}+y_{Ar}$<4%	Markewitz et al., 2012
Recovery	50%	—
Specific energy demand [b]	< 45.4 MJ $kgCO_2{}^{-1}$	—
Surface area for 1 $GtCO_2$ capture	< 50 000–87 000 km^2	—
Capture Rate	> 380–660 tCO_2 ha^{-1} yr^{-1}	—
Pressure	> supercritical (73.8 bar for pure CO_2)	Mazzoccoli et al., 2014
Wind energy available [c]	0.7 MJ m^{-2} day^{-1}	—

[a] Assuming 50% of solar energy collection efficiency.
[b] Optimistic value obtained from the calculations of the value function (Ruthven, 2014; Ruthven et al., 2015).
[c] The available wind energy is presented here for comparison with the available solar energy. An installed capacity density of 8 MW km^{-2} has been used as considered by Dupont et al. (2018).

Therefore, if energy costs are dominant, the system should operate at high y_2, low fractional recovery with y_2 approaching y_0 (Ruthven, 2014).

1.4 The Use of Adsorption Based Systems

1.4.1 Performance and Limitations of Air Capture

Table 1.2 summarises the specifications and performance of an air capture system considering the requirements that should be fulfilled by a DAC technology to enable long-term geological storage. By setting a goal to capture 3.3 Gt CO_2 yr^{-1}, to achieve the 2 °C target[4], and by designing our process using the cascade method (assuming 2 MJ $molCO_2{}^{-1}$ or else 45.4 MJ $kgCO_2{}^{-1}$ specific energy), 150×10^9 GJ yr^{-1} are required. This is equivalent to a power of 4.6 TW. To put this into perspective, around 11 840 TW is the world's energy demand which, by considering 100% to come from solar and wind energy, is supplied from about 40% wind and 60% solar (Jacobson et al., 2017). Therefore, DAC is expected to require, per year, 0.04% of the total world's energy consumption, if it is powered only by renewables. Among all the renewable energy primary sources, only solar energy can deal with the DAC scale of deployment unless smaller scales are deployed. For instance, the installed capacity density of wind is much smaller than that obtained from solar (see Table 1.2). In case of the employment of solar thermal energy, the capture rate will be as high as 380–660 tCO_2 ha^{-1} yr^{-1}. To put it in context, trees with high carbon capture rate, like Fagus Sylvatica, can capture around 4.9 tCO_2 ha^{-1} yr^{-1} (Song et al., 2014).
Among all the renewable energy primary sources, only solar energy can deal with the DAC scale of deployment unless smaller scales are deployed. For instance, the installed capacity density of wind is much smaller than that obtained from solar (see Table 1.2).

As stated in the literature, CO_2 abatement costs for DAC are high, ideally quoted between 100–200 US$ $tCO_2{}^{-1}$ (Jones, 2008). In order to capture 3.3 $GtCO_2$ yr^{-1}, an investment amounting to $330–660 bn yr^{-1} is then required. This is equivalent to the total charitable donations of $390 bn yr^{-1} in 2016 (Giving USA, 2017). Studies on air capture predict air capture cost between $100 and $1000 per tonne CO_2. Simon et al. (2011) reported that by

[4]The maximum level of deployment of DAC could yield to ∼10 GtCeq yr^{-1} in 2100, as reported by Smith et al. (2016) and Fuss et al. (2014). Levels of implementation of NETs that are consistent with a <2 °C target (i.e. with concentration levels of 430–480 ppm CO_2-eq. in 2100), as investigated in the IPCC AR5 report for the deployment of BECCS, were 3.3 GtCeq yr^{-1} in 2100. 3.3 GtCeq yr^{-1} is equivalent to 6% of the global CO_2 emissions by 2020.

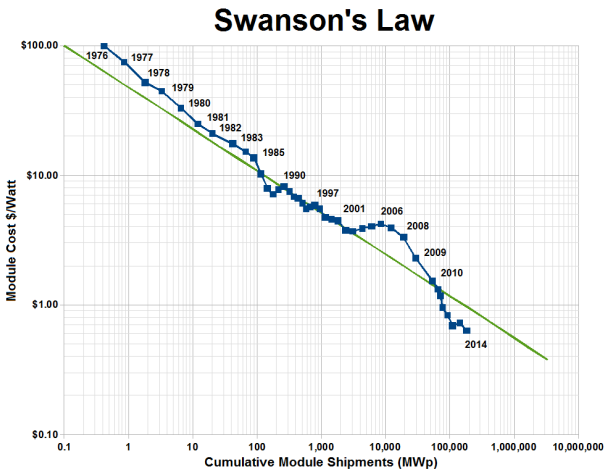

Figure 1.9. Swanson's law: the learning curve of photovoltaics.

Source: Wu et al. (2017).

achieving high second law capture efficiencies (on the order of 10%) and relatively inexpensive capture devices (on the order of \$0.5M per capturing device of 1 tCO_2 day^{-1}), the cost can be reduced down to 300 US\$ ${tCO_2}^{-1}$. At this stage of development, by considering the costs of the capture devices, energy supplies, water supplies (if any), and sequestration resources, this value has not been reached yet. Further research and development is expected to reduce the cost of the process, especially when it targets on minimising the capture device capital cost and the energy system overall cost. Solar PV in the 1980s can provide an analogue; costs for PV panels have come down by nearly two orders of magnitude over the past 30 years (see Figure 1.9). As stated by Lackner (2009), DAC cost can be competitive, between \$30–100 ${tCO_2}^{-1}$ of compressed CO_2, once direct air capture systems are manufactured at scale. However, the uncertainty of this estimated cost is high and a reliance on its value will put the readers off the scent by creating unrealistic expectations.

DAC technologies could follow steep cost reduction curves like solar PV, but only a few projects have been built, and cost data for these projects is scant. Since there are only limited projects of DAC that have published cost estimations for their initial pilots, further deployment is needed in order to confirm the slope of the cost reduction curve.

1.4.2 Design Strategy and Design Criteria

As previously discussed, only adsorption systems can still efficiently work at such low partial pressures required for air capture. Adsorption based separation has already been used to remove trace gas impurities and achieve extremely high purities. The design of sorption systems is based on few underlying principles (LeVan et al., 1998):

(i) The knowledge of adsorption equilibrium between solutes in the fluid phase and the solute-enriched phase of the solid is fundamental. The selection of the adsorbent material is primarily based on its equilibrium properties (i.e., capacity and selectivity as a function of temperature and component concentrations).

(ii) Since the adsorption takes place in batch, fixed beds, the process has a dynamic character. Fixed bed processes often approach a periodic condition or cyclic steady state with several different steps constituting a cycle. Thus, some knowledge on how

transition travels through the bed is important. This approach introduces both time and space into the analysis as for a good design it is crucial to understand the fixed beds performance in relation to the equilibrium and dynamic behaviour.

(iii) Many practical aspects must be considered. These aspects are process-specific including at first an understanding of dispersive phenomena at the bed scale, then for regenerative processes, knowledge of ageing characteristics of the adsorbent material, with consequent changes in sorption equilibrium and at last, the correct design of the operational steps and instrumentation.

One may recognise five important criteria for any relevant DAC process via adsorption (Jones, 2013):

(i) The ultra-dilute nature of CO_2 (ca. 400 ppm) in the atmosphere requires very large volumes of air to be moved through the process. Since power is a function of the flow rate and pressure as: $\text{Power} = \dot{V}\,\Delta P$, any air capture process must have very low pressure drops associated with flow through the process to prevent excessive energy requirements for gas movement.

(ii) Since the ambient CO_2 concentration is extremely low, air capture processes must employ solid materials or fluids with high CO_2 capture capacities, via use of materials with a very high density of adsorption sites and/or very strong CO_2-adsorbent interactions.

(iii) A practical air capture process must also have favourable adsorption kinetics to allow for short cycle times, as long cycle times would lead to impractical plant sizes associated with large inventories of adsorption media.

(iv) Because absorption and adsorption are exothermic processes, the removal of CO_2 from the capture media for concentration is endothermic and can require significant energy input. This regeneration energy must be provided at low cost, ideally in the form of low-grade waste heat or renewables. It will be futile for a DAC process if CO_2 is captured using energy that, as a net effect, produces CO_2.

(v) Finally, the process equipment and adsorption media must have a suitably long lifetime, as the above factors will make air capture a capital-intensive process with large plant sizes compared to many traditional gas separation processes.

The underlined design strategy has been followed here in order to identify the design parameters and characteristics of the present process. In addition, the design criteria have been considered in order to improve the overall performance of the process and make it competitive with other technological alternatives.

1.5 Objectives and Outline of this Thesis

The world's incomparable economic growth and prosperity unearth new needs and requirements and subsequently demand new sustainable technological options. One of the main challenges of this century is to transition to technologies that simultaneously address the world's most fundamental demands, i.e. efficient systems, energy and economic competitiveness, and environmental responsibility. Only with careful targeted research and development, improvements in the cost and performance of a new technology can be achieved. Advanced technologies can have significant impact on the next generation of challenges; especially

deep reductions in GHG emissions have been proved essential (Fuss et al., 2014). Deep reductions in emissions from power, heating, and transport, where zero-carbon options already exist, can be achieved. More challenging sectors, i.e. agriculture, aviation, and industry, are not expected to reduce significantly their emissions in the short term and a combination of NETs may be required (IPCC, 2014; Gummer et al., 2016).

At this stage, air capture is the only technological option available today able to remove massive amounts of the already emitted CO_2 from the atmosphere and eventually from the oceans. Since DAC is still at a very early stage of deployment, further research and development becomes essential, especially due to economic and technological challenges arising from the dilute nature of CO_2 in air. In order to make DAC competitive with other GGRs, cost and energy requirements have to be significantly reduced. Here, a competitive temperature swing adsorption process able to capture, compress, and purify CO_2 in subsequent steps is presented. Challenges such as lower energy consumption, higher final purity and recovery, elimination of pressure drops especially in the capture unit, identification of the most suitable adsorptive and physical properties of the selected material and process operational conditions have been addressed. Other parameters, such as mass and heat transfer inside the adsorbent material and diffusion and dispersion along the bed, have also been investigated. Finally, an experimental apparatus has been designed in order to prove the concept and the simulation results and improve the overall performance of the process.

Chapter 2

A number of researchers have demonstrated different paths to extract CO_2 from ambient air and various process designs that might be used as a mode of combating climate change. Currently, few academic groups and start-up companies work exclusively on direct air capture. Some of the most interesting air capture prototypes of few start-up companies, i.e. Carbon Engineering, Climeworks, and Global Thermostat, are analysed in this chapter. Also, a description and a comparison of several evaluated potential air capture approaches that are still under research are investigated.

Chapter 3

The first stage to design and model an adsorption process is to study its adsorption equilibrium behaviour so that the process can be proved and improved and its inherent limits imposed by thermodynamics can be identified. Principally, the study of the adsorption equilibrium of the process requires the consideration and determination of four parameters. These are: *(i)* the components that the process consists of, i.e. the fluid, the solid or else adsorbent, the adsorption column, *etc.*, *(ii)* the thermodynamic phases of the system, i.e. the gas phase, the liquid phase, the solid phase, *(iii)* the physical and adsorption properties of all the above, and *(iv)* the suitable conditions under which the process must operate. Thus, this chapter focuses on: *(i)* describing a thermal swing adsorption process for the removal, concentration, and compression of a trace contaminant from a gas fluid, *(ii)* modelling the multi-component adsorption equilibria of the process, and *(iii)* designing and improving the performance of the process through optimisation techniques. By the end of this chapter, directions to the optimal characteristics of the process cycle, operational conditions, and the chosen adsorbent material are proposed in order to achieve the best process performance.

Chapter 4

Theoretically, by optimising the adsorptive and physical properties of the adsorbent, the over-

all performance of the process can be improved. The process investigation and optimisation of the previous chapter aimed to elucidate the key features of the process and the material based on equilibrium approach. By embodying these optimal equilibrium adsorption and process characteristics, this chapter focusses firstly on the theoretical investigation of other aspects that have not yet been considered, such as the bed void fraction, which depends strongly on the design of the bed, and the crystal density of the adsorbent material. This chapter also provides an experimental investigation of two competitive air capture adsorbents by equilibrium gravimetric adsorption measurements. Results have shown that further research is needed in order to design the most suitable adsorbent. In addition, directions on the ideal structural characteristics of each fixed bed and physical parameters of the solid have been suggested.

Chapter 5

Besides the adsorption equilibria, to properly design an adsorption process, improve, and optimise its overall performance, the overall packed-bed system dynamics including the intrinsic sorption kinetic behaviour of a single particle, axial dispersion, and mass and heat transfer resistances are required (Ruthven, 1984). The reason for this additional investigation is simply that most practical solids in industries are porous and the overall adsorption rate is limited by the ability of adsorbate molecules to diffuse inside the particle interior (Do, 1998). This chapter focused on addressing the process non-equilibrium and its influence on the adsorption rate and consequently on the overall process performance.

Chapter 6

The target of this study is to develop an efficient unit, a prototype cable of capturing CO_2 and releasing a compressed and purified CO_2 stream for CO_2 storage. Therefore, after the examination of the adsorption equilibrium of the DAC system, the optimisation of the process and the theoretical and experimental investigation of possibly used adsorbent materials, the design and development of the experimental system follows. The experimental apparatus is designed to prove the concept of separation, concentration, and compression of the system. Further improvements of the performance of the system are also proposed.

Chapter 7

The last chapter addresses the final conclusions based on process evaluation, process design limitations and performance, scaling up considerations of the presented air capture system, and future improvements and recommendations.

2 Direct Air Capture: Necessity, Feasibility, Affordability, Performance and Limitations

An air capture technology able to capture CO_2 directly from ambient air was first proposed by Lackner et al. (1999) as a way to address global CO_2 emissions and climate change. The authors suggested an air flowing system over recycled chemical sorbents such as highly alkaline solutions, moderate alkaline solutions, and activated carbon substrates (Lackner et al., 1999; Dubey et al., 2002; Lackner, 2003). Since then, a number of researchers have demonstrated different paths to extract CO_2 from ambient air and various process designs that might be used as a mode of combating climate change. Currently, few academic groups and start-up companies work exclusively on direct air capture. Some of the most interesting air capture prototypes of few start-up companies, i.e. Carbon Engineering, Climeworks, and Global Thermostat, will be analysed here. This chapter also includes a description and a comparison of several potential air capture approaches that are still under research.

2.1 The Direct Air Capture Technologies

Following Lackner's suggestion to develop air capture technologies as a mode of combating climate change, initial attempts centred on existing technologies for CO_2 removal from air (Jones, 2011) concentrated on absorption via aqueous hydroxide solutions (Tepe and Dodge, 1943; Spector and Dodge, 1946; Blum et al., 1952; Steinberg and Dang, 1977). Thus, Zeman and Lackner (2004) described the thermodynamic feasibility of a specific hypothetical method of DAC, which is presented in Figure 2.1. This method is based on a web scrubbing technique to absorb CO_2 from air into an aqueous sodium hydroxide solution, NaOH, to give dissolved sodium carbonate, $NaCO_3$, as

$$2\,NaOH(aq) + CO2(g) \longrightarrow Na2CO3(aq) + H2O(l), \quad \Delta H^{o} = -109.4\ \text{kJ mol}^{-1}.$$

The resultant carbonate is then transferred from sodium ions to calcium ions via causticisation and the captured CO_2 is released from the calcium carbonate through calcination, thermal decomposition. The hydration of the lime completes the cycle producing calcium hydroxide ($Ca(OH)_2$) that is recycled and produced through the electrolysis of sodium chloride with a small amount produced via causticisation process as

$$Na2CO3(aq) + Ca(OH)2(s) \longrightarrow 2\,NaOH(aq) + CaCO3(s), \quad \Delta H^{o} = -5.3\ \text{kJ mol}^{-1}.$$

The produced calcium carbonate results, due to its low solubility, in the formation of precipitates that are removed from solution and dried prior to calcination. Once dry, the calcite precipitate is thermally decomposed in a kiln, which is fired with oxygen to regenerate the gaseous CO_2 at temperatures higher than 900 °C (best reached efficiency is 90%) as

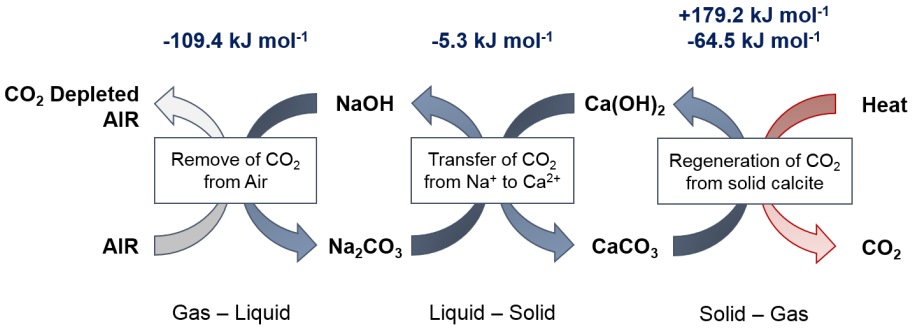

Figure 2.1. A schematic overview of the first process proposed for air capture. An alkaline sodium air capture process including an air separation unit (ASU).

$$\mathrm{CaCO3}(s) \longrightarrow \mathrm{CaO(s)\,CO2}(g), \quad \Delta \mathrm{H^o} = +179.2\ \mathrm{kJ\ mol^{-1}}.$$

Finally, the hydration of the lime as

$$\mathrm{CaO(s)} + \mathrm{H2O(l)} \longrightarrow \mathrm{Ca(OH)2}(s), \quad \Delta \mathrm{H^o} = -64.5\ \mathrm{kJ\ mol^{-1}},$$

completes the cycle. Then, CO_2 has to undergo pressurisation and storage steps (Baciocchi et al., 2006).

Later on, Keith et al. (2006), Baciocchi et al. (2006), and Zeman (2007) examined the energetic and economic analysis of the sodium/calcium cycle using packed column contactors. Moreover, Stolaroff et al. (2006) and Zeman (2008) investigated experimentally the combined sodium/calcium capture process. The researchers proposed the use of the state-of-the-art structured packings; designs involved a spray tower design with a vertical flow pattern or intermittently-wetted cross-flow packed tower geometries, for lower pressure drop and high throughput (Zeman, 2007; Holmes and Keith, 2012). Since the overall energy requirements were quite significant, as the carbon intensity of electricity production varies from 190–1900 kJ mol$CO_2{}^{-1}$ (Lackner, 2009), research moved towards new or modified designs.

Traditional kilns could not be used for regeneration, since they are typically fired with fossil fuels and air resulting in the dilution of CO_2 in the fuel gas. For this reason, oxy-firing kilns would be needed and additional costs for the production of pure oxygen would need to be included. This approach requires energy range of 350–750 kJ mol$CO_2{}^{-1}$ (Baciocchi et al., 2006; Zeman, 2007) with drying, pre-heating and calcining of the $CaCO_3$ (energy required to break the strong carbonate bond) accounting for the majority of the total energy demand. As consequence, CO_2 abatement costs for this process are high, typically quoted between 100–200 US$ t$CO_2{}^{-1}$ (Jones, 2008), 300 US$ t$CO_2{}^{-1}$ (Simon et al., 2011; Zeman, 2014), 600 US$ t$CO_2{}^{-1}$ (Socolow et al., 2011), and 1000 US$ t$CO_2{}^{-1}$ (House et al., 2011).

Figure 2.2 summarises some of the suggested technologies, which are discussed extensively later on: *(i)* The sodium hydroxide scrubbing technique or else wet absorption/scrubbing, *(ii)* the calcium oxide pellets that adsorb CO_2 at moderate temperatures, ca. 400 °C, and release it at high temperatures, ca. 1000 °C, and *(iii)* the use of ion exchange resins in a novel humidity swing process. Adsorption-based systems via TSA and temperature and vacuum swing adsorption (TVSA) have also been considered as a more efficient separation

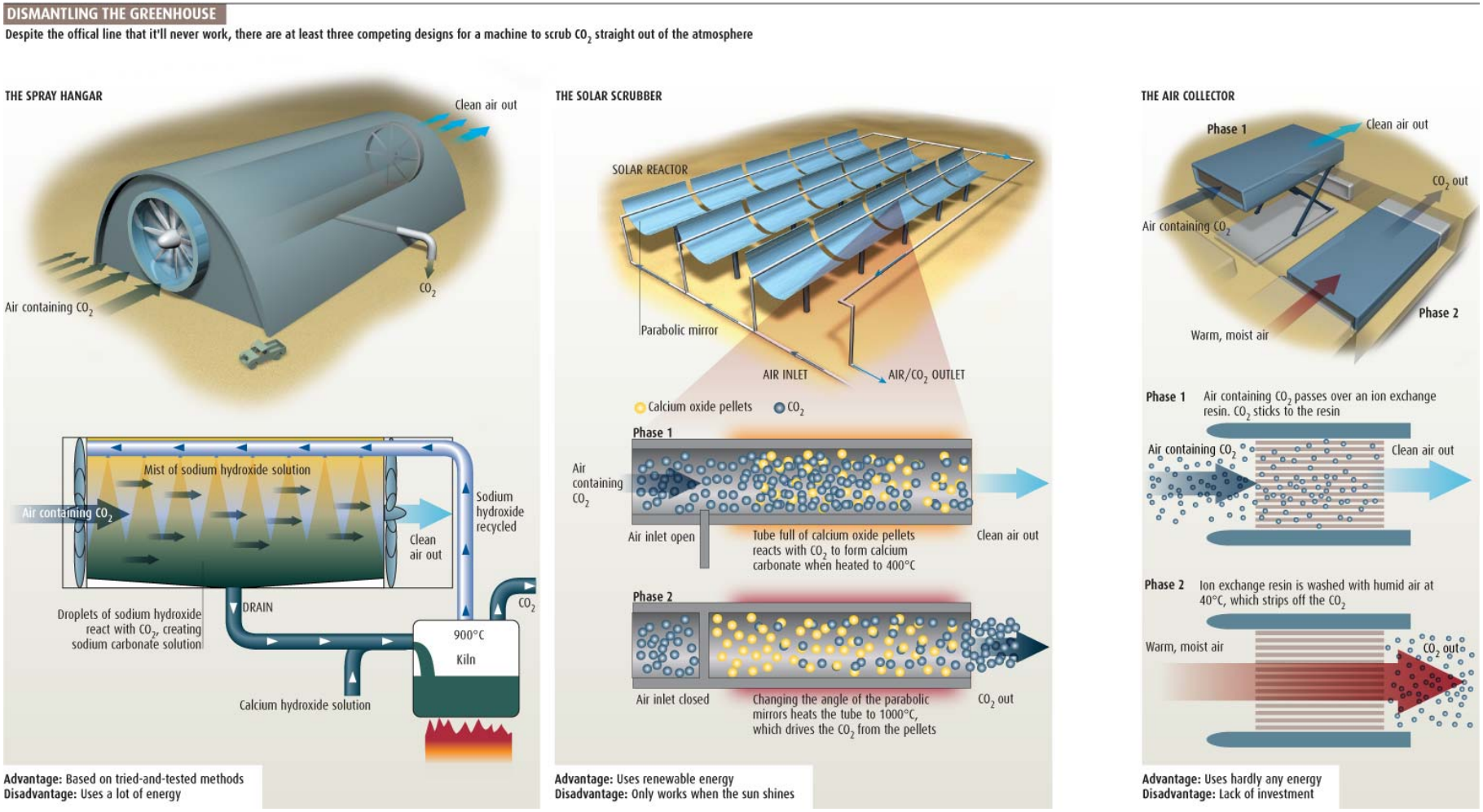

Figure 2.2. The air capture approaches: *(i)* the sodium hydroxide scrubbing that requires the use of natural gas in a kiln and heat at 900 °C to release CO_2, *(ii)* the calcium oxide pellets to adsorb CO_2 and release it in a solar reactor, and *(iii)* the ion exchange resin that requires the flow of warm moist air to strip off the CO_2.

Source: Kunzig and Broecker (2009).

for extremely dilute processes and for providing high purities. A TSA process via physical adsorption has also been developed for the purpose of this study and thus it is more analytically discussed.

Classical CO_2 adsorbents have been primarily evaluated for separation of moderately dilute CO_2 from gas mixtures, such as fuel gases, and not for separation of extremely low CO_2 partial pressures such those found in ambient air (Choi et al., 2011c). This constraint significantly cuts down further the list of potential adsorbents for the air separation of CO_2, where CO_2 occurs to the extent of 350–400 ppm in atmospheric air. The selection of the proper adsorbent is a critical step in adsorption applications mostly because sorbents affect the overall process performance and economics (Choi et al., 2009b). Industrial processes frequently use zeolite 13X for the removal of CO_2 impurity during air pre-purification due to the high capacity and the steep nature of the CO_2 isotherm at low pressure (Rege et al., 2000). Indeed, according to Choi et al. (2009b), physisorbents such as activated carbons and zeolites exhibit competitive CO_2 adsorption capacities near ambient temperature and display excellent regenerability. However, physisorbents are typically hindered by the moisture resulting in the necessity of pre-treatment steps prior to adsorption (Choi et al., 2009b; Choi et al., 2011c; Rege et al., 2000).

Thus, few groups have been investigating the capture of CO_2 through chemisorption to avoid the high water uptake of the physisorbents. However, chemisorbents result in higher heat of adsorption such that more energy is required for regeneration. In addition, often in the literature, high uptakes are measured at elevated temperatures, which require the feed stream to be pre-heated. All these alternative routes to air capture are analysed here.

2.1.1 Alkaline Sodium Systems and Alternatives

A group led by David Keith, the University of Calgary and Harvard University, and the Calgary-based start-up company Carbon Engineering Ltd. (Keith and Mahmoudkhani, 2012) have adopted the well-known in the pulp and paper industry 'caustic recovery' process for the absorption of CO_2 from atmospheric air (Heidel et al., 2011; Holmes and Keith, 2012). Their process, as illustrated in Figure 2.3, consists of an air-contactor and a regeneration cycle (Keith et al., 2010). The regeneration step (in the kiln) raises the energy cost of the process as CO_2 is recovered at 900 °C (Zeman, 2007). The natural gas and oxygen requirements and the amount of water lost to evaporation (20 $molH_2O/molCO_2$ (Zeman, 2008; Stolaroff et al., 2008)) may be a significant economic and environmental penalty that still have to be clarified and resolved. A fully integrated end-to-end pilot plant is almost released and is expected to capture 1 $ktCO_2$ per year to high purity (Holmes et al., 2013). A full process description is available in Holmes and Keith (2012) and Holmes et al. (2013).

An energetic and economic analysis from Stolaroff et al. (2008) estimated that the CO_2 capture process cost, without solution regeneration considered, would be around 100 US$ tCO_2^{-1} captured (compared with 50 US$ tCO_2^{-1} total for conventional CCS process using MEA absorption cycles). Considering the solution regeneration and sequestration steps, the estimated cost was approximately four times higher than the cost of a modern MEA-based CCS process (Stolaroff et al., 2008; Jones, 2011). In attempts to optimise the process, modified kilns heated by waste heat from nuclear reactors as described by Sherman (2009) or energy from solar radiation as described by Nikulshina et al. (2006) were also considered. Besides the use of different sources of thermal energy, additional work has been performed with the

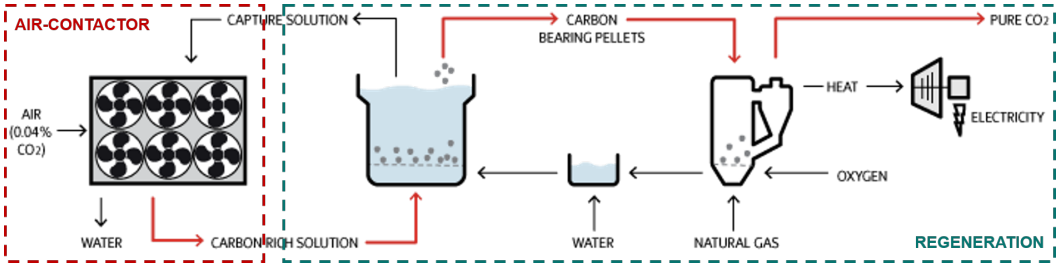

Figure 2.3. A schematic overview of the air capture approach with alkali hydroxide solutions.

Source: Carbon Engineering Ltd (2017).

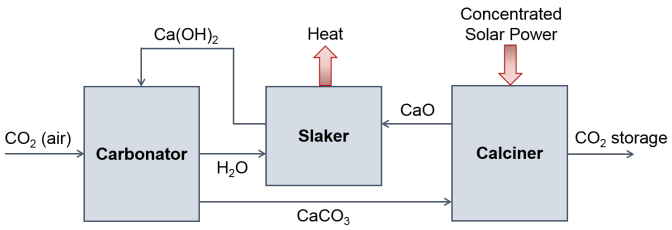

Figure 2.4. A schematic overview of the solar thermochemical cycle for CO_2 capture from air using concentrated solar power for the endothermic calcination process and/or pre-heating air in the carbonation process.

Source: Nikulshina et al. (2007).

aim of decreasing the energy requirement by changing the contactor configuration (Stolaroff et al., 2008) and using alternative regeneration chemistry (Mahmoudkhani and Keith, 2009).

Mahmoudkhani and Keith (2009) investigated an alternative 'caustic recovery' method via the titanate cycle. The energy required to regenerate titanates is much lower than for CaO, 90 kJ mol$CO_2{}^{-1}$ (Mahmoudkhani et al., 2009; Keith and Mahmoudkhani, 2012) compared to 179 kJ mol^{-1} (Dahlquist and Jones, 2005). It is stated in the literature that the titanate cycle may require around 50% less high-grade heat, required for regeneration, than conventional causticisation with the maximum temperature reduced by at least 50 °C (Mahmoudkhani and Keith, 2009). However, contamination by degradation of titanate particles must be carefully controlled and such large masses of titanate particles must be heated and cooled cyclically for heat recovery from solids (Keith et al., 2010). Therefore, the suggested fourfold higher cost of alkali-based air capture process relative to conventional CCS, make the process unlikely to ever compete directly with conventional CCS on an energy or cost basis (Jones, 2011).

A group under the supervision of Aldo Steinfeld, ETH Zurich, developed a thermochemical consecutive CaO-carbonation and $CaCO_3$-calcination adsorption cycle for DAC driven by concentrated solar irradiation, a solar kiln (Nikulshina et al., 2006; Nikulshina et al., 2007; Nikulshina et al., 2008; Nikulshina et al., 2009; Nikulshina and Steinfeld, 2009). The cycle encompasses three reactors: *(i)* an aerosol-type carbonator for capturing CO_2 from air using a spray of $Ca(OH)_2$ aqueous solution, *(ii)* a solar calciner for thermally decomposing $CaCO_3$ into CaO using concentrated solar energy, and *(iii)* a conventional slaker for regeneration $Ca(OH)_2$. The process, as illustrated in Figure 2.4, was expected to require approximately 2.5 MJ mol$CO_2{}^{-1}$ of solar radiation (Nikulshina et al., 2009), around 2–3 times the current conventional lime (Meier et al., 2006).

More recently, Nikulshina et al. (2009) reported that the required solar thermal energy input for the complete CaO-$CaCO_3$ thermochemical cycle is 10.6 MJ mol$CO_2{}^{-1}$ captured. This assumed 3% water (H_2O)-air during the carbonation step and the use of heat exchangers to partially recover the sensible heat of hot air exiting during the CaO-carbonation step at 375 °C and of hot CO_2 exiting during $CaCO_3$-calcination step at 875 °C (Nikulshina and Steinfeld, 2009). This study was also investigated at the University of Ottawa (Samari, 2014).

2.1.2 An Alternative Absorption System: A Humidity Swing Process

In 2009, moisture swing driven absorption cycles were introduced by Klaus Lackner, Columbia University and Arizona State University (the Centre of Negative Carbon Emissions), the start-up company Kilimanjaro Energy Inc. (Lackner and Wright, 2010; Wright et al., 2012; He et al., 2013) and more recently Carbon Sink Inc. (Wright et al., 2017). The process considers the use of solid sorbents in the form of an anionic exchange resin, functionalised with quaternary ammonium ligands. Those solids are able to absorb CO_2 in a dry form and release CO_2 in a presence of moisture. The reaction path of CO_2 absorption and desorption process of the recommended moisture swing adsorption (MSA) is illustrated in Figure 2.5. The overall process includes the steps (Lackner and Liu, 2008; Lackner and Brennan, 2009; Wang et al., 2011):

(i) The carbonate ion in the "Empty-Wet" resin is stabilised by the presence of water. By reducing the water content of the resin, the carbonate ion becomes less stable, and eventually by splitting one of the remaining water molecules, it forms a bicarbonate ion and a hydroxide ion as: $OH^-R^+ + HCO3^-R^+ \longleftrightarrow CO3^{2-}(R^+)2 + H2O$.

(ii) The "Empty-Dry" resin has a strong affinity to CO_2 due to the presence of the hydroxide ions.

(iii) By taking up CO_2, the resin becomes completely bicarbonate ("Full-Dry" state).

(iv) Wetting the resin leads to the full hydration of the bicarbonate ions ("Full-Wet"). The aqueous equilibrium between the carbonate and bicarbonate ions dictates a high pressure of CO_2. Allowing CO_2 to escape results in the "Empty-Wet" state and the cycle is completed.

The MSA process is carried out in nearly dry conditions and recovery is accomplished by exposing the system to moisture. Then, the separation of the resin from the water follows by heating the mixture of resin and entrained water to a temperature and for a duration of heating such that the ion exchange resin remains largely unchanged over a number of cycles.

In contrast to other absorption and adsorption processes, thermodynamic analyses of MSA have shown that evaporation provides the free energy required for the CO_2 concentration process (Wang et al., 2011). In a more recent work, the CO_2 adsorption isotherms in dry and humid conditions for the ion-exchange resin have been reported at different temperatures hypothesising a mechanism for the uptake of CO_2 based on absorption by the mobile hydroxide and carbonate counter ions present in the system as (Wang et al., 2011)

$$OH^-R^+ + CO2 \longrightarrow HCO3^-R^+,$$

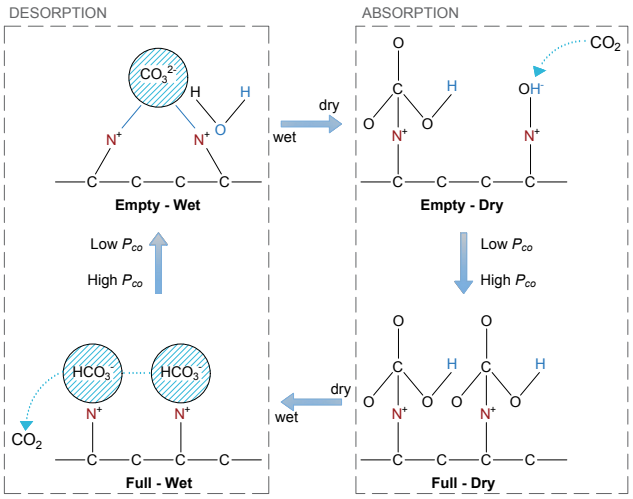

Figure 2.5. The reaction path of CO_2 absorption and desorption during a moisture swing.
Source: Wang et al. (2011).

$$CO_3{}^{2-}(R^+)_2 + H_2O + CO_2 \longleftrightarrow 2\,(HCO_3{}^-R^+).$$

Here, R^+ represent the quaternary ammonium ion in the resin. The uptake of CO_2 depends strongly on the partial pressure of water in air because of the possibility of forming both carbonate and bicarbonate products (Kulkarni and Sholl, 2012). The authors stated that the entire process could be operated by electrical energy, which is estimated at 50 kJ mol$CO_2{}^{-1}$ (Lackner, 2009). Lackner proposed that the first prototypes could break even at 200 US$ t$CO_2{}^{-1}$, and with-learning-by-doing and further advances in the technology the cost could drop within a target of 30 US$ t$CO_2{}^{-1}$ (Lackner, 2009). It is important to note that this technology can only work in low humidity/dry regions where it is possible to dry the resin after regeneration, unless the regeneration step is performed with an additional temperature swing (Santori et al., 2018). In that case, the process energy requirements will be much higher. Besides, this solution provides a maximum purity ranging between 0.02-0.05 molar fraction at ambient pressure. The author does not define the purification method, besides, additional energy will be needed to purify the product stream. Also, an intermediate rapid vacuum step is required to remove most of the air in the absorption bed and the residual gas co-absorbed on the solid (Brandani, 2012). Experimental results and details on an actual process or on a proof-of-the-concept experimental device have not been proved yet.

2.1.3 Adsorbent Based Systems: Temperature and Temperature-Vacuum Swing Adsorption

Solid amine-modified sorbents were investigated by the group of Christopher W. Jones, Georgia Institute of Technology, in collaboration with the start-up company Global Thermostat (Eisenberger and Chichilnisky, 2014; Eisenberger, 2015). Different amine materials, ranging from poly-(ethylene imine)-impregnated silica, over hyperbranched aminosilicas to mesoporous alumina-supported amines, and metal organic frameworks, have been investigated as adsorbents for the extraction of CO_2 from simulated air (Choi et al., 2009b; Choi et al.,

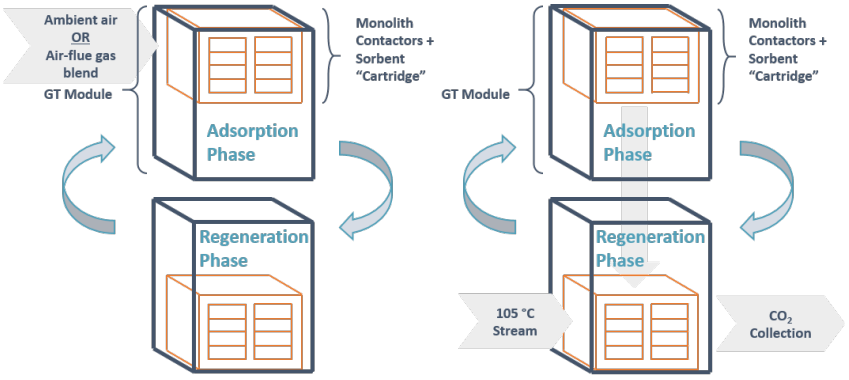

Figure 2.6. Global Thermostat's first prototype capturing CO_2 from the ambient air using a temperature swing adsorption, utilising waste heat and providing pure CO_2.

Source: Global Thermostat (2017).

2009a; Choi et al., 2011c; Choi et al., 2011b; Chaikittisilp et al., 2011c; Chaikittisilp et al., 2011a; Chaikittisilp et al., 2011b; Choi et al., 2012; Didas et al., 2012; Alkhabbaz et al., 2014; Darunte et al., 2016). Global Thermostat under the management of Graciela Chichilnisky and Peter Eisenberger, Columbia University, uses amine-based chemical sorbents bonded to porous honeycomb ceramic monoliths for the efficient temperature swing adsorption of CO_2 directly from the atmosphere, from smokestacks, or from a combination of both. The plant is completely modular, where each module captures around 40 $ktCO_2\ yr^{-1}$. In order to accomplish the separation of pure CO_2 from an air stream, a steam purge process was suggested where steam at 100 °C was introduced into a sorbent material bed for regeneration (Li et al., 2010a; Choi et al., 2011a; Kulkarni and Sholl, 2012) as illustrated in Figure 2.6. Thus, by heating up the material and reducing the CO_2 partial pressure around the material, pure CO_2 can be captured. However, while the steam purge allows fast heating-regeneration of the material, it might be condensed in the material (Li et al., 2010b; Wurzbacher, 2015). Information based on the measured final purities, energy consumption, and cost are still undefined by the company.

Steinfeld and co-workers, ETH Zürich, have analysed a TVSA process capable of extracting pure CO_2 from dry and humid atmospheric air (Wurzbacher et al., 2011; Wurzbacher et al., 2012). The ETH Spin-off company Climeworks LLC (2017) have recently built a prototype for air capture and its process is based on a cyclic adsorption/desorption process of a novel filter sorbent as presented in Figure 2.7 and in Gebald et al. (2012) and Climeworks LLC (2017). During adsorption, atmospheric CO_2 is chemically bound to the sorbent's surface. Once the sorbent is saturated, the CO_2 is driven off the sorbent by heating it at 95 °C under vacuum at 0.05 bar, thereby delivering high-purity gaseous CO_2. The CO_2-free sorbent can be re-used for many adsorption/desorption cycles. An attractive aspect of the process is the fact that around 90% of the energy demand can be supplied by low-temperature heat; the remaining energy is required in the form of electricity for pumping and control purposes (Climeworks LLC, 2017). However, the use of an ultra-vacuum pump relies on components which require high power input, maintenance, and low scalability (Santori et al., 2018). The energy consumption for sorbent regeneration reaches the unattractive value of 7.2 MJ $molCO_2^{-1}$. The same group, using the same TVSA system, have reported an energy for sorbent regeneration around 0.6 MJ $molCO_2^{-1}$ (Gebald et al., 2012). The authors suggested the use of solid sorbent materials over liquid scrubbing systems due to

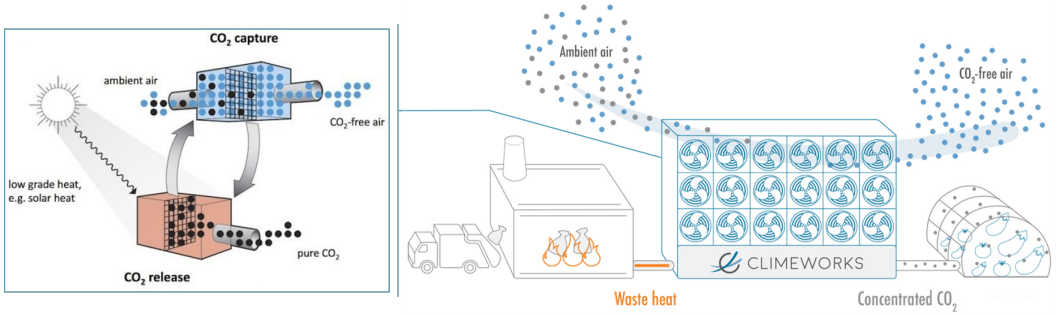

Figure 2.7. Climeworks' first prototype capturing CO_2 from the ambient air utilising waste heat and providing pure CO_2 to a greenhouse via a temperature vacuum swing adsorption process.

Source: Climeworks LLC (2017).

their reduced thermal mass and resistance to corrosion. They worked extensively with amine-functionalised materials with high specific surface area, high selectivity at low concentration, tolerance to moisture, and stability (Gebald et al., 2011; Wurzbacher et al., 2012; Gebald et al., 2013; Gebald et al., 2014; Wurzbacher et al., 2016).

Experimental results utilising a packed bed of a sorbent material made of diamine-functionalised commercial silica gel indicate a purity of up to 97.6% per adsorption/desorption cycle at a thermal energy requirement of 440 kJ $molCO_2^{-1}$ for desorption at 90 °C (Wurzbacher et al., 2011; Gebald et al., 2012; Wurzbacher et al., 2012). They have also predicted that if a higher working capacity could be achieved (from 0.2 to 2 mmol g^{-1} adsorbent), the energy requirements would decrease to 166 kJ $molCO_2^{-1}$. It is important to note that stable performance of the sorbent material in the TVSA process was demonstrated over 40 consecutive adsorption/desorption cycles (Wurzbacher et al., 2011). However, higher adsorbent cycle times are still needed in order to reduce the cost of the material. The same group has also reported a cyclic capacity of 0.69 mmol g^{-1} of adsorbent, an amine-functionalised nanofibrillated cellulose (Gebald et al., 2011), far lower than zeolites.

Stuckert and Yang (2011) have compared zeolites and amine-grafted silica of air capture. Using a TVS adsorption, they have obtained purities >90% during desorption concluding that zeolites have faster uptake rates than amine functionalised SBA-15 but are not suitable for operation under humid conditions (Stuckert and Yang, 2011). Since zeolites perform better under dry conditions providing a greater cycle lifetime, higher adsorption capacities, lower energy for regeneration, and physical adsorption, they may still be more promising candidates for air capture.

The carbon capture group at the University of Edinburgh has been investigating the carbon dioxide adsorption, compression, and purification by a temperature swing intermittent process (Ferrari et al., 2013; Charalambous et al., 2016; Santori et al., 2018), as illustrated in Figure 2.8. Generally, the process consists of a series of packed beds, which are connected together but differ in size. The decrease in their size follows the direction of the flow from bed to bed in order to achieve high compression and purification. This process aims at tackling climate change as it produces a stream with ideal properties for CO_2 geological storage. The deployment of a process that enables not only the separation but also the purification and compression of carbon dioxide can be very competitive and challenging. This process is still at an initial stage of investigation and laboratory-scale development

considering the use of benchmark adsorbents, such as zeolite 13X. This DAC approach via TSA will be extensively analysed in the following chapters.

Adsorption based-materials have continued gaining interest as potential candidates for DAC. Belmabkhout et al. (2010) provided the first detailed report on silica-supported amines for DAC. Many other research groups followed, i.e. Goeppert et al. (2011), McDonald et al. (2012), Wang et al. (2012), Zhang et al. (2014), Shekhah et al. (2015), Sayari et al. (2016), Sanz-Peez et al. (2016), Shi et al. (2016), Gibson et al. (2016), Curtin et al. (2017), and Elfving et al. (2017), investigating the adsorption properties of novel materials for DAC. Adsorption-based systems seem to gain more and more interest as the most suitable approach to DAC. Others also consider the possibility of DAC as a negative mitigation strategy (Stuckert and Yang, 2011; Ruthven, 2014; Wilcox et al., 2017).

2.2 Energy Requirements of Air Capture Systems

Figure 2.9 presents the energy consumption of the above-described processes. It has to be noticed here that not all the reported values include the total specific energy consumption and the 400 ppm initial CO_2 concentration in the feed stream. In addition, the final total energy use is a contribution of thermal and electrical energy. Therefore, since different sources of energy are considered, a quantitative evaluation of the thermodynamic efficiency of each process can be given only by exergy analysis (Borel and Favrat, 2010), which is not considered in this study. In addition, Figure 2.9 compares the energy use of each process with the thermodynamic minimum and the work of separation, as have been discussed in Chapter 1, Section 1.3.

The processes in Figure 2.9 are divided into six main categories: *(i)* the aqueous systems, *(ii)* the MSA or else moisture swing absorption system, *(iii)* the adsorption systems, *(iv)* other reported energy values for air capture, *(v)* the air revitalisation systems, i.e. the one used in the ISS of NASA for life support of the crew, and *(vi)* the carbon capture from a gas-fired plant. The categories *(iv)*, *(v)*, and *(iv)* are presented for comparison with air capture. It is illustrated that the adsorption systems, in general, require less energy to concentrate CO_2 compared to the other reported air capture systems. It is important to note here that the considered inlet CO_2 concentration in the enclosed atmosphere of the ISS is one order of magnitude higher than that in the DAC systems. Also, the CO_2 concentration in the flue gas of a gas-fired plant is around 8 mol% CO_2. This explains why the energy cost is lower compared to air capture. In addition, the separation work is, as stated from Ruthven (2014), a better indication for the energy requirements of DAC systems than the thermodynamic minimum as it provides similar values with the simulated or measured ones from all the DAC technologies and processes.

2.3 Main Conclusions

DAC is still at a very early stage of development. The operational and capital costs of the process can be reduced if more sophisticated models will be developed for correctly capturing the process behaviour and optimising its performance. A number of starting up companies, i.e. Carbon Engineering, Climeworks, and Global Thermostat, built the first DAC prototypes. Carbon Engineering uses an absorption-based approach where the last

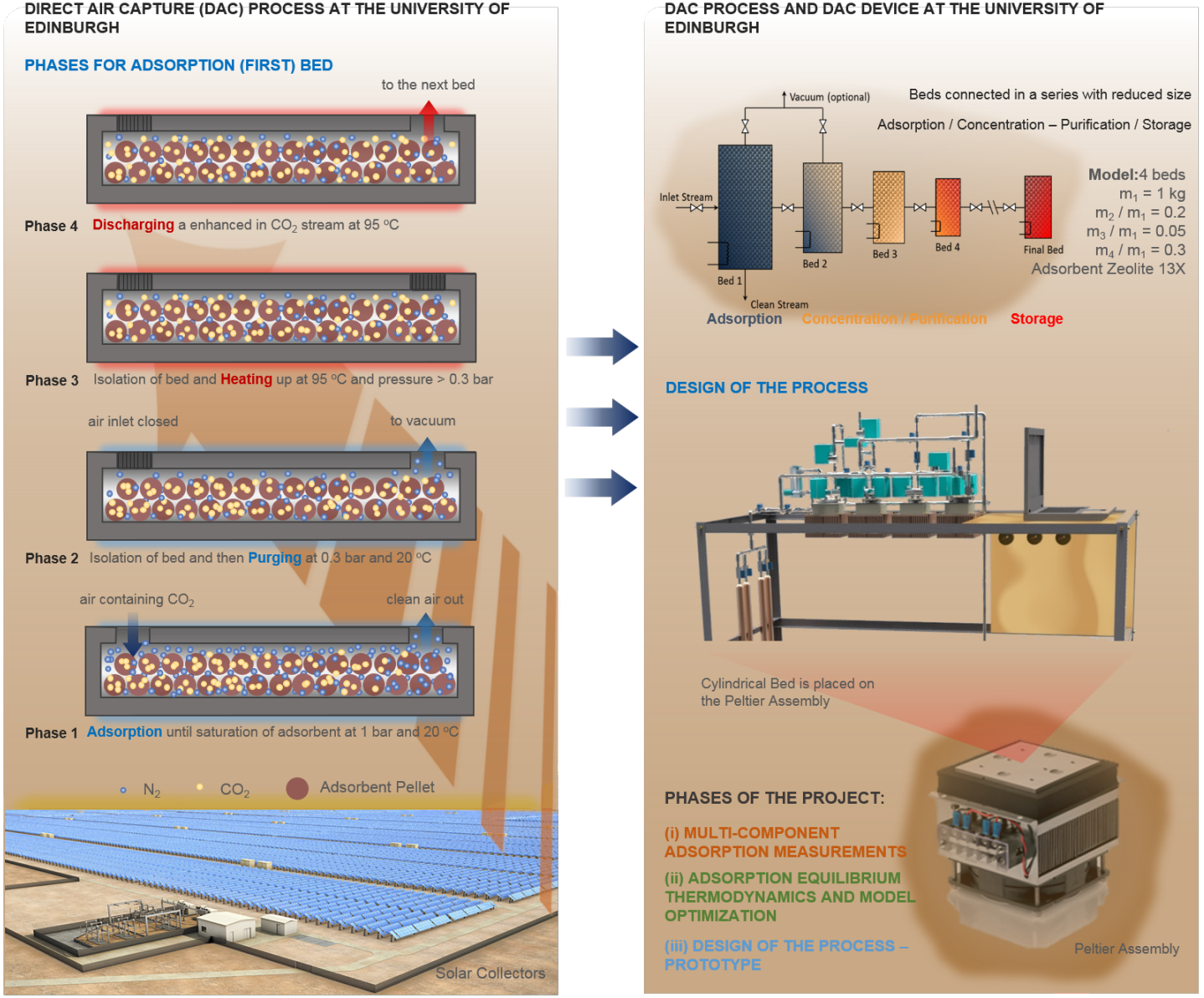

Figure 2.8. A Temperature Swing Adsorption process for the capture, compression, and purification of CO_2 directly for the atmospheric air as developed at the University of Edinburgh.

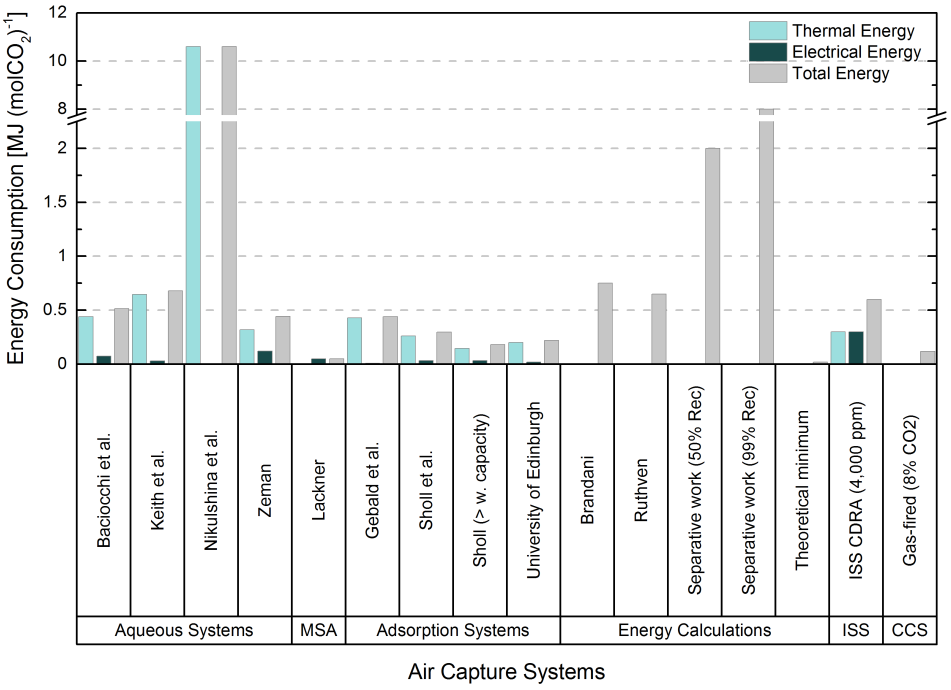

Figure 2.9. Reported energy consumption of the direct air capture processes as described in literature. The thermodynamic minimum work and separation work required to separate CO_2 from a 400 ppm stream are also considered. Energy requirements in air revitalisation systems and conventional CCS are also presented.

two companies use adsorption-based technologies. The absorption-based system of Carbon Engineering requires a great amount of water for the hydration of the lime and the use of natural gas and pure oxygen in the kiln for providing heat for regeneration at 900°C. This is not even competitive to the low-grade heat (<100°C), which can be provided by renewable sources or waste heat, of the adsorption-based systems of Climeworks and Global Thermostat. Since to tackle climate change the adsorption systems have to provide ideal conditions for CO_2 geological storage, the captured CO_2 has to be purified at >95% and compressed at pressures >73.8 bar (Mazzoccoli et al., 2014).

Adsorption-based systems and especially TSA systems may be most suitable for the separation of very dilute streams. However, favourable operation conditions have to be considered. Restrictions are not applied only on the general capture technique, but most importantly on the process operational steps. For instance, Climeworks prototype desorbs purified CO_2 at around 100°C but also under extremely low vacuum at 0.050 bar, which requires the use of electrical energy. In addition, Global Thermostat regenerates the adsorbent under a flow of steam, which requires additional feed treatment to collect the purified product. Several concluding points have to be highlighted here: *(i)* adsorption at low temperatures favours the adsorption capacity of the material and reduces the energy use of the process since no pre-treatment is required; *(ii)* heating at high temperatures, still <100°C to allow the low-grade heat integration, enhances desorption; *(iii)* since the required atmospheric air stream is relatively high due to the dilution of CO_2 in air, pressure drops through the capture unit have to be eliminated; *(iv)* any pre-treatment of the initial feed can have major drawbacks to the process because of the extremely high volumes of air that have to be processed for the separation; *(v)* low process recoveries will lead to an even greater amount of processed air, which requires larger equipment and therefore, it increases the capital

cost; if high recovery is selected, then the separative work (operational cost) of the process increases; and *(vi)* the purified CO_2 has to be further compressed to high pressure levels imposed by geo-engineering.

Therefore, once the use of adsorption-based processes is recognised as an efficient way to air capture, the best suitable process operation and process conditions, ideal adsorptive and physical properties of the adsorbent, and favour adsorption kinetics and therefore favour capture rates have to be investigated with a high degree of accuracy. In addition, suitably long-time equipment and material lifetime have to be employed. The main target of the following chapters is to address most of these issues for a DAC application via temperature swing adsorption, which integrates both the compression and the purification of CO_2.

3 Temperature Swing Adsorption Process for Adsorption, Compressions, and Purification of Highly Dilute Gases: Thermodynamics

> *All things are created twice; first mentally; then physically. The key to creativity is to begin with the end in mind, with a vision and a blue print of the desired result.*
>
> **— Stephen R. Covey**
> (American educator, author, businessman, keynote speaker)

The first stage to design and model an adsorption process is to study its thermodynamics so that the process can be proved and improved and its inherent limits can be identified. Principally, the study of the adsorption equilibrium of the process requires the consideration and determination of four parameters. These are: *(i)* the components that consist the process, i.e. the fluid, the solid or else adsorbent, the adsorption bed, *etc*., *(ii)* the thermodynamic phases of the system, i.e. the gas phase, the liquid phase, and the solid phase, *(iii)* the physical and adsorption properties of all the above, and *(iv)* the suitable conditions under which the process must operate. Thus, this chapter focuses on: *(i)* describing a temperature swing adsorption process for the removal, compression, and purification of a trace contaminant from a gas fluid, *(ii)* modelling the multi-component adsorption equilibria of the process, and *(iii)* designing and improving the performance of the process through optimisation. By the end of this chapter, guidelines for the design of an optimal process are proposed.

3.1 Introduction to Adsorption Thermodynamics

The separation and purification of gas mixtures by adsorption on micro- and meso-porous solid adsorbents[1] are widely used in commercial applications in the chemical, petrochemical, environmental, and medical industries (Sircar, Shivaji, 2003). This is due to their ability to reversibly adsorb (accumulate or deplete) large volumes of gas molecules at an interface (Ruthven, 1984; LeVan et al., 1998). Under certain conditions, there is an enhancement in the concentration of a particular component on the surface of a porous material that is considered as a separate phase from the point of view of thermodynamics (Rouquerol et al., 1999). Since the accumulation per unit surface area is small, highly porous solids with very large internal area per unit volume, generally around 100 $m^2\ g^{-1}$ (Rouquerol et al.,

[1] Adsorbents are natural or synthetic materials of amorphous or micro-crystalline structure (Chakraborty and Sun, 2014).

Table 3.1. Key commercial applications for gas separation and purification by adsorption technology.

Trace or Dilute Removal	Bulk-Gas Separation
• Trace organic and inorganic impurity removal	• Air separation (O_2 and N_2 from air)
• Gas drying	• Hydrogen and carbon dioxide production from steam-methane reformer off gas
• Air pollution control	• Production of ammonia synthetic gas
• Nuclear waste management	• Hydrogen recovery from refinery off gases
• Solvent vapor recovery	• Methane-carbon dioxide separation from landfill gas
• Electric gas purification	• Carbon monoxide-hydrogen separation
	• Normal-isoparaffin separation
	• Alcohol dehydration

Note: The table is taken from (Sircar, Shivaji, 2003).

1999) are favoured as high adsorptive capacity can be achieved (Do, 1998). Adsorbent surfaces are physically and/or chemically heterogeneous and bonding energies may vary widely from one site to another. Physical adsorption or physisorption involves only relatively weak intermolecular forces and is a well-suited approach for a regenerable process (LeVan et al., 1998). However, the chemical adsorption or chemisorption involves the formation of a chemical bond between the sorbate molecule and the surface of the adsorbent and generally hinders the properties of the adsorbent material (Ruthven, 1984; LeVan et al., 1998).

Searching for a suitable material is generally the first step in the design of an adsorption separation process. Ruthven (1984) stated that the primary requirement for an economic adsorption separation process is an adsorbent with sufficiently high selectivity, capacity, and life. For instance, the selectivity[2] principally varies with temperature and composition. Thus, finding a suitable condition to maximise the separation factor is a major consideration in process design. A successful adsorptive process depends on both the optimum adsorbent and the efficient process design. Numerous families of solids with varying pore structures and surface properties have been synthesised and are now available on the market, which offer multiple choices of core adsorptive properties, such as equilibria, kinetics, and regeneration energy, for a given separation application (Sircar et al., 1996; Sircar, Shivaji, 2003).

The generic adsorption-based cyclic process concepts used in adsorption gas separation and purification are: *(i)* the temperature swing adsorption (TSA), *(ii)* the pressure swing adsorption (PSA), *(iii)* the vacuum swing adsorption (VSA), *(iv)* the electric swing adsorption (ESA), and *(v)* the combination of some of the above. The most widely used technologies are TSA, PSA, and VSA, where the difference between them lies in the strategy to regenerate the adsorbent after the adsorption step, the type of energy consumed by the process, and the time duration of an individual adsorption circle (Banaszkiewicz and Chorowski, 2015). Table 3.1 presents the key commercial application for gas separation and purification by adsorption technologies. Generally, TSA is used in gas purification applications (Ahn and Lee, 2003; Nastaj and Ambrożek, 2009), except in gas drying and solvent vapour recovery application where both TSA and PSA are used. PSA is used in bulk-gas separation (Sircar, Shivaji, 2003; Voss, 2005). Besides, when the concentration of the treated/targeted component in the feed stream is low, TSA is likely to be more efficient as the adsorption step takes much longer (Grande, 2012), and the utilisation of other technologies, such as PSA or VSA, requires extreme vacuum for causing desorption and proceeding regeneration (Mason et al., 2011).

[2]The selectivity, or else the separation factor, is defined as (Ruthven, 1984)
$\alpha_{12} = \frac{x_1/x_2}{y_1/y_2}$,
where x_1 and y_1 are, respectively, the molar fractions of component '1' in the adsorbed and gas phases at equilibrium.

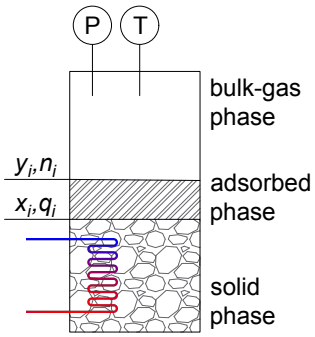

Figure 3.1. A schematic representation of the thermodynamic phases of an adsorption system and the adsorption parameters. Abbreviations: P, bulk pressure; T, temperature; y_i and n_i, molar fraction and moles of species i in the bulk-gas phase, respectively; and x_i and q_i, molar fraction and moles of species i in the adsorbed phase, respectively.

The relative performance of different porous solids are highly dependent on the internal pore structure of each material. Therefore, in order to better understand an adsorption process, it is necessary to fully characterise the various properties of porous solids, i.e. internal geometry, size, connectivity, *etc*. According to the IUPAC classification, pores are divided into three categories (Ruthven, 1984):

(i) Micropores: < 20 Å,

(ii) Mesopores: 20–500 Å,

(iii) Macropores: > 500 Å.

All the molecules within the micropores, the so called adsorbed layer, are referred as the 'adsorbed phase' (Ruthven et al., 1994), a distinct phase in the thermodynamic sense. Ordinary laws of thermodynamics can accurately describe the equilibrium of the adsorbed phase with the surrounding gas. The physical adsorption of molecules from the gas phase is an exothermic process. Hence, equilibrium favours adsorption at lower temperatures and desorption at higher temperatures. Figure 3.1 represents the thermodynamic phases of an adsorption system and the parameters of each phase.

At significantly low concentrations, the equilibrium relationship generally approaches a linear form (Henry's law), which is governed by

$$q = K\,P, \tag{3.1}$$

where q [mol kg^{-1}] is the amount adsorbed, P [kPa] is the pressure in the gas phase, and K [mol kPa^{-1} kg^{-1}] is the Henry's law constant.

The temperature dependence of the Henry constant obeys the van't Hoff relations as

$$\frac{\mathrm{d}\ln K}{\mathrm{d}T} = \frac{\Delta H_0}{RT^2}, \tag{3.2}$$

where ΔH_0 represents the differences in enthalpy between the adsorbed phase and the gaseous phase. Since, for an exothermic process ΔH is negative, the Henry's law constant decreases with increasing temperature. Neglecting differences in heat capacity between the phases, Eq. 3.2 may be integrated to yield (Ruthven, 1984)

$$K = K_0\,\mathrm{e}^{\frac{-\Delta H_0}{RT}}, \tag{3.3}$$

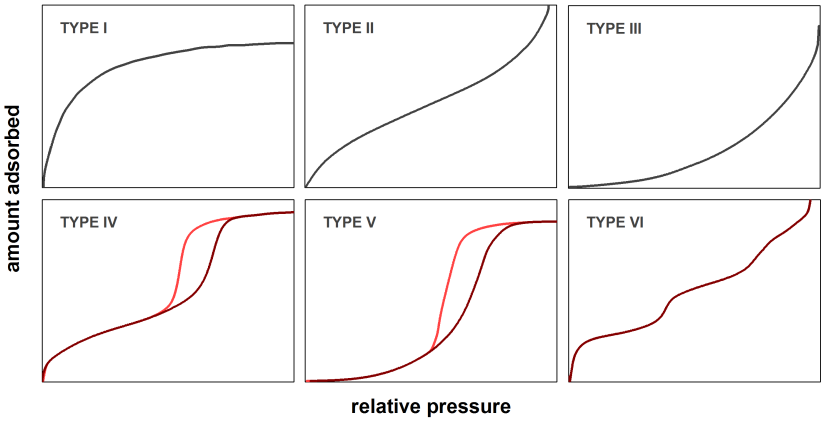

Figure 3.2. The IUPAC classification of adsorption isotherms for gas-solid equilibria. *Source*: Sing et al. (1985).

where K_0 [mol kPa^{-1} kg^{-1}] is the Henry's law reference constant at equilibrium.

At higher concentrations, the equilibrium relationship becomes curved. Figure 3.2 illustrates the IUPAC classification of the isotherms for physical adsorption (Sing et al., 1985; Thommes et al., 2015). The type I isotherm function corresponds to microporous adsorbents, for which the pore size is slightly bigger than the molecular diameter of the sorbate. These adsorbents have a definite saturation limit that is associated with the complete filling of the micropores. The types II and III isotherms are generally observed in adsorbents with a wide range of pore sizes. In such systems, a continuous progression with increasing loading from monolayer to multilayer adsorption and then to capillary condensation is observed. The type III isotherm is called the unfavourable adsorption isotherm. An isotherm type IV suggests the formation of two surface layers far wider than the molecular diameter of the sorbate. The types IV and V show adsorption hysteresis, and type VI isotherm has steps that are typical of multi-layering adsorption.

The simplest theoretical model for monolayer adsorption (type I isotherm) was formulated by Langmuir (1918). The model assumes that (Ruthven, 1984):

(i) the molecules are adsorbed at a fixed number of well-defined localised sites,

(ii) each site can hold one adsorbate molecule,

(iii) all sites are energetically equivalent,

(iv) there is no interaction between molecules adsorbed on neighbouring sites.

This model can be described by

$$q = q_{\mathrm{s}} \frac{b\,P}{1 + b\,P}. \tag{3.4}$$

At saturation $P \to \infty$, then $q \to q_{\mathrm{s}}$ while at low sorbate concentration it becomes the Henry's law constant as

$$\lim_{P \to 0} \left(\frac{q}{P} \right) = b\,q_{\mathrm{s}} = K, \tag{3.5}$$

where q_{s} [mol kg^{-1}] is the saturation capacity and b [kPa^{-1}] denotes the temperature dependence of the equilibrium constant. The latter follows a van't Hoff equation as

$$b = b_0\, \mathrm{e}^{\frac{-\Delta H}{R\,T}}. \tag{3.6}$$

Since adsorption is exothermic, b decreases with increasing temperature. The assumption of identical sites with no interaction between adsorbed molecules implies that the heat of adsorption is independent of coverage. Therefore, the isosteric heat of adsorption is given by the Clausius-Clapeyron equation as

$$\left(\frac{\partial \ln P}{\partial T}\right)_q = \frac{\Delta H}{R T^2}. \tag{3.7}$$

The Langmuir model yields a simple extension to binary and multi-component systems, reflecting the competitive adsorption of different adsorbates on the adsorption sites. The extended Langmuir model is governed by

$$q_i = q_s \frac{b_i\, p_i}{1 + \sum_j^{N_C} b_j\, p_j}, \qquad i, j = 1, 2, ..., N_C, \tag{3.8}$$

where N_C denotes the number of components in the gas-solid system. For thermodynamic consistency, it is required that q_s has to be the same for all the components in the system. Thus, fitting errors for pure-component isotherms would increase when different components are forced to obey the thermodynamic consistency condition (Bai et al., 2003).

The separation factor or else selectivity for a system, which is described by Eqs. 3.8 and 3.6, is given by the ratio of the adsorption equilibrium constants for the two components and is independent of concentration. The separation factor follows

$$\alpha_{12} = \frac{x_1/x_2}{y_1/y_2} = \frac{q_s\, b_1}{q_s\, b_2} = \frac{b_1}{b_2}, \tag{3.9}$$

where x_1 and y_1 are the molar fractions of species '1' in the adsorbed and bulk-gas phases, respectively.

The equilibrium state of the process is reached after a certain time and establishes the thermodynamic limit of the adsorbent loading for a given fluid phase composition, temperature, and pressure. Information about the adsorption equilibrium of the different species is vital to design and model adsorption process. Principally, no matter how many components are presented in the system, adsorption equilibrium of pure components is essential for understanding the adsorption capacity of each component on specific adsorbent. This information is vital in the study of adsorption equilibria of multi-component systems and adsorption kinetics of single- or multi-component systems. In this chapter, the equilibrium approach to our process for the separation of an extremely dilute component, compression, and purification are extensively analysed. Since the challenges to gas separation and concentration at extremely dilute conditions are proportional to the energy requirements, economic viability, and operational separation performance, a process optimisation in terms of the energy use and the purity level is performed.

3.2 Description of the Process

A simple, comprehensive overview of the process is depicted in Figure 3.3. The process consists of three consecutive sections. These are: *(i)* a capture section of an extremely dilute

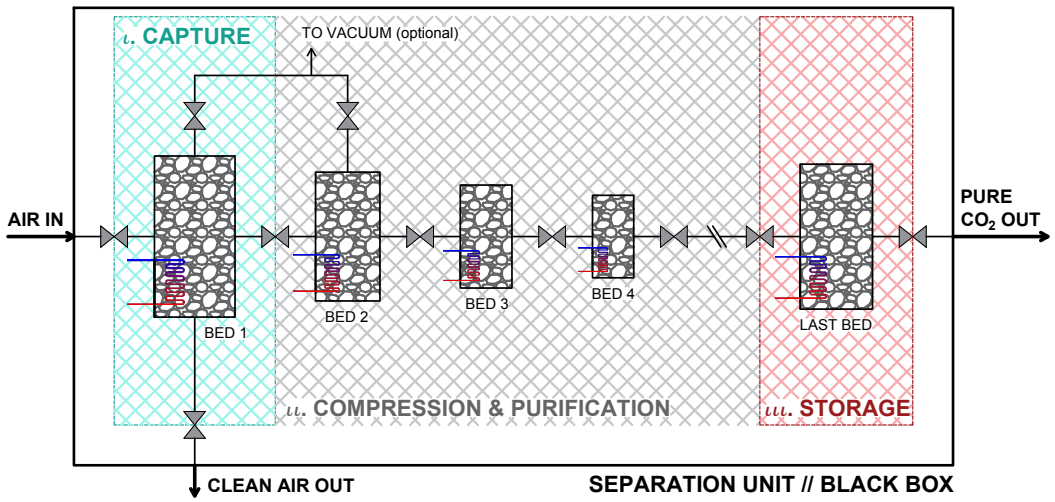

Figure 3.3. A block diagram representing a thermally driven adsorption process for the capture, compression, and purification of an extremely dilute impurity.

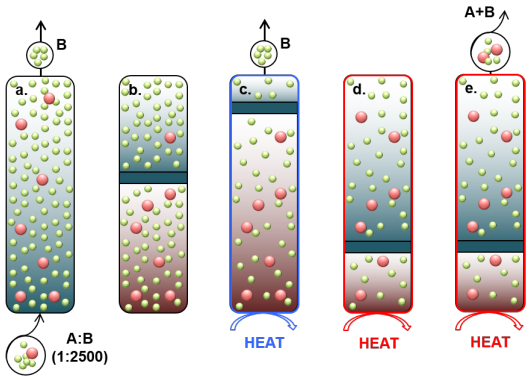

Figure 3.4. The process steps for the operation of a single adsorption column: **(a)** adsorption of the binary feed of components (A) and (B) with (A) to be the dilute species (red sphere), **(b)** illustration of the adsorbed phase (red block) and bulk-gas phase (green block) with the adsorbed phase to be concentrated in (A), **(c)** evacuation at T_{low}, **(d)** heating up at T_{high} (desorption), and **(e)** discharge of the higher in concentration of component (A) stream at T_{high}.

impurity[3] in the adsorption bed (Bed 1), *(ii)* a compression and purification section of the trace component accomplished by a series of k connected adsorption beds (Bed 2, Bed 3, ..., Bed k), and *(iii)* a storage section of the purified key component in the last storage bed (Bed $k+1$).

The process operates as described in Tables 3.2 and 3.3 and has also been explained elsewhere (Charalambous et al., 2016). An extremely dilute stream flows through the first adsorption bed, where the dilute component in the stream is most strongly adsorbed over other secondary components. For example, in case of DAC, CO_2 is adsorbed along other less strongly adsorbed compounds, such as nitrogen (N_2), oxygen (O_2), argon (Ar), *etc.* By heating up Bed 1 (at T_{high}), the trace component, which is stored inside the pores of the adsorbent material, is desorbed in the bulk-gas phase. These steps of the process are depicted in Figure 3.4. Let us assume that Bed 1 is packed with 1 kg of microporous adsorbent material (i.e. zeolite 13X) and a binary feed stream of components '1' and '2'

[3]The 'dilute impurity' is also referred in this study as 'trace gas' or 'key component'.

Table 3.2. The list of the operational states of each bed.

Bed	State [a]	Temperature	Description
Bed 1	Adsorption (AD)	T_{low}	The feed stream[b] flows through the bed at constant temperature and pressure until saturation.
	Vacuum (P) – *optional*	T_{low}	An optional rapid vacuum assuming frozen adsorbed phase[c].
	Heating (H)	T_{high}	Bed 1 is isolated and then heated at constant volume resulting in pressure increase.
	Equilibration Beds 1–2 (E12)	T_{high}	Bed 1 is connected with Bed 2 such that gas stream is desorbed by Bed 1 and adsorbed by Bed 2 until equilibrium pressure and gas composition. First enrichment of (A).[d]
	Cooling (C)	T_{low}	Bed 1 is isolated and then cooled at constant volume.
Bed 2	Cooling (C)	T_{low}	Bed 2 is isolated and then cooled at constant volume.
	Equilibration Beds 1–2 (E12)	T_{low}	Bed 2 adsorbs from Bed 1.
	Vacuum (P) – *optional*	T_{low}	Optional quick vacuum assuming frozen adsorbed phase.
	Heating (H)	T_{high}	Bed 2 is isolated and then heated at constant volume.
	Equilibration Beds 2–3 (E23)	T_{high}	Bed 2 desorbs an enriched in (A) stream in Bed 3.
Bed 3	Cooling (C)	T_{low}	Bed 3 is isolated and then cooled at constant volume.
	Equilibration Beds 2–3 (E23)	T_{low}	Bed 3 adsorbs from Bed 2.
	Heating (H)	T_{high}	Bed 3 is isolated and then heated at constant volume.
	Equilibration Beds 3–4 (E34)	T_{high}	Bed 3 desorbs an enriched in (A) stream in Bed 4.
... Bed *k* [e]	Cooling (C)	T_{low}	Bed *k* is isolated and then cooled at constant volume.
	Equilibration Beds (*k*–1)–*k* (Ek1k)	T_{low}	Bed *k* adsorbs from Bed (*k*–1).
	Heating (H)	T_{high}	Bed *k* is isolated and then heated at constant volume.
	Equilibration Beds *k*–(*k*+1) (Ekk1)	T_{high}	Bed *k* desorbs an enriched in (A) stream in Bed (*k*+1).
Bed *k*+1	Cooling (C)	T_{low}	Bed (*k*+1) is isolated and then cooled at constant volume.
	Equilibration Beds *k*–(*k*+1) (Ekk1)	T_{low}	Storage of the purified trace component in the last bed. The final stream is compressed and purified.

[a] Parentheses include the code used in Table 3.3 for the identification of bed states.
[b] The feed stream is assumed to be a binary mixture of a trace impurity (A) and excess secondary gas (B).
[c] The adsorbed phase is assumed to be 'frozen' during blowdown in the sense that the quick change in the bulk pressure does not affect the adsorbed phase concentrations (Pigorini and LeVan, 1997).
[d] Enrichment of gas stream in the trace impurity (A).
[e] The *k*th compression bed is connected on one side with Bed (*k*–1) and on the other side with Bed (*k*+1) (Final/Storage Bed).

Table 3.3. The process steps sequence.

Bed	Steps [a]												
	1	2	3	4	5	6	7	8	9	... *i* [b]	*i*+1	*i*+2	*i*+3
1	AD	P	H	E12	C	—	—	—	—	—	—	—	—
2	—	—	C	E12	P	H	E23	—	—	—	—	—	—
3	—	—	—	—	—	C	E23	H	E34	—	—	—	—
... *k*	—	—	—	—	—	—	—	C	E34	... C	Ek1k	H	Ekk1
***k*+1**	—	—	—	—	—	—	—	—	—	—	—	C	Ekk1

[a] Symbols used to identify bed states as described in Table 3.2.
[b] The *i*th step of the process.

flows through the bed at atmospheric conditions (P=1 atm, T=20 °C) until the material reaches its saturation state. After saturation, the bed is isolated and heated up at various temperatures. An approximation of the pressure and the concentration differences in both

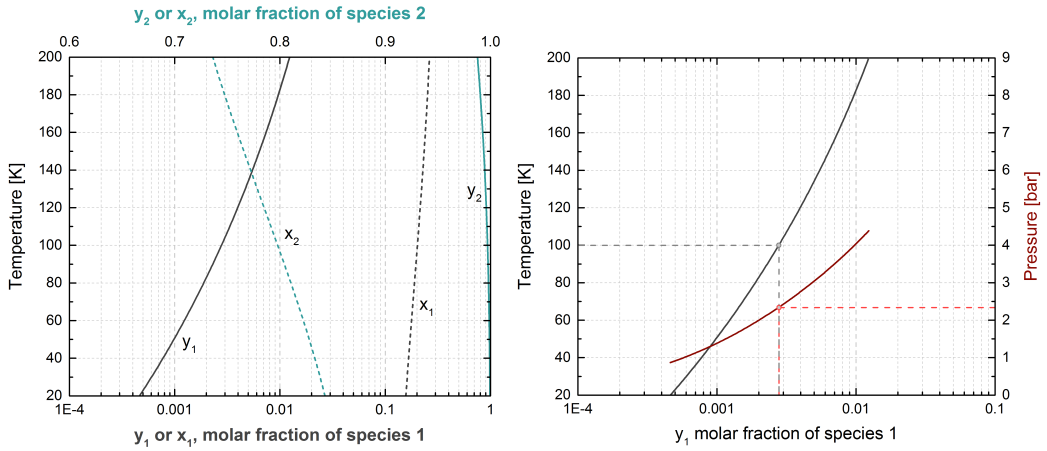

(a) T-x-y **(b)** P-T-y

Figure 3.5. **(a)** Heating up temperature versus molar fractions of species '1' (gray curves) and species '2' (green curves) in the bulk-gas and adsorbed phases and **(b)** temperature (gray curve) and equilibrium pressure (red curve) versus the molar fraction of species '1' in the bulk-gas phase.

bulk-gas and adsorbed phases as the temperature increases are depicted in Figure 3.5. Thus, by heating up the bed, the concentration of the dilute component increases in the bulk-gas phase as well as the pressure.

Then, by connecting Bed 1 (at $T_{\text{high}} \geqslant 95$ °C and P>1 atm) with the next following bed (Bed 2), the bulk-gas phase of Bed 1 is adsorbed from Bed 2, which operates at T_{low}. Thus, the pressure and concentration of trace component in Bed 2 increases. For the sake of simplicity, this system is illustrated in Figure 3.6. Let us simply assume that the bed of the previous example, as investigated in Figure 3.5, is kept at 100 °C, which results in a pressure of >2 bar (see Figure 3.5b). It is then connected with another bed, which is referred here as Bed 2 and operates at a range of temperature between 20–200 °C. The mass ratio between the two beds is fixed at 1:1, 1:5, and 1:10 (Bed 1:Bed 2). Figure 3.7 illustrates the resulting pressure and concentration of species '1' in both the phases and the beds as obtained from this analysis. By decreasing the temperature of Bed 2, a more concentrated stream flows into the next bed and thus a greater amount of species '1' is adsorbed from Bed 2. Hence, the adsorbed amount of species '1' in Bed 2 increases. Figure 3.7b also illustrates that a higher mass ratio between the beds increases the pressure and molar fraction of species '1' in Bed 2. Figures 3.5 and 3.7 present the importance of the adsorbed phase since two orders of magnitude higher mass is transferred and stored inside the pores of the solid. The solid controls the separation of the fluid such that the adsorptive and the thermo-physical and -chemical properties of the material are crucial properties of the process performance.

An optional purge step at 30–40 kPa is suggested to remove most of the secondary components from the bulk-gas phase of Bed 1 and Bed 2. Steps of cooling and heating are repeated for all the compression and purification beds (Bed 2, Bed 3, ..., Bed k). By heating Bed k and connecting Bed k and Bed k+1, an amount of the purified key component is stored, adsorbed at T_{low}, in Bed k+1.

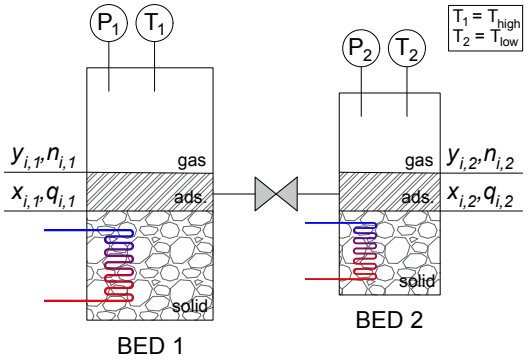

Figure 3.6. A schematic representation of the connection between Bed 1 and Bed 2. Abbreviations: P_k, bulk pressure in Bed k; T_k, operating temperature in Bed k; $y_{i,k}$ and $n_{i,k}$, molar fraction and moles of species i in the bulk-gas phase in Bed k, respectively; and $x_{i,k}$ and $q_{i,k}$, molar fraction and moles of species i in the adsorbed phase in Bed k, respectively.

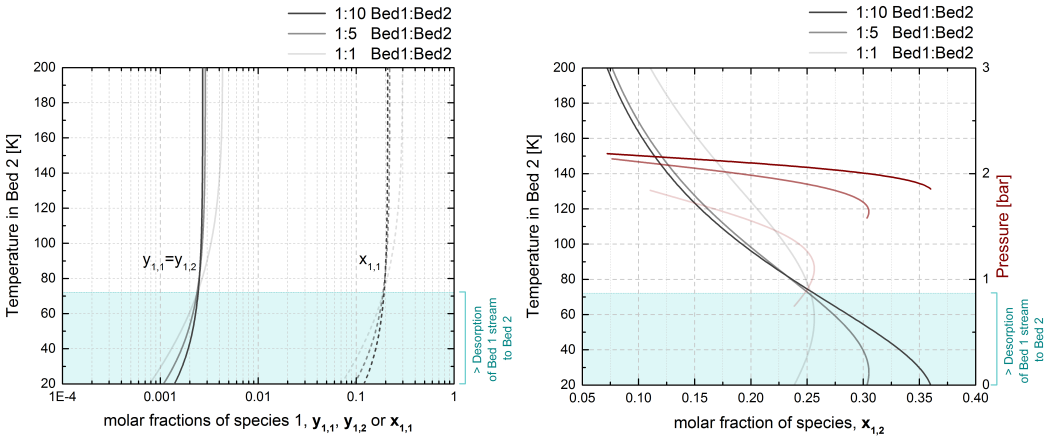

(a) T-x-y for the connection between Bed 1 and Bed 2

(b) P-T-x for Bed 2

Figure 3.7. **(a)** Bed 2 operating temperature versus the molar fraction of species '1' in both the bulk-gas and adsorbed phases in Bed 1 and **(b)** temperature (gray curves) and pressure (red curves) versus the molar fraction of species '1' in the adsorbed phase of Bed 2 ($x_{1,2}$), for the different bed mass ratios.

The process step sequence of Table 3.3 is repeated for a number of times (runs/cycles of the process) until the concentration of the trace component reaches the required final purity[4] in the storage bed. An additional benefit of this process is the significant pressure increase along the 'beds' train' until reaching a maximum in the last bed, which has been extensively observed and explained elsewhere (Hoover and Wankat, 2002; Santori and Luberti, 2016; Ferrari et al., 2013; Charalambous et al., 2016). The process offers the following additional characteristics:

(i) Intermittent process, where the last bed is fed only at the end of each cycle.

(ii) Continuous process, where more than one 'beds' train' can be assembled on one common storage bed.

(iii) Natural day and night operation.

(iv) Thermally driven by heat at <100 °C, which allows the low-grade heat available from solar thermal, geothermal or industrial heat sources to be used.

[4]The final purity is defined as the total amount of key component in both phases divided by the total amount of the mixture inside the storage bed.

(v) Final compression in the end of all process cycles, which is completed by isolating and heating the storage bed at T_{high}.

In order to minimise the amount of the excess gases in the system before the operation of the process, a preliminary regeneration is needed. This process includes steps of heating at T_{high} and constant volume, blowdown (Kumar, 1989) of all beds at 30–40 kPa at vacuum levels technically reasonable for large-scale operations, and then isolation of each bed and cooling down at T_{low} and constant volume. This strategy results in a <40 kPa initial pressure of the beds, depending on the vacuum level, a minimum amount of residual gases[5], and an initial bed temperature T_{low}.

3.3 Process Thermodynamic Equilibrium Model

3.3.1 Process Material Balance: The Simplified Case

The inlet stream is assumed to be a binary mixture of general components (A) and (B), where (A) is the more strongly adsorbed compound or trace impurity. For sake of simplicity, adsorption of pure (A) and (B) is described by the fundamental adsorption (and temperature dependent) Langmuir isotherm (Langmuir, 1918) as

$$q_i = q_{\text{s},i} \frac{b_{0,i} \exp\left(\frac{-\Delta H_i}{R_{\text{g}}\, T}\right) P}{1 + b_{0,i} \exp\left(\frac{-\Delta H_i}{R_{\text{g}}\, T}\right) P}, \tag{3.10}$$

where q_i [mol kg^{-1}] is the adsorbed amount of component i, $q_{\text{s},i}$ [mol kg^{-1}] denotes the saturation adsorption capacity, $b_{0,i}$ [kPa^{-1}] refers to the pre-exponential adsorption constant of component i. Also, ΔH_i [kJ mol^{-1}] represents the isosteric heat of adsorption of component i at zero coverage, R_{g} [kJ mol^{-1} K^{-1}] is the universal gas constant, T [K] is the temperature, and P [kPa] is the pressure in the bulk-gas phase.

The adsorption of the binary mixture has been interpreted with extended single Langmuir (ESL) model (Kapoor et al., 1990; Yang, Ralph T., 1997) assuming an ideal behaviour in both adsorbed and bulk-gas phases. During adsorption, it is assumed that Bed 1 operates at constant temperature and pressure so that the adsorbed concentration of the species i in the multi-component system is governed by

$$q_i = q_{\text{s},i} \frac{b_i\, p_i}{1 + \sum_{j=1}^{N_{\text{C}}} b_j\, p_j}, \quad \text{where} \quad i, j = 1, ..., N_{\text{C}}, \tag{3.11a}$$

$$b_i = b_{0,i} \exp\left(\frac{-\Delta H_i}{R_{\text{g}}\, T}\right), \tag{3.11b}$$

where N_{C} is the total number of compounds in the feed stream and b_i [kPa^{-1}] denotes the adsorption equilibrium constant of component i. For the binary system, the thermodynamic consistency requires $q_{\text{s},1} = q_{\text{s},2}$ [6] (Kemball et al., 1948; Broughton, 1948).

[5] Approximately, 60–70% of the gases are removed from the bed.

[6] However, such an assumption is unrealistic for physical adsorption of molecules of widely different size (Ruthven, 1984), while it is realistic in the case of CO_2 and N_2 molecules.

During heating and cooling of the beds at constant volume, the conservation of mass of each single component is required. The amount of each component i in the isolated Bed k at equilibrium is defined by

$$n_{i,k}^{(\mathrm{eq})} = \frac{(y_{i,k}\, P_{\mathrm{bulk},k})\, V_{\mathrm{void},k}}{R_{\mathrm{g}}\, T_k} + m_{\mathrm{bed},k}\, \frac{q_{\mathrm{s},i}\, b_i\, (y_{i,k}\, P_{\mathrm{bulk},k})}{1 + \sum_{j=1}^{N_{\mathrm{C}}} b_j\, (y_{j,k}\, P_{\mathrm{bulk},k})}, \tag{3.12a}$$

$$n_{i,k}^{(\mathrm{eq})} = n_{i,k}^{(\mathrm{ini})}, \tag{3.12b}$$

$$y_{N_{\mathrm{C}}} = 1 - \sum_{i=1}^{N_{\mathrm{C}}-1} y_i, \tag{3.12c}$$

where

$$V_{\mathrm{void},k} = \frac{m_{\mathrm{bed},k}}{\rho_{\mathrm{bed},k}}\, \left(\varepsilon_{\mathrm{bed},k} + (1 - \varepsilon_{\mathrm{bed},k})\, \varepsilon_{\mathrm{p}}\right), \tag{3.12d}$$

$$\rho_{\mathrm{bed},k} = (1 - \varepsilon_{\mathrm{bed},k})\, (1 - \varepsilon_{\mathrm{p}})\, \rho_{\mathrm{cry}}. \tag{3.12e}$$

Here, $n_{i,k}$ [mol] represents the moles of component i in Bed k with its superscripts 'eq' and 'ini' being the amounts at equilibrium or initial state, respectively. $V_{\mathrm{void},k}$ [m^3] denotes the volume of the bulk-gas phase of Bed k, $m_{\mathrm{bed},k}$ [kg] refers to the mass of the adsorbent in Bed k, and $y_{i,k}$ is the molar fraction of the ith component in the bulk-gas phase. Also, $P_{\mathrm{bulk},k}$ [kPa] is the bulk-gas phase pressure in Bed k, $\rho_{\mathrm{bed},k}$ and ρ_{cry} [kg m^{-3}] refer to the bulk-gas phase density of Bed k and crystal density, respectively, and $\varepsilon_{\mathrm{bed},k}$ and ε_{p} are the void fraction of Bed k and the pellet void fraction, respectively.

The first term of Eq. 3.12a corresponds to the moles of each component in the bulk-gas phase by simply applying the ideal gas equation of state. The last term represents the moles of each species in the adsorbed phase by applying Eq. 3.11a. Eq. 3.12b refers to the conservation of mass of each single component and Eq. 3.12c is required for closing the system of equations with holding variables $P_{\mathrm{bulk},k}$ and $y_{i,k}$ with $i = 1, ..., N_{\mathrm{C}} - 1$. Eqs. 3.12d and 3.12e consider the use of an adsorbent in the form of pellets that consist of microporous crystallites, which are held together by a binder. Thus, the pellet has inter-crystalline macropores and intra-crystalline micropores such that the volume of the bulk-gas phase requires the consideration of the void volume outside the pellet and the macropore volume.

During desorption of the gas mixture into the next following bed, the connected beds share the same gas phase but operate at different temperatures. Here, the two beds have different volumes and different initial pressures, temperatures, and concentrations. Nevertheless, at infinite time, both beds reach the same pressure and steady state gas phase concentrations (Hoover and Wankat, 2002). In such a case, the term 'equilibrium' cannot be used as the equilibrium conditions are the equality in all phases of temperature, pressure, and chemical potential of each gaseous component (Myers and Monson, 2014; Sirkar, 2014) (see also Appendix A, Sections A.1 and A.2 for more information).

The driving forces in developing separation in this closed two-bed system are the pressure, temperature, and the concentration gradients. Once the two beds are connected together, the following effects occur:

(i) Non-equilibrium pressure gradient causes a bulk motion of molecules from high to low pressure regions.

(ii) Molecules diffuse from high concentration regions to low concentration regions, known as self-diffusion effect.

(iii) The existence of a temperature gradient exerts unequal forces on molecules of different kinds such that the lighter gas species concentrates in the hotter region and the heavier gas species concentrates in the cooler region, known as *thermal diffusion* or *Soret effect* (Bird et al., 1960; Sirkar, 2014).

Under the assumption of a quasi-steady state, the concentration gradient in the bulk-gas phase driven by the temperature gradient between the two beds has to be considered (Bird et al., 1960). At steady state, the temperature-gradient-driven flux is in balance with the concentration-gradient-driven flux in the opposite direction, since the two generated forces from the opposite direction must balance each other (Sirkar, 2014). By considering the extensive analysis on thermal- and self-diffusion in Appendix A, Section A.3, the differences in the molar fraction of species i between the two beds is given by

$$-k_{\mathrm{T}} \ln\left(\frac{T_{\mathrm{A}}}{T_{\mathrm{B}}}\right) = y_i|_{\mathrm{T_A}} - y_i|_{\mathrm{T_B}} = y_{i,\mathrm{A}} - y_{i,\mathrm{B}}. \tag{3.13}$$

Here, the subscripts 'A' and 'B' denote the Bed A and Bed B, which operate at high temperature and low temperature, respectively. k_{T} is a thermal diffusion ratio[7] that can be calculated or estimated. For example, estimated values of k_{T} for the binary mixture of CO_2 and N_2 are given by Bastick et al. (1939). For illustration, a rough estimate of k_{T} for temperature below 143 °C is 0.0119 (Bastick et al., 1939). Thus, in the case of $\mathrm{T_A}$=95 °C and $\mathrm{T_B}$=20 °C, $(y_{i,\mathrm{A}} - y_{i,\mathrm{B}})$ the value is -0.0027, indicating about a 0.3% higher concentration of the heavier species CO_2 in the cool region (Bed B).

Due to the very small difference in the concentration of species i between the two beds, the bulk-gas phase of both connected beds, for sake of simplicity, is assumed to be homogeneous such that $y_{i_{|_{\mathrm{T_A}}}} = y_{i_{|_{\mathrm{T_B}}}}$. Hence, the total amount of the ith component in both connected beds at quasi-steady state is governed by

$$\begin{aligned} n_{i,\mathrm{tot}}^{(\mathrm{eq})} = &\left[\frac{(y_{i,k}\, P_{\mathrm{bulk},k})\, V_{\mathrm{void},k}}{R_{\mathrm{g}}\, T_{\mathrm{high},k}} + m_{\mathrm{bed},k}\, \frac{q_{\mathrm{s},i}\ (b_i)_{T_{\mathrm{high},k}}\, (y_{i,k}\, P_{\mathrm{bulk},k})}{1 + \sum_{j=1}^{N_{\mathrm{C}}} (b_j)_{T_{\mathrm{high},k}}\, (y_j\, P_{\mathrm{bulk},k})}\right]_{\mathrm{Bed}\ k} \\ &+ \left[\frac{(y_{i,k+1}\, P_{\mathrm{bulk},k+1})\, V_{\mathrm{void},k+1}}{R_{\mathrm{g}}\, T_{\mathrm{low},k+1}}\right. \\ &\left. + m_{\mathrm{bed},k+1}\, \frac{q_{\mathrm{s},i}\ (b_i)_{T_{\mathrm{low},k+1}}\, (y_{i,k+1}\, P_{\mathrm{bulk},k+1})}{1 + \sum_{j=1}^{N_{\mathrm{C}}} (b_j)_{T_{\mathrm{low},k+1}}\, (y_{j,k+1}\, P_{\mathrm{bulk},k+1})}\right]_{\mathrm{Bed}\ k+1}, \end{aligned} \tag{3.14}$$

[7] The k_{T} has been defined as (Bird et al., 1960; Brodkey and Hershey, 1988)

$$k_{\mathrm{T}} = \frac{\rho_{\mathrm{t}}\, D_1^{\mathrm{T}}}{C_{\mathrm{t}}^2\, M_1\, M_2\, D_{12}},$$

where D_1^{T} [kg m^{-1} s^{-1}] is the thermal diffusion coefficient of species 1 in a binary mixture of 1 and 2, D_{12} [m^2 s^{-1}] is the ordinary diffusion coefficient, C_{t} [mol m^{-3}] denotes the total number of molecules per unit of volume, ρ_{t} [kg m^{-3}] is the density of the mixture, and M_1 [kg mol^{-1}] is the molar mass of species 1. An approximation for the coefficient D_{12} is given by Srivastava and Madan (1953).

where $n_{i,\mathrm{tot}}$ [mol] refers to the total moles of the ith component in connected Beds k and $k+1$. Eq. 3.14 requires a global mass balance for each single component, that being

$$n_{i,\mathrm{tot}}^{(\mathrm{eq})} = n_{i,k}^{(\mathrm{ini})} + n_{i,k+1}^{(\mathrm{ini})}. \tag{3.15}$$

3.3.2 Process Energy Balance: The Simplified Case

For the calculation of the specific thermal energy consumption of the process, the multi-component enthalpy of adsorption and sensible heat have to be considered. The mixture enthalpy of adsorption, $\Delta H_{\mathrm{ads},k}$ [kJ], is governed by (Siperstein and Myers, 2001)

$$\Delta H_{\mathrm{ads},k} = m_{\mathrm{bed},k} \sum_{i=1}^{N_\mathrm{C}} \left(\int_0^{q_i} \Delta \bar{h}_i \, \mathrm{d}q_i \right), \tag{3.16a}$$

$$\Delta \bar{h}_i = \Delta h_i^0 + \frac{1}{q_i^0} \left(\frac{\sum_{j=1}^{N_\mathrm{C}} x_j \, G_j^0 \, q_j^0 \, \left(\Delta \bar{h}_j^0 - \Delta h_j^0 \right)}{\sum_{j=1}^{N_\mathrm{C}} x_j \, G_j^0} \right), \tag{3.16b}$$

$$G_j^0 \equiv \frac{1}{\left(n_i^0\right)^2} \left(\frac{\partial \ln \left(n_i^0\right)}{\partial \ln \left(f_i^0\right)} \right)_T, \tag{3.16c}$$

$$\Delta \bar{h}_i^0 = R T^2 \left(\frac{\partial \ln P}{\partial T} \right)_{q_i} \equiv q_{\mathrm{st},i} = -\Delta H_i, \tag{3.16d}$$

$$\Delta h_i^0 = \frac{\int_0^{q_i} \Delta \bar{h}_i^0 \, \mathrm{d}q_i}{q_i} = -\Delta H_i. \tag{3.16e}$$

Here, q_i^0 [mol kg^{-1}] represents the specific adsorbed amount of pure component i and n_i^0 [mol] is the moles of component i, at the same T and ψ as the mixture, and $q_{\mathrm{st},i}$ [kJ mol^{-1}] is the isosteric heat. Also, $\Delta \bar{h}_i$ [kJ mol^{-1}] denotes the mixture differential enthalpy of adsorption of species i, and $\Delta \bar{h}_i^0$ and Δh_i^0 [kJ mol^{-1}] are the pure-component differential and integral enthalpies of species i, respectively, at the same T and ψ as the mixture. For the rare case of single Langmuir, Eqs. 3.16d and 3.16e prove that the pure-component integral and differential enthalpies are equal and consequently, the differential enthalpies of an ideal solution are equal to their (constant) pure-component values (Sircar, 1995). In case of single Langmuir adsorption, Eq. 3.16a is then simplified to

$$\Delta H_{\mathrm{ads},k} = m_{\mathrm{bed},k} \sum_{i=1}^{N_\mathrm{C}} \left(-\Delta H_i \, q_i \right). \tag{3.17}$$

The sensible heat, $\Delta H_{\mathrm{sens},k}$ [kJ], follows Eq. 3.18 under the assumption that the specific heat of each component is constant in the operating range of temperature and the specific heats in the adsorbed and the bulk-gas phases are constant and identical (Santori et al., 2013). Therefore,

$$\Delta H_{\mathrm{sens},k} = m_{\mathrm{bed},k} \left(\int_{T_{\mathrm{low},k}}^{T_{\mathrm{high},k}} c_{\mathrm{p,s}} \, \mathrm{d}T \right) + \left(T_{\mathrm{high}} - T_{\mathrm{low}} \right) \sum_{i=1}^{N_\mathrm{C}} \left(n_{\mathrm{bulk},i,k} + n_{\mathrm{ads},i,k} \right) c_{\mathrm{p},i}, \tag{3.18}$$

where $c_{\mathrm{p,s}}$ [J kg^{-1} K^{-1}] is the specific heat capacity of the adsorbent, $c_{\mathrm{p},i}$ [kJ mol^{-1} K^{-1}] is the specific heat capacity of the ith component of the mixture in the bulk-gas phase, and

$n_{\mathrm{bulk},i,k}$ and $n_{\mathrm{ads},i,k}$ [mol] are the number of moles of the ith component in the bulk-gas and adsorbed phases, respectively.

Finally, the optional vacuum steps of Beds 1 and 2 require the determination of the specific electrical energy consumption. The power contribution is derived from the expression of the adiabatic compression work following (LeVan et al., 1998)

$$W_{\mathrm{el},k} = \frac{1}{\vartheta_v} \frac{\gamma_{\mathrm{mix}}}{\gamma_{\mathrm{mix}} - 1} n_{\mathrm{proc}} R_{\mathrm{g}} T_{\mathrm{vac}} \left[\left(\frac{P_{\mathrm{atm}}}{P_{\mathrm{vac}}} \right)^{\frac{\gamma_{\mathrm{mix}}}{\gamma_{\mathrm{mix}}-1}} - 1 \right], \tag{3.19a}$$

$$\gamma_{\mathrm{mix}} = \frac{\sum_{i=1}^{N_{\mathrm{C}}} y_i \, c_{\mathrm{p},i}}{\sum_{i=1}^{N_{\mathrm{C}}} y_i \, c_{\mathrm{v},i}}. \tag{3.19b}$$

Here, $W_{\mathrm{el},k}$ [kJ] is the energy consumed for vacuum in Bed k, ϑ_{v} denotes the overall vacuum system efficiency, n_{proc} [mol] is the number of moles processed under vacuum, T_{vac} [K] denotes the vacuum temperature, and P_{vac} and P_{atm} [kPa] are the vacuum level and the atmospheric pressure, respectively. For sake of simplicity, it is assumed that ϑ_v=1.

The final enthalpy of adsorption/desorption in Bed k at step j, $E_{j,k}^{(\mathrm{ads})}$ [kJ], follows

$$E_{j,k}^{(\mathrm{ads})} = \Delta H_{j,k}^{(\mathrm{ads})} - \Delta H_{j-1,k}^{(\mathrm{ads})}. \tag{3.20}$$

The total specific thermal energy that is required for heating, $E^{(\mathrm{th})}$ [kJ mol^{-1}], is a function of the total sensible heat required for heating up the beds, $E^{(\mathrm{sens})}$ [kJ], and the total heat of desorption required for heating, vacuum, and discharging in the next connected bed, $E^{(\mathrm{ads})}$ [kJ], as

$$E^{(\mathrm{th})} = \frac{\sum_{j}^{N_{\mathrm{St}}} E_j^{(\mathrm{sens})} + E_j^{(\mathrm{ads})}}{n_{\mathrm{stored},i}}. \tag{3.21}$$

Here, N_{St} represents the total number of steps of the process, which depends on the number of cycles and the number of beds in the compression and purification section. Also, the term $n_{\mathrm{stored},i}$ [mol] denotes the moles of the trace impurity i that are stored in both phases of the final bed.

3.3.3 Additional Considerations: Adiabatic Blowdown and Heat Recovery Strategies

The efficiency of a separation process is defined by the separation factor or the selectivity of adsorbent material. Given the adsorbed phase composition $x_i = \frac{q_i}{q_{\mathrm{t}}}$, where q_{t} denotes the total adsorbed amount in the adsorbed phase, the selectivity of the adsorbent for component i relative to component j ($S_{i,j}$) is given by

$$S_{i,j} = \frac{x_i / y_i}{x_j / y_j} = \frac{q_i / p_i}{q_j / p_j}. \tag{3.22}$$

The larger the selectivity, the easier the separation of species i over j by adsorption (Myers, 2006).

The recovery of the process is calculated as follows

$$Rec = \frac{n_{(i,j=N_{\mathrm{R}},k=N_{\mathrm{B}})}}{\sum_{j=1}^{N_{\mathrm{R}}} n_{(i,j,k=1)} + \sum_{k=1}^{N_{\mathrm{B}}} n_{(i,j=0,k)}}, \tag{3.23}$$

where the subscripts 'i', 'j', and 'k' denote the trace species, the number of run, and the bed number under consideration, respectively. The term $n_{(i,j=0,k)}$ is the number of moles of component i that accumulates in Bed k at the end of the preliminary regeneration procedure. By excluding this term, recovery can be simply derived by

$$Rec = \frac{n_{(i,j=N_{\mathrm{R}},k=N_{\mathrm{B}})} - n_{(i,j=0,k=N_{\mathrm{B}})}}{\sum_{j=1}^{N_{\mathrm{R}}} n_{(i,j,k=1)}}. \tag{3.24}$$

3.3.3.1 Adiabatic Blowdown

An adiabatic equilibrium model for bulk binary gas mixtures is considered in the preliminary regeneration step and as an alternative to the optional instantaneous vacuum steps in Bed 1 and Bed 2. This model is based on a system of ordinary differential equations as developed by Kumar (1989), which considers the simple extended Langmuir model and is governed by

$$\frac{\mathrm{d}y}{\mathrm{d}P} = \frac{X_1\,X_2 + E\,X_3 + X_8\,X_4}{X_5\,X_2 + F\,X_3 - X_8\,X_6 - X_7}, \tag{3.25}$$

$$\frac{\mathrm{d}\theta}{\mathrm{d}P} = \frac{\mathrm{d}y}{\mathrm{d}P}\left(\frac{F + n_y\,X_8}{X_2 - n_\theta\,X_8}\right) + \frac{E + n_p\,X_8}{X_2 - n_\theta\,X_8}, \tag{3.26}$$

where

$$\begin{aligned}
X_1 &= y\,n_P - n_{1P}, & n_P &= \sum_i n_{iP},\\
X_2 &= c_{\mathrm{p,s}} + A\,P\,c_{\mathrm{p,gas}} - B, & n_y &= \sum_i n_{iy},\\
X_3 &= y\,n_\theta - n_{1\theta}, & n_\theta &= \sum_i n_{i\theta},\\
X_4 &= n_{2\theta}\,n_{1P} - n_{1\theta}\,n_{2P}, & n_{1P} &= \frac{q_{\mathrm{s}}\,b_1\,y}{Z},\\
X_5 &= A\,P + n_{1y} - y\,n_y, & n_{2P} &= \frac{q_{\mathrm{s}}\,b_2\,(1-y)}{Z},\\
X_6 &= n_{2\theta}\,n_{1y} - n_{1\theta}\,n_{2y}, & n_{1y} &= \frac{q_{\mathrm{s}}\,b_1\,P\,(1+b_2\,P)}{Z},\\
X_7 &= A\,P\,\theta\,c_{\mathrm{p,gas}}\,n_\theta, & n_{2y} &= -\frac{q_{\mathrm{s}}\,b_2\,P\,(1+b_1\,P)}{Z},\\
X_8 &= \theta\,c_{\mathrm{p,gas}}, & n_{1\theta} &= \frac{q_{\mathrm{s}}\,b_1\,P\,y}{Z\,R\,(T_{\mathrm{s}}+\theta)^2}\,\left[P\,b_2\,(1-y)\,(q_2-q_1) - q_1\right],\\
A &= \frac{\varepsilon}{\rho_{\mathrm{s}}\,R\,T}, & n_{2\theta} &= \frac{q_{\mathrm{s}}\,b_2\,P\,(1-y)}{Z\,R\,(T_{\mathrm{s}}+\theta)^2}\,\left[P\,b_1\,y\,(q_1-q_2) - q_2\right],\\
B &= q_1\,n_{1\theta} + q_2\,n_{2\theta}, & Z &= \left[1 + b_1\,P\,y + b_2\,P\,(1-y)\right]^2.\\
E &= q_1\,n_{1P} + q_2\,n_{2P},\\
F &= q_1\,n_{1y} + q_2\,n_{2y},
\end{aligned}$$

Here, $\theta = T - T_{\mathrm{s}}$ [K], y is the molar fraction of the strongly adsorbed component, ε denotes the bed void fraction, and ρ_{s} [kg m^{-3}] refers to the adsorbent density.

3.3.3.2 Heat Recovery Strategies

For heat recovery considerations, it is assumed that thermal energy can be recovered and stored in water reservoirs. For the sake of simplicity, the assumption that heat losses and heat exchange with the surrounding environment are negligible is considered. It is assumed that the packed beds are heated up by means of a heat exchanger. It is also assumed that the Bed k is initially at T_{high} and heat is transferred from Bed k to Bed k+1, which is initially at T_{low}. This heat is used to heat up Bed k+1 up to T_{eq} as

$$\begin{aligned} &m_{\mathrm{ads},k}\, c_{\mathrm{p,s}}\, T_{\mathrm{high},k} + \sum_{i}^{N_{\mathrm{C}}} n_{i,k}\, c_{\mathrm{p},i}\, T_{\mathrm{high},k} + m_{\mathrm{ads},k+1}\, c_{\mathrm{p,s}}\, T_{\mathrm{low},k+1} + \sum_{i}^{N_{\mathrm{C}}} n_{i,k+1}\, c_{\mathrm{p},i}\, T_{\mathrm{low},k+1} \\ &= (m_{\mathrm{ads},k} + m_{\mathrm{ads},k+1})\; c_{\mathrm{p,s}}\, T_{\mathrm{eq}} + \sum_{i}^{N_{\mathrm{C}}} (n_{i,k} + n_{i,k+1})\; c_{\mathrm{p},i}\, T_{\mathrm{eq}}. \end{aligned} \tag{3.27}$$

Thus, less energy is needed to heat up Bed k+1 from T_{eq} to T_{high}.

By the end of the heating and equilibration steps of all beds, heat can be recovered before cooling down the bed to T_{low}. By assuming that the process consists of 4 beds, as illustrated in Figure 3.8, the equilibrium temperature by heat recovery at the end of steps (b) for Bed 1, (d) for Bed 2, and (e) for Bed 3, is calculated by

$$\begin{aligned} &m_{\mathrm{ads},1}\, c_{\mathrm{p,s}}\, T_{\mathrm{eq},1} + \sum_{i}^{N_{\mathrm{C}}} n_{i,1}\, c_{\mathrm{p},i}\, T_{\mathrm{eq},1} + m_{\mathrm{ads},2}\, c_{\mathrm{p,s}}\, T_{\mathrm{eq},2} \\ &+ \sum_{i}^{N_{\mathrm{C}}} n_{i,2}\, c_{\mathrm{p},i}\, T_{\mathrm{eq},2} + m_{\mathrm{ads},3}\, c_{\mathrm{p,s}}\, T_{\mathrm{high},3} + \sum_{i}^{N_{\mathrm{C}}} n_{i,3}\, c_{\mathrm{p},i}\, T_{\mathrm{high},3} \\ &+ m_{\mathrm{tank}}\, c_{\mathrm{p,w}}\, T_{\mathrm{w}} = (m_{\mathrm{ads},1} + m_{\mathrm{ads},2} + m_{\mathrm{ads},3})\; c_{\mathrm{p,s}}\, T_{\mathrm{w,eq}} + \sum_{i}^{N_{\mathrm{C}}} (n_{i,1} + n_{i,2} + n_{i,3})\; c_{\mathrm{p},i}\, T_{\mathrm{w,eq}}. \end{aligned} \tag{3.28}$$

By the end of each cycle, the heat that is stored in the water tank, at $T_{w,\mathrm{eq}}$, can be used to heat up the first bed at the beginning of the next cycle. Therefore,

$$m_{\mathrm{ads},1}\, c_{\mathrm{p,s}}\, T_{\mathrm{low},1} + \sum_{i}^{N_{\mathrm{C}}} n_{i,1}\, c_{\mathrm{p},i}\, T_{\mathrm{low},1} + m_{\mathrm{tank}}\, c_{\mathrm{p,w}}\, T_{\mathrm{w,eq}} = m_{\mathrm{ads},1}\, c_{\mathrm{p,s}}\, T^{\mathrm{t}}_{\mathrm{w,eq}} + \sum_{i}^{N_{\mathrm{C}}} n_{i,1}\, c_{\mathrm{p},i}\, T^{\mathrm{t}}_{\mathrm{w,eq}}, \tag{3.29}$$

where $T^{\mathrm{t}}_{\mathrm{w,eq}}$ is the reached equilibrium temperature between the water tank and the first bed. Thus, less heat is required to heat up the first bed from $T^{\mathrm{t}}_{\mathrm{w,eq}}$ to T_{high}.

3.3.3.3 The Common Tangent Plane Approach

The common tangent plane approach of adsorption is applied at the end of each step calculation, and specifically to the system where more than one solution is obtained, to

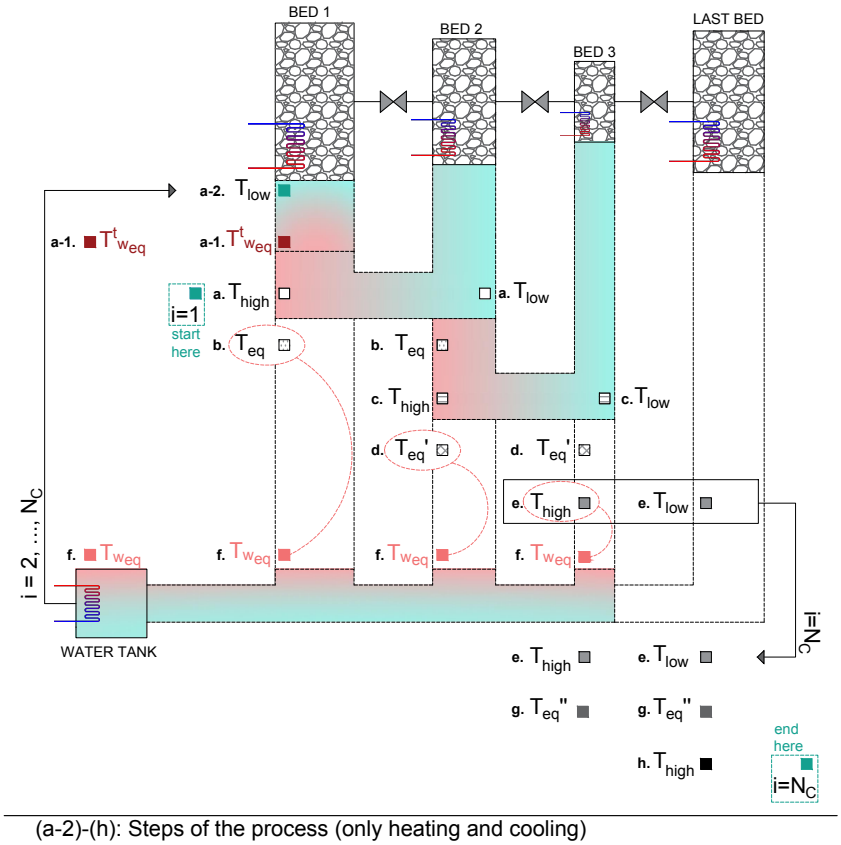

Figure 3.8. A schematic representation of the heat recovery strategies. Abbreviations: T_{eq}, is the reached equilibrium temperature between the heat transfer from $T_{\mathrm{high},k}$ to $T_{\mathrm{low},k+1}$; $T_{\mathrm{w,eq}}$, is the equilibrium temperature reached between the beds and the water tank for heat storage; and $T^{\mathrm{t}}_{\mathrm{w,eq}}$, is the equilibrium temperature reached between the water tank and the first bed after the end of each cycle i.

validate the selected solution. This method has been studied by Santori et al. (2015) and it considers the molar Gibbs energy of mixing, Δg_{mix} [kJ mol^{-1}], in the bulk-gas and adsorbed phases of a bed as

$$\Delta g_{\mathrm{mix}} = RT \sum_{i}^{N_{\mathrm{C}}} w_i \ln\left(w_i\right), \tag{3.30a}$$

$$\frac{g}{RT} = \begin{cases} \frac{g_{\mathrm{gas,mix}}}{RT} = y_1 \ln\left(y_1\right) + y_2 \ln\left(y_2\right), \\ \\ \frac{g_{\mathrm{ads,mix}}}{RT} = x_1 \ln\left(\frac{P_1^0\, x_1}{P_{\mathrm{bulk}}}\right) + x_2 \ln\left(\frac{P_2^0\, x_2}{P_{\mathrm{bulk}}}\right). \end{cases} \tag{3.30b}$$

Here, w_i refers to the molar fraction of component i in the specific phase considered. The subtraction of the slopes of Eqs. 3.30b must be equal to zero for the selected solution to be right.

For implementing this approach, the calculation of surface pressure (P_i^0) [kPa] is required. Assuming a system of an ideal gas mixture adsorbed ideally and considering the equilibrium criterion, the P_i^0 follows the Raoult's law for component i (Myers and Prausnitz, 1965; Myers, 1968) and becomes

$$P_i^0 = \frac{y_i\, P_{\mathrm{bulk}}}{x_i}, \tag{3.31}$$

Table 3.4. Mono-site Langmuir isotherm parameters for CO_2 and N_2.

Parameter	Unit	CO_2		N_2	
		298.15 [K]	353.15 [K]	298.15 [K]	353.15 [K]
q_s	mol kg^{-1}	4.00	4.00	4.00	4.00
b	kPa^{-1}	0.144	0.019	0.0004	0.0002
K_H	mol kg^{-1} kPa^{-1}	0.577	0.078	0.0016	0.0006
$\left(10^{-7}\right) b_0$	kPa^{-1}	3.76	3.76	9.74	9.74
$(-)\,\Delta H$	kJ mol^{-1}	31.86	31.86	14.92	14.92

Note: Data obtained from Xiao et al. (2008) and regressed using the linear form of Langmuir isotherm (see Appendix B.1).

where x_i is the molar fraction of the ith component in the adsorbed phase. P_i^0 is also defined as the bulk-gas pressure of pure species i in its standard state, which is defined by the surface potential (Φ) (Siperstein and Myers, 2001).[8] Φ is a function of ψ that by definition follows (Myers and Monson, 2014)

$$\psi_i = \frac{\Phi_i}{RT} = \int_0^{P_i^0} q_i^0\left(P_{\text{bulk}}\right)\,\mathrm{d}\left(\ln P\right), \tag{3.32}$$

where q_i^0 [mol kg^{-1}] is the pure adsorbed amount of species i. The constant reduced grand potential follows $\psi_1 = \psi_2 = ... = \psi_i = \psi_{\text{eq}}$. For the case of single Langmuir model, ψ_i results as

$$\psi_i = q_s \ln\left(1 + b_i\,\frac{P_{\text{bulk}}\,y_i}{x_i}\right). \tag{3.33}$$

3.4 The Case of Direct Air Capture: Process Material and Energy Balance

3.4.1 Process Considerations

A benchmark case has been developed to confirm that the proposed process is thermodynamically feasible. The present case is restricted to the simple case of binary adsorption of trace impurity CO_2 (species (1) of the mixture) and secondary gas N_2 (species (2) of the mixture) on a commercial sorbent zeolite 13X in pellet form. Fixed-bed operation with the sorbent in pellet or bead form is the principal way of conducting sorption separations and purifications (LeVan et al., 1998). Zeolite 13X was selected as it is a well-known adsorbent material with a relatively high CO_2 adsorption capacity at low pressure (Hefti et al., 2015; Mangano et al., 2013), high CO_2 selectivity over N_2 (Gibson et al., 2016), favourable adsorption kinetics and quick desorption rates for shorter cycle times (Rege et al., 2000). For this reason, data on pure-component adsorption of CO_2 and N_2 gases on zeolite 13X from Xiao et al. (2008) had been used and the parameters obtained from the simultaneous non-linear regression of the experimental isotherm data are listed in Table 3.4 and extensively discussed in Appendix B.1.

For the benchmark case, all the operating parameters of the process are listed in Table 3.5. A batch of 4 beds connected in series, characterised by reduced size, and loaded with zeolite 13X pellets has been examined. The operation of the system includes the optional vacuum

[8] The surface potential has been traditionally expressed as a function of a two-dimensional spreading pressure (Π) and specific surface area (A): $\Phi = -\Pi\,A$ (Myers and Prausnitz, 1965). Later on, surface potential has be expressed in adsorption thermodynamics as a function of the reduced grand potential (ψ): $\Phi = -\psi\,RT$ (Siperstein and Myers, 2001).

Table 3.5. Parameters related to the operation of the process and considered adsorbent material for the benchmark case.

Process Parameters	Value	Unit	Reference
Number of beds, N_{B}	4	—	—
Number of runs, N_{R}	60	—	—
Mass of Bed 1, $m_{\mathrm{bed},1}$	1	kg	—
Relative mass of Bed 2, $m_{\mathrm{bed},2}/m_{\mathrm{bed},1}$	0.20	—	—
Relative mass of Bed 3, $m_{\mathrm{bed},3}/m_{\mathrm{bed},1}$	0.05	—	—
Relative mass of Bed 4, $m_{\mathrm{bed},4}/m_{\mathrm{bed},1}$	0.30	—	—
Void fraction in Bed 1, $\varepsilon_{\mathrm{bed},1}$	0.50	—	Rezaei and Webley (2009)
Inter particle void fraction, $\varepsilon_{\mathrm{bed},(2-4)}$	0.25	—	Balahmar et al. (2016) [a]
Operating Conditions			
Adsorption temperature, T_{low}	293.15	K	—
Regeneration temperature, T_{high}	368.15	K	—
Atmospheric pressure, P_{atm}	101.325	kPa	—
Vacuum pressure, P_{vac}	30	kPa	—
Zeolite 13X Physical Properties			
Crystal density, ρ_{cry}	1500	kg m^{-3}	Oreggioni et al. (2015)
Pellet void fraction, ε_{p}	0.2	—	Hu et al. (2014)
[b] Adsorbent specific heat capacity, $c_{\mathrm{p,s}}$	858	J kg^{-1} K^{-1}	Santori et al. (2013)
Components Properties			
Number of components in the feed, N_{C}	2	—	—
Feed molar fraction of CO_2, y_1	0.0004	—	—
Feed molar fraction of N_2, y_2	0.9996	—	—
[b] Specific heat capacity of CO_2, $c_{\mathrm{p},1}$	38.51	J mol^{-1} K^{-1}	Lemmon et al. (2013)
[b] Specific heat capacity of N_2, $c_{\mathrm{p},2}$	29.16	J mol^{-1} K^{-1}	Lemmon et al. (2013)
[b] Specific heat capacity of CO_2, $c_{\mathrm{v},1}$	30.30	J mol^{-1} K^{-1}	Lemmon et al. (2013)
[b] Specific heat capacity of N_2, $c_{\mathrm{v},2}$	20.85	J mol^{-1} K^{-1}	Lemmon et al. (2013)

[a] Reported packing density of zeolite 13X.
[b] Average value in the range of 293.15–368.15 K.

steps in Bed 1 and Bed 2 of Tables 3.2 and 3.3. A binary mixture of CO_2, which exists at 400 ppm in feed stream, and N_2, which is the main component of the mixture, has also been considered.

3.4.2 Material Balance

Figure 3.9 summarises the trends of concentrations (in both the bulk-gas and adsorbed phases) and of the total pressure in Bed 4 (storage bed) after performing 60 cycles of the process. The composition of component (1) increases in both phases and reaches a purity of 0.76 (z_1 in molar fraction) in the final 60th cycle, as composition in the adsorbed phase reaches 0.85 (x_1). The pressure in the final bed is built up cycle after cycle reaching the maximum pressure of 18 bar. The compression can be obtained by exclusively employing thermal energy at 95 °C, which can be obtained by solar heating systems (Santori et al., 2012; Duffie and Beckman, 2013).

The concentrations in the storage bed do not reach a steady state after 60 cycles of the process. Therefore, more cycles of the process are presented in Figure 3.10, where the concentration and pressure profiles reach a steady state after operating 150 cycles of the process. Figure 3.10a shows that zeolite 13X can achieve, under the parameters specified in Table 3.5, 90% purity in the storage bed (z_1) by having only 4 beds connected. It is expected that higher purities can be achieve by having more beds in the compression and purification section or by optimising the mass of the adsorbent material inside each bed. Figure 3.10b shows the pressure profile and equilibrium amount of moles of each component in Bed 4. It is shown that the pressure profile follows the concentration profile of species 2 in the storage bed. Around 1.1 molCO_2 and 0.1 molN_2 are stored in 0.3 g of Bed 4. Therefore, the storage

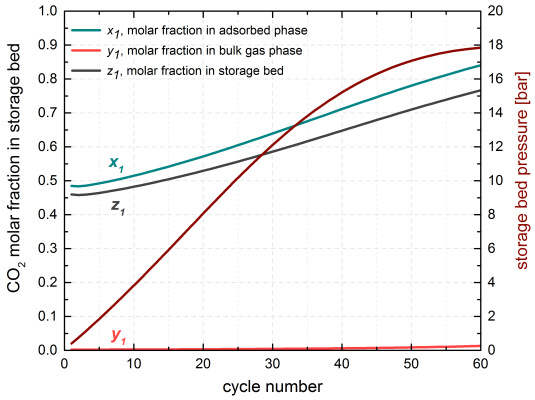

Figure 3.9. Storage bed pressure (dark red curve), global concentration of CO_2 (gray curve, z_1), and concentration of CO_2 in the bulk-gas phase (red curve, y_1) and adsorbed phase (green curve, x_1) of Bed 4 at each operational cycle.

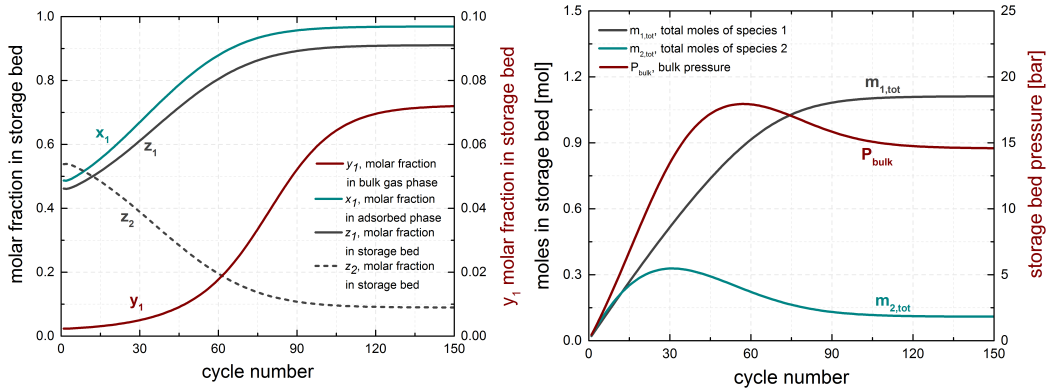

(a) x-y-z in the storage bed

(b) P-moles in the storage bed

Figure 3.10. **(a)** Overall storage bed concentration of CO_2 (gray continuous curve, z_1) and N_2 (gray dashed curve, z_2), CO_2 concentration in the bulk-gas phase (red curve, y_1), and CO_2 concentration in the adsorbed phase (green curve, x_1) of Bed 4 at each operational cycle. **(b)** Total moles of stored CO_2 (gray curve, $m_{1,\text{tot}}$) and N_2 (green curve, $m_{2,\text{tot}}$) and bulk pressure (dark red curve) profiles of Bed 4 at each operational cycle.

bed reaches its adsorption capacity (q_s=4 mol kg^{-1} with zeolite 13X) at 90% purity. It also operates at a constant selectivity ($S_{1/2} = \frac{x_1/x_2}{y_1/y_2}$=403) at each cycle of the process.

Figure 3.11 shows the number of moles of each species entering the storage bed at each cycle of the process. The number of moles of CO_2 that can be stored is decreasing over the number of cycles indicating that a compromise in the amount of moles stored and therefore, in the storage bed purity and pressure, with the process energy consumption has to be reached. Since this is not the optimal operation of the process having 4 beds connected, at 60 cycles, at the point where the pressure reaches a maximum, the process stops and the material and energy balances are analysed. A more detailed analysis on mass balance of the process (up to 150 cycles) is presented in Appendix C, Section C.1.

Figure 3.12 shows the material balance across the system after operating 60 cycles of the process. 2460 moles of air flows in Bed 1 from which 99.85% leaves the system as clean air, purified in N_2, and 0.09% during the vacuum steps in Beds 1 and 2. Captured CO_2 and co-adsorbed N_2 are processed along the compression and purification beds. At the final cycle, a portion of process fluid is accumulated in Beds 1–3 and in Bed 4 where 3.07 molCO_2

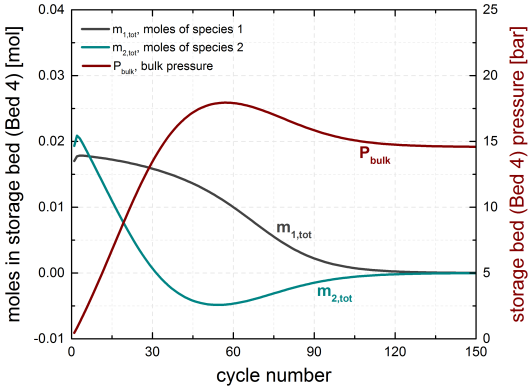

Figure 3.11. Moles of CO_2 (gray curve, $m_{1,\mathrm{tot}}$) and moles of N_2 (green curve, $m_{2,\mathrm{tot}}$) entering Bed 4 and bulk pressure (dark red curve) of Bed 4 at each operational cycle.

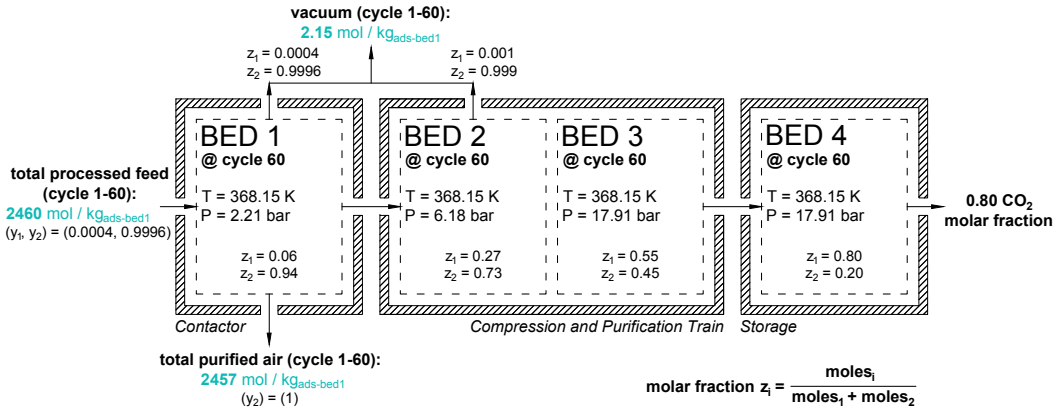

Figure 3.12. System material balance after operating 60 cycles of the process. Abbreviations: index 1, refers to the trace impurity; index 2, denotes the secondary excess gas; y_i, is the molar fraction of species i in the bulk-gas phase; and z_i is the overall molar fraction of species i in both phases.

per $\mathrm{kg_{ads}}$ of Bed 4 are stored. A recovery of 92.5% is obtained considering the gas already present in the system after the preliminary regeneration procedure (see Eq. 3.23). A 90.9% recovery is obtained by applying Eq. 3.24.

For the closed system of two connected beds, T-x-y equilibrium phase diagrams for a two component gas-solid system can simply explain how the most strongly adsorbed compound can be concentrated and purified. Figure 3.13 represents isobaric phase equilibrium diagrams for two different cases, where two beds are connected together sharing the same bulk-gas phase (same equilibrium pressure and composition of species i). The two beds have different reduced grand potentials as the first bed, Bed (A), desorbs at T_{high} (95 °C) and the second bed, Bed (B), adsorbs at T_{low} (20 °C) under the assumption of constant temperature.

In Figure 3.13a, the equilibrium pressure between Beds 2 and 3 reaches 6.2 bar and the bulk-gas phase composition is almost purely saturated in component (2) (0.995 N_2 molar fraction) at cycle 60. The adsorbed phases of Beds 2 and 3 have a greater concentration of key component (1) (CO_2) reaching 0.32 and 0.66, respectively. Since Bed 2 operates at T_{high} and Bed 3 at T_{low}, as also illustrated from the pure adsorption isotherms of each species in the mixture in Figure B.1, Appendix B, a greater amount of the strongly adsorbed species (1) is expected to move from the bed with high temperature (desorption) to the bed with low

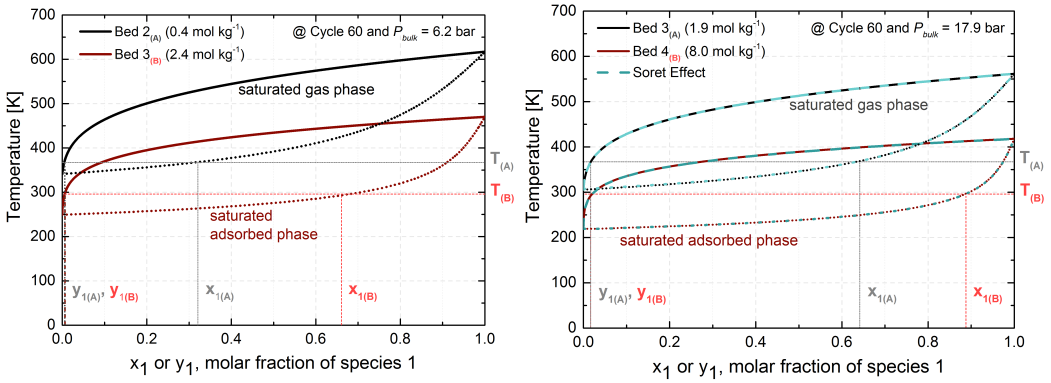

(a) Equilibration Beds 2–3 at cycle 60

(b) Equilibration Beds 3–4 at cycle 60

Figure 3.13. T-x-y equilibrium phase diagrams for the equilibration state between two beds (desorption of Bed (A) at T_{high} (black curves) and adsorption of Bed (B) at T_{low} (red curves)): **(a)** Bed 2 and Bed 3 and **(b)** Bed 3 and Bed 4 at the 60th cycle. Green curves represent the results obtained from Soret effect, considering 0.3% higher CO_2 concentration in the second connected bed (Bed 4).

Notes:
(i) Lines represent the bulk-gas phase composition of species (1), y_1, and dots the adsorbed phase composition of species (1), x_1. The subscript '1' represents the most strongly adsorbed compound.
(ii) The subscript (A) refers to the bed that operates at T_{high} and subscript (B) to the bed that operates at T_{low}.
(iii) The values inside the brackets in the legends correspond to the reduced grand potential (ψ) for each bed operated under different conditions (T, ψ, x_1, x_2).

temperature (adsorption). Hence, both pressure and purity increase in Bed 3. After heating the bed at the regeneration temperature, the composition in the adsorbed phase moves to the bulk-gas phase resulting in an even higher pressure. By connecting Bed 3 and Bed 4 (Figure 3.13b), the concentration of species (1) in the adsorbed phase of Bed 4 reaches a higher purity (x_1=0.88). This is due to the strongly adsorption of the key component by the second connected bed, which operates at lower temperature. This fact always results in an enhanced in component (1) stream that passes from bed to bed. At steady state, Bed 3 and Bed 4 reach 17.9 bar equilibrium pressure and their bulk-gas phase composition y_1 reaches 0.02. Finally, Figure 3.13b illustrates the results obtained by considering the Soret effect that is occured between the two connected beds, as a higher concentration of CO_2 (around 0.3%) is expected to accumulate in the bed that operates at lower temperature.

By increasing the number of beds, N_{B}, and the runs of the process, N_{R}, a greater amount of the key component at higher pressure is more likely to be reached at the end of the process. Similarly, by increasing the reduced grand potential, the T-x-y phase envelope moves down towards lower temperatures resulting in higher concentrations of component (1) at lower T.

3.4.3 Energy Balance

Three different types of energy are consumed in the process: *(i)* heat at 95 °C, *(ii)* cold at 20 °C, and *(iii)* electricity for the optional vacuum steps in the first beds (in this case Beds 1 and 2). Thermal energy is composed by heat of adsorption/desorption and sensible heat. The energy needed to flow the air through Bed 1 is expected to be constant in cases where the material in Bed 1 is used in the same amount and form, e.g., pellet or powder, the adsorption contactor (Bed 1) has the same configuration and operates at the same

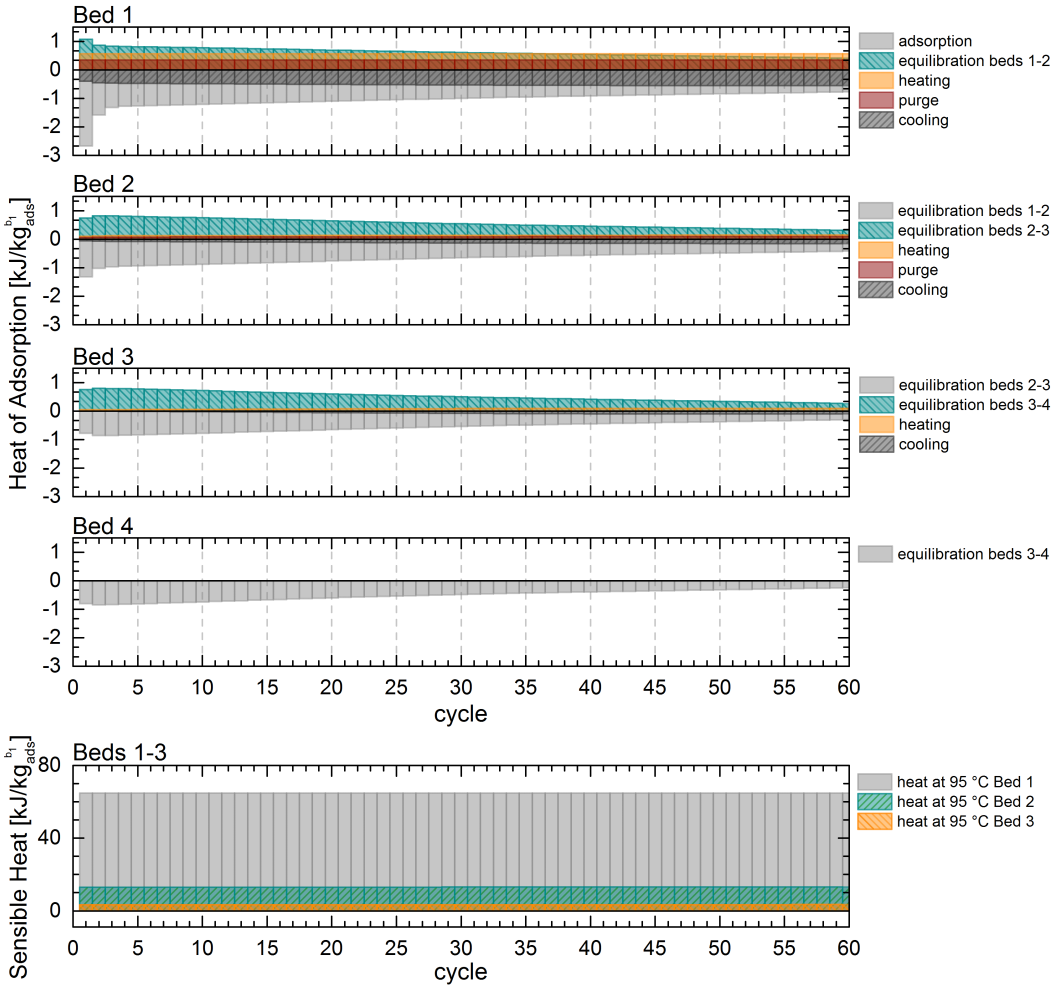

Figure 3.14. Thermal energy consumption due to the heat of adsorption/desorption and sensible heat consumed at each cycle of the process in each Bed per kg of adsorbent in Bed 1.

conditions, and the feed stream has the same properties. In addition, the energy needed to flow the air, using a blower or a fan, is relative to the pressure drop across the bed. This investigation on pressure drop is considered in Chapter 4 and therefore, calculations on the required electrical energy to operate a fan or a blower are presented there. Also, Section C.1 considers the contribution of the electric energy consumption for the operation of the fan to the total energy consumption of the process.

Figure 3.14 illustrates the trend of adsorption and desorption thermal energy and sensible heat that are required at each state of the process from cycle 1 to cycle 60 for each bed. The adsorption and desorption thermal energy trends at each state have the following characteristics:

Bed 1 The thermal energy required for the adsorption step (cold energy) and the heating and vacuum steps (heat energy) is constant along all the cycles of the process. The heat required during the equilibration of Beds 1 and 2 decreases over the cycles due to the reduced amount of CO_2 moving to Bed 2. The heat required during the adsorption step to keep the bed operating under isothermal conditions is identical in magnitude to the sum of the energy contributions for heating, vacuum, and equilibration.

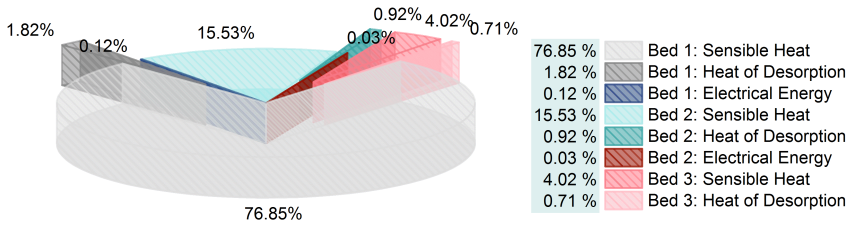

Figure 3.15. Percentage of specific energy consumptions due to the heat of desorption, sensible heat, and electrical energy consumed at the end of the process for each Bed.

Bed 2 The amount of thermal energy in the equilibration steps decreases as the cycles increase due to a reduced amount of CO_2 moving from Bed 1 to Bed 2 and from Bed 2 to Bed 3. Heating and cooling contributions increase over the cycles because of the increased presence of CO_2 in the bed.

Bed 3 A similar behaviour to Bed 2 is observed. The amount of CO_2 moving from Bed 2 to Bed 3 and from Bed 3 to Bed 4 during the equilibration steps decreases along the cycles resulting in the decrease of the energy demand. Here, the effect of the required energy for heating and cooling is stronger compared to Bed 2 due to the presence of a higher amount of CO_2 in the bed.

Bed 4 This bed is always kept at 20 °C. Cooling energy variations are related to the amount of CO_2 delivered from Bed 3, which decreases after the 2nd cycle as CO_2 begins to be stored in the bulk-gas phase.

Since thermal energy for cooling is required at 20 °C, ambient air is suitable as cold utility. The total thermal specific energy consumption[9] of the process is 0.19 MJ_{th} $molCO_2^{-1}$ due to the heat of desorption from which 52.75% of this energy is required by Bed 1, 26.69% by Bed 2, and 20.56% by Bed 3. Bed 4 does not contribute to the heat of desorption because it is always in an adsorption state.

Figure 3.14 shows that the sensible heat is an order of magnitude higher than the adsorption and desorption thermal energy at each cycle of the process. The total specific sensible heat required by the process is 5.33 MJ_{th} $molCO_2^{-1}$. The adsorbent material is the main contributor accounting for 98.92% of the total energy for sensible heating. As illustrated in Figure 3.15, 76.85% of total specific sensible heat is required by Bed 1 and only 15.53% and 4.02% are required from Bed 2 and Bed 3 respectively. These values suggest that a significant energy saving can be expected by applying heat recovery strategies.

5.52 MJ_{th} $molCO_2^{-1}$ of thermal energy was consumed by the process in the form of heating. The total specific electrical energy consumption for the optional vacuum steps of Bed 1 and Bed 2 is only 0.01 MJ_{el} $molCO_2^{-1}$.

3.4.4 Alternative Application: Air Revitalisation Systems and A Comparison with Direct Air Capture

Applications that are characterised by an order of magnitude higher initial composition of trace impurity than DAC, are expected to require significantly lower amount of thermal

[9]The total thermal specific energy consumption is defined over the moles of CO_2 in the storage bed (Bed 4) at the end of the process (after 60 cycles).

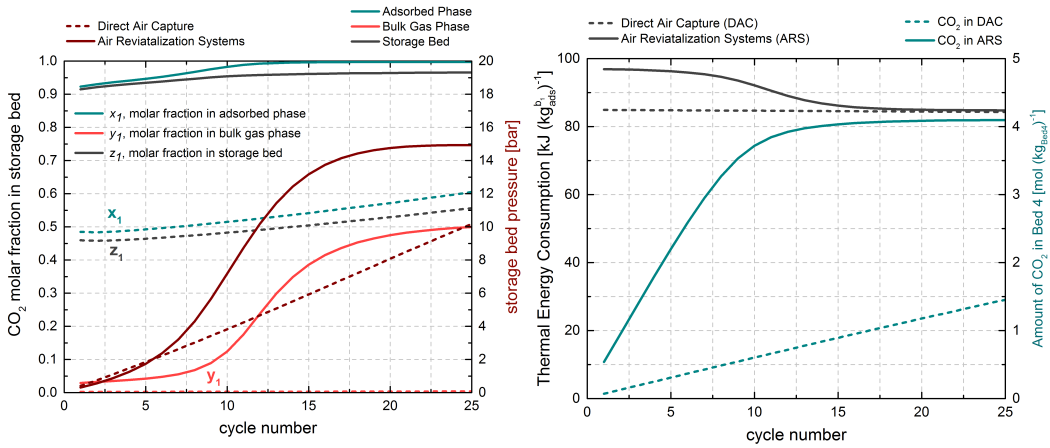

(a) $P - x_1 - y_1 - z_1$ **(b)** $E_{\text{th}} - molCO_2$

Figure 3.16. **(a)** Storage bed pressure (dark red curves), global concentration of CO_2 (gray curves), concentration of CO_2 in the bulk-gas phase (red curves) and adsorbed phase (green curves) of Bed 4 at each cycle and **(b)** thermal energy consumption and moles stored in Bed 4 for the case of 400 ppm (DAC) and 4,000 ppm (ARS) CO_2 concentration in the inlet stream.

energy to proceed compression and purification. The reduction of the thermal energy is directly related to the increase of the feed trace component concentration. Such applications can be found in air revitalisation systems (ARSs) used to sustain the quality of the breathing air in a closed cabin atmosphere. It is predicted that each person produces about 1 $kgCO_2$ day^{-1} (Barta and Henninger, 1994) that has to be treated before reaching the maximum recommended occupational exposure limit of 5,000 ppm (Satish et al., 2012). NASA has established effective processors, such as the CDRA of ISS, to remove CO_2 generated by the human crew from the air in the cabin (ElSherif and Knox, 2005; Mattox et al., 2013) and subsequently to deliver it for the recovery of O_2 (Rosen et al., 2005; Mulloth et al., 2004).

The same process parameters, operating conditions, and adsorbent physical properties used for the case of DAC (see Table 3.5) are used also to compare the performance of the process in case of higher inlet concentration of the dilute component, in this case CO_2. The inlet concentration of CO_2 is fixed at 4,000 ppm, 0.4%. Figure 3.16a represents the performance of both cases in terms of purity and pressure in the storage bed (Bed 4). By processing a stream with one order of magnitude higher concentration of trace impurity than CO_2 concentration in the atmosphere, an extremely high purity >96% can be obtained. This does not only benefit the process final purity, but also the number of cycles of the process, which has been reduced from 60 to 25 for DAC and ARSs, respectively. Subsequently, the process operation time can be reduced significantly. Finally, the pressure in the storage bed is a third higher than that obtained in the case of DAC at the 25th cycle. The resulting final pressure is at around 15 bar.

4.85 $MJ_{\text{th+el}}$ $molCO_2{}^{-1}$, after 25 cycles of operation, is required for DAC application. 1.83 $MJ_{\text{th+el}}$ $molCO_2{}^{-1}$ is required for ARSs from which 92.5% is required for sensible heating and 7.5% for thermal heating. The required total thermal energy consumption in each run of the process is plotted in Figure 3.16b. Due to the higher amount of CO_2 stored in the case of ARSs, a higher thermal energy for cooling is required. Finally, the total specific electrical energy use for the optional vacuum steps of Bed 1 and Bed 2 is estimated to be only 2.7 kJ_{el} $molCO_2{}^{-1}$. It is also important to consider that all the reported values for

Table 3.6. Investigated factors and levels for 2^5 full factorial design.

	Parameter	Low Level (–)	High Level (+)
P1	Number of cycles/runs, N_{R}	30	50
P2	[a] Mass ratio, $m_{\mathrm{bed},i}/m_{\mathrm{bed},i+1}$	4	5
P3	Saturation capacity, q_{s}	4	5
P4	Selectivity of (A) over (B), $S_{\mathrm{A/B}}$	400	600
P5	Number of beds, N_{B}	4	5

[a] The subscript i refers to the number of bed, $i = 1, ..., N_{\mathrm{B}} - 1$.

Note: For sake of simplicity, masses of Bed 1 ($m_{\mathrm{bed},1}$) and storage bed ($m_{\mathrm{bed},N_{\mathrm{B}}}$) are fixed at 1 kg and 0.3 kg, respectively, and the isosteric heat of adsorption of species (A), ΔH_{A}, and (B), ΔH_{B}, are fixed at -35 kJ mol^{-1} and -15 kJ mol^{-1}, respectively. Here, (A) denotes the most strongly adsorbed compound and (B) the less strongly adsorbed one.

purity, pressure, and energy use can be further improved by applying different optimisation techniques.

3.5 A Generic Case: Sensitivity Analysis and Optimisation

Since this application can be used for the separation, compression, and purification of a dilute stream, a general case is presented and optimised. It is assumed that the gas steam consists of a binary mixture of a trace impurity (A) and the main component (B). Since the components (A) and (B) are generalised, their thermochemical properties have also been generalised. By investigating different concentrations of component (A), the resulting energy, purity, pressure, and recovery give an indication on the design parameters for various dilute streams.

3.5.1 Process Analysis

Sensitivity analysis and optimisation are the key aspects of successful process design aimed at maximising process performance, minimising project cost, and facilitating the selection of the best process components (Towler and Sinnott, 2013). Sensitivity analysis is used as a preliminary investigation for finding the optimal performance of the process in terms of specific energy consumption, final purity and pressure in the storage bed, and process recovery. Since there are several parameters affecting the process, a 2^5 full factorial design (FFD) is introduced for the sensitivity analysis. This is used to evaluate the significant effects and interactions of different independent variables of the system and adsorbent material (i.e., number of beds, number of process cycles, adsorption saturation capacity, *etc*.) on dependent variables (objective functions) and to reduce the dimension of the optimisation problem (Santori et al., 2013; Freni et al., 2008). The investigated parameters for the sensitivity analysis are listed in Table 3.6. The additional parameters of the equilibrium model are fixed and are presented in Table 3.7, unless they are specified in Table 3.6.

The 32 cycles with the corresponding values of the five investigated parameters and the results of the performance parameters (or else objective functions, which are the specific energy, purity, pressure, and recovery) are listed in Table C.2 in Appendix C. The effects of these parameters and of their higher order interactions on the performance parameters are estimated using the Yate's algorithm (Box et al., 2005; Di Nicola et al., 2008) and the

Table 3.7. Considered input parameters and variables of the model for process optimisation.

Fixed Parameters	Symbols	Input Parameters				Unit
		Lower Limit	Intermediate Step(s)		Upper Limit	
			1	2		
Number of beds	N_{B}	4	5	—	6	—
Number of runs	N_{R}	10	20	50	100	—
Feed concentration of species (A)	y_{A}	0.0004	0.0006	0.0008	0.001	—
Mass of Bed 1	$m_{\mathrm{bed},1}$	1	—	—	—	kg
Void fraction of Bed 1	$\varepsilon_{\mathrm{b},1}$	0.5	—	—	—	—
Void fraction of Bed (2–N_{B})	$\varepsilon_{\mathrm{b},2-N_{\mathrm{B}}}$	0.25	—	—	—	—
Mono-site Langmuir parameters						
Saturation capacity	q_{s}	4	6	—	8	mol kg^{-1}
Heat of adsorption of species (A)	ΔH_{A}	–35 [a]	—	—	—	kJ mol^{-1}
Equilibrium constant coefficient of (A)	$\left(10^{-7}\right) b_{0,\mathrm{A}}$	4	—	—	—	kPa^{-1}
[b] Selectivity of species (A) over (B) at T_{low}	$\left(S_{\mathrm{A/B}}\right)_{T_{\mathrm{low}}}$	300	600	900	1200	—
[b] Selectivity of species (A) over (B) at T_{high}	$\left(S_{\mathrm{A/B}}\right)_{T_{\mathrm{high}}}$	100	120	180	$\frac{1200}{7}$	—
Material physical properties						
Crystal density	ρ_{cry}	1500	—	—	—	kg m^{-3}
Pellet void fraction	ϵ_{p}	0.2	—	—	—	—
Adsorbent specific heat capacity	$c_{\mathrm{p,s}}$	858	—	—	—	J kg^{-1} K^{-1}
Specific heat capacity						
[c] Specific heat capacity of species (A) or (B)	$c_{\mathrm{p,A\ (B)}}$	29.10	—	—	—	J mol^{-1} K^{-1}
[c] Specific heat capacity of species (A) or (B)	$c_{\mathrm{v,A\ (B)}}$	20.79	—	—	—	J mol^{-1} K^{-1}
Input Variables	**Symbols**	**Entities to Define the Design Space**				**Unit**
		Lower Limit		**Upper Limit**		
Mass of Bed k over Bed 1	$m_{\mathrm{bed},k}/m_{\mathrm{bed},1}$	0.0001		1.0		—
Mass of Bed k+1 (storage bed) over Bed 1	$m_{\mathrm{bed},k+1}/m_{\mathrm{bed},1}$	0.0001		10.0		—

[a] Considering that for physisorption, the heat of adsorption is 5–45 kJ mol^{-1} (Bolis, 2013).

[b] Selectivity is fixed at each temperature and $\left(S_{\mathrm{A/B}}\right)_{T_{\mathrm{low}}} = X\left(S_{\mathrm{A/B}}\right)_{T_{\mathrm{high}}}$ where X is specified in Table 3.8.

[c] Specific heat capacity at constant pressure of species (A), $c_{\mathrm{p,A}}$, is taken as equal for both the components ((A) and (B)) considering the heat capacity of a diatomic molecule to be: $c_{\mathrm{v}} = \frac{5}{2}R$ (where R is the universal gas constant) and $c_{\mathrm{p}} = c_{\mathrm{v}} + R$ as described in Atkins and Paula (2006).

Operating conditions of Table 3.5 have also be considered.

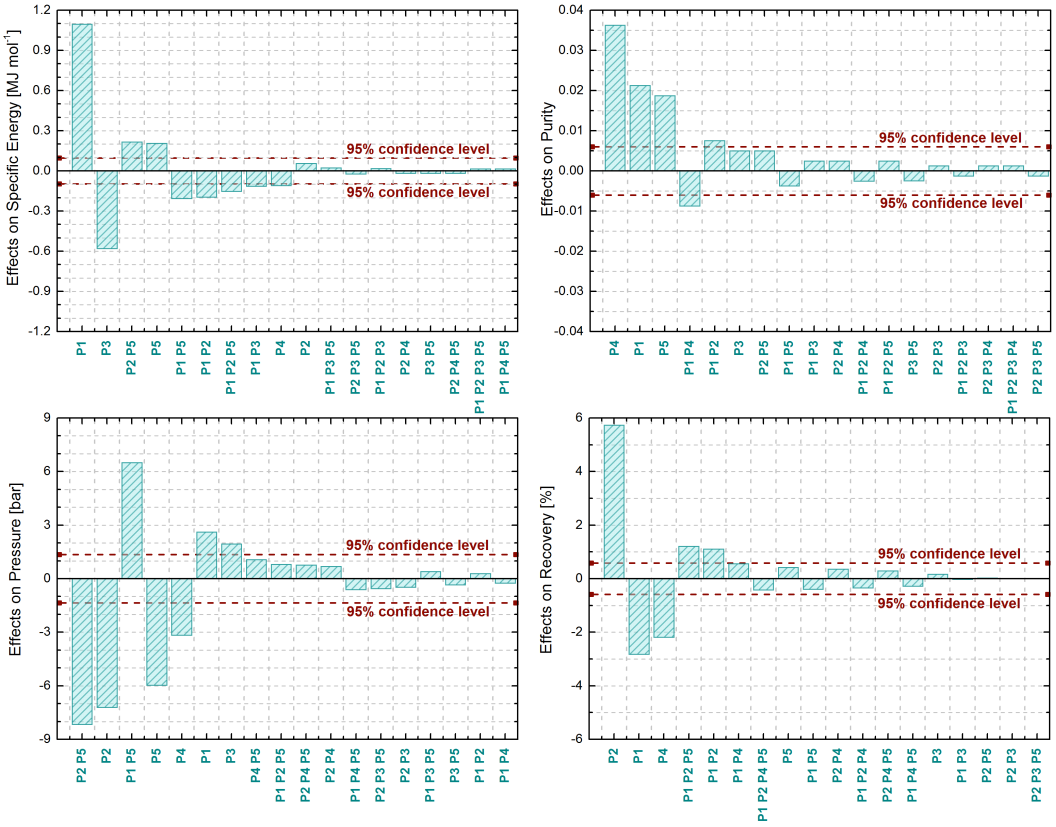

Figure 3.17. Pareto plots for the effects of 2^5 full factorial design on the specific energy, purity, pressure, and recovery. The plotted results correspond to the first 18 most significant effects.

Note: 95% confidence level is calculated from Student's *t*-distribution.

results are presented in Tables C.3 and C.4 in Appendix C. The results from this analysis are also presented in Figure 3.17. The effects are the weights of the single parameters and their higher order interactions on each performance parameter. Appendix C contains more information on this analysis and an extensive discussion on the calculations and the results.

A Student's distribution is applied in order to identify the significant factors and interactions. Considering a 95% confidence interval based on the trend of Student's *t*-test (5 variables, 16 degrees of freedom), single parameters and interactions of two parameters, and in few cases three-level interactions, have a non-negligible effect on the system. For instance, N_{R}, N_{B}, and the two-level interaction between the mass ratio ($m_{\mathrm{bed},i}/m_{\mathrm{bed},i+1}$) and N_{B}, $m_{\mathrm{bed},i}/m_{\mathrm{bed},i+1}$–$N_{\mathrm{B}}$, have a positive effect on energy use. q_{s}, $S_{\mathrm{A/B}}$, the two-level interactions N_{R}–N_{B}, N_{R}–$m_{\mathrm{bed},i}/m_{\mathrm{bed},i+1}$, and N_{R}–q_{s}, and the three-level interaction N_{R}–$m_{\mathrm{bed},i}/m_{\mathrm{bed},i+1}$–$N_{\mathrm{B}}$ have a non-negligible negative effect of energy. Positive effects on purity have the $S_{\mathrm{A/B}}$, N_{R}, N_{B}, and N_{R}–$m_{\mathrm{bed},i}/m_{\mathrm{bed},i+1}$, where the interaction of the single parameters N_{R} and $S_{\mathrm{A/B}}$ has a negative effect. In case of pressure in the storage bed, N_{R}–N_{B}, N_{R}, q_{s}, $S_{\mathrm{A/B}}$–N_{B}, N_{R}–$m_{\mathrm{bed},i}/m_{\mathrm{bed},i+1}$–$N_{\mathrm{B}}$, $m_{\mathrm{bed},i}/m_{\mathrm{bed},i+1}$–$S_{\mathrm{A/B}}$–$N_{\mathrm{B}}$, and $m_{\mathrm{bed},i}/m_{\mathrm{bed},i+1}$–$S_{\mathrm{A/B}}$ have a positive impact. However, $m_{\mathrm{bed},i}/m_{\mathrm{bed},i+1}$, N_{B} and $S_{\mathrm{A/B}}$, and the interaction $m_{\mathrm{bed},i}/m_{\mathrm{bed},i+1}$–$N_{\mathrm{B}}$ have a significant negative influence. Finally, $m_{\mathrm{bed},i}/m_{\mathrm{bed},i+1}$, N_{R}–$m_{\mathrm{bed},i}/m_{\mathrm{bed},i+1}$–$N_{\mathrm{B}}$, and N_{R}–$m_{\mathrm{bed},i}/m_{\mathrm{bed},i+1}$ have a positive effect on recovery and N_{R} and $S_{\mathrm{A/B}}$ a negative.

The second- and third-order effects require a better assessment on how the result responds to variations of the involved parameters. An improved 2^6 FFD is applied in Appendix C, Section C.2 for a better understanding of the significant effects of the configuration of the system and of the adsorbent material on system's performance. Similar to the 2^5 FFD results are obtained and discussed in Appendix C. Since the optimisation strategy focuses on two objective functions, the specific energy consumption and the purity in the storage bed, the results of the sensitivity analysis to these two parameters are more important. The following outcomes have to be considered:

(i) The number of beds can have a positive or negative effect on the specific energy and pressure of the process depending on the mass of adsorbent in each bed (as sensible heat has a significant contribution to the specific thermal energy consumption) and the mass ratio between the beds.

(ii) The number of cycles has an expected unfavourable effect on the specific energy consumption and a positive effect on purity. It may be a parameter for optimisation in order to increase the performance of the system.

(iii) Selectivity is not an important parameter on the specific energy but it has a major positive effect on the purity of the most strongly adsorbed compound.

(iv) The adsorption capacity affects negatively the specific energy use of the process and positively the purity. An adsorbent material characterised by higher adsorption capacity rather than higher selectivity of the key component (A) over (B) is found to be more effective for the performance of the process and thus it might be preferable.

(v) Another parameter that is relevant to the adsorbent material is the heat of adsorption of species (B). This parameter has a significant negative effect on the purity of the process and a positive effect on pressure and recovery.

However, the parameters are correlated and a better understanding on how they affect the process performance, and more precisely the specific energy consumption and purity of the process, is expected to be obtained from process optimisation (Konak et al., 2006). Since there are two objective functions to be optimised, the maximisation of the purity in the final bed and the minimisation of the specific energy consumption, a multi-objective global optimisation is required. For this reason, the NSGA-II multi-objective global optimisation algorithm (Deb et al., 2000) is applied to the model to optimise the performance of the system. By identifying the optimum characteristics of the system, the system can operate at the lower specific energy consumption and at the higher purity of the key component in the storage bed.

Before applying the optimisation strategy, the above thermodynamic model has been slightly modified by embodying dimensionless quantities, to analyse the effects of the main characteristic parameters of the system (i.e. the ratio between bed masses, the number of compression beds, the properties of the adsorbent, *etc*.) and to generalise the process regarding the inlet stream. The selectivity of the key component (A) over the main component (B) in the feed stream is a dimensional temperature dependent parameter and is defined by

$$\left(S_{\mathrm{A/B}}\right)_T = \frac{q_{\mathrm{s,A}}}{q_{\mathrm{s,B}}} \left(\frac{b_{\mathrm{A}}}{b_{\mathrm{B}}}\right)_T = \left(\frac{b_{\mathrm{A}}}{b_{\mathrm{B}}}\right)_T = \frac{b_{0,\mathrm{A}}\, \mathrm{e}^{\left(\frac{-\Delta H_{\mathrm{A}}}{RT}\right)}}{b_{0,\mathrm{B}}\, \mathrm{e}^{\left(\frac{-\Delta H_{\mathrm{B}}}{RT}\right)}} = \frac{b_{0,\mathrm{A}}}{b_{0,\mathrm{B}}}\, \mathrm{e}^{\left(\frac{\Delta H_{\mathrm{B}} - \Delta H_{\mathrm{A}}}{RT}\right)}, \tag{3.34}$$

Table 3.8. Considerations based on selectivity at low and high temperatures, ratio of selectivities at low and high temperatures, heat of adsorption of species (B), and equilibrium constant coefficient of species (B) for process optimisation.

Parameter	Symbol	Input Values				Unit
		1	2	3	4	
Selectivity at low temperature	$S_{T_{\text{low}}}$	300 [a]	600	900	1200	—
Selectivity at high temperature	$S_{T_{\text{high}}}$	100 [a]	120	180	1200/7	—
Ratio of Selectivities	X	3 [a]	5	5	7	—
Heat of adsorption of (A)	$(-)\,\Delta H_{\text{A}}$	35.00	—	—	—	kJ mol^{-1}
Equilibrium constant coefficient of (A)	$\left(10^{-7}\right)\, b_{0,\text{A}}$	4.00	—	—	—	kPa^{-1}
Heat of adsorption of (B)	$(-)\,\Delta H_{\text{B}}$	21.86	15.74	15.74	11.72	kJ mol^{-1}
Equilibrium constant coefficient of (B)	$\left(10^{-7}\right)\, b_{0,\text{B}}$	2.93	17.99	11.99	46.90	kPa^{-1}

[a] For fixed $S_{T_{\text{low}}}$=300, different ratios $X(=\frac{S_{T_{\text{low}}}}{S_{T_{\text{high}}}})$ are investigated for comparison. For X = 3, 4, 5, and 10, the corresponding values for $S_{T_{\text{high}}}$, ΔH_{B}, and $b_{0,\text{B}}$ are: *(i)* $S_{T_{\text{high}}}$ = 100, 75, 60, and 30, *(ii)* $\Delta H_{\text{B}} = -$(21.83, 18.41, 15.74, and 7.45) kJ mol^{-1}, and *(iii)* $b_{0,\text{B}}$ = (2.93, 12.03, 35.97, and 1080.45) $\times 10^{-7}$ kPa^{-1}, with respect to X value.

where the substitutions (A) and (B) represent any gas under the conditions specified in this subsection. For sake of simplicity, the following assumptions are considered:

$$\left(S_{\text{A/B}}\right)_{T_{\text{low}}} = X\ \left(S_{\text{A/B}}\right)_{T_{\text{high}}}, \tag{3.35a}$$

where X is defined as the ratio between $S_{T_{\text{low}}}$ and $S_{T_{\text{high}}}$,

$$\Delta H_{\text{B}} = R\left(\frac{T_{\text{low}}\, T_{\text{high}}}{T_{\text{high}} - T_{\text{low}}}\right) \ln\left(\frac{(b_{\text{B}})_{T_{\text{high}}}}{(b_{\text{B}})_{T_{\text{low}}}}\right), \tag{3.35b}$$

where b_{B} is given from $(b_{\text{B}})_T = \left(\frac{b_{\text{A}}}{S_{\text{A/B}}}\right)_T$, and

$$b_{0,\text{B}} = \frac{b_{0,\text{A}}}{\left(S_{\text{A/B}}\right)_{T_{\text{low}}}} \mathrm{e}^{\left(\frac{\Delta H_{\text{B}} - \Delta H_{\text{A}}}{R\, T_{\text{low}}}\right)} = \frac{b_{0,\text{A}}}{\left(S_{\text{A/B}}\right)_{T_{\text{high}}}} \mathrm{e}^{\left(\frac{\Delta H_{\text{B}} - \Delta H_{\text{A}}}{R\, T_{\text{high}}}\right)}. \tag{3.35c}$$

Eq. 3.35b is derived from the van't Hoff equation as described in Appendix B, Section B.1. By fixing selectivity $S_{\text{A/B}}$ at low and high temperatures and the Langmuir parameters ΔH_{A} and $b_{0,\text{A}}$, the parameters ΔH_{B} and $b_{0,\text{B}}$ are calculated by applying Eqs. 3.35b and 3.35c, respectively. More analytically, ΔH_{A} and $b_{0,\text{A}}$ parameters allow the calculation of $(b_{\text{A}})_T$, which then gives $(b_{\text{B}})_T$ by knowing $\left(S_{\text{A/B}}\right)_T$.

Table 3.7 presents the variables for optimisation and the entities to define the design space of the optimisation system. Only the relative masses of Bed 2 to Bed N_{B} were considered as variables. The multi-objective global optimisation algorithm has been applied several times considering different values for the following fixed parameters: *(i)* the inlet composition of trace impurity (A), *(ii)* the selectivity of component (A) over (B) ($S_{\text{A/B}}$) at T_{low} and T_{high}, *(iii)* the ratio between the $S_{\text{A/B}}$ at T_{low} and at T_{high} (X), *(iv)* the adsorption capacity of the most strongly adsorbed component ($q_{\text{s,A}}$), *(v)* the enthalpy of adsorption of the component (A) (ΔH_{A}), *(vi)* the mass of adsorbent in Bed 1 ($m_{\text{bed},1}$), *(vii)* the feed concentration of species (A) (y_{A}), *(viii)* the number of beds, and *(ix)* the number of runs, which as presented in Tables 3.7 and 3.8.

The ratio between selectivities (X), so as the selectivity at low temperature ($S_{T_{\text{low}}}$), are fixed at different values. These parameters allow the calculation of other fixed parameters,

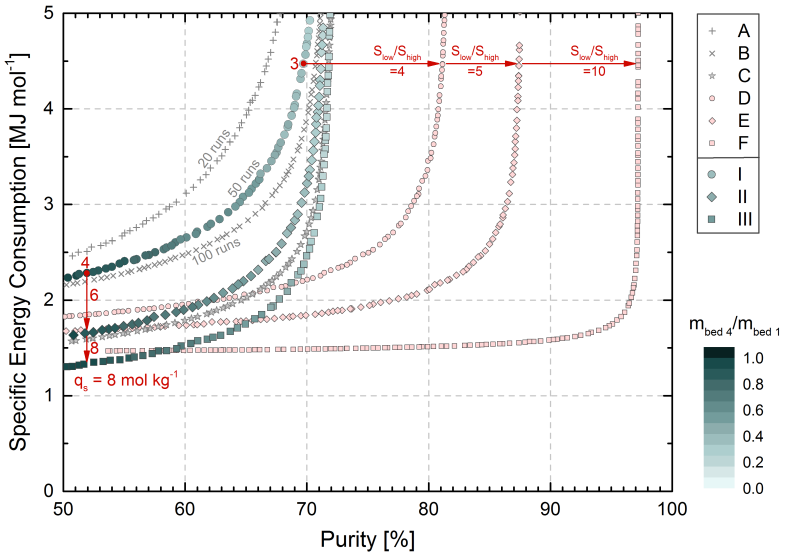

Figure 3.18. Colour mapped plot of the total energy consumption [MJ mol^{-1}] versus the purity [%] in the storage bed as a function of the relative mass of the storage bed for the separation of species (A) existing at 400 ppm in a binary mixture of (A) and (B).

4 beds, $S_{T_{\text{low}}}$=300 and:
A: $S_{T_{\text{high}}}$=100, q_{s}=4 mol kg^{-1}, 20 cycles
B: $S_{T_{\text{high}}}$=100, q_{s}=4 mol kg^{-1}, 100 cycles
C: $S_{T_{high}}$=100, q_{s}=6 mol kg^{-1}, 100 cycles
D: $S_{T_{\text{high}}}$=75, q_{s}=4 mol kg^{-1}, 50 cycles
E: $S_{T_{\text{high}}}$=60, q_{s}=4 mol kg^{-1}, 50 cycles
F: $S_{T_{\text{high}}}$=30, q_{s}=4 mol kg^{-1}, 50 cycles
I: $S_{T_{\text{high}}}$=100, q_{s}=4 mol kg^{-1}, 50 cycles
II: $S_{T_{\text{high}}}$=100, q_{s}=6 mol kg^{-1}, 50 cycles
III: $S_{T_{\text{high}}}$=100, q_{s}=8 mol kg^{-1}, 50 cycles

such as ΔH_{B}, $b_{0,\text{B}}$, and $S_{T_{\text{high}}}$, and are listed in Table 3.8. The rest of the input parameters are reported in Table 3.7. One parameter from *(i)* to *(ix)* is changing every time that the optimiser runs to investigate how these parameters affect the performance of the process. The variables/entities for optimisation are the relative bed masses excluding Bed 1, which are as defined in Table 3.7. Searching in between the whole range of entities, multiple iterations were implemented. The results converge to global Pareto-optimal fronts (or else frontiers) as set of optimal trade-offs. The resulting Pareto fronts define the optimal relative masses in each bed, excluding Bed 1.

It should also be noted here that the pressure in the storage bed is constrained to be greater than the atmospheric pressure (>1 bar) and the recovery of the process is constrained to be >10%. Besides, the following assumptions were made: *(i)* all the beds are filled with the same adsorbent material, *(ii)* the adsorbent material is a composite material in the form of pellets, and *(iii)* the adsorbent material has physical properties similar to zeolite 13X pellets as listed in Table 3.5.

Figure 3.18 summarises the optimisation results considering 4 beds, 400 ppm y_{A} (or else 0.04%), $\left(S_{\text{A/B}}\right)_{T_{\text{low}}}$=300 and $\left(S_{\text{A/B}}\right)_{T_{\text{high}}}$=100. By increasing the number of cycles from

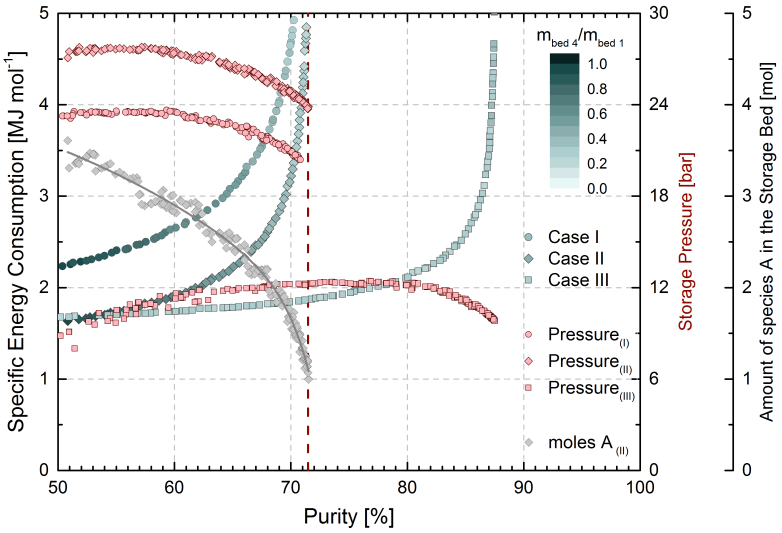

Figure 3.19. Colour mapped plot of the total energy consumption [MJ mol^{-1}] versus the purity [%] in the storage bed as a function of the relative mass of the storage bed for the separation of species (A) existing at 400 ppm in a binary mixture of (A) and (B). The plot also illustrates the storage pressure (light red points) and the amount of species (A) present in the storage bed (gray points) versus the purity in the storage bed.

4 beds, $S_{T_{\text{low}}}$=300 and:
I: $S_{T_{\text{high}}}$=100, q_{s}=4 mol kg^{-1}, 50 cycles
II: $S_{T_{\text{high}}}$=100, q_{s}=8 mol kg^{-1}, 50 cycles
III: $S_{T_{\text{high}}}$=60, q_{s}=4 mol kg^{-1}, 50 cycles

20 to 50 and 100, a better performance in terms of energy consumption and purity is obtained. These results are illustrated in Figure 3.18 in the Pareto fronts A, I, and B and the Pareto fronts II and C. Also, by increasing the adsorption capacity of the material from 4–8 mol kg^{-1}, a significant positive effect (reduction) of the specific energy consumption and a minor positive effect (increase) of the purity are achieved. A higher adsorption capacity implies a higher loading of the most adsorbed component inside the pores of the solid during adsorption. This decreases the concentration of the unwanted component(s) inside an adsorption bed with a direct positive effect on the process purity. In addition, the increase of the storage pressure at higher adsorption capacity, and consequently the amount of species (A) in the final bed as reported in Figure 3.19, proves the higher loading of the key component (A). The reduction in the energy use can be explained by the consideration of heat recovery strategies. The higher adsorption loading increases the exothermic energy such that the energy needed to heat up the bed decreases.

An additional investigation on the ratio between the selectivity at T_{low} and T_{high} is also plotted in Figure 3.18 to demonstrate its importance. According to Table 3.8, the ratio between the selectivities is related to ΔH_{B} and $b_{0,\text{B}}$ as $\left(S_{\text{A/B}}\right)_{T_{\text{low}}}$, ΔH_{A}, and $b_{0,\text{A}}$ are fixed. Consequently, the ratio X is affected by the operating temperature and the ΔH_{B} (as ΔH_{A} here is constant). The higher the ratio, the more the adsorption isotherm of species (B) moves at lower adsorbed amounts. This has a significant effect on the purity of the process. A smaller effect on the specific energy use of the process is also obtained. This can be explained due to the lower heat of adsorption of species (B) as the ratio between selectivities increases (see Table 3.8).

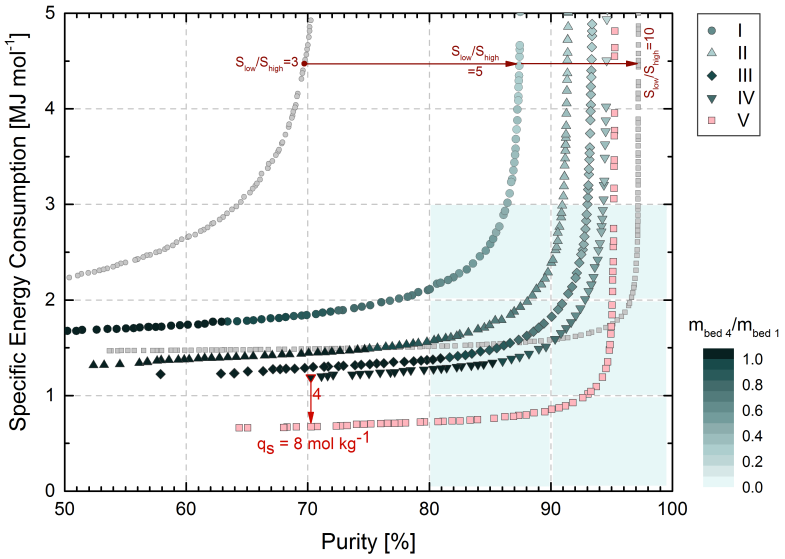

Figure 3.20. Colour mapped plot of the total energy consumption [MJ mol^{-1}] versus the purity [%] in the storage bed as a function of the relative mass of the storage bed for the separation of species (A) existing at 400 ppm in a binary mixture of (A) and (B).

4 beds, 50 cycles and:
I: $S_{T_{\text{low}}}$=300, $S_{T_{\text{high}}}$=60, q_{s}=4 mol kg^{-1}
II: $S_{T_{\text{low}}}$=600, $S_{T_{\text{high}}}$=120, q_{s}=4 mol kg^{-1}
III: $S_{T_{\text{low}}}$=900, $S_{T_{\text{high}}}$=180, q_{s}=4 mol kg^{-1}
IV: $S_{T_{\text{low}}}$=1200, $S_{T_{\text{high}}}$=240, q_{s}=4 mol kg^{-1}
V: $S_{T_{\text{low}}}$=1200, $S_{T_{\text{high}}}$=240, q_{s}=8 mol kg^{-1}

Note: The gray-coloured Pareto fronts represent results obtained in Figure 3.18.

So far, an investigation on the ratio between selectivities has been investigated by keeping $S_{T_{\text{low}}}$ constant. The effect of $S_{T_{\text{low}}}$ is illustrated in Figure 3.20, which shows the resulting Pareto fronts considering 4 beds, 400 ppm y_{A}, X=5, and 50 cycles of the process. By increasing the selectivity from 300 to 1200, a positive effect on purity and negative effect on specific energy consumption can be obtained (Pareto fronts from I to IV). The increased $S_{T_{\text{low}}}$ has high effect on the energy and the purity of the process. This outcome can be explained by the lower adsorbed amount of species (B), especially during step 1 — adsorption in Bed 1, which moves to the subsequent beds. In comparison, the increased ratio between selectivities has a higher effect on purity, which indicates the high effect of heating–cooling cycles, especially during the connection between two beds, on the purity of the process and consequently on the performance of the compression and purification train (see Figure 3.19). The V Pareto front of Figure 3.20 shows a major negative effect of the adsorption capacity on the energy consumption at a lower purity region. A slightly positive effect of the adsorption capacity on the purification of species (A) is also observed with an unfavourable positive effect on energy.

The light green-coloured box in Figure 3.20 represents the targeted energy use and purity such that this process is more affordable and worth investigating. A way predicted to improve the performance of the process further, in terms of purity, is by increasing the number of beds of the compression and purification train. Figure 3.21 illustrates the resulting Pareto fronts by increasing the number of beds of the compression and purification train considering 400 ppm y_{A}, $S_{T_{\text{low}}}$=900, X=5, q_{s}=4 mol kg^{-1}, and 50 cycles. Generally, by increasing

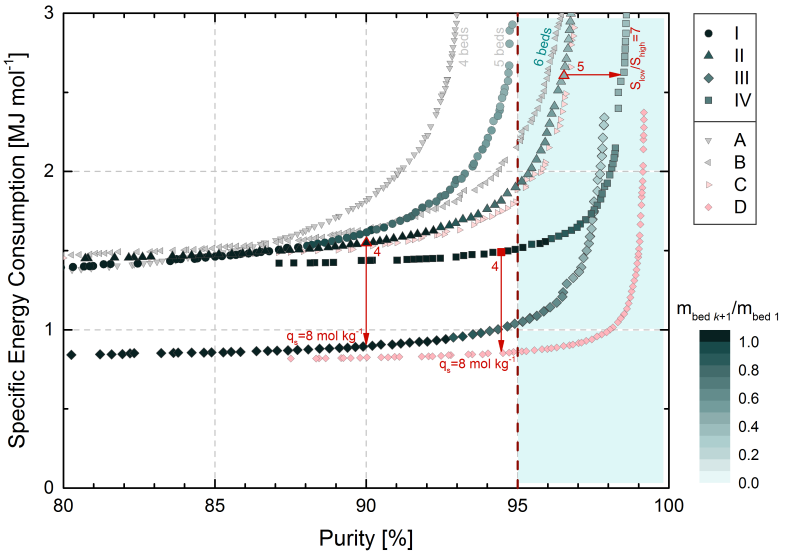

Figure 3.21. Colour mapped plot of the total energy consumption [MJ mol^{-1}] versus the purity [%] in the storage bed as a function of the relative mass of the storage bed for the separation of species (A) existing at 400 ppm in a binary mixture of (A) and (B).

$S_{T_{low}}$=900 and:
I: 5 beds, $S_{T_{\text{high}}}$=180, q_{s}=4 mol kg^{-1}, 50 cycles
II: 6 beds, $S_{T_{\text{high}}}$=180, q_{s}=4 mol kg^{-1}, 50 cycles
III: 6 beds, $S_{T_{\text{high}}}$=180, q_{s}=8 mol kg^{-1}, 50 cycles
IV: 6 beds, $S_{T_{\text{high}}}=\frac{900}{7}$, q_{s}=4 mol kg^{-1}, 50 cycles
A: 4 beds, $S_{T_{\text{high}}}$=180, q_{s}=4 mol kg^{-1}, 50 cycles
B: 6 beds, $S_{T_{\text{high}}}$=180, q_{s}=4 mol kg^{-1}, 20 cycles
C: 6 beds, $S_{T_{\text{high}}}$=180, q_{s}=4 mol kg^{-1}, 100 cycles
D: 6 beds, $S_{T_{\text{high}}}=\frac{900}{7}$, q_{s}=8 mol kg^{-1}, 50 cycles

Note: The gray-coloured Pareto fronts represent results obtained in Figure 3.20.

the number of compression beds, a higher purity is obtained in the final storage bed at similar specific energy consumption. However, up to a certain purity, lower specific energy is required by 4 beds (2 compression beds) and above that purity (where the Pareto fronts of different beds are crossed, see A, I and II Pareto fronts of Figure 3.21) a significant increase of the purity in the storage bed is obtained without increase in the required specific energy use. Thus, the number of beds is an important parameter that controls the performance of the process. By setting a required purity, the number of beds can be selected in order to achieve that purity and to minimise the energy consumption. For the case of 6 beds (4 compression beds), purities >95% can be obtained. Furthermore, as expected, a major effect on purity is obtained by increasing the ratio X and a significant effect on energy is procured by increasing q_{s}. By combining both higher q_{s} and ratio X, a >95% purity can be obtained by consuming <1 MJ mol^{-1} (see Pareto front D in Figure 3.20).

With reference to Figure 3.21, a further investigation on the pressure and recovery of the process versus the number of beds has been performed. As previously discussed, a higher adsorption capacity increases the final pressure in the storage bed as a higher amount of the key component is captured in Bed 1, where a higher ratio between selectivities decreases the pressure. The latter can be explained by the fact that the higher purity is achieved not by increasing the amount of the captured key component but by increasing the performance of the compression and purification train (CPT). Figure 3.22a shows that the effect of the

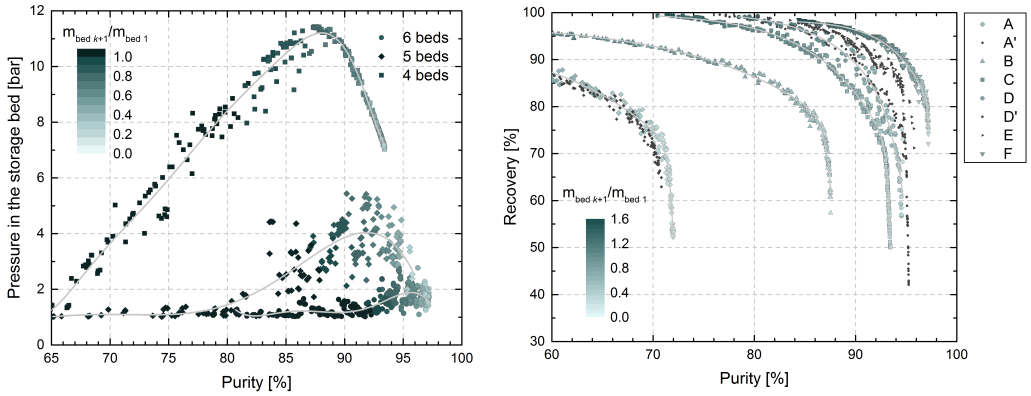

(a) pressure vs purity **(b)** recovery vs purity

Figure 3.22. **(a)** Correlation of pressure versus purity for the case of 4, 5, and 6 beds, 400 ppm y_{A}, $S_{T_{\mathrm{low}}}$=900, X=5, q_{s}=4 mol kg^{-1}, and 50 cycles. **(b)** Correlation of recovery versus purity for the cases of:

400 ppm y_{A}, 50 cycles and:
A: 4 beds, $S_{T_{\mathrm{low}}}$=300, X=3, q_{s}=8 mol kg^{-1}
A': 4 beds, $S_{T_{\mathrm{low}}}$=300, X=3, q_{s}=4 mol kg^{-1}
B: 4 beds, $S_{T_{\mathrm{low}}}$=300, X=5, q_{s}=4 mol kg^{-1}
C: 4 beds, $S_{T_{\mathrm{low}}}$=900, X=5, q_{s}=4 mol kg^{-1}
D: 4 beds, $S_{T_{\mathrm{low}}}$=1200, X=5, q_{s}=4 mol kg^{-1}
D': 4 beds, $S_{T_{\mathrm{low}}}$=1200, X=5, q_{s}=8 mol kg^{-1}
E: 5 beds, $S_{T_{\mathrm{low}}}$=900, X=5, q_{s}=4 mol kg^{-1}
F: 6 beds, $S_{T_{\mathrm{low}}}$=900, X=5, q_{s}=4 mol kg^{-1}

number of beds on the pressure in the storage bed is similar to that obtained by the ratio between selectivities. By increasing the performance of the CPT, a smaller amount of the undesired gas moves towards the storage bed, which has a positive effect on purity but a negative effect on pressure. In addition, each plot in Figure 3.22a follows a pressure increase with purity in low purity region and a pressure decrease in the high purity region after reaching a maximum. The pressure change is highly affected by the number of moles of each component that passes through the CPT and finally stored in the last bed and therefore, by the optimal mass of adsorbent material in each bed. Each point in Figure 3.22a represents a different configuration. Due to this configuration, pressure can increase or decrease with purity. Figure 3.22b shows that the recovery increases with decreased purity for all the investigated cases. A positive effect of recovery is observed by increasing the number of CPT beds and the selectivity of the adsorbent material. A minor positive effect on recovery is observed by increasing the adsorption capacity of the material. In general, a higher purity requires less undesired gas in the final bed. This affects not only the final pressure but also the process recovery.

Finally, the effect of the inlet concentration of the trace gas (A) on the performance of the system is presented in Figure 3.23 (considering $S_{T_{\mathrm{low}}}$=900, X=5, q_{s}=4 mol kg^{-1}, and 50 number of cycles/runs). It illustrates that by increasing the inlet concentration of species (A) from 400 ppm to 600 ppm, the effect on the highest-reached purity is similar to the case of increased $S_{T_{\mathrm{low}}}$ from 900 to 1200 (at 400 ppm y_{A}). Although, the Pareto front converges at lower specific energy consumption for a <94% purity. Since the energy consumption increases with dilution, the increase in the inlet concentration of component (A) moves the Pareto fronts to regions of a lower energy consumption and a higher purity. The small increase in purity is due to the increased concentration of the trace component (A)

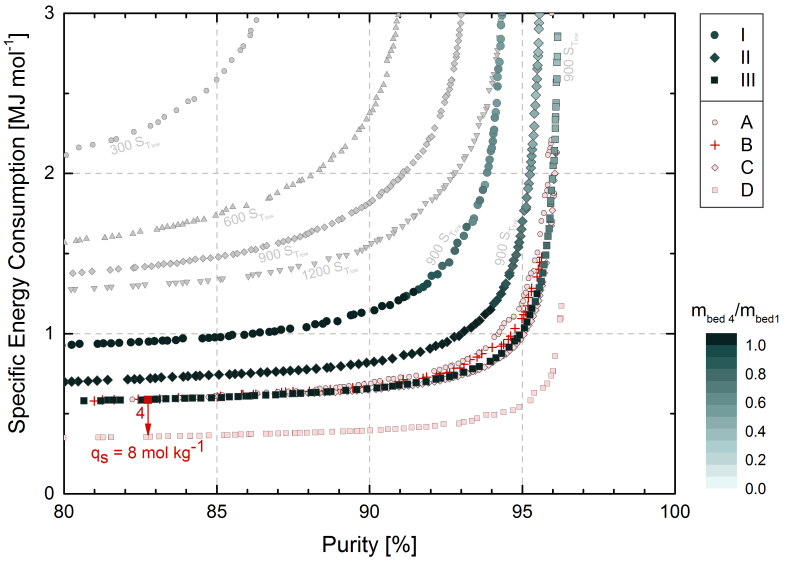

Figure 3.23. Colour mapped plot of the total energy consumption [MJ mol^{-1}] versus purity [%] in the storage bed as a function of the relative mass of the storage bed for the separation of species (A) existing at 600–1000 ppm in a binary mixture of (A) and (B).

4 beds, $S_{T_{\text{low}}}$=900, $S_{T_{\text{high}}}$=180 and:
I: 600 ppm, q_{s}=4 mol kg^{-1}, 50 cycles
II: 800 ppm, q_{s}=4 mol kg^{-1}, 50 cycles
III: 1000 ppm, q_{s}=4 mol kg^{-1}, 50 cycles
A: 1000 ppm, q_{s}=4 mol kg^{-1}, 10 cycles
B: 1000 ppm, q_{s}=4 mol kg^{-1}, 20 cycles
C: 1000 ppm, q_{s}=4 mol kg^{-1}, 100 cycles
D: 1000 ppm, q_{s}=8 mol kg^{-1}, 50 cycles

Note: The gray-coloured Pareto fronts represent results obtained in Figure 3.20.

in the feed stream. In addition to this investigation, Figure 3.23 illustrates the effect of the number of cycles on the colour mapped Pareto front of 1000 ppm y_{A}. It reveals that as the selectivity and inlet composition of species (A) increase, the number of cycles of the process has no effect on the performance of the system (see A, B, III, and C Pareto fronts in Figure 3.23).

Generally, each Pareto front follows a similar trend, this being that extremely high purities, even >90%, require greater energy consumption. By increasing the selectivity of (A) over (B), the ratio between $S_{T_{\text{low}}}$ and $S_{T_{\text{high}}}$, the adsorption capacity of the material (q_{s}), the number of cycles/runs (N_{R}) and the number of beds (i.e. the number of the compression beds) (N_{B}), the performance of the system in terms of specific energy use and purity is improved. In addition, a feed stream of higher concentration of species (A) converges to a Pareto front of lower energy consumption and higher purity. Finally, the relative mass[10] of the storage bed has a correlation with purity. In general, an increased purity requires lower relative mass of the storage bed. A lower mass of the storage bed also increases the final pressure. Thus, by setting a required purity, the mass of the storage bed can be obtained. So far, only an indication of the relative mass of the storage bed has been presented. The following subsection on 'Process Design', gives a set of design rules by specifying the essential purity.

[10]Here, the relative mass of Bed k is defined as the mass of Bed k over the mass of Bed 1.

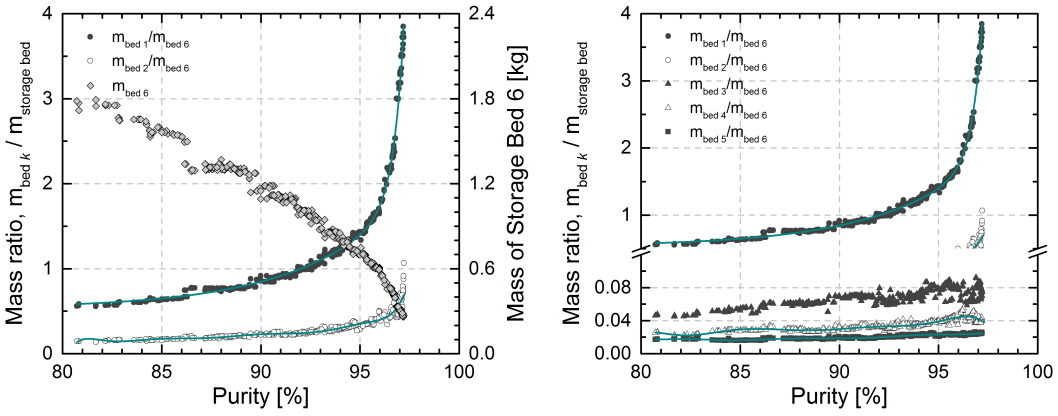

Figure 3.24. Correlation between purity, mass of storage bed, and mass ratio of each bed over the mass of the storage bed for the case of 6 beds, 400 ppm y_{A}, $S_{T_{\mathrm{low}}}$=900, X=5, q_{s}=4 mol kg^{-1}, and 50 cycles.

3.5.2 Process Design

The most important design parameter to enable the process to lie on the Pareto front is the relative mass of each bed or the mass ratio between the beds. Based on the results obtained from process analysis, a number of general design rules can be inferred. To simplify the presentation of the results, a 95% purified stream is considered. According to Figure 3.21, 95% pure in component (A) stream requires the application of six beds, or else four compression beds.[11] Figure 3.24 highlights the non-linear direct correlation between the mass of storage bed, the mass ratio $m_{\mathrm{bed},i}/m_{\mathrm{bed},N_{\mathrm{B}}}$ (where $i = 1, ..., N_{\mathrm{B}} - 1$), and purity. By defining the required purity of species (A), the optimal masses of all beds are fixed instantaneously. The derived masses of each bed are: *(i)* 1 kg in Bed 1, *(ii)* 0.16–0.18 kg in Bed 2, *(iii)* 0.02–0.08 kg in Bed 3, *(iv)* 0.014–0.045 kg in Bed 4, *(v)* 0.006–0.027 kg in Bed 5, and *(vi)* 1.8–0.25 kg in Bed 6, with respect to the 80–97% purity. For instance, at 95% purity the required masses, from Bed (1–6), are around (1, 0.29, 0.05, 0.028, 0.015, 0.7) kg. However, especially at higher purities, the process does not require absolute precision especially for the masses of Beds 2, 3 and 4 since the correlation between these design parameters and the purity is weaker (as illustrated by the larger deviation in Figure 3.24) compared to that obtained from the mass ratios of $m_{\mathrm{bed},1}/m_{\mathrm{bed},6}$ and $m_{\mathrm{bed},5}/m_{\mathrm{bed},6}$.

For the selection of 4 and 5 beds, the design rules are highlighted in Figures 3.26a and 3.25, respectively. For the case of 5 beds, the derived masses of each bed are: *(i)* 1 kg in Bed 1, *(ii)* 0.24–0.26 kg in Bed 2, *(iii)* 0.02–0.08 kg in Bed 3, *(iv)* 0.005–0.04 kg in Bed 4, and *(v)* 2.6–0.2 kg in Bed 5, with respect to the 70–96% purity. For the case of 4 beds, the derived masses of each bed are: *(i)* 1 kg in Bed 1, *(ii)* 0.24–0.8 kg in Bed 2, *(iii)* 0.05–0.09 kg in Bed 3, and *(iv)* 1.6–0.3 kg in Bed 4, with respect to the 70–94% purity.

Figure 3.26b compares the mass of the storage bed of this example with the optimised results of CO_2 and N_2 co-adsorption on zeolite 13X. It also provides the amount of CO_2 that can be stored per unit of mass of the storage bed. Around 4 molCO_2 kg^{-1} can be stored compared to other adsorbents for air capture that can achieve <1 molCO_2 kg^{-1} under the same feed concentration conditions (Chaikittisilp et al., 2011b; Wurzbacher et al., 2011).

[11] A smaller number of beds can also be applied in case of high selectivity and high ratio between selectivities at low and high temperatures.

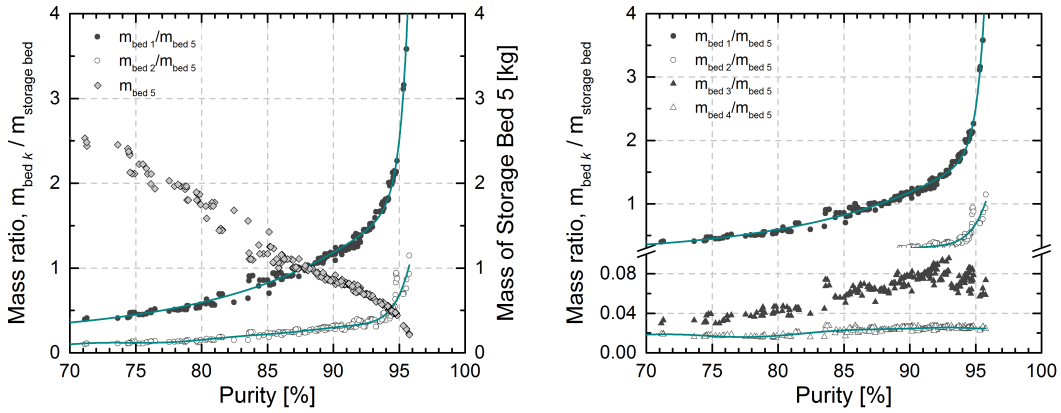

Figure 3.25. Correlation between purity, mass of storage bed, and mass ratio of each bed over the mass of the storage bed for the case of 5 beds, 400 ppm y_A, $S_{T_{low}}$=900, X=5, q_s=4 mol kg^{-1}, and 50 cycles.

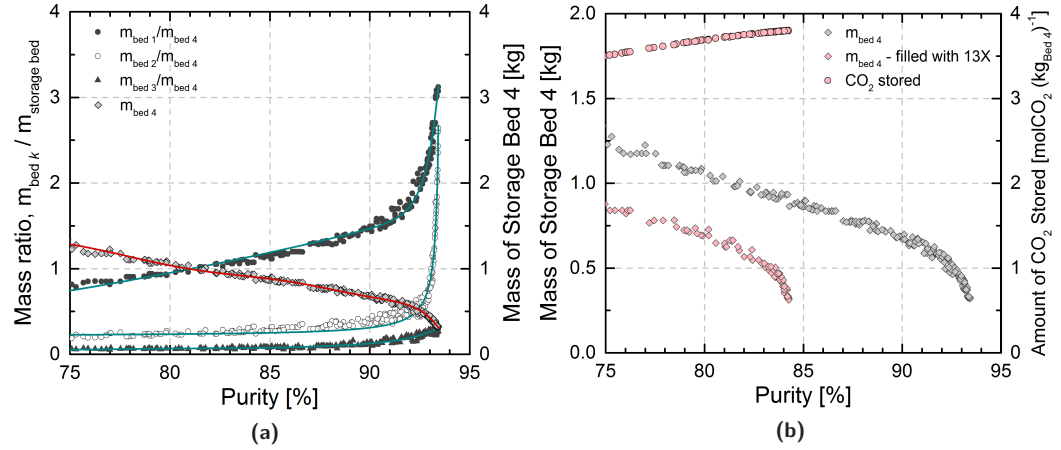

Figure 3.26. Correlation between purity, mass of storage bed, and mass ratio of each bed over the mass of the storage bed for the case of: 4 beds and 400 ppm y_A, and **(a)** $S_{T_{low}}$=900, X=5, q_s=4 mol kg^{-1}, and 50 cycles and a comparison with **(b)** the CO_2 and N_2 co-adsorption on zeolite 13X ($S_{T_{low}}$=360, X=3.8, q_s=4 mol kg^{-1}, and 60 cycles).

It is important to note here that the amount that can be stored approaches the adsorption capacity of the solid. A higher purity and greater stored amounts can be achieved if an adsorbent with higher selectivity and higher adsorption capacity is used. Olah, Prakash, and co-workers reported a CO_2 uptake of 2.44 molCO_2 kg^{-1} on a branched poly(ethylenimine) PEI (Goeppert et al., 2014). However, the reported heat of adsorption of PEI is >80 kJ mol^{-1}, which is expected to significantly increase the regeneration energy and consequently the energy consumption of the process.

3.6 Process Improvements and Recommendations

For the application of DAC, the assumption of a binary mixture of CO_2 and N_2 can be assumed as conservative to the tertiary mixture of CO_2–N_2–O_2. The consideration of O_2 is a conservative measure since O_2 is presented in a high concentration in the inlet stream (around 20%) and is less adsorbable compared to N_2 (Park et al., 2006). Therefore, it is

Table 3.9. Mono-Site Langmuir isotherm parameters for CO_2, N_2 and O_2.

Parameter	Unit	CO_2		N_2		O_2	
		298 K	353 K	298 K	353 K	298 K	353 K
$\mathbf{q_s}$	mol kg^{-1}	4.00	4.00	4.00	4.00	4.00	4.00
b	kPa^{-1}	0.144	0.019	0.0004	0.0002	0.000008	0.000007
$\mathbf{K_H}$	mol kg^{-1} kPa^{-1}	0.577	0.078	0.0016	0.0006	4.00	4.00
$\left(10^{-7}\right)$ $\mathbf{b_0}$	kPa^{-1}	3.76	3.76	9.74	9.74	41.59	41.59
$(-)$ $\Delta\mathbf{H}$	kJ mol^{-1}	31.86	31.86	14.92	14.92	1.71	1.71

Note: Data obtained from Xiao et al., 2008 and regressed using the linear form of Langmuir isotherm (see Appendix B.1).

expected that the final purity will increase due to the higher selectivity of N_2 over O_2 and the energy use will decrease since the heat of adsorption of O_2 is lower than N_2.

In addition, the process consists of optional instantaneous vacuum steps (assuming frozen adsorbed phase) in Bed 1 and Bed 2. The replacement of these steps with the adiabatic blowdown, as reported in Section 3.3, is expected to increase the purity in the final bed, since a higher amount of the undesired gas (B) is removed from both the gas and adsorbed phases of the beds. However, an amount of the key component (A) is also removed, which is expected to decrease the stored amount of that component, the final storage pressure, and the recovery of the process.

Finally, the consideration of heat recovery strategies, as explained extensively in Section 3.3, is expected to reduce the thermal energy consumption of the process. The total thermal heat that can be recover from the process is estimated.

Here, a comparison between the model as presented in Section 3.4, the simple case of DAC assuming a CO_2–N_2 binary mixture, and: *(i)* the CO_2–N_2–O_2 tertiary mixture model, *(ii)* the adiabatic blowdown in Bed 1 and/or Bed 2 model, instead of the instantaneous vacuum steps, and *(iii)* the exclusion of any heat recovery scheme, are presented.

3.6.1 The Use of a Tertiary Mixture

The feed stream consists of a tertiary mixture of CO_2, N_2, and O_2, where the adsorption parameters of those gases as adsorbed by zeolite 13X are given in Table 3.9. Both the process and the adsorbent material follow the parameters presented in Table 3.10. Figure 3.27 compares the results as obtained from the consideration of binary and tertiary mixtures. Before analysing the results, it is important to note here that the design parameters, i.e. mass of each bed, have not been optimised.

Figure 3.27a illustrates that a higher purity can be achieved in the case of a tertiary mixture since O_2 is less selective than CO_2 and N_2. Almost the same energy consumption and amount of CO_2 stored in the final bed are obtained for both cases, the binary and the tertiary mixtures. By assuming that the real DAC process operates under equilibrium conditions and at 100% efficiency, a higher purity may be obtained in a real operation. Even though a slightly higher amount of CO_2 is stored in the final bed, the total amount of gases reduces and consequently the purity increases and the final pressure decreases.

Table 3.10. Parameters of the process and adsorbent for the benchmark case.

Process Parameters	Value	Unit	Reference
Number of beds, N_B	4	—	—
Mass of bed 1, $m_{bed,1}$	1	kg	—
Relative mass of bed 2, $m_{bed,2}/m_{bed,1}$	0.20	—	—
Relative mass of bed 3, $m_{bed,3}/m_{bed,1}$	0.05	—	—
Relative mass of bed 4, $m_{bed,4}/m_{bed,1}$	0.30	—	—
Void fraction in bed 1, $\varepsilon_{b,1}$	0.50	—	Rezaei and Webley (2009)
Inter particle void fraction, $\varepsilon_{b,2-4}$	0.25	—	Balahmar et al. (2016) [a]
Components Properties			
Number of components in the feed, N_C	3	—	—
Feed molar fraction of CO_2, y_1	0.0004	—	—
Feed molar fraction of N_2, y_2	0.7897	—	—
Feed molar fraction of O_2, y_3	0.2099	—	—
[b] Specific heat capacity of CO_2, $c_{p,1}$	38.51	J mol^{-1} K^{-1}	Lemmon et al. (2013)
[b] Specific heat capacity of N_2, $c_{p,2}$	29.16	J mol^{-1} K^{-1}	Lemmon et al. (2013)
[b] Specific heat capacity of O_2, $c_{p,2}$	29.63	J mol^{-1} K^{-1}	Lemmon et al. (2013)
[b] Specific heat capacity of CO_2, $c_{v,1}$	30.30	J mol^{-1} K^{-1}	Lemmon et al. (2013)
[b] Specific heat capacity of N_2, $c_{v,2}$	20.85	J mol^{-1} K^{-1}	Lemmon et al. (2013)
[b] Specific heat capacity of O_2, $c_{v,2}$	21.28	J mol^{-1} K^{-1}	Lemmon et al. (2013)

[a] Reported packing density of zeolite 13X.
[b] Average value in the range of 293.15–368.15 K.

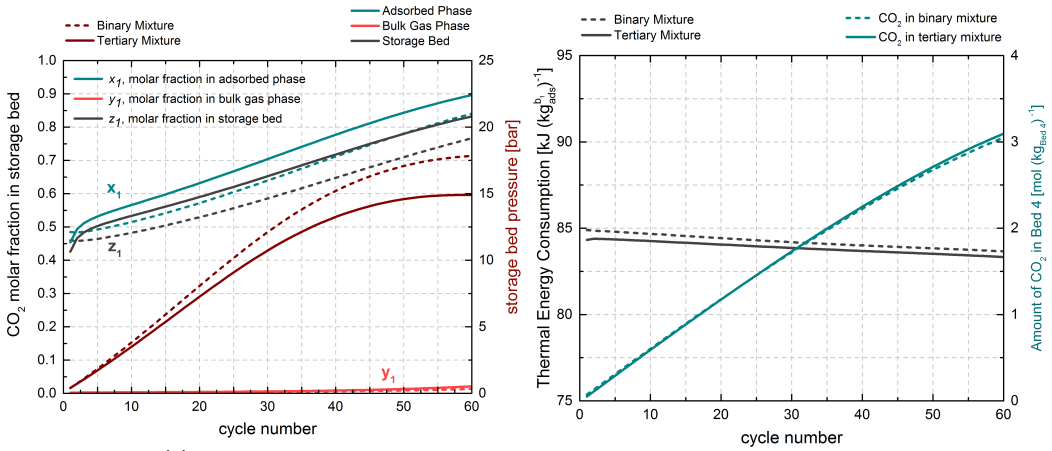

(a) $P - x_1 - y_1 - z_1$ **(b)** $E_{th} - molCO_2$

Figure 3.27. **(a)** Storage bed pressure (dark red curves), global concentration of CO_2 (gray curves), concentration of CO_2 in the bulk-gas phase (red curves) and adsorbed phase (green curves) of Bed 4 at each cycle and **(b)** thermal energy consumption (gray curves) and moles stored in Bed 4 (green curves) for the case of binary and tertiary mixtures.

3.6.2 Adiabatic Blowdown Instead of Instantaneous Evacuation

The blowdown, as explained in Section 3.3, has been considered here in order to improve the performance of the process. For the case of optional instantaneous evacuation (assuming frozen adsorbed phase) in Beds 1 and 2, for comparison, an adiabatic blowdown is applied in: *(i)* Bed 1 and (ii) Bed 1 and Bed 2. Figure 3.28 highlights the main results from these analyses.

As expected, Figure 3.28a illustrates that the adiabatic blowdown in Bed 1 and/or Bed 2 increases the purity in the final bed and reduces the amount of stored CO_2. Adiabatic blowdown reduces the amount of all the gases in the storage bed (as purity increases) and consequently the pressure in the storage bed. The energy of the process, by applying

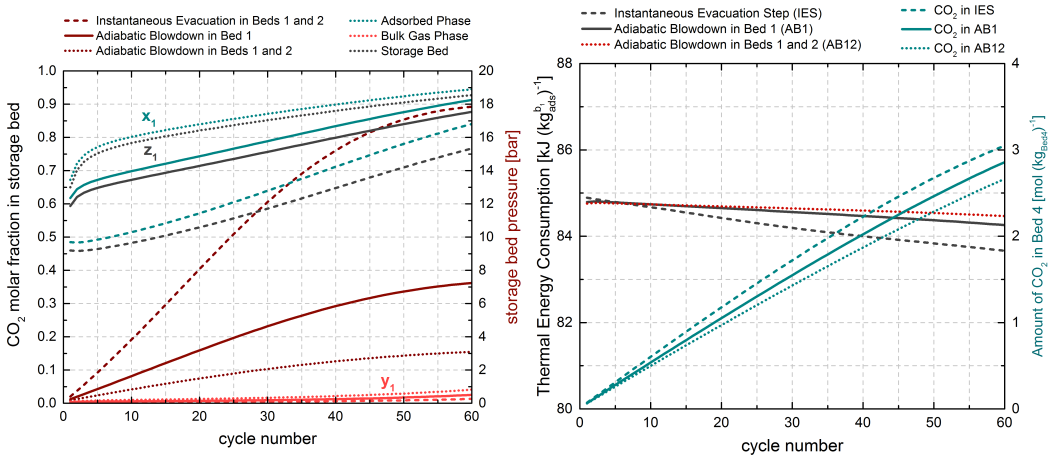

(a) $P - x_1 - y_1 - z_1$ **(b)** $E_{\text{th}} - mol\text{CO}_2$

Figure 3.28. **(a)** Storage bed pressure (dark red curves), global concentration of CO_2 (gray curves), concentration of CO_2 in the bulk-gas phase (red curves) and adsorbed phase (green curves) of Bed 4 and **(b)** thermal energy consumption (gray and red curves) and moles stored in Bed 4 (green curves) at each cycle for the case of adiabatic blowdown and instantaneous evacuation steps.

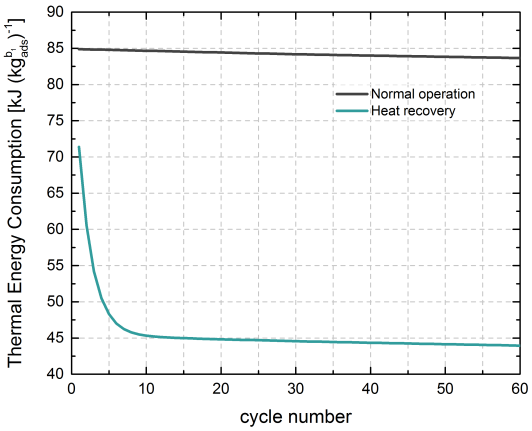

Figure 3.29. Total thermal energy consumption due to the heat of desorption and sensible consumed at each cycle of the process with and without including heat recovery.

adiabatic blowdown, increases slightly due to the electric energy for compression. The energy use of the process that considers: *(i)* instantaneous evacuation steps is 5.5 MJ $\text{molCO}_2{}^{-1}$, *(ii)* adiabatic blowdown in Bed 1 and instantaneous evacuation in Bed 2 is 5.9 MJ $\text{molCO}_2{}^{-1}$, and *(iii)* adiabatic blowdown in Bed 1 and Bed 2 is 6.4 MJ $\text{molCO}_2{}^{-1}$.

3.6.3 Heat Recovery Strategies

Figure 3.29 shows that a great amount of thermal energy can be recovered by considering the heat recovery strategies as discussed in Section 3.3. Around 50% of the total thermal energy of the DAC process can be recovered. More specifically, the thermal energy reduces from 5.5 MJ $\text{molCO}_2{}^{-1}$ to 2.7 MJ $\text{molCO}_2{}^{-1}$.

Thus, the inclusion of a tertiary mixture and adiabatic blowdown in Bed 1 and/or Bed 2 have a positive effect on the final purity of the process. However, the adiabatic blowdown reduces the amount of stored CO_2 and the final pressure and increases the energy require-

ments of the process. Finally, by considering the energy strategies of the process, a great advantage/reduction in energy can be gained.

3.7 Conclusions

From a solely thermodynamic viewpoint, this process can be used to separate any dilute component in the binary mixture, compress, and purify the dilute key component at purities as high as 99%. The configuration of the system, such as the number of compression beds, number of process cycles, operating temperature, and vacuum pressure have an effect on the specific energy and purity of the process. Also, the adsorptive properties of the solid, such as the adsorption capacity, the selectivity of the dilute component, and heat of adsorption, have a significant effect on system's performance.

Ideally, an adsorbent having a greater adsorption capacity in Bed 1 can significantly increase the final pressure and decrease the energy use of the process. Also, an adsorbent having a high ratio between selectivities at two different temperatures can be beneficial in the CPT to increase the purity of the process. A relatively high positive effect on the purity of the process can also be obtained by increasing the number of beds of the CPT. Even though the final pressure of the process reduces by increasing the number of the beds, an increase of the lower limit/constraint of the design pressure in the storage bed not only causes an increase in the final pressure but also utilises the same amount of energy. These results are presented in Appendix C, Sections C.3 and C.4. In addition, a higher number of beds has a positive effect on the recovery of the process.

Based on the results obtained from the process optimisation, a number of general design rules can be inferred. These rules are:

(i) At first, a targeted purity has to be fixed.

(ii) The required purity is related to the number of beds in the compression and purification train. Generally, greater purities require a higher number of beds. Also, the adsorptive parameters of the solid, such as the saturation capacity and the selectivity, have a high effect on the final purity. These parameters can give an indication on the most suitable adsorptive parameters of the solid for the specific application.

(iii) Since the saturation capacity of the material is the maximum amount that can be stored, by knowing the saturation capacity (in mol kg^{-1}) and the amount that has to be capture (in mol per unit of time), the mass of the storage bed can be obtained.

(iv) By identifying the required number of beds and the mass of the storage bed, the mass of the other beds can be calculated.

(v) Finally, by considering adiabatic blowdown in Bed 1 and/or Bed 2, even higher purities can be achieved. Also, the employment of heat recovery strategies significantly reduces the energy use of the process. A higher concentration of the key component in the inlet stream not only reduces the energy requirements but also increases the final purity.

4 Theoretical and Experimental Investigation on Different Adsorbent Materials for Air Capture

> *The number measures reality and allows to penetrate its meaning.*
>
> **— Pythagoras**
> (Mathematician and Philosopher)

The overall performance of an adsorption process does not only depend on the design of the process cycle and operating conditions but also on the chosen adsorbent material for the specific application. As previously resulted, the selectivity ratio X and ΔH_{B} are pivotal in process performance. Theoretically, by optimising the adsorptive and physical properties of the adsorbent, the overall performance of the process can be improved. The process investigation and optimisation of the previous chapter sought to elucidate the key features of the process and the material based on an equilibrium approach. By embodying these optimal equilibrium adsorption and process characteristics, this chapter focusses firstly on the theoretical investigation of other aspects that have not been considered yet, such as the bed void fraction, which strongly depends on the design of the bed, and the crystal density of the adsorbent material. This chapter also provides an experimental investigation of two different advanced adsorbents by equilibrium gravimetric adsorption measurements.

4.1 Introduction to the Adsorbent Materials

Efficient and cost effective adsorption-based separation technologies require an ideal adsorbent material with: *(i)* high working capacity[1], *(ii)* high selectivity, *(iii)* fast adsorption and desorption kinetics, *(iv)* low to negligible pressure drop, *(v)* stability, and *(vi)* recyclability. For instance, materials operating at high working capacities reduce both energy and capital costs, while mass-transfer kinetics also play an important role on a large scale. The term mass transfer kinetics refers to the diffusion and convective transport of the feed within the system and thus it is not an equilibrium term. Its contribution to the overall system performance is discussed in Chapter 5. Generally, the solid must have reasonably high surface area or micropore volume and relatively large pore network for the quicker transport of molecules to the interior (Do, 1998).

Most commonly used porous adsorbents in industries are activated carbon, zeolite, activated alumina, carbon molecular sieve, and silica gel. Table 4.1 classifies common adsorbents by structure type and water adsorption characteristics. Commercial activated carbon has a very

[1] The working capacity of a material is defined as the difference in the adsorbed amount at the adsorption and desorption pressures or temperatures. The adsorption capacity is the total capacity of the sorbent to its original condition at the start of a new cycle (Wilcox et al., 2014).

Table 4.1. Classification of common adsorbents.

	Amorphous	Structured
Hydrophobic	Activated carbon Polymers	Carbon molecular sieves Silicalite
Hydrophilic	Silica gel Activated alumina	Common zeolites: 3A (KA), 4A (NaA), 5A (CaA), 13X (NaX), Mordenite, Chabazite, etc.

The table is obtained from LeVan et al. (1998).

wide range of properties depending on the application since it has a complex pore network and chemical nature (Do, 1998). The active sites of the functional groups of alumina surface make alumina a good desiccant for the removal of polar molecules at elevated temperature such as the removal of water from gas streams or warm air (Do, 1998; Ruthven, 1984). Silica gel is widely used for water removal due to its strong hydrophilicity of its surface towards water and its ultimate capacity at low temperatures (Do, 1998). However, water is adsorbed more strongly on molecular sieve, a material with pores of uniform size, than alumina or silica gel (Ruthven, 1984). Finally, zeolites are crystalline[2] aluminosilicates with a wide variety of volume fractions and pore walls of different surface chemistry that may offer great adsorption selectivity and adsorption properties. A good overview of the zeolites are given in Ruthven (1984).

The major challenge in applying physisorbents is the existence of water in the feed stream, owing to the competitive adsorption of water over other components in the feed due to the strong dipole-ion interaction between water and adsorbent (Brandani and Ruthven, 2004). In particular, for the DAC application, water has a negative effect on CO_2 adsorption as CO_2 interacts with the polar adsorbent creating a weaker quadrupole-ion interaction that reduces the CO_2 selectivity (Sircar et al., 1996; Brandani and Ruthven, 2004). For this reason, a drying process prior to adsorption step of Bed 1 must occur, which is energy intensive, especially, for the case of air capture where extremely large volumes of air have to be processed. Alternatively, chemisorbents can be employed, which can selectively adsorb CO_2 over H_2O. However, in case of chemisorption, higher heat of desorption is required to break the strong chemical bonds, and often, adsorption is accomplished at higher temperatures and desorption at much harsher conditions than physisorption (Sanz-Peez et al., 2016). Therefore, ideally, a physisorbent able to capture H_2O at higher partial pressures and CO_2 at very low partial pressures can be superior for DAC.

Conventional gas separation systems are usually operated using porous solids in the form of beads, pellets, or granules. However, limitations in operating the process at the optimum energy consumption and overall efficiency are imposed by both mass transfer and pressure drop drawbacks associated with conventional packed beds (Rezaei and Webley, 2010). As Rezaei and Webley (2010) reported, over the last few decades a trend to reduce particle sizes from 2–3 mm down to less than 0.7 mm has been observed since smaller particle sizes permit lower mass transfer resistance. Combating the accompanying increase in pressure drop with reduction in particle size has led to novel adsorbent structures[3], such as monoliths, laminates, foams, and fabrics (Rezaei and Webley, 2010). However, structured adsorbents

[2]Crystalline cages are well-defined openings and they are created by removing the water of hydration via calcination process (LeVan et al., 1998).

[3]The novel adsorbent structures provide: *(i)* fast mass transfer kinetics (due to shorter diffusion path), *(ii)* easier heat transfer in all direction, and *(iii)* uniform temperature distribution (Li et al., 2009; Rezaei and Webley, 2010).

often offer lower throughput compared to the conventional adsorbents. It should be noted here that those aspects are non-equilibrium, thus they are not considered further in this chapter.

Due to the several physical and chemical (i.e. chemical composition and facile functionality) adsorbent properties that govern the performance of adsorptive gas separation for a given adsorption isotherm, a determination of other optimised characteristics of the adsorbent material on system's performance (in terms of energy use and purity) has to be investigated further. That's the principal target of the first half of this chapter. The second half focuses on the experimental investigation of two different novel adsorbents for their potential application in DAC; i.e., AQSOA-FAM-Z02 as developed by Mitsubishi Plastics Inc. (1962) and Y-S3-50 as designed by Bonaccorsi et al. (2017).

4.2 Theoretical Investigation on Materials for Air Capture

4.2.1 Material Physical Properties in Air Capture Process

Some of the identified characteristics of the adsorbent material that may affect the system's performance are the: *(i)* crystal density[4], *(ii)* pellet density, *(iii)* pellet void fraction, and *(iv)* adsorbent heat capacity. The form of the adsorbent material or bed structure, i.e. pellet, powder, monolith, *etc*., also affects the: *(v)* bulk density and *(vi)* bulk (packing) void fraction. Four of the above characteristics of the adsorbent are enough to describe the current system: *(i)*, *(iii)*, *(iv)*, and *(vi)*, as the pellet density (ρ_{p}) is given from

$$\rho_{\mathrm{p}} = (1 - \varepsilon_{\mathrm{p}})\ \rho_{\mathrm{cry}}, \tag{4.1a}$$

and the bulk density (ρ_{b}) is governed by

$$\rho_{\mathrm{b}} = (1 - \varepsilon_{\mathrm{b}})\ \rho_{\mathrm{p}} = (1 - \varepsilon_{\mathrm{b}})\ (1 - \varepsilon_{\mathrm{p}})\ \rho_{\mathrm{cry}}. \tag{4.1b}$$

Since the inlet feed stream is extremely diluted, large volumes of the stream have to be processed in order to adsorb or remove a significant amount of the trace impurity. By considering the extremely high flow rates, pressure drops have to be eliminated to prevent high power consumptions. This is due to the high pressure required in the inlet of the adsorption bed, which requires the use of fans that consume energy. For this reason, Bed 1 should be designed in such way that the pressure drops along the bed will be eliminated along with the energy consumption of this step. The high pressure drop and a poor mass transfer are typical for a conventional bed of granulated or beaded adsorbents. Thus, the first adsorption bed of the DAC system should have:

(i) A higher bulk void fraction to eliminate pressure drops and subsequently to reduce the energy use of the process.

[4]The crystal density is defined in terms of internal void fraction. By considering that the adsorbent materials is in pellet form, then $\rho_{\mathrm{cry}} = \frac{m_{\mathrm{p}}}{V_{\mathrm{cry}}} = \frac{m_{\mathrm{ads}}}{V_{\mathrm{micro}}+V_{\mathrm{skel}}} = \frac{\rho_{\mathrm{p}}}{1-\varepsilon_{\mathrm{p}}}$, where the subscripts 'micro' and 'skel' refer to the volume of micropores and skeletal volume, respectively. There are several techniques to experimentally measure V_{micro} which are discussed in the second half of this chapter.

Table 4.2. System parameters for the calculation of pressure drop.

Parameter	Symbol	Value	Unit
Diameter of beads	d_{p}	0.004	m
Bed voidage	ε	0.4	—
Air velocity	υ	15	m s^{-1}
Air viscosity	η_{f}	18.3 10^{-6}	Pa s
Density of air	ρ_{f}	1.2	kg m^{-3}

(ii) A monolithic or laminar structure to increase the mass transfer effect and subsequently to reduce the process time.

4.2.2 Pressure Drop and Energy Consumption in the Adsorption Contactor

The pressure across a packed bed is given by the Ergun equation as

$$\frac{\Delta P}{L} = 150\,\frac{(1-\varepsilon)^2}{\varepsilon^3}\,\frac{\eta_{\mathrm{f}}}{{d_{\mathrm{p}}}^2}\,\upsilon + 1.75\,\frac{(1-\varepsilon)}{\varepsilon^3}\,\frac{\rho_{\mathrm{f}}}{d_{\mathrm{p}}}\,\upsilon^2, \tag{4.2}$$

where η_{f} [kPa s] is the fluid viscosity, υ [m s^{-1}] defines the interstitial flow velocity, ρ_{f} [kg m^{-3}] is the fluid density, and d_{p} [m] is the diameter of a spherical pellet. Let us consider the parameters of Table 4.2, assuming a flow of atmospheric air across a bed packed with spherical pellets in order to compare the pressure drop across the bed over the bed void fraction, the diameter of the pellet, and the flow velocity. The results are presented in Figure 4.1. Eq. 4.2 and Figure 4.1a suggest that the adsorbent should be structured with higher void fraction and large pellet size in order to reduce pressure drops. Figure 4.1b shows that higher velocities result in a higher pressure drop across the packed bed. However, lower velocities reduce the productivity[5] of the system. However, this needs to be in balance with the requirements for rapid diffusion and high volumetric efficiency[6] that can be achieved by small pellet size and small void fraction, respectively (Akhtar et al., 2014; Rodriguez-Illera et al., 2015).

By assuming different bed structures, the pressure drop can change significantly as:

(i) The pressure drop in a packed bed can be obtained from Eq. 4.2.

By considering the general parameters of Table 4.2 and the L=0.5 m, then the resulting pressure drop is at 5.61 bar (10^5 Pa), such that the inlet pressure has to be at 6.62 bar to have a 1.01 bar atmospheric pressure in the outlet.

(ii) The pressure drop in a squared structured packing, which is the same as the catalytic converter in cars, is governed by

$$\Delta P = L\,\frac{16}{0.562}\,\frac{\eta_{\mathrm{f}}\,\upsilon}{b^2}. \tag{4.3}$$

By assuming b=4 mm then, the pressure drop is at 244 Pa, so that the inlet pressure has to be at 1.02 bar.

[5] Productivity is related to the rate in which the trace component is separated and is defined as the amount of the captured trace component over the operational time of the process.
[6] The volumetric efficiency is defined as the mass uptake per unit volume.

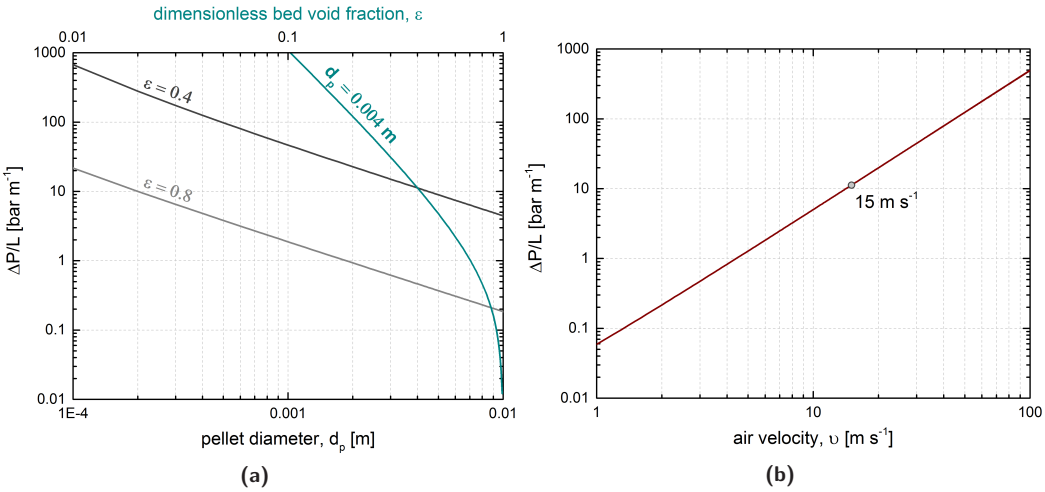

Figure 4.1. The profile of the pressure drop [bar m^{-1}] across a packed bed versus **(a)** the pellet diameter [m] and the packed bed void fraction and **(b)** the air feed velocity [m s^{-1}].

The importance of the pressure drop through the bed can be obtained from the specific energy needed to operate a fan to provide the required pressure in the inlet. The minimum thermodynamic isothermal compression work is governed by

$$W_{\mathrm{IsoT}} = \int_{P_1}^{P_2} V \mathrm{d}P = n\,R\,T \int_{P_1}^{P_2} \frac{1}{P} \mathrm{d}P = n\,R\,T \ln\left(\frac{P_2}{P_1}\right), \tag{4.4}$$

where P_1 and P_2 are the pressure in the inlet and outlet of the unit, respectively, and the ideal gas equation of state has been used. Now, by assuming an overall fan efficiency ϑ_{f} of 0.6 then,

$$W = \frac{W_{\mathrm{IsoT}}}{\vartheta_{\mathrm{f}}} = \frac{n\,R\,T}{0.6} \ln\left(\frac{P_1}{P_2}\right), \tag{4.5a}$$

which corresponds to a power of

$$\mathrm{Power} = \frac{W}{24 \times 3600}. \tag{4.5b}$$

Let us simply assume that 10 tCO_2 per day need to be passed through the adsorption bed and that the CO_2 concentration in the inlet is 400 ppm. Thus, the specific energy use of a fan to capture 10 tCO_2 in a packed bed is 18.9 MJ mol^{-1} (50 MW power). This is not a feasible approach. On the other hand, 24.5 kJ mol^{-1} (64.5 kW power) is the specific energy use of a fan in a structured packing. To put this into perspective, approximate 120 kJ mol^{-1} is consumed for the post-combustion capture of CO_2 from the flue gas stream of a gas-fired power plant for urea production (Courtesy of Mitsubishi Heavy Industries Ltd.) in Malaysia (IPCC, 2005). Approximately one fifth of its energy requirements are needed to drive the fan in a structured packing of DAC, but it is worth investigating.

Wind could be used as an alternative to a fan to drive air through the unit. To investigate whether this is feasible, the Bernoulli's equation is used by assuming low pressure such that the density remains approximately constant as

$$\frac{1}{2}\rho\,\upsilon^2 + \rho\,g\,z + P = \mathrm{const}, \tag{4.6}$$

where the first term $\left(\frac{1}{2}\,\rho\,v^2\right)$ is the kinetic energy consideration, the second term $(\rho\,g\,z)$ is the potential energy, and finally the last term (P) is the mechanical work. This equation allows to understand how the kinetic energy change (slowing down or accelerating fluids) leads to changes in pressure. Let us assume that the system is horizontal so that $z = 0$, then Bernoulli's equation becomes

$$\frac{1}{2}\,\rho\,\Delta v^2 + \Delta P = 0. \tag{4.7}$$

By considering Eq. 4.7, the wind velocity becomes

$$v_{\text{wind}} = \sqrt{\frac{\frac{1}{2}\,\rho\,v^2 + \Delta P}{\frac{1}{2}\,\rho}}. \tag{4.8}$$

Thus, by using the values obtained from the structured packing, the wind velocity results at 25.15 m s^{-1} or else 90.5 km hr^{-1}. Considering this wind velocity, it is not feasible to power the device using the wind.

Wang et al. (2011) proposed another strategy that involved a targeted pressure drop of 4 Pa through a prototype air conductor. They have achieved this value through the use of large void volumes that help to reduce the pressure drop but hurt the concentration step. The difficult part in direct air capture is the concentration step. By considering a pressure drop at 4 Pa and an inlet velocity at 5 m s^{-1}, instead of 15 m s^{-1}, the wind velocity becomes 20 km hr^{-1}, which is a bit more reasonable. It is therefore feasible to improve the structure of the beds, especially Bed 1, such that the energy requirements due to the pressure drop across the bed become far less significant.

4.2.3 Optimisation Method: Assumptions and Considerations

This section aims at the theoretical investigation of the optimal characteristics (material equilibrium properties) of the adsorbent. A similar multi-objective global optimisation algorithm to that described in Section 3.5 has been applied here not for the optimisation of the relative mass of adsorbent in each bed but for the optimisation of the physical properties of the material. Figure 4.2 illustrates four points (A, A', B, and C) along two Pareto fronts. These optimal fronts resulted from the optimisation of the relative mass of adsorbent in each bed as presented in Section 3.5 and consider: *(a)* the implementation of instantaneous vacuum step in Bed 1 and Bed 2 (see Section 3.2), and *(b)* the implementation of adiabatic blowdown in Bed 1 (see Section 3.3) with an instantaneous vacuum step in Bed 2. The parameters considered for obtaining those Pareto fronts can be found in Table 4.3 under the tags 'Fixed Parameters' and 'Mono-site Langmuir Parameters' and in Table 3.7 (see Section 3.5) under the tag 'Material physical properties'.

For the study of *(a)*, three different cases (points A, B, and C on the Pareto front of Figure 4.2) have been considered: *(i)* case A at 95% purity and 2.15 MJ mol^{-1} total specific energy consumption, *(ii)* case B at 90% purity and 1.23 MJ mol^{-1}, and *(iii)* case C at 85% purity and 1.09 MJ mol^{-1}. For the Pareto front *(b)*, the case A' at 95% purity and 1.71 MJ mol^{-1} (see point A' in Figure 4.2) is used as a comparison. Each point of Figure4.2 (A, A', B, or C) illustrate four optimal configurations at different purities that have been selected as fixed parameters for this process optimisation. These parameters are presented in Table 4.3. Fixing the optimal masses (the masses that converge at the minimal energy consumption

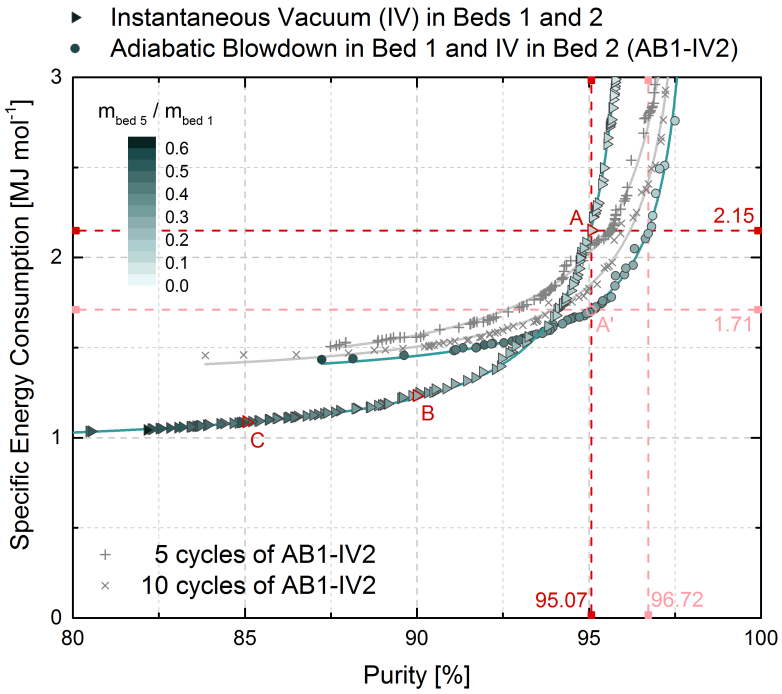

Figure 4.2. Colour mapped plot of the total energy consumption [MJ mol^{-1}] versus purity [%] in the storage bed as a function of the relative mass in the storage Bed 5 for the separation of species (A) existing at 400 ppm in a binary mixture of (A) and (B).

The plot considers two cases: *(a)* instantaneous vacuum (IV) step in Beds 1 and 2 and *(b)* adiabatic blowdown in Bed 1 and instantaneous vacuum in Bed 2 (AB1-IV2).

and maximal purity — along the Pareto front) and considering the parameters of Table4.3, the new multi-objective global optimisation could be performed.

The system is restricted to the case of 5 beds and the process parameters, operational conditions, and adsorptive properties of the solid are listed in Table4.3. Table 4.4 illustrates the entities used to define the design space of the optimisation system, which are the: *(i)* Bed 1 void fraction, $\varepsilon_{\mathrm{b},1}$, *(ii)* Bed 2 to Bed N_{B}–1 void fraction, $\varepsilon_{\mathrm{b},2-(N_{\mathrm{B}}-1)}$, *(iii)* Bed N_{B} void fraction, $\varepsilon_{\mathrm{b},N_{\mathrm{B}}}$, *(iv)* internal void fraction, ε_{p}, and *(v)* crystal density, ρ_{cry}. Different void fractions are considered for the adsorption bed, the beds that consist the compression and purification train, and the storage bed as each section of the process is designed for a different purpose. For sake of simplicity, Table 4.3 does not include all the considered parameters. If it is of interest, these parameters can be found in Table 3.7 of Section 3.5.

An adsorption bed can be structured in different geometries according to the requirements of a process. For instance, a TSA technology requires fast heat transfer. This effect is reduced by low thermal conductivity of the adsorption materials. Figure 4.3 illustrates the different structured adsorbent material inside cylindrical packed beds or rectangular structures. Since the range of bed void fractions can vary, the effect of this variable on the process performance is investigated.

Table 4.3. Considered input parameters of the model for material optimisation.

Fixed Parameters	**Symbols**	**Value**	**Unit**
Number of beds	N_{B}	5.00	—
Number of cycles/runs	N_{R}	20.00	—
Adsorption temperature	T_{low}	293.15	K
Regeneration temperature	T_{high}	368.15	K
Atmospheric pressure	P_{atm}	101.325	kPa
Vacuum pressure	P_{vac}	30.00	kPa
Feed concentration of species (A)	y_{A}	0.04	%
Mass of Bed 1	$m_{\mathrm{bed},1}$	1.00	kg
Mono-site Langmuir Parameters			
Saturation capacity	q_{s}	6	mol kg^{-1}
Heat of adsorption of species (A)	ΔH_{A}	35	$(-)$ kJ mol^{-1}
Heat of adsorption of species (A)	ΔH_{B}	15.74	$(-)$ kJ mol^{-1}
Equilibrium constant coefficient of (A)	$b_{0,\mathrm{A}}$	4	$\left(10^{-7}\right)$ kPa^{-1}
Equilibrium constant coefficient of (A)	$b_{0,\mathrm{B}}$	11.99	$\left(10^{-7}\right)$ kPa^{-1}
Selectivity of species (A) over (B) at T_{low}	$\left(S_{\mathrm{A/B}}\right)_{T_{\mathrm{low}}}$	900	—
Selectivity of T_{low} over T_{high}	$\left(\frac{S_{T_{\mathrm{low}}}}{S_{T_{\mathrm{high}}}}\right)$	5	—

Relative Masses for Each Case	**Symbols**	**Value**				**Unit**
		Case A [a]	**Case B** [a]	**Case C** [a]	**Case A'** [b]	
Relative mass of Bed 2 over Bed 1	$m_{\mathrm{bed},2}/m_{\mathrm{bed},1}$	0.18	0.22	0.28	0.22	—
Relative mass of Bed 3 over Bed 1	$m_{\mathrm{bed},3}/m_{\mathrm{bed},1}$	0.03	0.05	0.07	0.06	—
Relative mass of Bed 4 over Bed 1	$m_{\mathrm{bed},4}/m_{\mathrm{bed},1}$	0.01	0.02	0.03	0.02	—
Relative mass of Bed 5 over Bed 1	$m_{\mathrm{bed},5}/m_{\mathrm{bed},1}$	0.14	0.30	0.45	0.31	—

[a] Instantaneous vacuum/evacuation of Bed 1 and Bed 2.
[b] Adiabatic blowdown of Bed 1 and instantaneous vacuum/evacuation of Bed 2.

Table 4.4. Considered variables for process optimization.

Input Variables	Symbols	Entities to Define the Design Space		Unit
		Lower Limit	Higher Limit	
Bed 1 void fraction	$\varepsilon_{\mathrm{b},1}$	0.1	0.9	—
Bed 2–($N_{\mathrm{B}}-1$) void fraction	$\varepsilon_{\mathrm{b},2-(N_{\mathrm{B}}-1)}$	0.1	0.9	—
Bed N_{B} (last bed) void fraction	$\varepsilon_{\mathrm{b},N_{\mathrm{B}}}$	0.1	0.9	—
Pellet or Internal void fraction	ε_{p}	0.1	0.9	—
Crystal density	ρ_{cry}	10.0	5000.0 [a]	kg m^{-3}

[a] Higher upper limit as reported crystal density of common zeolites is stated at < 2000 kg m^{-3} (Sircar and Myers, 2003).

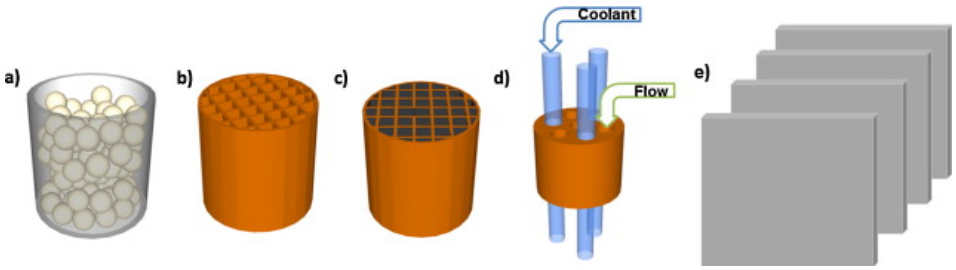

Figure 4.3. Schematic examples of structured adsorbents: **(a)** beads; **(b)** honeycomb; **(c)** coated honeycomb; **(d)** monoliths with channels for flow of heat conducting media and mass transfer; and **(e)** laminates.

Source: The graph is taken from Akhtar et al. (2014).

4.2.4 Results and Discussion: Analysis and Design of the Process and the Material

Figure 4.4 illustrates the optimisation results following the parameters of Table 4.3. In general, adiabatic blowdown in Bed 1 can help to increase the purity, by 5–10% depending on the design purity, and to reduce the energy consumption of the process. In addition, by optimising the bed void fractions and physical properties of the adsorbent, a significant improvement in the purity of the process can be achieved by consuming almost the same energy. Specifically, Figure 4.4 shows that for all the considered cases, a decrease in the void fraction of the storage bed causes a significant improvement in purity, >98%. This can be explained by the fact that less N_2 is initially stored in the last bed. Therefore, with the same number of cycles, a higher purity can be achieved. The specific energy use remains almost the same since the number of cycles is fixed and only the captured amount of CO_2 slightly increases. Therefore, an adsorbed in the form of pellets (<2 mm) can be used in the storage bed to achieve lower void fractions and higher purities.

Apart from Figure 4.4, the following Figure 4.5 represents the optimisation results of the other bed void fractions. Specifically, an increase in the bed void fraction of Bed 1 (see Figure 4.5a) and Bed 2 to Bed (N_{B}–1) (see Figure 4.5b) can significantly improve the purity of the process. The results in Section C.1 show that the concentration of CO_2 is built up in each bed cycle after cycle. This causes a decrease in N_2 concentration as more CO_2 is getting adsorbed in each bed. Therefore, N_2 is flowing from storage bed back to Bed 1 and Bed 2 where it can exit the system during the evacuation step. A way to reduce the amount of undesired gas is either by adiabatic blowdown in Bed 1 and/or Bed 2 or by backflow of the undesired gas from bed to bed. Due to these effects, a higher amount of undesired gas can either be removed from the process or avoided in the last bed. Since the model does not take into account mass transfer, the increase in the bed void fraction is reasonable.

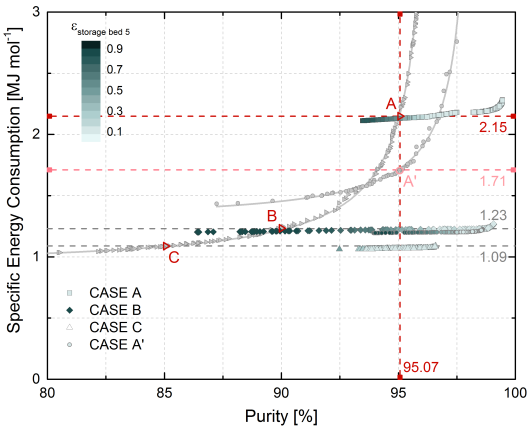

Figure 4.4. Colour mapped plot of the total energy consumption [MJ mol^{-1}] versus purity [%] in the storage bed as a function of the storage bed void fraction for the separation of species (A) existing at 400 ppm in a binary mixture of (A) and (B).

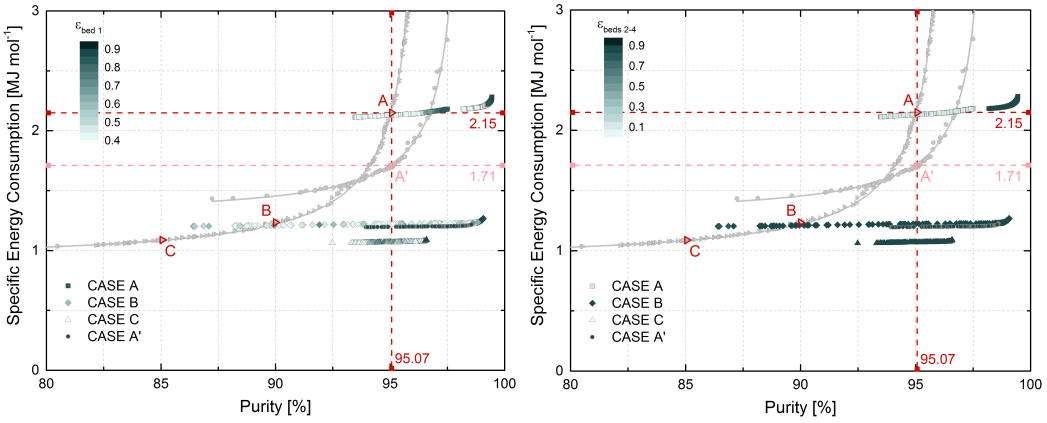

(a) Bed 1 void fraction

(b) Beds 2–4 void fraction

Figure 4.5. Colour mapped plots of the total energy consumption [MJ mol^{-1}] versus purity [%] in the storage bed as a function of: **(a)** the Bed 1 void fraction and **(b)** the Beds 2–4 void fraction, for the separation of species (A) existing at 400 ppm in a binary mixture of (A) and (B).

Laminate structures can be used in these beds as they typically achieve higher void fractions and reduce the pressure drops across the bed.

Figure 4.6a shows the optimised values of pellet void fraction. The same pellets were assumed to be used in each bed of the system. In addition, the pellet void fraction is proportional to the volume of the macropores and therefore, contributes to the bulk gas phase of each bed. Figure 4.6a illustrates that the lower the pellet voidage, the higher the purity that can be achieved. This outcome is reasonable as the lower pellet void fraction increases both the density of the bed and the density of the pellet. As a result, the volume of the gas surrounding the pellets (V_g) and the volume of the macropores or else the volume of the gas inside the pellet surrounding the crystals (V_{macro}) decrease since

$$V_g = \varepsilon_b V_c = \varepsilon_b \frac{m_{ads}}{\rho_b} = \varepsilon_b \frac{m_{ads}}{(1-\varepsilon_b)\ \rho_p} = \varepsilon_b \frac{m_{ads}}{(1-\varepsilon_b)\ (1-\varepsilon_p)\ \rho_{cry}}, \tag{4.9}$$

and

$$V_{macro} = \varepsilon_p V_p = \varepsilon_p \frac{m_{ads}}{\rho_p} = \varepsilon_p \frac{m_{ads}}{(1-\varepsilon_p)\ \rho_{cry}}. \tag{4.10}$$

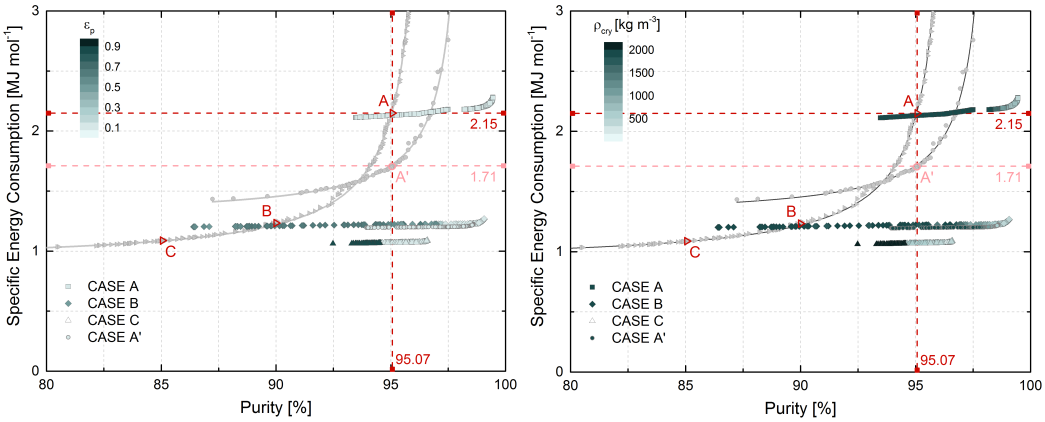

(a) Pellet void fraction **(b)** Crystal density

Figure 4.6. Colour mapped plots of the total energy consumption [MJ mol^{-1}] versus purity [%] in the storage bed as a function of: **(a)** the pellet void fraction and **(b)** the crystal density, for the separation of species (A) existing at 400 ppm in a binary mixture of (A) and (B).

Therefore, the volume of the gas phase decreases, which represents the decreased amount of component (B) inside each bed. As has been shown above, this effect is important in order to avoid the large amounts of undesired gas, especially in the storage bed (see Figure 4.4). The resulting lower pellet porosity suggests that an adsorbent material with no binder is preferred to achieve higher purities. It is important to remember here that smaller material void fractions can result in a higher volumetric efficiency as stated earlier in this chapter.

Another parameter of the adsorbent that has been optimised is the crystal density. Again, the crystal density is the same in each bed as the same material has been used. Figure 4.6b shows that a decrease in crystal density leads to extremely high purities, >98%. This can be explained by the increase of the bulk void fraction of Beds 1–4 at higher purity regions. Therefore, in these regions the volume of the bulk gas phase increases. By decreasing the crystal density, the bulk gas phase can be further increased. However, higher values of crystal densities, i.e. >1000 kg m^{-3}, can also converge to high purities. Hence, it is important to distinguish the most strongly affecting parameters in order to give guidelines concerning design requirements and adsorbent structural characteristics. This is analysed in the following subsection.

According to Figure 4.7, the final pressure of the process decreases. The reason for this is that the masses of the beds were optimised for different parameters. By decreasing, for instance, the mass of the storage bed, a higher pressure can be achieved.

4.2.5 Guidelines to Design

Before giving directions for the design of the beds, related to their void volumes, and the material characteristics, it is important to remember that the Pareto fronts have converged based on the optimisation of the objective functions of energy and purity. The consideration of other objective functions such as pressure and purity would have different impacts on the optimised parameters.

In general, the contribution of the void fraction of the beds is the strongest parameter affecting the process final purity, energy use, pressure, and recovery. Specifically, the void

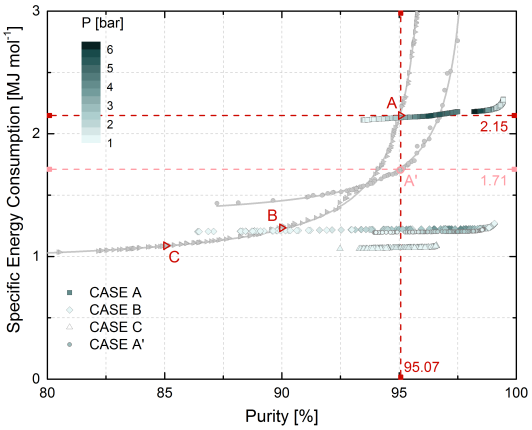

Figure 4.7. Colour mapped plot of the total energy consumption [MJ mol^{-1}] versus purity [%] in the storage bed as a function of the final pressure in the storage bed for the separation of species (A) existing at 400 ppm in a binary mixture of (A) and (B).

fraction of the storage bed, Bed 5, has the highest contribution to the product final purity and pressure; however, the void fraction of Bed 2–(N_{B}–1) has the greatest effect on the energy use and recovery. This gives a degree of flexibility in the void fraction of Bed 1 that, as has been previously explained, has to be high in order to eliminate pressure drops. A higher $\varepsilon_{\mathrm{b},1}$ will also result in higher purity. So, values as high as >0.8 for Bed 1 can be considered.

The void fraction of the storage bed is very important since it controls the final purity and pressure of the process. Low values of $\varepsilon_{\mathrm{storage\,bed}}$, $\leq$0.2, lead to significantly higher purities and greater product pressures. These values will then have a minor positive effect on the energy requirements of the process and minor negative effect on the process recovery.

The void fraction of the beds that contain the compression and purification train has a positive effect on energy and a negative effect on recovery. Thus, low void fractions in Bed 2 to Bed N_{B}–1 can reduce the energy consumption of the process, enhance the recovery, and contribute slightly to higher purities.

So far, the effect of the pellet porosity and crystal density on the performance of the process have not found to be significant. Although, ε_{p} has a negative effect on the final pressure of the process such that moderated values, around 0.3–0.6, can be more beneficial. If the pressure and recovery are included as objective functions for optimisation, then higher values of crystal density, may lead to higher pressures and recoveries.

4.3 Experimental Investigation on Materials for Air Capture

Capture of carbon dioxide by adsorptive processes is based on preferential adsorption of carbon dioxide on porous adsorbents. The first and most important step in the design of an adsorption separation process is to find a suitable adsorbent with large CO_2 working capacity and selectivity over the additional components in the mixture and ideally with a large cycle lifetime (Ruthven, 1984). As previously discussed, in industrial processes,

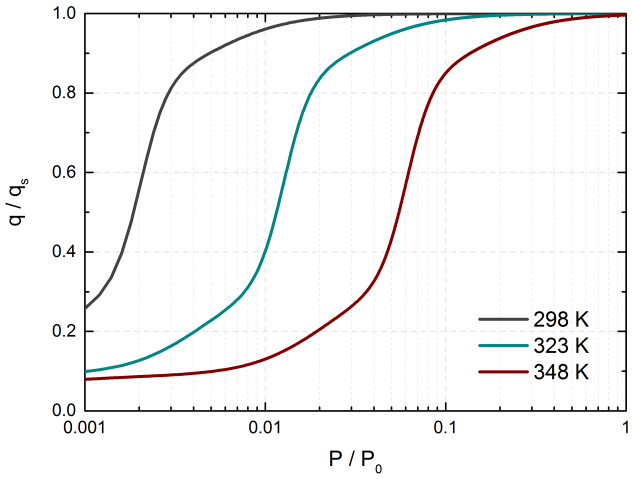

Figure 4.8. H_2O uptake on AQSOA-Z02 at (298, 323 and 348) K. Data were taken from Goldsworthy (2014).

zeolite 13X is frequently used as an adsorbent due to its high adsorption capacity (Pulin et al., 2001; Rother and Fieback, 2013) and high CO_2 selectivity over other gases (Dunne et al., 1996; Hefti et al., 2015; Harlick and Tezel, 2004). Although, when H_2O is present in the mixture, in applications such as CO_2 capture from flue gases and CO_2 removal in closed-circuit breathing systems, it adsorbs near its pure component isotherm (Joos et al., 2013) making zeolite 13X an unfavorable sorbent for carbon dioxide removal applications. Alternatively, the initial stream has to undergo preliminary drying, which removes nearly 99.9% of water from the mixture before further treatment. Consequently, the drying step adds a cost to the gas separation process and it is most likely not feasible on large scale applications (Lee and Sircar, 2008).

Ideally, an adsorbent with a hydrophobic nature or with a relatively low uptake from low to moderate levels of humidity, which follows an unfavorable adsorption isotherm or the type III and V isotherms according to the IUPAC classification of adsorption isotherms (Sing et al., 1985), can be superior for carbon dioxide separation and purification processes. The Functional Adsorbent Material Zeolite, (FAM Z-series), commercialised by Mitsubishi Plastics Inc., show most advantageous adsorption isotherms when in contact with water. AQSOA®-FAM-Z02, based on the SAPO-34 zeotype with CHA-structure, hereafter referred in this work as AQSOA-Z02, shows very suitable adsorption characteristics — a type V adsorption isotherm as investigated by Goldsworthy (2014) — to recover CO_2 from a gas mixture containing H_2O (Mitsubishi Plastics Inc., 2009). Due to the stepwise uptake of water, the partial pressure of water has to exceed a threshold value before water can be adsorbed. This is a feature of AQSOA-Z02 that makes it more favourable than other benchmarking materials (see Figure 4.8) such as zeolite 13X which instead shows type I isotherm for water with very steep trend at low pressure.

A low humidity content feed can be found in applications such as the CO_2 removal from the atmospheric air (Lackner, 2009) and from the closed cabin atmospheres (ElSherif and Knox, 2005) to sustain the quality of the breathing air. There, CO_2 exists in the feed stream in parts per million (ppm) while N_2 and O_2 are the main components of the fluid. In order to study the separation of CO_2 for these applications, at least the adsorption of CO_2, N_2, and H_2O on the selected adsorbent is required. Hence, a study on the adsorption equilibrium of

Table 4.5. Physical and surface properties of AQSOA®-FAM-Z02 and Y-S3-50.

Material	Material Property	Value	Reference
AQSOA-Z02	Crystal size [μm]	5–10	Mitsubishi Plastics Inc., 1962
	Specific surface area [$m^2\ g^{-1}$]	650–770	Mitsubishi Plastics Inc., 1962
	Mean pore diameter [nm]	0.38	Mitsubishi Plastics Inc., 2009
	Pellet particle density [$g\ cm^{-3}$]	1.081 [a]	—
	Skeleton density [$g\ cm^{-3}$]	2.256 [a]	—
	Micropore volume [$cm^3\ g^{-1}$]	0.279 [a]	—
Y-S3-50	Crystal size [μm]	2–4	Bonaccorsi et al., 2017
	Micropore volume [$cm^3\ g^{-1}$]	0.33	Bonaccorsi et al., 2017

[a] Data measured in the Adsorption Laboratory of the University of Edinburgh. Micropore volume measurement confirmed data disclosed in Kayal et al. (2016).

carbon dioxide, nitrogen, and carbon dioxide–nitrogen mixtures on AQSOA-Z02 was carried out with a gravimetric apparatus from vacuum to high pressures. The Toth isotherm model and the ideal adsorbed solution theory (IAST) in conjunction with Toth model were applied to describe single component and mixture equilibria. Consequently, this step adds a cost to the gas separation process.

4.3.1 Experimental Methods: Materials, Apparatus, Data and Error Analyses

4.3.1.1 Materials

Adsorption of carbon dioxide, nitrogen, and carbon dioxide – nitrogen binary system of: *(i)* 15 mol% CO_2 and 85 mol% N_2, *(ii)* 50 mol% CO_2 and 50 mol% N_2, and *(iii)* 80 mol% CO_2 and 20 mol% N_2 on AQSOA-Z02 are reported. The adsorbent is a CHA-type (silico)aluminophosphate in the form of loose grains with sizes ranging from 0.25–0.45 mm (Sapienza et al., 2011; Santori et al., 2013). The physical properties of the adsorbent material are given in Table 4.5. CO_2 (99.6%) and N_2 (99.995%) were obtained from White Martins-Praxair (Brazil).

Adsorption of pure carbon dioxide and nitrogen on Y-S3-50, a S3 propyltrimethoxy (C_3H_7–$Si(OCH_3)_3$), is also reported. Y-S3-50 is a modified zeolite Y with silane in powder form (Bonaccorsi et al., 2017) and was provided by the CNR-ITAE research institute. The physical properties of the adsorbent Y-S3-50 are also included in Table 4.5.

4.3.1.2 AQSOA-Z02 Material Skeleton Density and Porosity

An adsorbent pellet consists of microporous crystalites that are held together by a binder. Thus, a pellet consists of inter-crystalline macropores, which refer to the inside of the adsorbent pellet, and intra-crystalline micropores, which refer to the inside of the adsorbent crystal. The determination of each volume is important since adsorption occurs in the micropores and macropores, which preliminary act as transport pores and are consider as part of the bulk-gas phase.

A Quantachrome UltraPyc 1200e He pycnometer was used to determine the skeleton density or non-accessible specific volume of the AQSOA-Z02 sample (Brandani et al., 2016). A NIST

certified stainless steel sphere of volume 7.07 cm^3 was used to calibrate the volume of the cell. The cell was calibrated with and without the sphere prior to the collection of data.

Once the sample was regenerated at 473 K under vacuum for 2 hr, in an outgassing station of an Autosorb iQ, 4.37 g of the sample was loaded into the cell. A purge step was carried out for 3 mins to evacuate the pores of the sample and the cell. After the purge step, 10 volume measurements were carried out and the results of the last 5 runs were collected and averaged to calculate the skeleton density, which is given in Table 4.5.

An Autosorb Poremaster mercury porosimeter was used to measure the volume of the macropore of the AQSOA-Z02 sample. 1.03 g of regenerated sample was loaded into a porosimeter cell and the procedure, as described by Brandani et al. (2016), was followed for the investigation of the pellet density and macropore volume. From these results, the micropore volume was calculated. The outcomes are summarised in Table 4.5.

4.3.1.3 Gravimetric Apparatus

The adsorption experiments were performed using a Rubotherm (Bochum, Germany) magnetic suspension microbalance, as illustrated in Figure 4.9, equipped with a gas mixture dosing unit. The sample was exposed to the measuring atmosphere while the balance was located outside this atmosphere under ambient conditions, which was achieved using a magnetic suspension coupling, as described by Dreisbach et al. (2002). Pure component experiments were performed using the two-position mode of the permanent magnet, the so-called "Zero Point Position" and "Measuring Point Position". The mass at zero point position was calibrated and tared for more accurate weight measurements and the data at both positions were used to correct the buoyancy effect. A comprehensive description of the experimental apparatus and the measurement procedure is given by Bezerra et al. (2011).

Around 0.5 g of adsorbent was outgassed at 473 K until no mass variation in the system was observed. It was then cooled down to experimental temperature while the gas pressure was increased stepwise until a 20 bar maximal pressure was reached. Mass variation at equilibrium was recorded for each pressure step. Pure component measurements were performed using the gravimetric setup described by Bezerra et al. (2011).

The three-position mode automatic magnetic suspension microbalance, consisting of the "Zero Point Position", "Measuring Point 1" and "Measuring Point 2" positions, with an automatic gas mixture dosing system (Vilarrasa-García et al., 2015) was used for binary mixture adsorption equilibria measurements and density determination. A titanium sinker was added to the sample container as demonstrated in previous reports by May et al. (2001) and McLinden and Lösch-Will (2007). By lifting up the sample holder (measuring point 1 position), the sorption measurement was collected. By raising and weighing the Ti sinker (measuring point 2 position), the density of the fluid phase was determined. These positions are illustrated in Figure 4.9.

A procedure similar to that used for the regeneration of 0.5g of adsorbent in the two-position magnetic suspension balance was also implemented on the three-position balance prior to recording data. The peripherals and magnetic suspension coupling were operated automatically using MessPro software (Rubotherm) for the collection of adsorbed mass and density at each pressure step at isothermal conditions. Rubotherm is integrated with a gas

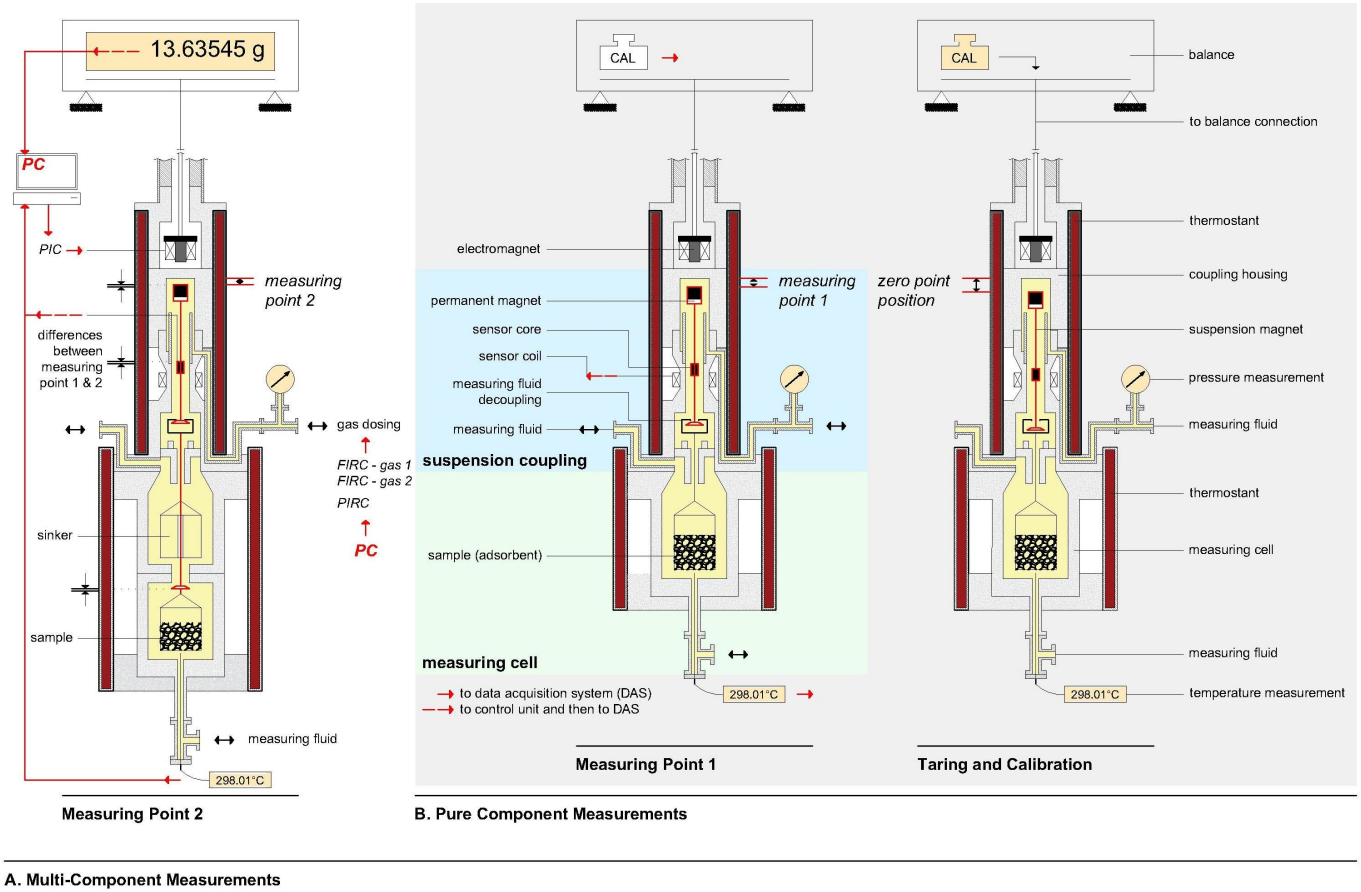

Figure 4.9. Experimental apparatus: magnetic suspension microbalance for the pure component (two-position mode) and multi-component (three-position mode) measurements.

The diagram includes all the parts of the magnetic suspension microbalance, the components to the data acquisition system and to the control unit, the indicators, and the different measuring positions.

Note: The graph is created based on material from Rubotherm Präzisionsmesstechnik GmbH (*Analytical Measuring Instruments*) online.

dosing system where by setting the flow rates through the MessPro software, the molar fraction of the gases in the binary mixture are automatically set. An inclusive description for the collection of data is given by Dreisbach et al. (2003).

A procedure similar to that used for the regeneration of the adsorbent in the two-position magnetic suspension balance was also implemented on the three-position balance prior to the recorded data. The peripherals and magnetic suspension coupling were operated automatically using *MessPro* software (Rubotherm) for the collection of adsorbed mass and density at each pressure step at isothermal conditions.

4.3.1.4 Data Analysis

Since the adsorption data were obtained gravimetrically, the balance reading $m_{\mathrm{Bal}}(P,T)$ had to be corrected due to the buoyancy effects acting on the adsorbent and components of the balance holding the sample. This was done by

$$m_{\mathrm{Bal,Corr}}(P,T) = \Delta m_{\mathrm{spec}}(P,T) + (V_{\mathrm{s}} + V_{\mathrm{sc}})\,\rho(P,T), \tag{4.11}$$

where $m_{\mathrm{Bal,Corr}}$ [g] denotes the mass of the adsorbate after buoyancy correction, V_{s} [cm^3] represents the specific volume of adsorbent sample displacing the atmosphere, V_{sc} [cm^3] is the volume of the balance suspended components, ρ [g cm^{-3}] denotes the density of the atmosphere surrounding the sample, P is the pressure [bar], and T is the temperature [K].

Δm_{spec} [g] indicates the specific mass change of the sample due to adsorption. This was governed by

$$\Delta m_{\mathrm{spec}}(P,T) = m_{\mathrm{Bal,Corr}}(P,T) - m_{\mathrm{sc}}(P,T) - m_{\mathrm{s}}(P,T), \tag{4.12}$$

where m_{sc} [g] is the mass of the sample container in vacuum obtained from black measurement without sample and m_{s} [g] denotes the mass of reactivated sample calculated in the loading and reactivation of sample step with an inert gas. Information about the black measurement and the loading and reactivation of sample steps is given by Weireld et al. (1999). V_{sc} in Eq. 4.11 does not depend on pressure and was measured in a calibration experiment without sample (Dreisbach et al., 2002).

By considering V_{s} as equal to the skeleton volume (V_{sk}), the surface excess adsorbed amount was evaluated as

$$q^{\mathrm{exc}} = \frac{\Delta m_{\mathrm{spec}}(P,T) + (V_{\mathrm{s}} + V_{\mathrm{sc}})\,\rho(P,T)}{m_{\mathrm{s}}(P,T)\,M_{\mathrm{w}}}. \tag{4.13}$$

Although, to model adsorption processes, absolute adsorption had to be determined since the excess mass is not a well-defined property for microporous materials as stated by Brandani et al. (2016) and Myers and Monson (2014). The difference between the absolute and the excess adsorption was governed by

$$q^{\mathrm{abs}} = q^{\mathrm{exc}} + \frac{\rho_{\mathrm{g}}(P,T)\,V_{\mathrm{ads}}}{m_{\mathrm{s}}(P,T)\,M_{\mathrm{w}}}, \tag{4.14}$$

where q^{abs} [mmol g^{-1}] represents the absolute adsorbed amount, q^{exc} [mmol g^{-1}] denotes the excess adsorbed amount, ρ_{g} [g cm^{-3}] is the density of the gas phase, V_{ads} [cm^3] indicates

the pore volume participating to the adsorption, equivalent to the micropore volume in the present work, and M_{w} [g mmol^{-1}] is the molecular mass of the gas.

By consider the volume of the adsorbed layer, V_{s} in Eq. 4.11 becomes the volume of the solid including micropores, which cannot be measured directly in the same experimental setup. This value can be obtained experimentally by measuring the volume of the skeleton and the volume of the micropores (V_{micro}) independently. V_{sk} was measured in the same gravimetric system by carrying out experiments with an inert gas. In this work, helium was used for the determination of V_{sk}. An alternative method was implemented to examine the non-accessible volume of the sample using a helium pycnometer (HeP) as has been previously described. The volume of the adsorbed layer or else V_{micro} was calculated from

$$V_{\mathrm{micro}} = V_{\mathrm{s}} - V_{\mathrm{sk}} = (V_{\mathrm{pellet}} - V_{\mathrm{macro}})_{\mathrm{HgP}} - (V_{\mathrm{sk}})_{\mathrm{HeP}}\,, \tag{4.15}$$

where the volume of the pellet V_{pellet} [cm^3] and the volume of the macropores V_{macro} [cm^3] were obtained by means of mercury intrusion porosimetry (HgP).

4.3.1.5 Error Analysis

The parameters that theoretically affected the sorption measurements followed

$$q^{\mathrm{abs}} = f(m_{\mathrm{Bal}}, m_{\mathrm{sc+s}}, m_{\mathrm{s}}, \dot{v}_i, P, T, V_{\mathrm{micro}}), \tag{4.16}$$

where $\dot{v}_i$ [ml min^{-1}] denotes the measured volumetric flow rate of species i in the fluid gas.

To determine the effect of each parameter on uncertainty in the absolute adsorbed amount, the partial differentials of the independent errors were calculated by

$$\begin{aligned}\delta V_{\mathrm{sc+s}} &= f\left(m_{\mathrm{Bal}}, m_{\mathrm{sc+s}}, \rho\right)\\ &= \left[\left(\left(\frac{\partial V_{\mathrm{sc+s}}}{\partial m_{\mathrm{Bal}}}\right)\delta m_{\mathrm{Bal}}\right)^2 + \left(\left(\frac{\partial V_{\mathrm{sc+s}}}{\partial \rho}\right)\delta \rho\right)^2 + \left(\left(\frac{\partial V_{\mathrm{sc+s}}}{\partial m_{\mathrm{sc+s}}}\right)\delta m_{\mathrm{sc+s}}\right)^2\right]^{0.5},\end{aligned} \tag{4.17a}$$

$$\begin{aligned}\delta \rho &= f\left(P, T, y\right)\\ &= \left[\left(\left(\frac{\partial \rho}{\partial P}\right)\delta P\right)^2 + \left(\left(\frac{\partial \rho}{\partial T}\right)\delta T\right)^2 + \sum_{i=1}^{2}\left(\left(\frac{\partial \rho}{\partial y_i}\right)\delta y_i\right)^2\right]^{0.5},\end{aligned} \tag{4.17b}$$

$$\begin{aligned}\delta \Delta m_{\mathrm{spec}} &= f\left(m_{\mathrm{Bal}}, m_{\mathrm{s}}\right)\\ &= \left[\left(\left(\frac{\partial \Delta m_{\mathrm{spec}}}{\partial m_{\mathrm{Bal}}}\right)\delta m_{\mathrm{Bal}}\right)^2 + \left(\left(\frac{\partial \Delta m_{\mathrm{spec}}}{\partial m_{\mathrm{s}}}\right)\delta m_{\mathrm{s}}\right)^2\right]^{0.5}.\end{aligned} \tag{4.17c}$$

Here, $V_{\mathrm{sc+s}}$ is the volume of the sample container and the solid and y_i denotes the molar fraction of species i in the fluid gas. Eq. 4.17b is considered for multicomponent adsorption measurements. For pure component mixtures, the term δy_i is excluded.

Therefore, the dependent errors in excess and absolute adsorbed amount were calculated as follows

$$\begin{aligned}\delta q^{\mathrm{exc}} &= f\left(\Delta m_{\mathrm{spec}}, \rho, V_{\mathrm{sc+s}}, m_{\mathrm{s}}\right)\\ &= \left(\frac{\partial q^{\mathrm{exc}}}{\partial \Delta m_{\mathrm{spec}}}\right)\delta \Delta m_{\mathrm{spec}} + \left(\frac{\partial q^{\mathrm{exc}}}{\partial \rho}\right)\delta \rho + \left(\frac{\partial q^{\mathrm{exc}}}{\partial V_{\mathrm{sc+s}}}\right)\delta V_{\mathrm{sc+s}} + \left(\frac{\partial q^{\mathrm{exc}}}{\partial m_{\mathrm{s}}}\right)\delta m_{\mathrm{s}},\end{aligned} \tag{4.18a}$$

Table 4.6. Uncertainties in pure and binary adsorption equilibrium measurements using a magnetic suspension microbalance.

Uncertainty	Value	Reference
Standard deviation of mass reading [mg]	$\pm$ 0.02	Rubotherm Instruments
Standard deviation of mass of the solid [g]	$\pm$ 0.001	Pini, 2014
Standard uncertainty in temperature [K] [a]	$\pm$ 2	—
Accuracy of pressure measurements [%] [a]	$\pm$ 1	—
Accuracy of gas dosing [% FS]	$\pm$ 0.04 [b]	Rubotherm Instruments
Uncertainty in density measurement	$\pm$ (0.02 % + 0.01 kg m^{-3})	Rubotherm Instruments
Uncertainty in micropore volume [cm^3 g^{-1}]	$\pm$ 0.001 [c]	Quantachrome Instruments

[a] The temperature is measured beneath the sample in the measuring cell using a platinum resistance probe (Pt-100). Pressure measurements are also carried out in the measuring cell. The full pressure range of the balance used for single-component measurements is 200 bar. The balance used for multicomponent adsorption is equipped with two sensors: one up to 10 bar and a second up to 40 bar.
[b] Full scale error is considered as 100 ml min^{-1}.
[c] Considering $\pm$ 0.2 % volume accuracy in gas pycnometer and $\pm$ 9 10^{-5} cm^3 volume resolution in mercury porosimeter as obtained from the supplier Quantachrome Instruments.

$$\begin{aligned}\delta q^{\mathrm{abs}} &= f\left(q^{\mathrm{exc}}, \rho, V_{\mathrm{micro}}\right) \\ &= \left(\frac{\partial q^{\mathrm{abs}}}{\partial q^{\mathrm{exc}}}\right)\delta q^{\mathrm{exc}} + \left(\frac{\partial q^{\mathrm{abs}}}{\partial \rho}\right)\delta\rho + \left(\frac{\partial q^{\mathrm{abs}}}{\partial V_{\mathrm{micro}}}\right)\delta V_{\mathrm{micro}}.\end{aligned} \tag{4.18b}$$

Table 4.6 represents the uncertainties in the characteristic data. The accuracy of the gas dosing system and the uncertainty in density measurements were considered only for the multicomponent adsorption equilibrium measurements. The uncertainty for the density measurement over the whole temperature and pressure range of the apparatus was given by Rubotherm GmbH. This followed

$$\frac{\Delta\rho}{\rho} \leq \pm\left[0.02\,\% + 0.01\,\mathrm{kg\,m^{-3}}\right]. \tag{4.19}$$

At very low densities, the relative part of Eq. 4.19 (0.02%) is negligible compared to the absolute part (0.01 kg m^{-3}). The absolute part would, in fact, result in a very high relative error, especially for densities below 10 kg m^{-3} as discussed by Saleh and Wendland (2005).

4.3.2 Analytical Isotherm Model and Data Fit of the Pure- and Multi-Component Data

4.3.2.1 Pure Component Data Fit on AQSOA-Z02

The reported pure CO_2 and N_2 adsorption equilibrium data on AQSOA-Z02 were regressed using the semi-empirical Toth isotherm model. The Toth isotherm was selected since the Toth equation is valid at the low and high ends of the pressure range. This is because the equation agrees with the Henry law at low pressure and has a finite limit when the pressure is sufficiently high (Do, 1998). The Toth equation was governed by

$$q = q_{\mathrm{s}}\frac{b(T)\,f}{\left[1 + \left(b(T)\,f\right)^{a}\right]^{1/a}}, \tag{4.20}$$

where q [mol kg^{-1}] represents the amount adsorbed, q_{s} [mol kg^{-1}] denotes the monolayer adsorption capacity, $b(T)$ [bar^{-1}] and a are the temperature dependent parameters, and

f [kPa] is the fugacity of the adsorbate in the gas phase. The parameters b and a are specific for adsorbate-adsorbent pairs, where the parameter a characterises the system's structural heterogeneity in adsorbent micropores. For $a = 1$ the isotherm reduces to the fundamental Langmuir adsorption isotherm equation and further away from unity the system is supposed to be more heterogeneous (Do, 1998).

The differential adsorption enthalpy (or isosteric heat of adsorption) [kJ mol^{-1}] for pure fluids can be determined by solving the Clausius-Clapeyron relation:

$$-\frac{\Delta\bar{h}}{R_{\mathrm{g}}\,T^2} = \left(\frac{\partial \ln f}{\partial T}\right)_q . \tag{4.21}$$

A temperature-dependent expression for the fugacity f is obtained by inversion of the Toth isotherm and by expressing the heterogeneity constant t and the adsorption affinity b with temperature-dependent correlations. The adsorption affinity b follows the form:

$$b = b_0 \exp\left(\frac{E}{R_{\mathrm{g}}\,T}\right), \tag{4.22}$$

where b_0 [bar^{-1}] is the pre-exponential factor, E [kJ mol^{-1}] is the monolayer heat of adsorption, R_{g} [kJ mol^{-1} K^{-1}] is the universal gas constant, and i refers to the specific pure component isotherm. By letting general the expression for the heterogeneity coefficient t, the following is an expression of the differential enthalpy from Toth isotherm:

$$-\frac{\Delta\bar{h}}{R_{\mathrm{g}}\,T^2} = \frac{E}{R_{\mathrm{g}}\,T^2} + \left(\frac{\mathrm{d}t}{\mathrm{d}T}\right)\left[\frac{1}{t}\left(\frac{\ln\left(\frac{q}{q_{\mathrm{s}}}\right)}{1-\left(\frac{q}{q_{\mathrm{s}}}\right)^t}\right) + \frac{1}{t^2}\ln\left(\left(\frac{q_{\mathrm{s}}}{q}\right)^t - 1\right)\right]. \tag{4.23}$$

When the heterogeneity coefficient t is temperature independent, the differential enthalpy reduces to the monolayer heat of adsorption. The parameters obtained from the regression of single component data, i.e. q_{s}, b_0, E, and t, allow a good approximation of the mixture adsorption equilibria. Even small errors in the single component adsorption isotherm fitting can result in large errors in the description of multicomponent adsorption, especially at the low-coverage pressure range.

4.3.2.2 Pure Component Data Fit on Y-S3-50

The reported pure CO_2 and N_2 adsorption equilibrium data on Y-S3-50 were simply regressed using the fundamental dual-site Langmuir (DSL) isotherm. The DSL equation was governed by

$$q = q_{\mathrm{s}}^{(\mathrm{A})}\frac{b^{(\mathrm{A})}(T)\,f}{1+b^{(\mathrm{A})}(T)\,f} + q_{\mathrm{s}}^{(\mathrm{B})}\frac{b^{(\mathrm{B})}(T)\,f}{1+b^{(\mathrm{B})}(T)\,f}, \tag{4.24}$$

where the superscripts '(A)' and '(B)' denote the two distinct adsorption sites.

The knowledge of the adsorption equilibrium and isosteric heat of adsorption is essential for proper design and operation of any gas-phase adsorption process. The isosteric heat of

adsorption can be estimated from the temperature dependence of the adsorption isotherm. $b(T)$ is given by

$$b = b_0 \exp\left(\frac{-\Delta H}{R_g\, T}\right), \tag{4.25}$$

where, ΔH [kJ mol^{-1}] is the isosteric heat of adsorption at zero fractional loading.

The parameters obtained from the regression of single component data, i.e. $q_s^{(A)}$, $q_s^{(B)}$, $b_0^{(A)}$, $b_0^{(B)}$, $\Delta H^{(A)}$, and $\Delta H^{(A)}$, were used to predict mixture adsorption equilibria.

4.3.2.3 Multi-component Data Fit on AQSOA-Z02

Multi-component adsorption equilibrium data were predicted using ideal adsorbed solution theory (IAST) (Myers and Monson, 2014). The bulk-gas phase was assumed to be non-ideal and therefore, the subsequent system of equations for N_C components was

$$P_{\text{bulk}}\, y_i\, \phi_i = f_i^0\, x_i, \tag{4.26a}$$

$$\psi_i = \int_0^{f_i^0} \frac{n_i^0(f_i)}{f_i} \mathrm{d}f_i, \tag{4.26b}$$

$$1 - \sum_{i=1}^{N_C} x_i = 0, \tag{4.26c}$$

$$\frac{1}{n_t} = \sum_{i=1}^{N_C} \frac{m_i}{n_i^0\,(f_i^0)\; M_{w_i}}. \tag{4.26d}$$

Here, P_{bulk} [bar] denotes the bulk pressure, y_i and x_i are the concentrations of species i in the bulk-gas phase and adsorbed phase respectively, and ϕ_i represents the fugacity coefficient of the ith component. f_i^0 [bar] and n_i^0 [mol kg^{-1}] are the pure component fugacity in the adsorbed phase and the pure amount adsorbed of species i respectively, at the same temperature and reduced grand potential ψ_i [mol kg^{-1}] of the mixture. n_t [mol kg^{-1}] denotes the total amount adsorbed and m_i is the mass fraction of species i in the adsorbed phase.

IAST states that each component in the adsorbed phase has the same reduced grand potential at equilibrium (Santori et al., 2015) and therefore,

$$\psi = \psi_1 = ... = \psi_{N_C}. \tag{4.27}$$

For the case of a binary mixture, the Toth model has an analytical expression for reduced grand potential, but the pure component hypothetical fugacity had to be determined from a numerical method. The Toth expression of reduced grant potential was given by

$$\psi_i = f_i^0\, q_s\, b_i\, {}_2\mathrm{F}_1\left(\frac{1}{a_i}; \frac{1}{a_i}; \left(1 + \frac{1}{a_i}\right); -\left(f_i^0\, b_i\right)^{a_i}\right), \tag{4.28}$$

where ${}_2\mathrm{F}_1$ is the Gauss hyper-geometric function ${}_2\mathrm{F}_1$ (Santori et al., 2014).

4.3.3 Results and Discussion

4.3.3.1 Pure Component Adsorption Equilibria on AQSOA-Z02

Pure CO_2 and N_2 component data on AQSOA-Z02 were measured at (298.15, 323.15, and 348.15) K and pressure ranges from 0.2 bar to 20 bar. All measured and treated CO_2 and N_2 equilibrium data are presented in Tables 4.7 and 4.8. The best fitting parameters of single component data were obtained by performing a weighted fit to the definition of sum of squares due to error (SSE). To apply this method, weights were added to the definition of the sum of residuals divided by the sum of weights to normalise the objecting function as follows

$$f(q_s, b, t) = \frac{\sum_{i=1}^{N_{data}} [w_i \ (q_{exp} - q_{theor}(q_s, b, t))]^2}{\sum_{i=1}^{N_{data}} w_i}, \tag{4.29}$$

where $w_i = \frac{1}{i+1}$ is the ith weighting factor and i = 1, ..., N_{data}. N_{data} denotes the number of pressure steps (observations) at each isotherm. q_{exp} [g g^{-1}] is the ith experimental absolute adsorbed amount and q_{theor} [g g^{-1}] is the ith model-predicted adsorbed amount obtained from the Toth equation. The objective function $f(q_s, b, t)$ was then minimised using the nonlinear Conjugate Gradient model that is available in MathCAD and b_0 and E parameters were calculated from Eq. 4.22.

Table 4.7. Experimental CO_2 adsorption equilibrium data on AQSOA-Z02.

298 K		323 K		348 K	
f [bar]	q_{ads} [mol kg^{-1}]	f [bar]	q_{ads} [mol kg^{-1}]	f [bar]	q_{ads} [mol kg^{-1}]
0.005	0.058	0.200	0.482	0.200	0.220
0.010	0.102	0.579	1.124	0.499	0.542
0.021	0.182	0.996	1.652	0.997	0.992
0.028	0.239	1.492	2.058	1.493	1.366
0.039	0.309	1.985	2.371	1.988	1.600
0.048	0.368	2.966	2.811	2.983	1.994
0.058	0.429	4.915	3.332	4.946	2.511
0.068	0.489	6.842	3.655	6.866	2.856
0.079	0.547	10.546	4.047	10.647	3.306
0.087	0.592	14.152	4.281	14.346	3.563
0.099	0.650	18.501	4.516	18.843	3.855
0.199	1.062				
0.299	1.382				
0.398	1.639				
0.500	1.865				
0.600	2.056				
0.699	2.219				
0.799	2.364				
0.900	2.499				
0.993	2.609				
0.200	1.051				
0.499	1.864				
1.005	2.641				
1.489	3.081				
1.980	3.367				
2.965	3.752				
4.896	4.170				
6.758	4.421				
10.443	4.728				
13.905	4.916				
18.046	5.068				

The regressed parameters of the proposed model for describing pure adsorption isotherms and their estimated uncertainties are presented in Table 4.9. Here, q_s obtained from the

Table 4.8. Experimental N_2 adsorption equilibrium data on AQSOA-Z02.

298 K		323 K		348 K	
f [bar]	q_{ads} [mol kg^{-1}]	f [bar]	q_{ads} [mol kg^{-1}]	f [bar]	q_{ads} [mol kg^{-1}]
0.200	0.066	0.200	0.035	0.200	0.026
0.500	0.138	0.500	0.081	0.510	0.066
1.010	0.245	1.010	0.149	1.000	0.106
1.500	0.341	1.510	0.209	1.500	0.151
2.029	0.441	2.000	0.268	2.021	0.197
2.998	0.610	3.030	0.385	3.021	0.295
4.995	0.863	5.010	0.581	5.003	0.443
7.041	1.092	6.999	0.741	7.036	0.577
11.047	1.432	11.019	1.030	11.034	0.802
15.019	1.690	14.999	1.260	15.036	0.984
19.940	1.910	20.010	1.470	20.060	1.170

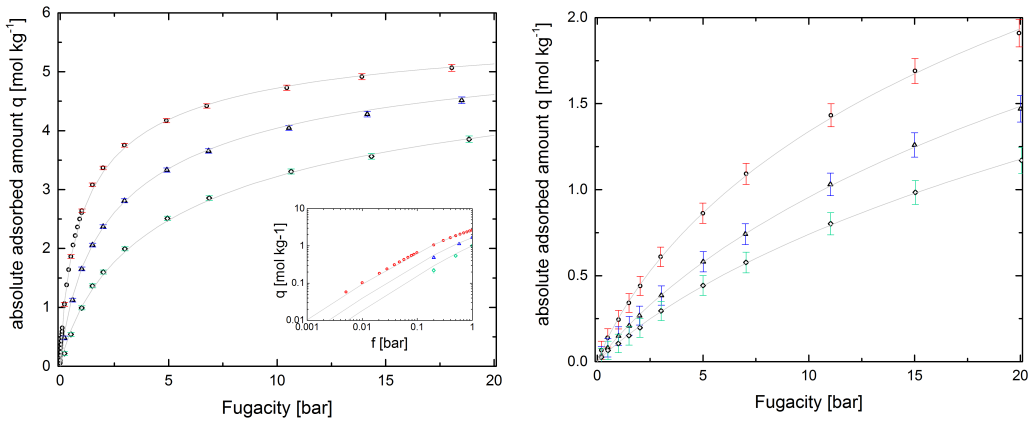

(a) CO_2 **(b)** N_2

Figure 4.10. Single component adsorption equilibrium isotherms of: **(a)** carbon dioxide and **(b)** nitrogen on AQSOA-Z02 at 298.15 K (○), 323.15 K (△), and 348.15 K (◇). The solid lines represent the best fit with the Toth isotherm.

regression of the isotherm of the most strongly adsorbed component, CO_2, at the lowest measured isotherm is kept constant in the regression of not only the other CO_2 isotherms but also all the N_2 isotherms. Rao and Sircar (1999) had demonstrated that the Toth model is thermodynamically consistent for multi-component mixtures only if $q_{s,i} = q_s$. In this study, instead of using the extended Toth model to predict the multi-component adsorption, the IAST has been used. Still, the use of the same saturation capacity of the most strongly adsorbed compound helps the application of the IAST theory that otherwise would be unnecessarily complicated. Also, the trend of the pure N_2 isotherms in the investigated pressure range do not show any asymptotic saturation value. These linear or weakly non-linear isotherms can be regressed with one or two parameters. Every other additional parameter added in the regression is going to provide an overfitting of data.

Experimentally collected adsorption isotherms of carbon dioxide and nitrogen on AQSOA-Z02 were plotted against the Toth equation and are illustrated in Figure 4.10. Solid lines represent the Toth isotherm fitting and symbols illustrate the experimental data for both gases at three different temperatures.

A correct fitting at low-pressure region (Henry region) is essential to describe multi-component data as the integration of reduced grand potential is sensitive to low surface coverage (Myers and Monson, 2014). For this reason, more data for the strongly adsorbed component were measured at low-pressure regions, from 0.005 bar to 1 bar, at 298 K

Table 4.9. Parameters of CO_2 and N_2 pure component data on AQSOA-Z02 regressed with the Toth equation.

Parameter	Unit	298.15 K		323.15 K		348.15 K	
		Value	Uncertainty [a]	Value	Uncertainty [a]	Value	Uncertainty [a]
CO_2							
Saturation capacity, q_s	mol kg^{-1}	6.06	± 0.159	—	± 0.2790	—	± 0.1650
Henry's law constant, K_H	mol kg^{-1} bar^{-1}	10.77	± 0.128	4.09	± 0.0750	1.92	± 0.0420
Heterogeneity constant, t	—	0.62	± 0.018	0.63	± 0.0310	0.63	± 0.0400
Pre-exponential factor, b_0	$\left(10^{-5}\right)$ bar^{-1}	1.06	± 0.078	—	± 0.1160	—	± 0.1430
Monolayer heat of adsorption, E	$(-)$ kJ mol^{-1}	29.78	± 0.182	—	± 0.2950	—	± 0.3950
N_2							
Saturation capacity, q_s	mol kg^{-1}	6.06	± 0.136	—	± 0.1370	—	± 0.2100
Henry's law constant, K_H	mol kg^{-1} bar^{-1}	0.34	± 0.019	0.18	± 0.0001	0.13	± 0.0002
Heterogeneity constant, t	—	0.58	± 0.016	0.62	± 0.0150	0.59	± 0.0200
Pre-exponential factor, b_0	$\left(10^{-5}\right)$ bar^{-1}	6.44	± 0.317	—	± 0.0200	—	± 0.0740
Monolayer heat of adsorption, E	$(-)$ kJ mol^{-1}	16.69	± 0.121	—	± 0.0900	—	± 0.0750

[a] The uncertainty in the fitted parameters values were determined from the Jacobian matrix as described by Bolster and Hornberger (2007) and Smith et al. (1998).

(see Figure 4.10a). Quantachrome IQ was used to obtain accurate measurements at such low-pressure regions and data are presented in Table 4.7. For the application of air capture, data at lower partial pressure could be more beneficial to describe accurately the adsorption equilibrium behaviour of CO_2, which exists at 0.0004 bar, in the adsorption contactor. Although, due to the linear relation between the pressure and adsorbed amount at Henry regions (see Figure 4.10a), it is expected that the parameters obtained from pure component measurements will give a good approximation of the multi-component adsorbed amounts even if the most strongly adsorbed compound exists at such a low pressure.

Figures 4.10a and 4.10b show that the isotherms are described well for all temperatures for all systems. At all pressures, carbon dioxide was the most strongly adsorbed gas. Both carbon dioxide and nitrogen isotherms are type I isotherms indicating adsorption of gases in micropores.

Similar CO_2 and N_2 adsorption isotherms on AQSOA-Z02 were recently reported from Couck et al. (2018) for AQSOA-FAM-Z02 powder. The powder AQSOA-Z02 reported slightly higher CO_2 uptakes, i.e. approximate 5.6 mol kg^{-1} at 303 K and 20 bar pressure. This is slightly higher than the CO_2 uptake on AQSOA-Z02 pellets at the same conditions, which is 5 mol kg^{-1}. N_2 uptakes are instead essentially identical in AQSOA-Z02 powder and pellets.

Table 4.10. Experimental CO_2 adsorption equilibrium data on Y-S3-50.

298 K		323 K		348 K	
f [bar]	q_{ads} [mol kg^{-1}]	f [bar]	q_{ads} [mol kg^{-1}]	f [bar]	q_{ads} [mol kg^{-1}]
0.200	3.624	0.300	2.636	0.200	1.175
0.499	4.695	0.499	3.398	0.499	2.212
0.995	5.288	0.996	4.309	0.997	3.170
1.489	5.549	1.492	4.754	1.493	3.760
1.980	5.944	1.985	5.056	2.087	4.323
2.955	6.160	3.064	5.422	2.974	4.751
4.876	6.430	4.905	5.787	4.927	5.262
6.758	6.577	6.910	6.026	6.952	5.538
11.556	6.824	10.544	6.304	10.646	5.861
18.203	6.954	14.155	6.490	14.343	6.062
		18.418	6.561	18.925	6.289

Table 4.11. Experimental N_2 adsorption equilibrium data on Y-S3-50.

298 K		323 K		348 K	
f [bar]	q_{ads} [mol kg^{-1}]	f [bar]	q_{ads} [mol kg^{-1}]	f [bar]	q_{ads} [mol kg^{-1}]
0.470	0.130	0.470	0.117	0.470	0.110
0.970	0.230	0.970	0.185	0.970	0.183
1.470	0.341	1.470	0.257	1.470	0.220
1.969	0.443	1.970	0.319	1.970	0.272
2.968	0.622	2.970	0.441	2.971	0.367
4.965	0.913	4.970	0.665	4.973	0.523
6.961	1.158	6.969	0.852	6.976	0.670
10.978	1.554	10.999	1.177	11.014	0.955
14.959	1.843	14.991	1.448	15.018	1.183
19.924	2.116	19.989	1.733	20.040	1.462

4.3.3.2 Pure Component Adsorption Equilibria on Y-S3-50

Pure CO_2 and N_2 component data on Y-S3-50 were measured at (298.15, 323.15, and 348.15) K and pressure ranges from 0.2 bar to 20 bar. All measured and treated CO_2 and N_2 equilibrium data are presented in Tables 4.10 and 4.11. The best fitting parameters of

Table 4.12. Parameters of CO_2 and N_2 pure component data on Y-S3-50 regressed with the dual-site Langmuir equation.

Gas	$q_s^{(A)}$ [mol kg^{-1}]	$b_0^{(A)}$ [bar^{-1}]	$\Delta H^{(A)}$ [kJ mol^{-1}]	$q_s^{(B)}$ [mol kg^{-1}]	$b_0^{(B)}$ [bar^{-1}]	$\Delta H^{(B)}$ [kJ mol^{-1}]
CO_2	5.10	$1.084\ 10^{-5}$	– 34.14	2.10	$1.780\ 10^{-5}$	– 24.98
N_2	5.10	$2.320\ 10^{-5}$	– 14.53	2.10	$1.048\ 10^{-3}$	– 11.40

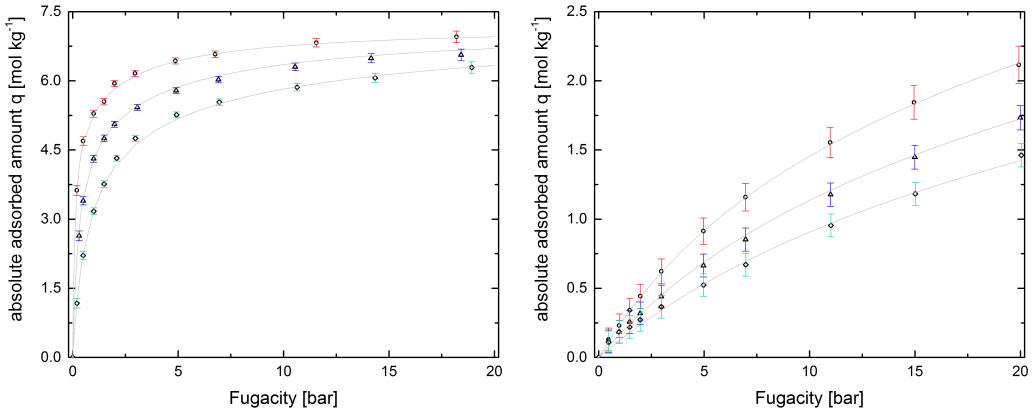

(a) CO_2 **(b)** N_2

Figure 4.11. Single component adsorption equilibrium isotherms of: **(a)** carbon dioxide and **(b)** nitrogen on Y-S3-50 at 298.15 K (○), 323.15 K (△), and 348.15 K (◇). The solid lines represent the best fit with the dual-site Langmuir isotherm.

single component data were obtained by the Dual-site Langmuir equation and b_0 and ΔH parameters were calculated from Eqs. 4.24 and 4.25.

The regressed parameters of the proposed model for describing pure adsorption isotherms and their estimated uncertainties are presented in Table 4.12.

Experimentally collected adsorption isotherms of carbon dioxide and nitrogen on Y-S3-50 were plotted against the DSL equation and are illustrated in Figure 4.11. Solid lines represent the DSL isotherm fitting and symbols illustrate the experimental data for both gases at three different temperatures.

At all pressures, carbon dioxide was the most strongly adsorbed gas. Both carbon dioxide and nitrogen isotherms are type I isotherms indicating adsorption of gases in micropores.

4.3.3.3 Binary Mixture Adsorption Equilibria on AQSOA-Z02

In order to characterise the co-adsorption behaviour of CO_2/N_2, binary adsorption equilibrium gravimetric experiments of CO_2/N_2 were carried out. Experiments for the co-adsorption of CO_2/N_2 mixtures of: *(i)* 15 mol% CO_2 and 85 mol% N_2, *(ii)* 50 mol% CO_2 and 50 mol% N_2, and *(iii)* 80 mol% CO_2 and 20 mol% N_2 on AQSOA-Z02 were performed at temperatures from 295 K to 348 K and pressure ranges from the lowest available pressure allowed from the experimental apparatus 1.5–2 bar up to 20 bar. Balance reading in [g], pressure in [bar], temperature in [K], and density in [g cm^{-3}] are listed in Table 4.13 along with all measured and treated binary data. Predicted results were obtained from the IAST model using the parameters obtained from the single component measurements. Figures 4.12a, 4.12b and

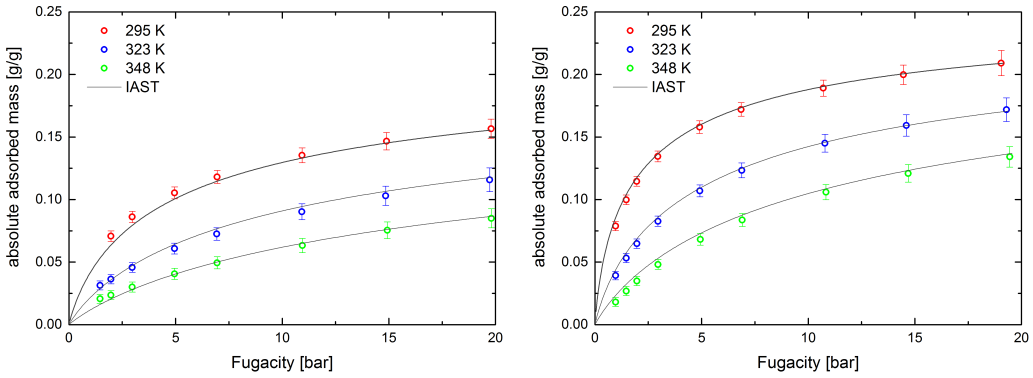

(a) 15 mol% CO_2 and 85 mol% N_2 **(b)** 50 mol% CO_2 and 50 mol% N_2

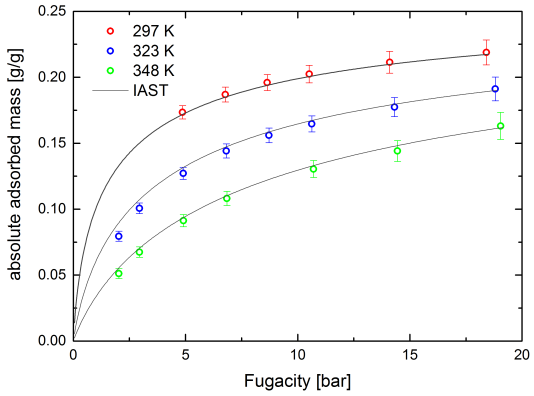

(c) 80 mol% CO_2 and 20 mol% N_2

Figure 4.12. Predicted (lines) and experimental (symbols) binary adsorption equilibria of CO_2 and N_2 mixtures: **(a)** 15 mol% CO_2 and 85 mol% N_2, **(b)** 50 mol% CO_2 and 50 mol% N_2, and **(c)** 80 mol% CO_2 and 20 mol% N_2 on AQSOA-Z02 at 295 K (red symbol), 323 K (blue symbol) and 348 K (green symbol)). Errors were calculated according to Table 4.6.

4.12c illustrate the measured and predicted binary adsorption isotherms at temperatures of (295 to 348) K.

As expected from the single component results, CO_2 was the strongly adsorbed component. Therefore, the measured CO_2/N_2 equilibrium compositions were shifted towards higher values as the feed was enriched in CO_2. In addition, the capacities for binary CO_2 adsorption were lower than for pure CO_2. For the sake of simplicity, the CO_2 concentration in the feed stream was plotted against the predicted CO_2 concentration in the adsorbed phase (as obtained from the IAST model) at 323 K and 348 K and is illustrated in Figure 4.13. According to Figure 4.13, even at very low CO_2 concentrations of the CO_2/N_2 mixture, the concentration of CO_2 in the adsorbed phase is expected to be high. For instance, a 5% CO_2 feed stream may give a >60% concentrated CO_2 in the adsorbed phase at temperatures below 323 K.

Figure 4.14 shows the relative error ($RE\%$) in the measured absolute adsorbed amount of the CO_2/N_2 mixture on AQSOA-Z02, which was defined as

$$RE\% = \left(\frac{q_{\text{exp}} - q_{\text{theor}}}{q_{\text{exp}}}\right) 100. \tag{4.30}$$

Table 4.13. Experimental binary mixture of mol% CO_2 and mol% N_2 adsorption equilibrium data on AQSOA-Z02.

15 % CO_2 – 85 % N_2 mixture				**50 % CO_2 – 50 % N_2 mixture**				**80 % CO_2 – 20 % N_2 mixture**			
T [K]	f [bar]	ρ_{exp} [g cm^{-3}]	q_{abs} [g g^{-1}]	T [K]	f [bar]	ρ_{exp} [g cm^{-3}]	q_{abs} [g g^{-1}]	T [K]	f [bar]	ρ_{exp} [g cm^{-3}]	q_{abs} [g g^{-1}]
295	1.97	0.0024	0.071	295	1.47	0.0021	0.100	297	4.87	0.0081	0.173
295	2.97	0.0037	0.086	295	1.96	0.0028	0.115	297	6.78	0.0116	0.187
295	4.94	0.0061	0.105	295	2.94	0.0043	0.134	297	8.65	0.0150	0.196
295	6.92	0.0086	0.118	295	4.91	0.0072	0.158	297	10.51	0.0186	0.202
295	10.87	0.0135	0.135	295	6.85	0.0101	0.172	297	14.10	0.0258	0.211
295	14.78	0.0184	0.147	295	10.71	0.0161	0.189	297	18.41	0.0351	0.219
295	19.61	0.0246	0.157	295	14.46	0.0222	0.200				
				295	19.05	0.0299	0.209				
323	1.97	0.0022	0.036	323	1.47	0.0019	0.053	323	2.03	0.0029	0.079
323	2.97	0.0033	0.046	323	1.96	0.0025	0.065	323	2.94	0.0043	0.101
323	4.95	0.0055	0.061	323	2.96	0.0039	0.083	323	4.90	0.0073	0.127
323	6.93	0.0078	0.073	323	4.92	0.0065	0.107	323	6.82	0.0104	0.144
323	10.92	0.0122	0.090	323	6.88	0.0092	0.123	323	8.72	0.0136	0.156
323	14.85	0.0167	0.103	323	10.78	0.0146	0.145	323	10.63	0.0168	0.165
323	19.73	0.0223	0.116	323	14.60	0.0201	0.159	323	14.31	0.0233	0.177
				323	19.29	0.0271	0.172	323	18.81	0.0316	0.191
348	1.97	0.0021	0.024	348	1.47	0.0017	0.027	348	2.03	0.0027	0.051
348	2.97	0.0031	0.030	348	1.97	0.0023	0.035	348	2.95	0.0040	0.067
348	4.96	0.0052	0.041	348	2.96	0.0035	0.048	348	4.91	0.0068	0.091
348	6.95	0.0073	0.049	348	4.94	0.0060	0.068	348	6.84	0.0097	0.108
348	10.95	0.0114	0.063	348	6.90	0.0085	0.084	348	10.71	0.0155	0.130
348	14.93	0.0156	0.075	348	10.83	0.0136	0.106	348	14.45	0.0213	0.144
348	19.81	0.0208	0.085	348	14.69	0.0185	0.121	348	19.05	0.0289	0.163
				348	19.45	0.0248	0.134				

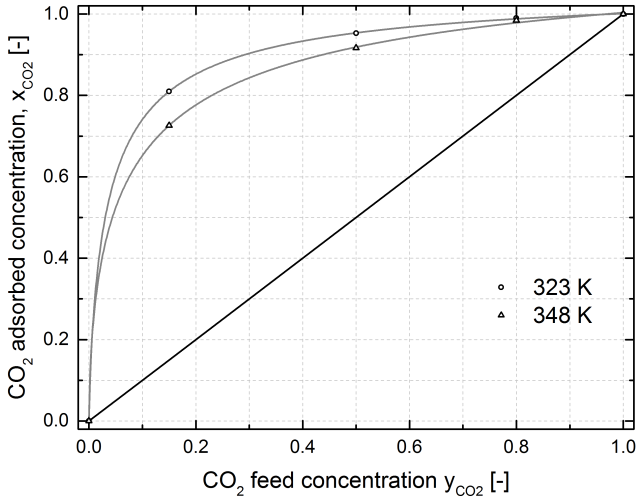

Figure 4.13. CO_2 concentration in the gas phase (y_{CO_2}) against the predicted CO_2 concentration in the adsorbed phase (x_{CO_2}) and the predicted selectivity of CO_2 over N_2 (red y-axis and red data points) on AQSOA-Z02 at (323 and 348) K.

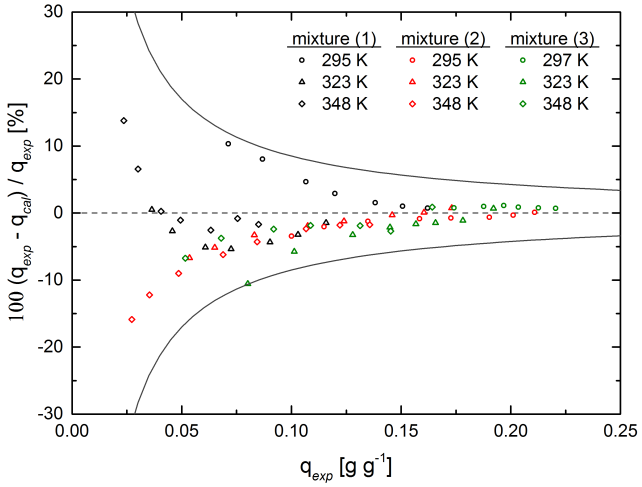

Figure 4.14. Percent differences between the experimental absolute adsorbed amount and estimated values from IAST: —, estimated uncertainties in the current measurements; •, mixture (1): 15 mol% CO_2 and 85 mol% N_2; •, mixture (2): 50 mol% CO_2 and 50 mol% N_2; and •, mixture (3): 80 mol% CO_2 and 20 mol% N_2.

The average relative error ($ARE\%$) in the measured absolute adsorbed amount was described by

$$ARE\% = \frac{100}{N_{\text{data}}} \sum_{i=1}^{N_{\text{data}}} \frac{q_{\text{exp}} - q_{\text{theor}}}{q_{\text{exp}}}, \tag{4.31}$$

where the subscripts 'exp' and 'theor' denote the experimental and the estimated values, respectively. The density of the mixture at each measured pressure step and temperature was also obtained theoretically by means of REFPROP (Lemmon et al., 2013) to provide a comparison with the experimental data. The $RE\%$ in density measurements followed Eq. 4.30 and the results are illustrated in Figure 4.15. Figure 4.15 also shows the estimated uncertainty in the density measurements, which was found to be $\pm(1.5\%+0.21$ kg m$^{-3})$. The maximum $RE\%$ in density was obtained at lower pressures. The deviation in density measurements is mainly due to the uncertainty in pressure, temperature, molar composition,

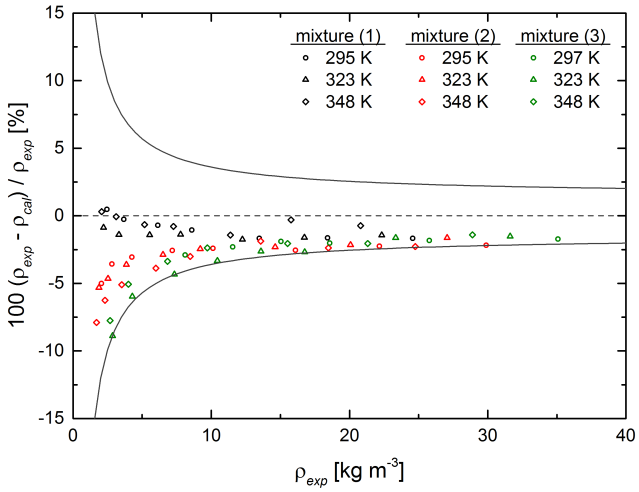

Figure 4.15. Percent differences between the experimental density and estimated values from REFPROP: —, estimated uncertainties in the current measurements; •, mixture (1): 15 mol% CO_2 and 85 mol% N_2; •, mixture (2): 50 mol% CO_2 and 50 mol% N_2; and •, mixture (3): 80 mol% CO_2 and 20 mol% N_2.

and mass and volume measurements of the sinker and the adsorbent. Minor errors, like the force transmission error caused by the magnetic behaviour of the cell, the suspension coupling, and the measured fluid, as it had been highlighted by Cristancho et al. (2010) and Atilhan et al. (2010), were not taken into consideration in this study.

Since the fit quality of the pure component isotherms is reasonable, as a <2% $RE\%$ at each measured point was obtained, the discrepancy between the measured and predicted absolute adsorbed amounts (Figure 4.14) can be explained by the deviation in density measurements (Figure 4.15). The absolute part of the estimated uncertainty in the density measurements (0.21 kg m^{-3}) explains the higher percent differences at lower density levels.

The $ARE\%$ in the measured amount adsorbed was <4% for each tested CO_2/N_2 mixture at each reported temperature. The estimated uncertainty in the absolute adsorbent amount was found to be $\pm$0.0085 g g^{-1} as illustrated in Figure 4.14. Therefore, the adsorption data of mixtures can be reasonable described over the entire composition range using the IAST model.

Adsorption selectivity is one of the most important parameters for separation applications. Equilibrium selectivity of CO_2 over N_2 was defined from

$$S_{\mathrm{CO_2/N_2}} = \frac{x_{\mathrm{CO_2}}/x_{\mathrm{N_2}}}{y_{\mathrm{CO_2}}/y_{\mathrm{N_2}}}. \tag{4.32}$$

Selectivity values are listed in Table 4.14. Selectivity increased with the CO_2 concentration in the feed stream and a reduction in temperature. Accordingly, the highest estimated selectivity was achieved at the 80 mol% CO_2 and 20 mol% N_2 mixture and the lowest reported temperature. Table 4.15 compares also the selectivity of AQSOA-Z02 with that obtained from Y-S3-50 and zeolite 13X based on their pure component adsorption data. Still, zeolite 13X is expected to have a higher performance in air capture applications due to higher selectivities. As previously observed, a higher selectivity in the present air capture process leads to a better performance of the compression and purification train and subsequently

Table 4.14. Estimated binary mixture of CO_2 and N_2 adsorption equilibrium data on AQSOA-Z02 using IAST.

Mixture	T [K]	q_{CO_2} [mmol g^{-1}]	q_{N_2} [mmol g^{-1}]	x_{CO_2} [a]	q_{tot} [g g^{-1}] [b]	Selectivity
15 mol% CO_2 – 85 mol% N_2	295	0.922	0.137	0.870	0.044	38
	323	0.430	0.101	0.809	0.022	24
	348	0.218	0.083	0.725	0.012	15
50 mol% CO_2 – 50 mol% N_2	295	1.929	0.049	0.975	0.086	39
	323	1.103	0.044	0.962	0.050	25
	348	0.578	0.041	0.934	0.026	14
80 mol% CO_2 – 20 mol% N_2	297	2.217	0.016	0.993	0.098	138
	323	1.462	0.015	0.990	0.065	97
	348	0.864	0.014	0.984	0.038	61

[a] Denotes the molar fraction of CO_2 in the adsorbed phase.
[b] Denotes the total absolute adsorbed amount of the mixture.

Table 4.15. Estimated binary mixture of CO_2 and N_2 adsorption equilibrium data on AQSOA-Z02 using IAST.

Material	T [K]	q_s [mol kg^{-1}]	Selectivity [a]
AQSOA-Z02	298	5.1	32
	348	5.1	12
Y-S3-50	298	7.2	96
	348	7.2	27
Zeolite 13X	298	4.0	361
	353	4.0	130
NaETS-4 [b]	298	3.5	1151
	353	3.5	286

[a] The selectivity is calculated based on the pure-component adsorption measurements. Therefore, it is governed by: $\left(S_{A/B} = \frac{b_A}{b_B}\right)_{T_i}$. Here, T_i is equal to 298 K and 358 K or 353 K.
[b] Pure component adsorption data was measured by Pillai et al. (2008).

higher amounts of CO_2 in the storage bed. NaETS-4, a zeolite type titanosilicate with adsorptive parameters as presented in Table 4.15 and by Pillai et al. (2008), is expected to have a higher performance than zeolite 13X due to the high selectivity of CO_2 over N_2 at low temperatures and high ratio between the selectivity at low temperature and the selectivity at high temperature.

4.4 Conclusions

In general, by setting the bed void fractions, ϵ_b, pellet void fraction, ϵ_p, and crystal density, ρ_{cry}, as variables and investigated their contribution to the process energy and purity, a great improvement of the process purity can by achieved. A great improvement on the energy consumption of the process can be achieved by adiabatic blowdown in Bed 1 as most of the undesired gas is removed and is not discharged in the compression and purification train. Thus, less energy, and subsequently a fewer number of runs, are needed to reach the required level of purity.

In general, the contribution of the void fraction of the beds is the stronger parameter affecting the process final purity, energy use, pressure, and recovery. Specifically, the void fraction of the storage bed, Bed 5, has the highest contribution to the product final purity and pressure; however, the void fraction of Bed 2–(N_B–1) has the greatest effect on the energy use and recovery. This gives a degree of flexibility in the void fraction of Bed 1 that, as has been previously explained, has to be high in order to eliminate pressure drops.

Table 4.16. Adsorptive and physical parameters of AQSOA-Z02 and zeolite 13X adsorbents.

Material Parameters	Unit	Value		Zeolite 13X Reference
		AQSOA-Z02	Zeolite 13X	
Pellet void fraction, ϵ_{p}	—	0.3	0.2	Hu et al. (2014)
Crystal density, ρ_{cry}	kg m^{-3}	1544	1500	Oreggioni et al. (2015)
Adsorption capacity, q_{s}	kg m^{-3}	5.1 [a]	4.0	Oreggioni et al. (2015)
CO_2 adsorption constant, b_0	$\left(10^{-7}\right)$ kPa^{-1}	63.42 [a]	3.76 [b]	—
N_2 adsorption constant, b_0	$\left(10^{-7}\right)$ kPa^{-1}	16.82 [a]	9.74 [b]	—
CO_2 heat of adsorption, ΔH	$(-)$ kJ mol^{-1}	29.95 [a]	31.86 [b]	—
N_2 heat of adsorption, ΔH	$(-)$ kJ mol^{-1}	13.21 [a]	14.92 [b]	—

[a] Data regressed using the single Langmuir equation.
[b] Data obtained from Xiao et al. (2008) and regressed using the linear form of Langmuir isotherm (see Appendix B.1).

Note: These parameters were used to compare the use of AQSOA-Z02 and zeolite 13X in the benchmark process as described in Section 3.4, Chapter 3. The process parameters and operational conditions are also presented there.

A greater $\varepsilon_{\mathrm{b},1}$>0.8 will result in higher purities. Values of $\varepsilon_{\mathrm{storage\,bed}}$ $\leq$0.2, lead to significantly high purities and greater product pressures. Low bed void fractions in Beds 2–(N_{B}–1) can reduce the energy consumption of the process, enhance the recovery, and contribute slightly to higher purities. Values of ε_{p} from 0.3 to 0.6 lead to increased final pressures in the storage bed. Finally, higher values of crystal density, >1000 kg m^{-3}, may lead to higher pressures and recoveries. colorredFor instance, zeotype adsorbent AQSOA-Z02 with ε_{p}=0.3 and ρ_{cry}=1544 kg m^{-3} [7] could be an ideal candidate for the present air capture process.

Table 4.16 compares the adsorptive and physical properties of AQSOA-Z02 with those of zeolite 13X. If AQSOA-Z02 is used in the benchmark case as studied in Section 3.4, Chapter 3, and if the process parameters and operational conditions are similar to those presented in Table 3.5 (Section 3.4), the resulting molar fractions, pressure, thermal energy, and moles of CO_2 in the storage bed at each cycle of the process are illustrated in Figure 4.16.

Due to the very low selectivity of AQSOA-Z02, the performance of the compression and purification train is much lower compared to that obtained from the use of zeolite 13X. Therefore, the final purity in the storage bed is much lower (Figure 4.16a) so as the amount of stored CO_2 (Figure 4.16b). However, due to the higher adsorption capacity of the material, a higher pressure is reached at the end of the 60th cycle. The higher adsorption capacity has also a similar effect on the thermal energy consumption. Figure 4.16b shows that a higher thermal energy is needed in case of the use of AQSOA-Z02 since a higher total number of moles is moved from bed to bed.

Pure component adsorption and co-adsorption equilibria measurements have been carried out for CO_2, N_2 and their mixtures on AQSOA-Z02 using a gravimetric apparatus. Single gas isotherms were obtained at pressures between 0.2 bar and 20 bar at (298, 323, and 348) K and were regressed with the Toth isotherm model. CO_2 was found to be the most strongly adsorbed compound with a reported adsorption capacity of 6.1 mmol g^{-1}.

Binary adsorption equilibria measurements were performed at pressures from 1.5 bar to 20 bar for different gas compositions at different temperatures. The IAST model in

[7] The crystal density is defined as
$\rho_{\mathrm{cry}} = \frac{\rho_{\mathrm{p}}}{1-\epsilon_{\mathrm{p}}}$,
where
$\epsilon_{\mathrm{p}} = \frac{V_{\mathrm{micro}}}{V_{\mathrm{p}}}$.
Both parameters can be calculated using data of Table 4.5.

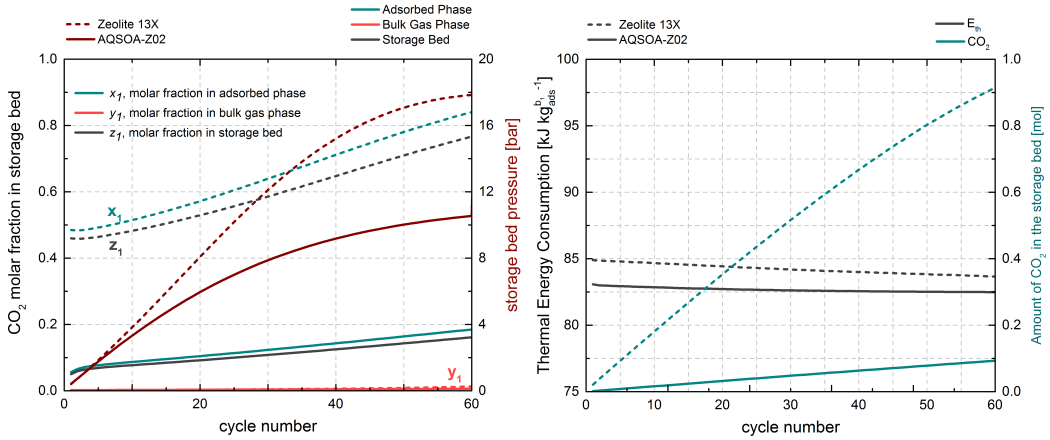

(a) $P - x_1 - y_1 - z_1$ **(b)** $E_{\text{th}} - mol\text{CO}_2$

Figure 4.16. **(a)** Storage bed pressure (dark red curves), global concentration of CO_2 (gray curves), concentration of CO_2 in the bulk-gas phase (red curves) and adsorbed phase (green curves) of Bed 4 at each cycle and **(b)** thermal energy consumption (gray curves) and moles stored in Bed 4 (green curves) for the case of zeolite 13X or AQSOA-Z02 as the adsorbent material in the present air capture process.

conjunction with the Toth equation was used to predict the adsorbed amount of each gas in the CO_2/N_2 mixture and to characterise the co-adsorption behaviour of the mixture. Results showed preferential adsorption of carbon dioxide over nitrogen even at lower concentrations of CO_2. The adsorption loadings for binary CO_2 were lower than for pure CO_2, which indicates that CO_2 and N_2 adsorbed competitively for the concentration range investigated.

The predictions of binary equilibria with IAST model showed a relatively good agreement with the experimental data giving a <4% $ARE\%$ in the measured absolute adsorbed amounts. The discrepancy between experimental and predicted adsorption equilibrium data at low pressure regions had been explained through the analysis of the uncertainties in the measurements.

Pure adsorption measurements have also been carried out for CO_2 and N_2 on Y-S3-50 using the same gravimetric apparatus. Single gas isotherms were obtained at pressures between 0.2 bar and 20 bar at (298, 323 and 348) K and were regressed with the dual-Langmuir model. CO_2 was found to be the most strongly adsorbed compound with a reported adsorption capacity of 7.2 mmol g^{-1}, higher than that obtained by AQSOA-Z02.

Since Y-S3-50 has a high adsorption capacity and selectivity of CO_2 over N_2, it can be more promising than AQSOA-Z02 for the application of DAC. A recent study on Y-S3-50 have shown that the water uptake of the material do not follow the type III isotherm as AQSOA-Z02 (Bonaccorsi et al., 2017). Thus, more research is still needed in order to design a suitable physisorbent with high CO_2 uptake over H_2O.

Physical adsorption is a rapid procedure and its rate is controlled by mass transfer resistances rather than by the intrinsic rate of equilibration at the active surface (Wilcox et al., 2014). Therefore, the design of an optimal coupled material and adsorption process requires an accurate description of the mass transfer between the fluid and the porous adsorbent particles. The next chapter aims to address these issues.

5 Dynamic Investigation of the Process: Adsorption Rate and Scaling Up Performance

> *According to the kinetic theory of gases, the mean kinetic energy of a molecule is a measure of absolute temperature.*
>
> — **Wilhelm Wien**
> German Physicist

Besides the adsorption equilibria, to properly design an adsorption process and improve and optimise its overall performance, the overall packed-bed system dynamics including the intrinsic sorption kinetic behaviour of a single particle, axial dispersion, and mass and heat transfer resistances are required (Ruthven, 1984). The overall adsorption rate is limited by the ability of adsorbate molecules to diffuse inside the particle interior and by the heating and cooling rate in temperature swing adsorption systems (Do, 1998). This chapter focuses on addressing the process non-equilibrium and its influence on the adsorption rate and consequently on the overall process performance.

5.1 Introduction to Adsorption Kinetics

The rate of physical adsorption can be controlled by diffusion limitation rather than the actual rate of equilibration at a surface. Many commercial adsorbents consist of small microporous crystals formed into a macroporous pellet, known as composite adsorbent particles, for example zeolite crystals. In a composite adsorbent, as illustrated in Figure 5.1, there are three distinct resistances to mass transfer: *(i)* external fluid film resistance, *(ii)* macropore diffusion, and *(iii)* micropore diffusion. The relative importance of macropore and micropore resistances depends on the ratio of the diffusional time constant, which varies widely depending on the system parameters and operating conditions (Ruthven, 1984). Since the diffusional time constant depends on the square of the particle radius, the variations of the particle size can provide a simple and straightforward experimental test in order to identify the nature of the controlling resistance (Ruthven, 1984).

Since there are different diffusion mechanisms in the particle, one of them or a combination of them can control the uptake. The following cases may be present:

(i) Micropore diffusion: becomes relevant when the diffusion into the particle interior through the large void between the microparticles (macropores and mesopores) is very fast. Generally, this exists when the pellet size is small, the temperature is low, and the bulk concentration is high.

(ii) Macropore diffusion: becomes relevant when the diffusion into the microparticle is fast and hence, the uptake is controlled by the ability of the molecules to diffuse through

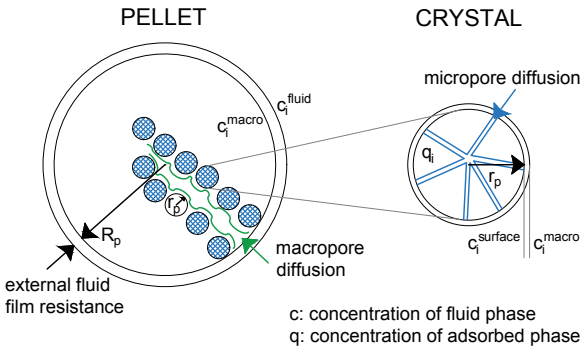

Figure 5.1. The three principal resistances to mass transfer in a composite adsorbent pellet. Abbreviations: r_p, microparticle radius; and R_p, particle radius.

the macropores and mesopores. Generally, this happens when the pellet size is large, the temperature is high, and the bulk concentration is low.

(iii) Macropore-micropore diffusion: becomes relevant when both macropore and micropore diffusions control the uptake, known as bimodal diffusion.

In the case of macropores and mesopores adsorbents, there are four distinguishable mechanisms that contribute to the mass transfer. These mechanisms are (Ruthven et al., 1994):

(i) Bulk or molecular diffusion: is dominant when the pore diameter is larger than the mean free path of the molecules (the distance that a molecule can travel without having collisions with other molecules or with the wall of the pores).

(ii) Knudsen diffusion: becomes relevant at low pressure in small pores when the molecular mean free path is equal to or greater than the pore diameter. This means that the flow is induced by collision between the diffusive molecule and the pore wall.

(iii) Poiseuille diffusion: is related to the flux from forced flow. Since Poiseuille diffusion is defined by $D_{\mathrm{v},i} = \frac{P\, r_{\mathrm{p}}^2}{8\,\eta_i}$, it becomes significant only in relatively large pores and at relatively high pressures. Here, η_i [kPa s] represents the viscosity of the ith component in the fluid.

(iv) Surface diffusion: contributes when the adsorbed phase is sufficiently mobile and the concentration sufficiently high. Surface diffusion is in parallel with the flux from Knudsen, Poiseuilli, and molecular diffusion and is therefore directly additive.

Diffusion in micropores is the diffusion in pores of dimensions comparable with the diameters of the diffusing molecules. The proper description for the driving force of diffusion in composite adsorbents is the chemical potential gradient of adsorbent species. The constitute flux equation (Fickian law equation) relates the flux and the concentration gradient inside a micro-particle. The flux can be written in terms of the chemical potential gradient J_μ [mol m^{-2} s^{-1}] as

$$J_\mu = -L_{\mathrm{m}}\, q_\mu\, \frac{\partial \mu}{\partial z}, \tag{5.1}$$

where L_{m} [mol m^2 J^{-1} s^{-1}] is the mobility coefficient of a molecule, which is temperature dependent, q_μ [mol m^{-3}] is the concentration of the species in the crystal, which is defined as moles per unit volume of the crystal, μ [J mol^{-1}] is the chemical potential of the adsorbed

phase, and z [m] is the axial coordinate, which in this case is the radial distance for the crystal.

If we assume the existence of a hypothetical system in which a gas phase and an adsorbed phase exist within a crystal and are also at equilibrium state, then the adsorbed phase chemical potential is the same as the gas phase chemical potential such that

$$\mu = \mu_{\mathrm{G}} = \mu^0 + R_{\mathrm{g}}\, T \ln p, \tag{5.2}$$

where μ^0 [kJ mol^{-1}] is the reference potential, which depends only on T and p. p is the hypothetical partial pressure, which is in equilibrium with the adsorbed concentration q_μ. The term is hypothetical because there is no gas phase within a crystal. Therefore, from Eqs. 5.1 and 5.2

$$J_\mu = -\left(L_{\mathrm{m}}\, R_{\mathrm{g}}\, T\right)\, q_\mu\, \frac{\partial \ln p}{\partial z} = -\left(L_{\mathrm{m}}\, R_{\mathrm{g}}\, T\right)\, \frac{\partial \ln p}{\partial \ln q_\mu}\, \frac{\partial\, q_\mu}{\partial z}. \tag{5.3}$$

If we define the corrected diffusivity D^0_μ [m^2 s^{-1}] as

$$D^0_\mu = L_{\mathrm{m}}\, R_{\mathrm{g}}\, T, \tag{5.4}$$

which is temperature dependent, then the constitutive flux Eq. 5.3 becomes

$$J_\mu = -D^0_\mu\, \frac{\partial \ln p}{\partial \ln q_\mu}\, \frac{\partial\, q_\mu}{\partial z} = -D_\mu\, \frac{\partial q_\mu}{\partial z}. \tag{5.5}$$

Here, D_μ [m^2 s^{-1}] is called the transport diffusivity (or else the Fickian diffusivity) and is referred as Darken's relation. The term $\frac{\partial \ln p}{\partial \ln q_\mu}$ is known as the thermodynamic correction factor. This factor describes the thermodynamic equilibrium between the two phases. When the isotherm is linear, the thermodynamic correction factor is unity. Thus, the transport diffusivity becomes independent of concentration, which means that the corrected diffusivity is the transport diffusivity at zero loading conditions, as described by Do (1998).

If the isotherm takes the form of the Langmuir equation, the thermodynamic correction factor becomes

$$\frac{\partial \ln p}{\partial \ln q_\mu} = \frac{1}{1 - q_\mu / q_{\mu \mathrm{s}}}. \tag{5.6}$$

Therefore, the transport diffusivity increases as the loading inside the crystal increases.

As mentioned earlier, the corrected diffusivity is temperature dependent and thus, it takes the following form of Arrhenius equation

$$D^0_\mu = D^0_{\mu\infty} \exp\left(-\frac{E_\mu}{R_{\mathrm{g}}\, T}\right), \tag{5.7}$$

where $D^0_{\mu,\infty}$ [m^2 s^{-1}] is the corrected diffusivity at infinite temperature and E_μ [kJ mol^{-1}] denotes the adsorption activation energy or else the energy barrier of the hopping process[1], which is usually less than the heat of adsorption.

[1] The hopping process can be defined as the diffusion process of a molecule within the micro-particle, in which the molecule diffuses from one low energy position to the next low energy position (Do, 1998).

The concentration distribution of the adsorbed species in a micro-particle of different geometry, such as a slab, a cylinder or a spherical geometry, is described by

$$\begin{aligned}\frac{\partial q_\mu}{\partial t} &= -\frac{1}{z^s}\frac{\partial}{\partial z}\left(z^s\, J_\mu\right)\\ &= \frac{1}{z^s}\frac{\partial}{\partial z}\left(z^s\, D_\mu^0\,\frac{\partial \ln p}{\partial \ln q_\mu}\frac{\partial q_\mu}{\partial z}\right)\\ &= \frac{1}{z^s}\frac{\partial}{\partial z}\left(z^s\, D_\mu^0\,\frac{1}{1-q_\mu/q_{\mu\mathrm{s}}}\frac{\partial q_\mu}{\partial z}\right),\end{aligned} \tag{5.8}$$

where the superscript 's' denotes the particle shape factor.

The crystal is assumed to be initially loaded with an amount that is in equilibrium with the gas phase pressure, p_i. Thus, Eq. 5.8 is subject to the following initial and boundary conditions

$$\textit{initial conditions}: \qquad t = 0; \qquad q_\mu = q_{\mu i} = q_{\mu\mathrm{s}}\,\frac{b\,p_i}{1+b\,p_i}, \tag{5.9}$$

$$\textit{boundary conditions}: \qquad z = 0; \qquad \frac{\partial q_\mu}{\partial z} = 0, \tag{5.10}$$

$$z = L^s; \qquad q_\mu = q_{\mu\mathrm{b}} = q_{\mu\mathrm{s}}\,\frac{b\,p_\mathrm{b}}{1+b\,p_\mathrm{b}}, \tag{5.11}$$

where L^s [m] is half the length of the slab crystal or the radius of the cylindrical and spherical crystals. The first boundary condition ($z = 0$) is the symmetric condition at the center of the micro-particle, and the second boundary condition ($z = L^s$) is the equilibrium condition at the exterior surface of the micro-particle, where the gas phase pressure is maintained at p_b.

Since adsorption is exothermic, when sorption is taking place there is, in general, a temperature difference between the fluid phase and the adsorbent particle. Whether or not this temperature difference is significant depends on the relative rates of mass and heat transfer. Thus, the crystal temperature increase (or decrease in the case of desorption) depends on the rate of heat release due to adsorption (or heat absorption due to desorption) and the dissipation rate of energy to the surroundings. The temperature within the particle can be assumed to be uniform, since the thermal conductivity of the micro-particle is greater that that of the fluid phase, and all the heat transfer resistance occurs in the gas film surrounding the micro-particle. In the case of a non-isothermal system, the solution of the mass balance equation is not enough to study the effects of heat transfer on the uptake behaviour. Thus, the heat balance of the system is also required.

5.2 Kinetic Considerations of Air Capture I: Mass, Energy, and Momentum Balances

The performance of the DAC process is expected to be influenced by various mass, heat, and momentum transfer processes. Examples of these include finite rates of gas-solid mass and heat transfer, existence of axial mass and heat dispersion in the gas phase inside the adsorbers, and pressure drop. Thus, the overall dynamic model for the DAC process is predicted by the simultaneous solution of a set of coupled nonlinear partial differential equations (PDEs) representing material, energy, and momentum balances over a packed bed

with the appropriate boundary and initial conditions (Hwang et al., 1995). For the sake of simplicity, the feed is considered as a binary mixture of a more adsorbable species (CO_2) and a less adsorbable species (N_2) throughout this work. Besides, the adsorbent is assumed to be a composite adsorbent with inter-crystalline structure, i.e. zeolite 13X, and therefore, two equations are necessary to describe the mass balance inside the particle and inside the crystal.

5.2.1 Assumptions for DAC Process

The mass transfer resistance into a zeolite pellet is generally controlled by the Knudsen diffusion of the gas into the macropores and the Fickian diffusion of the gas into the micropores (Vemula et al., 2017). Often macropore diffusion is the controlling mechanism due to the combined effect of small crystals in relatively large beads and the large value of the effective bead Henry law constant. Giesy et al. (2012) and Hu et al. (2014) studied the transport of pure CO_2 and 10% CO_2, respectively, in beads of zeolite 13X at pressures up to 1 bar. They found that the system is governed by a non-isothermal macropore diffusion resistance with diffusion occurring by a Knudsen-type mechanism. Adsorption of CO_2 on zeolite 13X was shown to be effectively heat transfer limited[2] at higher CO_2 concentrations (Hu et al., 2014).

Due to the extremely dilute gas stream in the inlet, the uptake rates are expected to be low such that the assumption of isothermal behaviour is a valid approximation especially during adsorption in the first bed. For the next steps of the process, since the heat of adsorption of CO_2 on zeolite 13X is expected to be high, the heat effects during the adsorption process of each bed have to be considered (Mérel et al., 2006). Thus, a non-isothermal macropore and micropore diffusion control system is expected to be a more accurate assumption. Also, in general, large industrial columns operate under near adiabatic conditions (Ruthven, 1984). Therefore, for sake of simplicity, a non-isothermal, adiabatic, macropore, and micropore diffusion system has been considered. Hence, a two-component non-isothermal adiabatic system in which both components are adsorbed competitive is assumed.

By assuming that the bed is packed with solid pellets, when a fluid flows there is a tendency for axial mixing to occur. However, such a mixing is undesirable since it reduces the efficiency of separation (Ruthven, 1984). Thus, the minimisation of axial dispersion is a major design requirement. More detailed models that consider radial dispersion are generally not necessary (Ruthven, 1984).

Figure 5.2 illustrates a schematic representation of the adsorption column and adsorbent pellet that have been considered for the development of the dynamic model. Although structural adsorbents have been proved to be essential, especially in the separation unit, they have not been considered for this analysis. Pellets are likely to be the first technological solution to be used in the present system because of the long standing engineering science around them. An in-house cycle simulator software, which considers adsorbent material in the form of pellets has been used. As these are preliminary considerations, for the sake of simplicity, all the beds have been considered that they are cylindrical and filled with the

[2]The adsorption curves are expected to exhibit a very fast uptake, followed by a slower adsorption rate in the long time region. That means that the kinetics are initially fast but then the slow delay is relative to the dissipation of the heat generated by adsorption (Hu et al., 2014). Due to the extremely dilute concentration of the more adsorable component in the binary mixture, the system can be assumed isothermal.

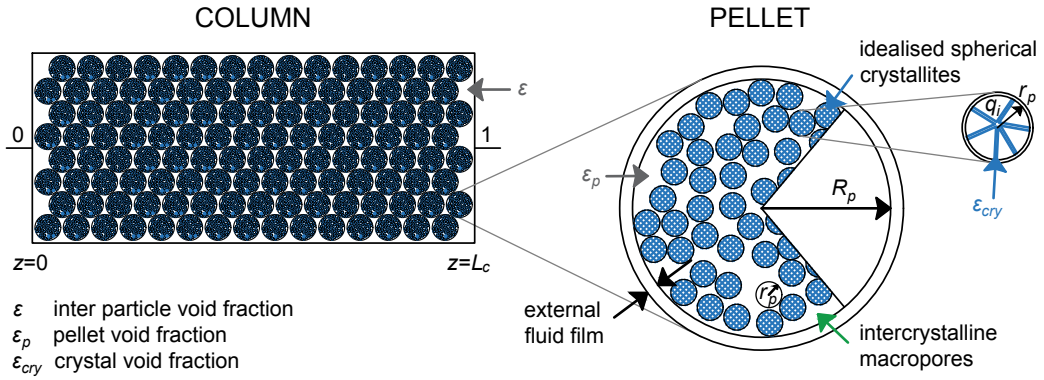

Figure 5.2. A schematic representation of an adsorption column showing the two inlets: '0' and '1', and the adsorbent pellets. The inset shows a schematic of an idealised adsorbent pellet including the spherical crystallites. Abbreviations: r_{p}, microparticle radius; R_{p}, particle radius; L_{c} column length.

same composite material. It is assumed that the adsorbent pellet has an idealised spherical shape and consists of intercrystalline macropores and intra-crystalline micropores. The microporous crystallites are also represented and modelled as spherical particles.

Therefore, the following assumptions to the adsorption kinetic model can be made:

(i) There are only two components in the gas stream from which both are adsorbable, and therefore material balance equations for each component are necessary.

(ii) The pressure drop across the bed is described by the Ergun equation.

(iii) Axial dispersed plug flow throughout the bed without radial mass dispersion is considered.

(iv) Mass transfer resistances, i.e. macro- and micropore diffusions are assumed.

(v) Negligible external mass transfer effect, i.e. film mass transfer.

(vi) The fluid phase is described by the ideal gas law.

(vii) The multi-component adsorption equilibrium is described by the extended single Langmuir model.

(viii) Internal energy accumulates in both the gas and adsorbed phases, kinetic energy and enthalpy convection and accumulation are neglected, and enthalpy changes by mass transferring between phases is considered.

(ix) Heat transfer is sufficiently rapid relative to the sorption rate, i.e. negligible thermal dispersion, such that the temperature gradients both through the particle and between particle and surrounding fluid are negligible.

(x) The system is adiabatic, i.e. there is no heat transfer through the ambient environment to the wall.

(xi) Constant wall temperature effect is considered.

(xii) Constant heat transfer coefficient, i.e. independent of composition, temperature, and pressure of the bulk-gas phase.

(xiii) All the properties are homogeneous over a phase, i.e. there is no difference in property between the bulk and the boundary within a phase.

(xiv) Constant and homogeneous bed porosity along the column.

5.2.2 Momentum Balance: Pressure Drop Considerations

Inside a packed bed, the adsorbent is in contact with the fluid phase such that the particle size, fluid velocity, and bed dimensions are important parameters of the process. These parameters determine the pressure drop and have a direct impact on the economics of the process. In packed beds, the pressure drop has been investigated by the Ergun equation. The Ergun equation is used for the pressure drop considerations as defined earlier in this study as(Macdonald et al., 1979)

$$-\frac{\mathrm{d}P}{\mathrm{d}z} = \frac{150\,\eta_\mathrm{f}\,(1-\varepsilon)^2}{\varepsilon^2\,{d_\mathrm{p}}^2\,{\phi_\mathrm{p}}^2}\,v + \frac{1.75\,(1-\varepsilon)\,\rho_\mathrm{f}}{\varepsilon\,d_\mathrm{p}\,\phi_\mathrm{p}}\,v\,|v|, \tag{5.12}$$

where η_f [kPa s] is the fluid viscosity, v [m s^{-1}] is the interstitial flow velocity, ρ_f [kg m^{-3}] is the fluid density, $d_\mathrm{p} = 2\,R_\mathrm{p}$ is the diameter of the equivalent-volume sphere and ϕ_p represents the non-spherical coefficient. For spherical pellets, ϕ_p becomes a unity.

Eq. 5.12 suggests that in a large-scale adsorption process where high flow rates are required and the maintenance of the pressure drop becomes essential, the use of relatively large adsorbent particles, typically 1–3 mm in diameter, is necessary. This concept has been already discussed in Chapter 4, Section 4.2.

5.2.3 Material Balance: Axial Dispersed Plug Flow Model with an Adsorption Source Term and Diffusion in the Adsorbent Pellet

The material balance in the packed bed is, as identified above, adequately described by the axial dispersed plug flow model (Hinduja et al., 1980) with an adsorption source term as (Khalighi et al., 2012; Gholami and Talaie, 2010)

$$0 = \frac{\partial c_i}{\partial t} + \frac{1-\varepsilon}{\varepsilon}\frac{\partial \bar{Q}_i}{\partial t} + \frac{\partial (v\,c_i)}{\partial z} + \frac{\partial J_i}{\partial z}, \tag{5.13}$$

where

$$\bar{Q}_i = \frac{3}{{R_\mathrm{p}}^3}\int_0^{R_\mathrm{p}} Q_i\,r^2\,\mathrm{d}r, \tag{5.14a}$$

$$Q_i = \varepsilon_\mathrm{p}\,c_i^\mathrm{m} + (1-\varepsilon_\mathrm{p})\,\bar{q}_i, \tag{5.14b}$$

$$\bar{q}_i = \frac{3}{{r_\mathrm{p}}^3}\int_0^{r_\mathrm{p}} q_i\,r^2\,\mathrm{d}r, \tag{5.14c}$$

$$J_i = -D_\mathrm{z}\,c_\mathrm{T}\,\frac{\partial y_i}{\partial z}. \tag{5.14d}$$

Here, c_i [mol m^{-3}] is the gas phase concentration of component i, c_i^m [mol m^{-3}] denotes the macropore concentration of component i, Q_i [mol m^{-3}] is the concentration of component i in the adsorbent pellet, and q_i [mol m^{-3}] is the sorbate concentration of the ith component or else the concentration of the ith component in the micropores. The bar atop the Q_i and q_i indicates the average concentrations. J_i [mol m^{-2} s^{-1}] denotes the diffusive flux of the

ith component in the fluid phase, D_{z} [m^2 s^{-1}] is the mass axial dispersion coefficient, υ is the interstitial flow velocity, R_{p} [m] represents the pellet radius, and r_{p} [m] the micropellet radius. Also, z [m] and r [m] are the axial coordinates over the length of the column and the radius of the material in a pellet form, respectively.

In this model, the effect of all mechanisms that contribute to the axial mixing are lumped together into a single effective axial dispersion coefficient, D_{z}. Guidelines on how to calculate D_{z} are given in Section 5.3. It is important to remind here that the radial dispersion has not been considered for simplification.

The boundary conditions for the gas phase concentrations are given by the Danckwerts boundary conditions for flow into the column and the diffusive flux for flow out of the column. With the convention that the positive flow direction across the column is from '0' to 'L_{c}', these can be written in a combined form as

$$\begin{aligned} J_i|_{z=0} &= -D_{\mathrm{z}} \left.\frac{\partial c_i}{\partial z}\right|_{z=0} = \frac{\upsilon+|\upsilon|}{2}(c_{i,0^-} - c_{i,0}), \\ J_i|_{z=L_{\mathrm{c}}} &= -D_{\mathrm{z}} \left.\frac{\partial c_i}{\partial z}\right|_{z=L_{\mathrm{c}}} = \frac{\upsilon-|\upsilon|}{2}(c_{i,L_{\mathrm{c}}^+} - c_{i,L_{\mathrm{c}}}), \end{aligned} \tag{5.15}$$

where the superscripts '$-$' and '$+$' denote the concentrations values to the left and right of the boundary, respectively.

The mass balance in the adsorbent pellet is more complex. By considering external film resistance at the pellet surface, marcopore diffusion, barrier and film resistance at the adsorbent crystals boundary, and micropore diffusion in the adsorbent crystal, the following macropore and micropore diffusion equations, Eq. 5.16 and Eq. 5.21, are applied.

The macropore diffusion equation with an effective macropore diffusion coefficient $D^{\mathrm{e}}_{\mathrm{m},i}$ [m^2 s^{-1}] and a concentration c_i^{m} [mol m^{-3}] in the macropores follows (LeVan et al., 1998)

$$\varepsilon_{\mathrm{p}} \frac{\partial c_i^{\mathrm{m}}}{\partial t} + (1-\varepsilon_{\mathrm{p}}) \frac{\partial \bar{q}_i}{\partial t} + \frac{1}{r^2}\frac{\partial}{\partial r}\left(-D_i^{\mathrm{p}}\, r^2 \frac{\partial c_i^{\mathrm{m}}}{\partial r}\right) = 0. \tag{5.16}$$

By assuming no external film resistance, then

$$c_i^{\mathrm{m}}(R_{\mathrm{p}}, z, t) = c_i(z,t), \tag{5.17a}$$

$$\left.\frac{\partial c_i^{\mathrm{m}}}{\partial r}\right|_{r=0} = 0. \tag{5.17b}$$

$D^{\mathrm{e}}_{\mathrm{m},i}$ [m^2 s^{-1}] is obtained by (Yang, 1987)

$$D^{\mathrm{e}}_{\mathrm{m},i} = \frac{\varepsilon_{\mathrm{p}}}{\tau_{\mathrm{p}}}\left[\left(\frac{1}{D_i^{\mathrm{m}}} + \frac{1}{D_i^{\mathrm{K}}}\right)^{-1} + D_i^{\mathrm{s}} + D_i^{\mathrm{v}}\right]. \tag{5.18}$$

For the case of a binary gas mixture of components '1' and '2' (Lopes et al., 2009; Hu et al., 2014),

$$D_i^{\mathrm{m}} = 1.6 \times 10^{-7} \frac{\sqrt{T^3 \left({MW_1}^{-1} + {MW_2}^{-1}\right)}}{P \, {\sigma_{12}}^2 \, \Omega_{12}}, \tag{5.19a}$$

$$D_i^{\mathrm{K}} = 97 \, r_{\mathrm{p}} \sqrt{\frac{T}{MW_i}}, \tag{5.19b}$$

$$D_i^{\mathrm{s}} = \frac{1 - \varepsilon_{\mathrm{p}}}{\varepsilon_{\mathrm{p}}} \, K \, D_{i,0}^{\mathrm{s}} \exp\left(\frac{-E}{RT}\right), \tag{5.19c}$$

$$D_i^{\mathrm{v}} = 10^5 \frac{P \, r_{\mathrm{p}}^2}{8 \eta_i}. \tag{5.19d}$$

Eq. 5.18 combines the molecular diffusion coefficient D_i^{m} [m^2 s^{-1}], the Knudsen diffusion coefficient D_i^{K} [m^2 s^{-1}], the surface diffusion coefficient D_i^{s} [m^2 s^{-1}], and the viscus diffusion coefficient D_i^{v} [m^2 s^{-1}]. τ_{p} denotes the pellet tortuosity factor, which is defined as the ratio between the actual diffusion path length and the radial distance. σ_{12} [Å] denotes the collision diameter from the Lennard-Jones potential for the component pair '1' and '2', Ω_{12} is a function depending on the Lennard-Jones force constant and temperature for the component pair '1' and '2', and η_i [kPa s] is the gas viscosity of the ith component.

By assuming LDF in the macropores, Eqs. 5.16 to 5.17b simplify to one single equation, which follows

$$\varepsilon_{\mathrm{p}} \frac{\mathrm{d}c_i^{\mathrm{m}}}{\mathrm{d}t} + (1 - \varepsilon_{\mathrm{p}}) \frac{\mathrm{d}\bar{q}_i}{\mathrm{d}t} = k_i^{\mathrm{p}} \frac{A_{\mathrm{p}}}{V_{\mathrm{p}}} \left(c_i - c_i^{\mathrm{m}}\right), \tag{5.20a}$$

where k_i^{p} [m s^{-1}] is the combined LDF coefficient in the pellet. A_{p} [m^2] and V_{p} [m^3] represent the pellet surface area and pellet volume, respectively. The pellets are assumed to be spherical such that $\frac{A_{\mathrm{p}}}{V_{\mathrm{p}}} = \frac{3}{R_{\mathrm{p}}}$ (Beck et al., 2015). k_i^{p} is calculated from the effective macropore diffusivity and is given by the correlation published by Nakao and Suzuki (1983), which follows

$$k_i^{\mathrm{p}} = \frac{5 \, D_{\mathrm{m},i}^{\mathrm{e}}}{R_{\mathrm{p}}}, \tag{5.20b}$$

where $D_{\mathrm{m},i}^{\mathrm{e}}$ [m^2 s^{-1}] is the effective macropore diffusivity or inter-particle diffusion coefficient as reported by Glueckauf (1955), Nakao and Suzuki (1983), and Beck et al. (2015).

The micropore diffusion equation with an effective micropore diffusion coefficient D_i^{μ} and an adsorbed concentration q_i follows (LeVan et al., 1998)

$$\frac{\partial q_i}{\partial t} + \frac{1}{r^2} \frac{\partial}{\partial r} \left(-D_i^{\mu} \, r^2 \, \frac{\partial q_i}{\partial r}\right) = 0, \tag{5.21}$$

where

$$D_i^{\mu} \left.\frac{\partial q_i}{\partial r}\right|_{r=r_{\mathrm{p}}} = k_{i,\mathrm{f}}^{\mu} \left(c_i^{\mathrm{m}} - c_i^{\mathrm{s}}\right) = k_{i,\mathrm{b}} \left(q_i^* \left(c_i^{\mathrm{s}}\right) - q_i|_{r_{\mathrm{p}}}\right), \tag{5.22a}$$

$$\left.\frac{\partial q_i}{\partial r}\right|_{r=0} = 0. \tag{5.22b}$$

Here, q_i^* [mol m^{-3}] denotes the adsorbed concentration of component i at equilibrium and c_i^{s} [mol m^{-3}] is the concentration of component i at the crystal boundary/surface. The boundary condition at the outer crystal boundary, i.e. $r = r_{\mathrm{p}}$, is given by the flux across

this boundary. This flux is equal to the flux through the external fluid film and to the flux through the crystal boundary. Thus, the mass transfer coefficients through the external fluid film and the crystal boundary are given by $k_{i,\mathrm{f}}^{\mu}$ and $k_{i,\mathrm{b}}$, respectively.

By considering LDF in micropores, Eqs. 5.21 to 5.22b become as (Cavenati et al., 2005)

$$\frac{\mathrm{d}\bar{q}_i}{\mathrm{d}t} = k_i^{\mathrm{cr}} \frac{3}{r_{\mathrm{p}}} \left(q_i^* - \bar{q}_i\right), \tag{5.23a}$$

where k_i^{cr} [m s^{-1}] is the combined LDF coefficient in the crystal and is given by

$$k_i^{\mathrm{cr}} \frac{3}{r_{\mathrm{p}}} = \frac{15\,\varepsilon_{\mathrm{cry}}\,D_i^{\mu}}{{r_{\mathrm{p}}}^2}, \tag{5.23b}$$

and, as has been described earlier in Arrhenius equation (i.e. in Eqs. 5.6 and 5.7) (Khalighi et al., 2012),

$$D_i^{\mu} = D_{0,i}^{\mu} \frac{\partial \ln p_i}{\partial \ln \bar{q}_i^{\mu}}. \tag{5.23c}$$

The adsorbed concentration of the ith component at equilibrium with the bulk-gas phase can be described by the ESL as

$$q_i^* = q_{\mathrm{s}} \frac{b_i\,P\,x_i}{1 + \sum_{j=1}^{N_{\mathrm{c}}} b_j\,P\,x_j}, \tag{5.24a}$$

where the temperature dependent equilibrium parameter b_i follows

$$b_i = b_{i,0}\,\exp\left(\frac{-\Delta H_i}{RT}\right). \tag{5.24b}$$

Here, the saturation capacity q_{s} is given in [mol m^{-3}].

The number of moles of each component passing through the top and bottom of the column are calculated from the mass balance ordinary differential equations (ODEs) as

$$\frac{\mathrm{d}n_i}{\mathrm{d}t} = \frac{F + |F|}{2} \frac{c_{i,\mathrm{n}}}{c_{\mathrm{T,n}}} + \frac{F - |F|}{2} \frac{c_i}{c_{\mathrm{T}}}, \tag{5.25a}$$

with initial values of

$$n_i(0) = 0. \tag{5.25b}$$

Here, F [mol s^{-1}] denotes the molar flow rate and c_{T} [mol m^{-3}] the total concentration of the fluid phase.

5.2.4 Energy Balance: A Non-Isothermal and Adiabatic Case with Constant Wall Temperature

In general, the energy balance in a column, a packed bed, contains two stages; the first stage describes the energy balance inside the column while the second describes the energy balance in the column wall. For the sake of simplicity, the process is assumed to be adiabatic and the wall temperature T_{w} is taken as a constant such that only the energy balance inside the column is required. Also, due to the very dilute stream, the heat transfer is assumed to be sufficiently rapid, relative to the sorption rate, such that the temperature gradients both

through the particle and between particle and surrounding fluid are negligible. In this case, we assume a non-isothermal model such that $T_\mathrm{f} = T_\mathrm{p}$, where T_f and T_p refer to the fluid and the pellet temperatures, respectively, and constant wall temperature T_w.

The governing equations for the energy balance inside the column is given by

$$0 = \varepsilon \frac{\partial \check{U}_\mathrm{f}}{\partial t} + (1-\varepsilon) \frac{\partial \check{U}_\mathrm{p}}{\partial t} + \varepsilon \frac{\partial \left(\check{H}_\mathrm{f} \cdot v\right)}{\partial z} + \frac{\partial J_\mathrm{T}}{\partial z} + \sum_{i=1}^{N_\mathrm{c}} \frac{\partial \left(J_i \, \tilde{H}_i\right)}{\partial z} + h_\mathrm{w} \frac{A_\mathrm{c}}{V_\mathrm{c}} \left(T_\mathrm{f} - T_\mathrm{w}\right). \quad (5.26)$$

Here,

$$J_\mathrm{T} = -k_\mathrm{z} \, \varepsilon \frac{\partial T_\mathrm{f}}{\partial z}, \quad (5.27a)$$

$$J_i = -D_\mathrm{z} \, c_\mathrm{T} \frac{\partial y_i}{\partial z}, \quad (5.27b)$$

where $\check{U}_\mathrm{f}$ [kJ m^{-3}] is the internal energy in the fluid phase per unit volume, $\check{U}_\mathrm{p}$ [kJ m^{-3}] is the internal energy in the pellet per unit volume, $\check{H}_\mathrm{f}$ [kJ m^{-3}] is the enthalpy in the fluid phase per unit volume, and $\tilde{H}_i$ [kJ mol^{-1}] represents the partial molar enthalpy of component i in the fluid phase. The heat transfer coefficient between the bed fluid and the column wall is given by h_w [kJ m^{-2} s^{-1} K^{-1}]. k_z [kJ m^{-1} s^{-1} K^{-1}] is the axial thermal dispersion coefficient of the fluid and D_z [m^2 s^{-1}] represents the axial dispersion coefficient in the fluid. The molar fraction of component i is represented as y_i. Finally, A_c [m^2] is the column surface area and V_c [m^3] represents the column volume.

The constitutive equations for the energy terms are given by the following set of equations:

$$\begin{aligned}
\check{U}_\mathrm{f} &= c_\mathrm{T} \, \tilde{U}_\mathrm{f,ref} + c_\mathrm{T} \int_{T_\mathrm{ref}}^{T_\mathrm{f}} \tilde{c}_\mathrm{v} \, \mathrm{d}T, \\
\check{H}_\mathrm{f} &= c_\mathrm{T} \, \tilde{H}_\mathrm{f,ref} + c_\mathrm{T} \int_{T_\mathrm{ref}}^{T_\mathrm{f}} \tilde{c}_\mathrm{p} \, \mathrm{d}T, \\
\check{U}_\mathrm{p} &= \varepsilon_\mathrm{p} \, \check{U}_\mathrm{p,f} + (1-\varepsilon_\mathrm{p}) \, \check{U}_\mathrm{p,s}, \\
\check{U}_\mathrm{p,f} &= c_\mathrm{T}^\mathrm{m} \, \tilde{U}_\mathrm{p,f,ref} + c_\mathrm{T}^\mathrm{m} \int_{T_\mathrm{ref}}^{T_\mathrm{p}} \tilde{c}_\mathrm{v}^\mathrm{m} \, \mathrm{d}T, \\
\check{U}_\mathrm{p,s} &= \check{U}_\mathrm{sol} + \check{U}_\mathrm{ads}, \\
\check{U}_\mathrm{sol} &= \rho_\mathrm{cry} \, \hat{U}_\mathrm{sol,ref} + \rho_\mathrm{cry} \int_{T_\mathrm{ref}}^{T_\mathrm{p}} \hat{c}_\mathrm{p,sol} \, \mathrm{d}T, \\
\check{U}_\mathrm{ads} = \check{H}_\mathrm{ads} &= q_\mathrm{T} \, \tilde{H}_\mathrm{ads,ref} + q_\mathrm{T} \int_{T_\mathrm{ref}}^{T_\mathrm{p}} \tilde{c}_\mathrm{p,ads} \, \mathrm{d}T - \left(-\Delta \check{H}_\mathrm{ads}\right)_{T_\mathrm{p}}, \\
\left(-\Delta \check{H}_\mathrm{ads}\right)_{T_\mathrm{p}} &= \sum_{i=1}^{N_\mathrm{C}} \int_0^{q_i} \left(-\Delta \tilde{H}_i\right)_{T_\mathrm{p}, q_{j \neq i}} \mathrm{d}q, \\
\tilde{H}_i &= \tilde{H}_{i,\mathrm{ref}} + \int_{T_\mathrm{ref}}^{T_\mathrm{f}} \tilde{c}_{\mathrm{p},i} \, \mathrm{d}T.
\end{aligned} \quad (5.28)$$

$\check{U}_\mathrm{sol}$ [kJ m^{-3}] and $\check{U}_\mathrm{ads}$ [kJ m^{-3}] are the internal energy per unit volume in the adsorbent and the adsorbed phase, respectively, $\check{U}_\mathrm{p,f}$ [kJ m^{-3}] denotes the internal energy in the macropore per unit volume, and $\check{U}_\mathrm{p,s}$ [kJ m^{-3}] is the internal energy in the solid and sorbate phase per unit volume. The tilde indicates the molar quantities and the subscript 'ref' refers to the reference value at T_ref and P_ref. The total concentration in the fluid phase and in the

macropore are given by c_{T} [mol m^{-3}] and $c_{\mathrm{T}}^{\mathrm{m}}$ [mol m^{-3}], respectively. Also, ρ_{p} [kg m^{-3}] is the pellet density, q_{T} [mol m^{-3}] is the total adsorbed concentration in the micropore and $\hat{c}_{\mathrm{p,sol}}$ [kJ kg^{-1} K^{-1}] denotes the specific heat capacity at constant pressure in the solid phase. The total heat of adsorption per unit volume $\Delta\check{H}_{\mathrm{ads}}$ [kJ m^{-3}] is calculated from the component heat of adsorption $\Delta\tilde{H}_i$ [kJ mol^{-1}].

The molar heat capacities at constant volume $\tilde{c}_{\mathrm{v}}$ [kJ mol^{-1} K^{-1}] and at constant pressure in the fluid phase $\tilde{c}_{\mathrm{p}}$ [kJ mol^{-1} K^{-1}] and the molar heat capacity at constant pressure in the adsorbed phase $\tilde{c}_{\mathrm{p,ads}}$ [kJ mol^{-1} K^{-1}] are calculated from the respective component heat capacities as follows

$$\begin{aligned} \tilde{c}_{\mathrm{v}} &= \textstyle\sum_{i=1}^{N_{\mathrm{C}}} \left(y_i\, \tilde{c}_{\mathrm{v},i}\right), & \tilde{c}_{\mathrm{v}}^{\mathrm{m}} &= \textstyle\sum_{i=1}^{N_{\mathrm{C}}} \left(y_i^{\mathrm{m}}\, \tilde{c}_{\mathrm{v},i}\right), \\ \tilde{c}_{\mathrm{p,ads}} &= \textstyle\sum_{i=1}^{N_{\mathrm{C}}} \left(\frac{q_i}{q_{\mathrm{T}}}\, \tilde{c}_{\mathrm{p},i}\right), & \tilde{c}_{\mathrm{p}} &= \textstyle\sum_{i=1}^{N_{\mathrm{c}}} \left(y_i\, \tilde{c}_{\mathrm{p},i}\right), \end{aligned} \tag{5.29}$$

where the superscript 'm' indicates the macropore concentrations and macropore heat capacities.

The boundary conditions for the bulk-gas phase concentrations and the enthalpy are given by the Danckwerts boundary conditions for flow into the column and the no diffusive flux for flow out of the column as

$$\begin{aligned} J_{\mathrm{T}}|_{z=0} &= -k_{\mathrm{z}}\,\varepsilon \left.\frac{\partial T_{\mathrm{f}}}{\partial z}\right|_{z=0} = \frac{v+|v|}{2}\left(\check{H}_{\mathrm{f},0^-} - \check{H}_{\mathrm{f},0}\right), \\ J_{\mathrm{T}}|_{z=\mathrm{L}} &= -k_{\mathrm{z}}\,\varepsilon \left.\frac{\partial T_{\mathrm{f}}}{\partial z}\right|_{z=\mathrm{L}} = \frac{v-|v|}{2}\left(\check{H}_{\mathrm{f},\mathrm{L}^+} - \check{H}_{\mathrm{f},\mathrm{L}}\right), \end{aligned} \tag{5.30}$$

where the superscripts '$-$' and '$+$' indicate the concentration values to the left and right of the boundary, respectively.

5.3 Kinetic Considerations of Air Capture II: Transport Parameters and Modelling by Means of an In-House Cyclic Simulator

5.3.1 Modelling by Means of an In-House Cyclic Simulator 'CySim'

The adsorption kinetic model of the process is designed using the in-house cycle simulator software (CySim) (Friedrich et al., 2013; Friedrich et al., 2015; Beck et al., 2015). A schematic representation of the process as design in CySim is given in Figure 5.3. The schematic illustrates the: *(i)* four beds connected together, *(ii)* valves for operational control, *(iii)* slitters, which are used as tanks to buffer the feed so that pumps, compressors and blowers can be run continuously, *(iv)* flow directions across the valves, *(v)* inlets of each unit, which is illustrated with the index '0', and *(vi)* outlet(s) of each unit, which is/are illustrated with the indexes '1' or '2' or '3'. The feed streams as also presented in Figure 5.3 and are explained under the legend. The inlet feed, atmospheric air, flows through a valve and then through Bed 1. The exit stream at position z=1 of Bed 1 is illustrated as 'Clean Air'. The main feed stream flows through bed to bed, following the steps as illustrated in Table 5.1,

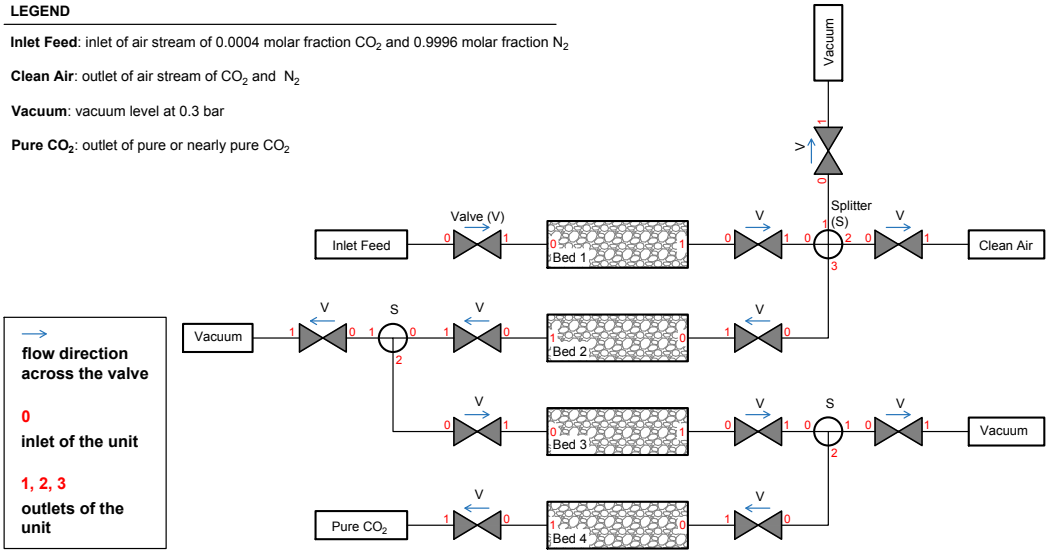

Figure 5.3. A schematic representation of the direct air capture process as has been designed in CySim simulator. Abbreviations: V, valve; S, splitter; '0', inlet of the unit; '1', '2', and '3', outlets of the unit. Flow direction always follows from the '0' index to the either '1' or '2' or '3' index.

Table 5.1. The list of the process operational steps and sequence of a single cycle.

Bed(s)	Step	Bed k Temperature [a]	Bed $k+1$ Temperature [a]
Bed 1	Adsorption	T_{low}	—
Bed 1	Vacuum LDF – *optional*	T_{low}	—
Bed 1	Heating	T_{high}	—
Beds 1–2	Equilibration Beds 1–2	T_{high}	T_{low}
Beds 1–2	Cooling Bed 1; Vacuum LDF Bed 2 – *optional*	T_{low}	T_{low}
Bed 2	Heating	T_{high}	—
Beds 2–3	Equilibration Beds 2–3	T_{high}	T_{low}
Beds 2–3	Cooling Bed 2; Heating Bed 2	T_{low}	T_{high}
Beds 3–4	Equilibration Beds 3–4	T_{high}	T_{low}
Beds 3–4	Cooling Beds 3–4	T_{low}	T_{low}

[a] In case of connection between Bed k and Bed $k+1$, Bed $k+1$ is the next following bed to Bed k. For instance, if Beds 2–3 are denoted under the column 'Bed(s)', Bed 2 is Bed k and Bed 3 is Bed $k+1$.

and finally the purified CO_2 exists at the position $z=1$ of Bed 4. The optional vacuum steps are also included in Figure 5.3.

To complete the adsorption dynamic model of the DAC process, the mathematical model of the adsorption columns is coupled with the individual models of ancillary equipment. The equipment includes:

Valve (V) The valve is assumed to have no volume and passes information on pressure, temperature, and gas composition to the next unit. The flow through the valve is obtained by assuming either a mass flow control operation as (Beck et al., 2015)

$$\begin{aligned} F &= F_i, && \text{if } \left|\tfrac{P_0-P_1}{P_0}\right| > 0.005, \\ F &= F_i\, 0.5\left(1+\cos\left(200\,\pi\left(0.005-\left|\tfrac{P_0-P_1}{P_0}\right|\right)\right)\right), && \text{else,} \end{aligned} \tag{5.31}$$

or a pressure-driven control operation as (Beck et al., 2015)

$$F = c_{\text{valve}}\, c_{\text{T}} \sqrt{\frac{|P_0 - P_1|}{\rho_{\text{f}}}}. \tag{5.32}$$

Here, c_{valve} indicates the valve coefficient and P_0 and P_1 are the pressures in the inlet and outlet of the valve, respectively. CySim allows the opening and closing of valves at specified times.

Splitter (S) The splitter works as a perfectly mixed tank and consists of an arbitrary number of connections. A small default dead volume of 10^{-6} m^3 is associated with this unit. The governing equations for this unit are given by (Beck et al., 2015)

$$P = f(c_{\text{T}}, T_{\text{f}}), \tag{5.33a}$$

$$F_j = -F_{\text{n}_j}, \quad \text{where } j = 1, ..., N_{\text{I}}, \text{ and } j \neq \text{d}, \tag{5.33b}$$

$$F_{\text{d}} = \begin{cases} -F_{n_{\text{d}}}, & \text{if } M_{\text{s}} = 0 \\ c_{\text{valve}} \left(P_{\text{n}_{\text{d}}} - P\right), & \text{if } M_{\text{s}} = 1 \end{cases}, \tag{5.33c}$$

$$V \frac{\text{d}c_i}{\text{d}t} = \sum_{j=1}^{N_{\text{I}}} \left(\frac{F_j + |F_j|}{2} \frac{c_{i,\text{n}_j}}{c_{\text{T},\text{n}_j}} + \frac{F_j - |F_j|}{2} \frac{c_i}{c_{\text{T}}} \right), \tag{5.33d}$$

$$\frac{\text{d}U_{\text{f}}}{\text{d}t} = \sum_{j=1}^{N_{\text{I}}} \left(\frac{F_j + |F_j|}{2} \tilde{H}_{\text{f},\text{n}_j} + \frac{F_j - |F_j|}{2} \tilde{H}_{\text{f}} \right) + h_{\text{w}} A \left(T_{\text{w}} - T_{\text{f}}\right), \tag{5.33e}$$

where f is an equation of state and N_{I} is the number of connections of the next independent units. Here, the subscripts 'd' and 'n_j' are the dependent unit and the next unit at connection j, respectively.

Feed The feed sets the boundary conditions for the simulated system. Pressure, temperature, and feed composition are kept constant at the initial conditions. The flow rate at the only inlet depends on the value of the so called feed mode flag. If it sets to the mass flow control, then the flow rate follows (Beck et al., 2015)

$$\begin{aligned} &F = F_i, && \text{if } \left|\tfrac{P - P_{\text{n}}}{P}\right| > 0.01, \\ &F = F_i \, 0.5 \left(1 + \cos\left(100 \, \pi \left(0.01 - \left|\tfrac{P - P_{\text{n}}}{P}\right|\right)\right)\right), && \text{else}, \end{aligned} \tag{5.34}$$

where P and P_{n} are the pressures in the feed unit and the neighbouring unit, respectively. The feed unit also calculates the number of moles of each component that pass through the outlet similar to the mass balance ODEs in the column unit as described by Eq. 5.25a. The energy consumption w [kJ] is governed by (Beck et al., 2015)

$$\frac{\text{d}w}{\text{d}t} = \begin{cases} \frac{\gamma}{\gamma - 1} R T F \left[\left(\frac{P_{\text{n}}}{P_{\text{atm}}} \right)^{\frac{\gamma}{\gamma - 1}} - 1 \right], & \text{if } P_{\text{n}} > P_{\text{atm}} \text{ and } F < 0, \\ \frac{\gamma_{\text{n}}}{\gamma_{\text{n}} - 1} R T_{\text{n}} F \left[\left(\frac{P_{\text{atm}}}{P_{\text{n}}} \right)^{\frac{\gamma_{\text{n}}}{\gamma_{\text{n}} - 1}} - 1 \right], & \text{if } P_{\text{n}} < P_{\text{atm}} \text{ and } F > 0, \\ 0, & \text{otherwise}, \end{cases} \tag{5.35a}$$

with an initial condition of

$$w(0) = 0. \tag{5.35b}$$

In order to run the process dynamics in CySim, an outlet to a vacuum feed had to be placed in between a connection of two columns. Here, the 'Vacuum' indexes in Figure 5.3 refer to the optional instantaneous vacuum and/or blowdown steps in Bed 1 and Bed 2. The 'Vacuum' between Bed 3 and Bed 4 was required in order to solve the connection step between Bed 3 and Bed 4. By setting the vacuum pressure closer to the 'expected' steady state pressure of the connection step between Bed 3 and Bed 4 (as connected from the

Table 5.2. Considered input parameters of the adsorption kinetic model required from CySim.

Parameter	Symbol	Value	Unit	Reference
Column Parameters				
Column length	L_{c_1}	0.526	m	
	$L_{c_{2-3}}$	0.070	m	
	L_{c_4}	0.105	m	
Column internal diameter	$D_{c_{1,2,4}}$	0.064	m	
	D_{c_3}	0.032	m	
External bed void fraction	ε_1	0.50		Xiao et al., 2008
	ε_{2-N_B}	0.25		Balahmar et al., 2016
Column wall thickness	d_w	0.005	m	
Axial mass dispersion coefficient	D_z	1.20×10^{-4}	$m^2\ s^{-1}$	Mulgundmath et al., 2012
Axial thermal dispersion coefficient	k_z	0.027	$J\ m^{-1}\ s^{-1}\ K^{-1}$	Mulgundmath et al., 2012
Column wall thermal conductivity	k_w	13.4	$J\ m^{-1}\ s^{-1}\ K^{-1}$	Dantas et al., 2011
Wall heat transfer coefficient	h_w	95	$J\ m^{-2}\ s^{-1}\ K^{-1}$	Mulgundmath et al., 2012
Heat transfer coefficient wall-oven	U	40	$J\ m^{-2}\ s^{-1}\ K^{-1}$	Cavenati et al., 2006
Column wall density	ρ_w	8238	$kg\ m^{-3}$	Dantas et al., 2011
Specific heat column wall	$c_{p,w}$	500	$J\ kg^{-1}\ K^{-1}$	Dantas et al., 2011
Adsorbent Properties				
Pellet density	ρ_p	1200	$kg\ m^{-3}$	Oreggioni et al., 2015
Pellet void fraction	ε_p	0.20		Hu et al., 2014
Pellet averaged diameter	d_p	0.002	m	Hu et al., 2014
Pellet-bed heat transfer coefficient	h_p	50	$J\ m^{-2}\ s^{-1}\ K^{-1}$	
Adsorbent specific heat capacity	$c_{p,s}$	858	$J\ kg^{-1}\ K^{-1}$	Santori et al., 2013
Macropore LDF coefficient	$k_i^p \frac{A_p}{V_p}\Big\vert_{CO_2}$	0.1	s^{-1}	Hu et al., 2014
	$k_i^p \frac{A_p}{V_p}\Big\vert_{N_2}$	0.5	s^{-1}	Hu et al., 2014
Micropore LDF coefficient	$k_i^{cr} \frac{3}{r_c}\Big\vert_{CO_2}$	0.0051	s^{-1}	Lopes et al., 2009
	$k_i^{cr} \frac{3}{r_c}\Big\vert_{N_2}$	0.1688	s^{-1}	Lopes et al., 2009
Adsorption Parameters				
Adsorption capacity	q_s	6400	$mol\ m^{-3}$	Xiao et al., 2008
Equilibrium constant for CO_2	$b_{0_{CO_2}}$	3.80×10^{-5}	bar^{-1}	Xiao et al., 2008
Equilibrium constant for N_2	$b_{0_{N_2}}$	9.70×10^{-5}	bar^{-1}	Xiao et al., 2008
Heat of adsorption for CO_2	ΔH_{CO_2}	–31.36	$kJ\ mol^{-1}$	Xiao et al., 2008
Heat of adsorption for N_2	ΔH_{N_2}	–14.92	$kJ\ mol^{-1}$	Xiao et al., 2008
Operating conditions				
Adsorption temperature	T_{ads}	293.15	K	
Regeneration temperature	T_{reg}	368.15	K	
Vacuum pressure	P_{vac}	30	kPa	
Feed flow rate	Q_{feed}	0.08	$mol\ s^{-1}$	
CO_2 feed composition	y_{CO_2}	0.0004		

equilibrium model), the results could be obtained. However, the steady state pressure of the connection step changes cycle after cycle. Therefore, results for more than one cycle of the process could not be produced at this stage. In addition to this, the way that a valve works in CySim is that it passes information on pressure, temperature, and concentration from one unit to another following the direction of the stream flux. In the case of air capture, due to a high concentration difference between the two columns, a backflow of the less adsorbed compound may be occurred. Therefore, CySim was modified in order to account for the diffusion across a valve from both directions.

The considered input parameters of the kinetic model as analysed in CySim are listed in Tables 5.2 to 5.4. The fundamental properties of the zeolite 13X beads as obtained by Hu et al. (2014) are given in Table 5.3. The numerical solution of the mathematical model in CySim is performed using the first order upwind spatial discretisation method with 10 grid points for each bed. The simulations are performed with an absolute and relative tolerance of 10^{-8}.

Table 5.3. Fundamental properties of zeolite 13X beads from mercury porosimetry characterisation.

13X bead radius, R_p [mm]	Average pore radius, r_p [μm]	Void fraction ε_p	Tortuosity τ	Knudsen diffusivity $D_\mathrm{k}^{\mathrm{CO_2}}$ [m^2 s^{-1}]
0.98	0.294	0.269	2.62	5.01×10^{-5}
1.95	0.516	0.143	2.83	8.79×10^{-5}

Source: Hu et al. (2014)

Table 5.4. Experimental diffusivity and limiting Schmidt number for the gas pair CO_2–N_2 at 1 atmosphere pressure as reported from Bird, Robert Byron et al. (2007).

Gas pair i–j	Temperature [K]	Diffusivity D_{ij} [cm^2 s^{-1}]	Sc $x_i \to 1$	Sc $x_j \to 1$
CO_2–N_2	273.2	0.144	0.48	0.91
	288.2	0.158	0.49	0.92
	298.2	0.165	0.50	0.93

It is important to note here that the dimensions of the columns, which are listed in Table 5.2, are derived from the masses of each bed and the parameters of the solid material. The exact parameters have been used in the equilibrium model in Chapter 3, Section 3.4, for comparison between the equilibrium and non-equilibrium models. Specifically, the volume of each bed was derived considering the equilibrium masses, and therefore the lengths and diameters were obtained. Since it is common to design a packed column having longer lengths (L) than diameters (D), L>D have been considered.

5.3.2 Process Transport Parameters and Physical Properties of Gases

The transport parameters and the physical properties of the gases encountered in the previous subsections are discussed here. There are two main mechanisms that contribute to axial mass dispersion, which are taken into account: the molecular diffusion and the turbulent mixing arising from the flows around the adsorbent particles (Ruthven, 1984). Thus, the axial mass dispersion coefficient D_z is estimated by (Wakao and Funazkri, 1978)

$$\frac{\varepsilon D_\mathrm{z}}{D_\mathrm{m}} = 20 + 0.5\, S_\mathrm{c}\, Re, \tag{5.36}$$

and the axial thermal dispersion coefficient k_z is estimated using the correlation (Wakao and Funazkri, 1978)

$$\frac{k_\mathrm{z}}{k_\mathrm{g}} = 7 + 0.5\, Pr\, Re. \tag{5.37}$$

Here,

$$Re = \frac{\rho_\mathrm{g}\, \upsilon\, d_\mathrm{p}}{\eta_\mathrm{f}}, \tag{5.38a}$$

$$Sc = \frac{\eta_\mathrm{f}}{\rho_\mathrm{g}\, D_\mathrm{m}}, \tag{5.38b}$$

$$Pr = \frac{c_\mathrm{p}\, \eta_\mathrm{f}}{k_\mathrm{g}}, \tag{5.38c}$$

where Re, Sc and Pr denote the dimensionless Reynolds, Schmidt, and Prandtl numbers, respectively. D_m [m^2 s^{-1}] is the molecular diffusivity, k_g [kJ m^{-1} s^{-1} K^{-1}] is the gas thermal conductivity, and η_f [kPa s] denotes the viscosity of the gas mixture.

The molecular diffusivity of the mixture D_m or else D_{ij} at low pressure can be estimated by (Mulgundmath et al., 2012)

$$D_\mathrm{m} = \frac{0.0018583\sqrt{T^3\left(\frac{1}{M_i}+\frac{1}{M_j}\right)}}{P\,{\sigma_{ij}}^2\,\Omega_{ij}} \tag{5.39}$$

where the subscripts 'i' and 'j' denote the component pair i and j.

The gas thermal conductivity k_g is evaluated using the Wassiljewa equation as (Poling et al., 2001)

$$k_\mathrm{g} = \sum_i^{N_\mathrm{C}} \frac{y_i\,k_i^\mathrm{g}}{\sum_j^{N_\mathrm{C}} y_j\,\Phi_{ij}}. \tag{5.40}$$

Here, the thermal conductivity of a pure polyatomic gas k_g [kJ m^{-1} s^{-1} K^{-1}] is given according to the Eucken equation as (Bird, Robert Byron et al., 2007)

$$k_i^\mathrm{g} = \left(\tilde{c}_{\mathrm{p},i} + \frac{5}{4}\,\frac{R_\mathrm{g}}{M_{\mathrm{w}_i}}\right)\eta_i, \tag{5.41}$$

where η_i [kPa s] is the viscosity of a pure gas and $M_{\mathrm{w},i}$ [kg mol^{-1}] is the molecular weight of species i.

The viscosity of the gas mixture η_f is calculated using the Wilke method as (Poling et al., 2001; Bird, Robert Byron et al., 2007)

$$\eta_\mathrm{f} = \sum_i^{N_\mathrm{C}} \frac{y_i\,\mu_i}{\sum_j^{N_\mathrm{C}} y_j\,\Phi_{ij}}, \tag{5.42}$$

where Φ_{ij} is the characteristic Lennard-Jones viscosity parameter, a function of the viscosities and molecular weights, for the component pair i and j.

The viscosity of a pure gas is given by the first order Chapman-Enskog equation as (Bird, Robert Byron et al., 2007)

$$\eta_i = 2.6693\times10^{-5}\,\frac{\sqrt{M_{\mathrm{w}_i}\,T}}{\sigma^2\,\Omega_\mu}, \tag{5.43a}$$

where Ω_μ is the characteristic Lennard-Jones viscosity parameter of the ith component. The dimensionless quantity Φ_{ij} is given by (Bird, Robert Byron et al., 2007)

$$\Phi_{ij} = \frac{1}{\sqrt{8}}\left(1+\frac{M_{\mathrm{w}_i}}{M_{\mathrm{w}_j}}\right)^{-1/2}\left[1+\left(\frac{\mu_i}{\mu_j}\right)^{1/2}\left(\frac{M_{\mathrm{w}_j}}{M_{\mathrm{w}_i}}\right)^{1/4}\right]^2, \tag{5.43b}$$

where the subscripts 'i' and 'j' denote the component pair i and j.

5.4 Adsorption Breakthrough and Cycle Simulation

The number of components and the process characteristics rapidly increase the difficulties associated with the mathematical modelling of the column. An analytical solution for the transient concentration and temperature profiles of the column is feasible only for a few limiting cases (Ruthven, 1984). Although the equilibrium theory can be an alternative since it offers a good qualitative understanding of the behaviour of the multi-component and non-isothermal systems, kinetic and dispersive effects can not be included in the theoretical model. The numerical solution of the differential heat and mass balance equations offers the only feasible alternative. However, the numerical approach has the disadvantage that solutions may be obtained only for specified sets of parameter values. For reducing this problem, a set of dimensionless numbers with a range of values have been established. Here, the adsorption breakthrough and the cycle simulation are presented together with a comparison between the results of the equilibrium and the kinetic models.

5.4.1 Adsorption Breakthrough Simulation Results

In a real system, the outlet response is dispersed as a result of the combined effects of axial dispersion and mass transfer resistance (Ruthven, 1984). Therefore, by measuring the time delay, information concerning the adsorption equilibrium can be obtained. The dispersion of the response provides information on the sorption kinetics and consequently on the axial mixing in the bed. Ideally, a match of the experimental response and the theoretical response curve, as calculated from a suitable dynamic model of the system, is needed to extract this information (Ruthven, 1984). If experimental data is not available, a prediction of the breakthrough curve from basic kinetic and equilibrium data can be essential to predict, in principle, the dynamic capacity of the adsorption bed.

First, adsorption breakthroughs of the binary mixture are simulated using the parameters in Table 5.2. Figure 5.4 shows the concentration profiles of CO_2 and N_2 with time at product end (at the exit of the adsorption contactor) in two different scales of concentration. This was obtained from the operation of the process as illustrated in Figure 5.3. It is assumed that the adsorption contactor is initially filled with 99.99% N_2. It is shown that the first contaminant to breakthrough the column is N_2 at the first few seconds of the process followed by CO_2. Since CO_2 breakthrough is at around 430 sec (or 7 min at 5% of the feed concentration), the adsorption step time of the DAC process at the 95% location of the gas phase concentration breakthrough curve is estimated to be at 1475 sec (25 min). The stoichiometric time, the time at which the CO_2 outlet concentration is half of that of the feed (Mérel et al., 2006), is at around 14 min.

The concentration profile in Figure 5.4 exhibits an abrupt decrease at the initial stage of the breakthrough. This is due to the initial conditions in the adsorption contactor prior to adsorption. In Section 3.2, it is stated that a preliminary regeneration before the operation of the process is needed to minimise the amount of excess gases in the system. Therefore, all the beds have to undergo steps of heating at constant volume, evacuation at high temperature, and then cooling at constant volume in order to reduce the amount of excess gases in the system. Therefore, the initial concentrations in each bed, which are set by the preliminary regeneration, are different than the atmospheric concentrations. Although, since at the beginning of each cycle the adsorption contactor is open to the atmospheric air (adsorption

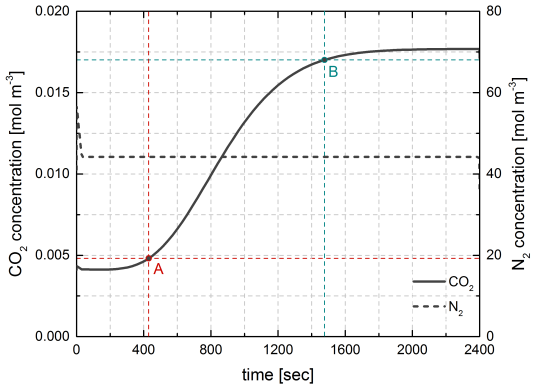

Figure 5.4. Breakthrough simulation results of the DAC process on zeolite 13X at 293 K and 1 bar. Points: (A) 5% CO_2 breakthrough and (B) 95% adsorption step time.

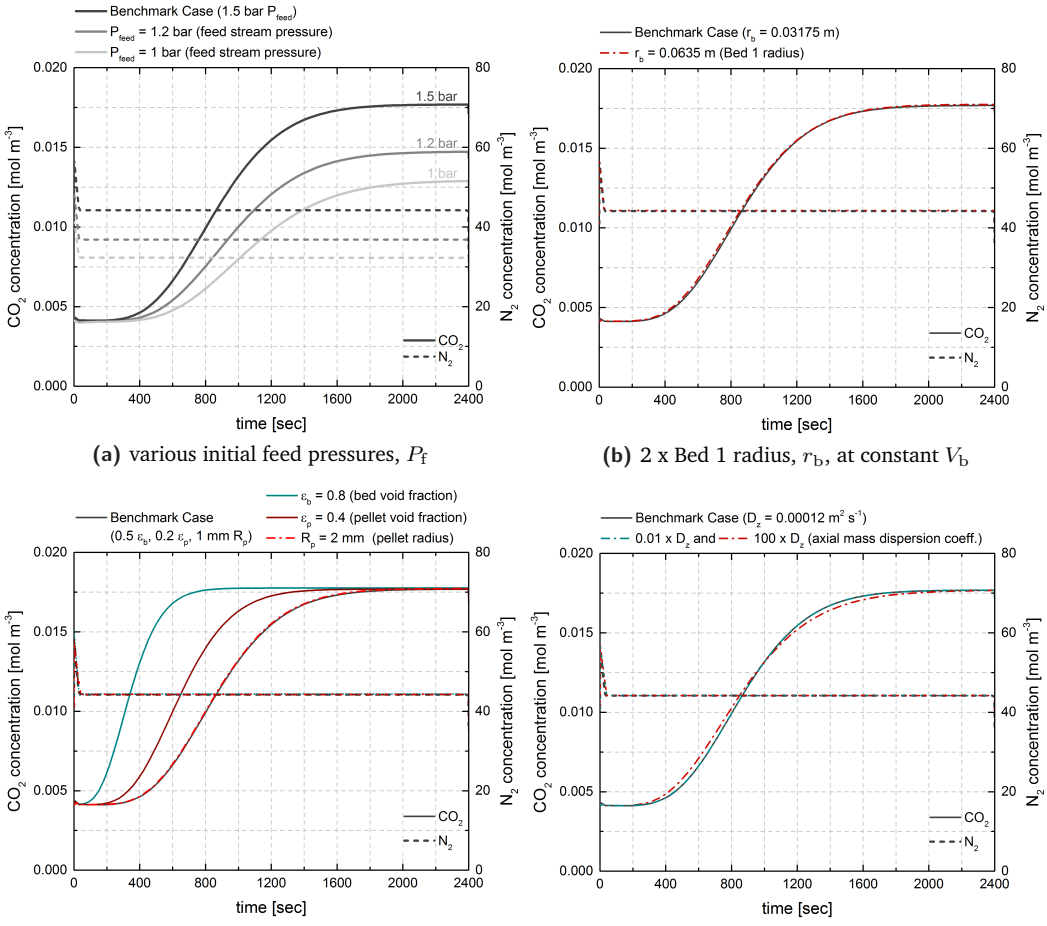

(a) various initial feed pressures, P_f

(b) 2 x Bed 1 radius, r_b, at constant V_b

(c) higher void fractions ε_b and ε_p at constant V_b

(d) different axial diffusion coefficient

Figure 5.5. Breakthrough simulation results of the DAC process on zeolite 13X for the case of: *(a)* lower inlet feed pressures, *(b)* higher bed diameter, *(c)* higher bed and pellet void fractions and higher pellet diameter, and *(d)* different axial diffusion coefficient.

step), the initial concentrations in that bed could also be assumed as the same to those in atmospheric air.

Sattler et al. (1995) stated that the first moment of the curve, the moment before the mass transfer zone (the moment where the concentration of CO_2 at the outlet is constant and at

the minimum), depends on the equilibrium properties, the length of the column, and the inlet flowrate. The second part, where the mass transfer zone begins, depends on the kinetic and dispersive phenomena. Thus, in order to understand the main factors that affect or can improve the breakthrough profiles different cases have been investigated here. The case as presented in Figure 5.4 is denoted here as the benchmark case. Figure 5.5a compares the benchmark case with different inlet stream pressures ('Inlet Feed' in Figure 5.3). Due to the pressure drop across the bed, to maintain a stream of around 1 bar throughout Bed 1, the inlet stream has to be supplied at around 1.5 bar. In case of 1.2 bar and 1 bar feed stream pressures, the pressure across Bed 1 decreases to 0.9 bar and 0.8 bar, respectively. The different feed pressures do not affect the breakthrough of N_2. However, the CO_2 breakthrough increases from 7 min to 8.5 min and 9.5 min as the pressure in the feed stream decreases from 1.5 bar to 1.2 bar and 1 bar, respectively. By doubling the radius of Bed 1 and keeping the bed volume constant, the same breakthroughs are obtained (see Figure 5.5b).

An increase in the bed void fraction has an effect on the adsorption breakthrough time of CO_2 as less adsorbent is present in the bed. Since the pressure drop across the bed is very important, an increase in the bed void fraction can be beneficial for the reduction of the process cycle time and energy requirements for feed stream compression and for the increase of the final purity. Figure 5.5c also shows that an increase in the pellet void fraction decreases the breakthrough of CO_2. At ϵ_b=0.8, the breakthrough reduces from 7 min to 2.5 min and at ϵ_p=0.4, the breakthrough reduces to 5 min. However, as previously discussed in Chapter 4, a higher pellet voidage in Bed 1 decreases the purity of the process. On the other hand, an increase in the pellet radius does not change the breakthrough times of both components. Finally, another case is investigated in Figure 5.5d. Here, a two orders of magnitude increase in the axial mass dispersion coefficient slightly changes the breakthrough of CO_2.

Figure 5.6 illustrates the trend of the pressure drop at the positions z=0 and z=1 along the length of Bed 1 considering the results as obtained from the benchmark case (1.5 bar feed pressure) and from 1 bar feed pressure. Also it shows that the pressure drop follows the N_2 breakthrough profile. As the pressure drop across the bed is around 0.3 bar, attention has to be taken in the structure design of the first bed in order to significantly reduce the pressure drop. As mentioned in Chapter 4, the pressure drop can be reduced by changing the way that the material is structured inside the bed.

5.4.2 DAC Cycle Simulation Results

Figures 5.7 and 5.8 illustrate the pressure and CO_2 concentration profiles at the product end of each column over a cycle approaching a cyclic steady state. It has to be noted here that the y-axis in Figure 5.8, 'fluid CO_2 concentration', refers to the CO_2 concentration in the bulk-gas phase (fluid). Figure 5.8 also includes the CO_2 fluid concentration at position z=0. It is illustrated that CO_2 concentrations at z=0 in Beds 2–4 are higher. This is because the adsorption process starts from this position. With reference to Figure 5.8, Figure 5.9 illustrates the temperature profiles at z=0 and z=1 in each bed.

As Figure 5.7 shows, heating steps can take less than half an hour to complete, $\leq$1200 sec. As investigated by Marx et al. (2016), heating and cooling can take around 1800 sec and 1200 sec, respectively, considering a heat transfer coefficient between the wall and the heat exchanging fluid as 220 J m^{-2} s^{-1} K^{-1} and a heat transfer coefficient between the

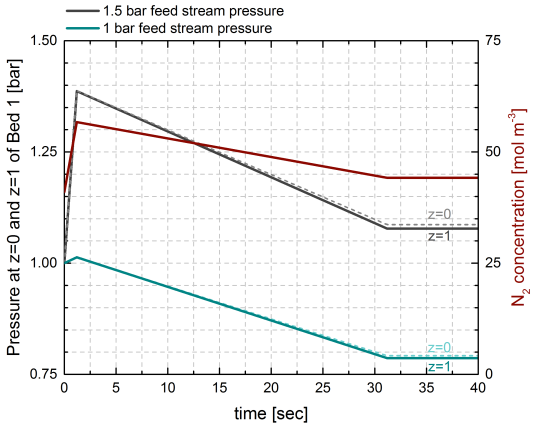

Figure 5.6. N_2 breakthrough simulation and pressure drop results of the DAC process on zeolite 13X at 293 K and 1 bar.

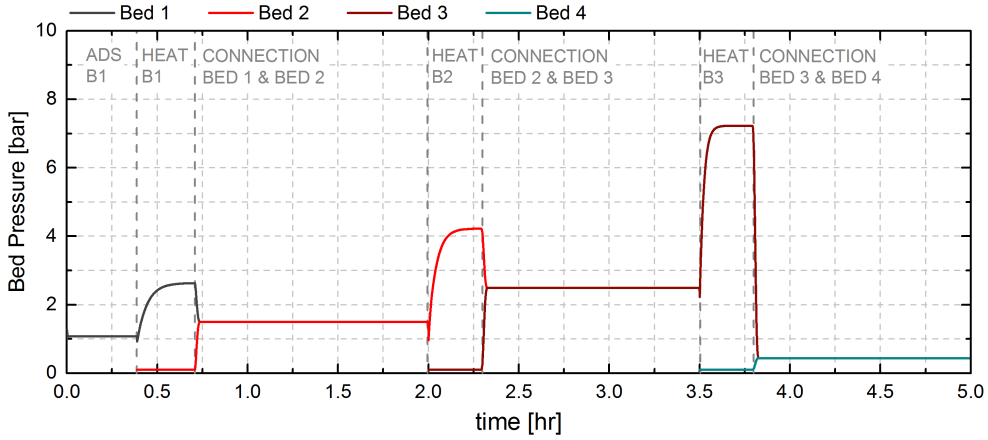

Figure 5.7. Pressure profiles at the product end of each column, z=1, over a cycle approaching a cyclic steady state of the four-column DAC unit (Run 1). Abbreviations: ADS, adsorption step; HEAT, heating step; B1, Bed 1; B2, Bed 2; B3, Bed 3.

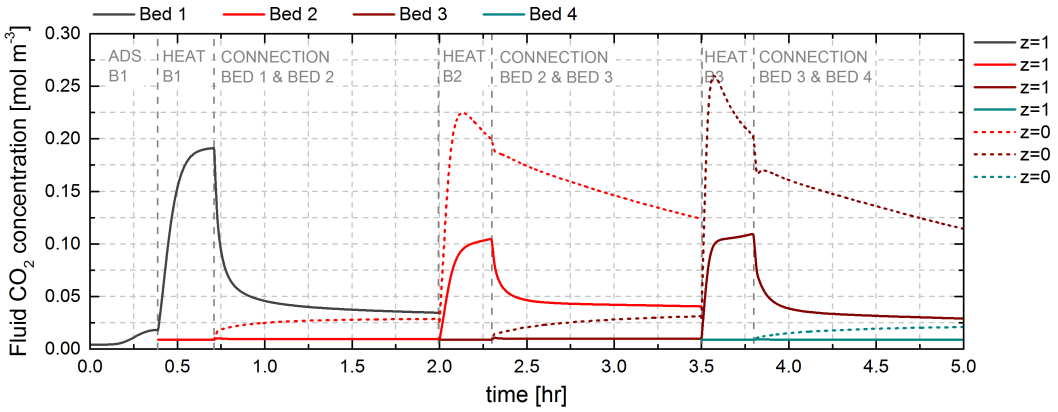

Figure 5.8. CO_2 concentration profiles at the product end of each column, z=1 (continuous curves), and at z=0 (dotted curves) over a cycle approaching a cyclic steady state at z=1 of the four-column DAC unit (Run 1). Abbreviations: ADS, adsorption step; HEAT, heating step; B1, Bed 1; B2, Bed 2; B3, Bed 3.

sorbent bed and the wall under conditions of flow as 35.3 J m^{-2} K^{-1}. Figures 5.10 and 5.11 represent the complete cyclic operation of Bed 1 considering the parameters of Table 5.2

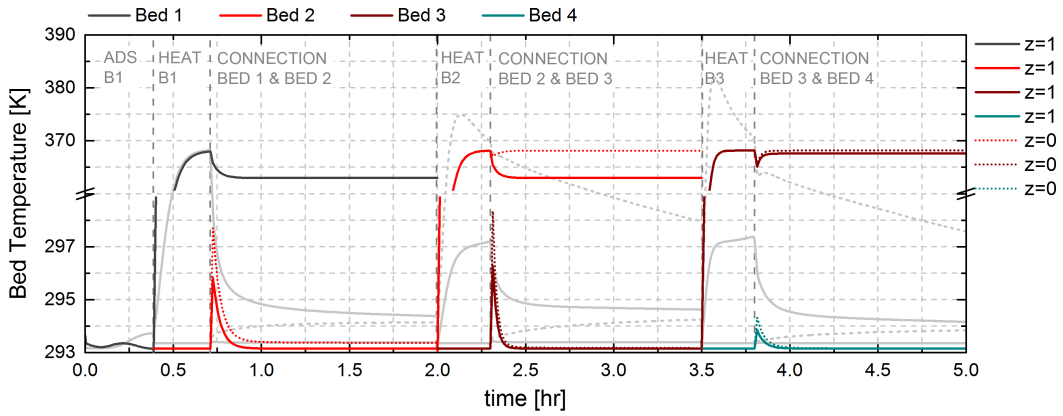

Figure 5.9. Temperature profiles at the product end of each column, z=1 (continuous curves), and at z=0 (dotted curves) over a cycle approaching a cyclic steady state of the four-column DAC unit (Run 1). Abbreviations: ADS, adsorption step; HEAT, heating step; B1, Bed 1; B2, Bed 2; B3, Bed 3.

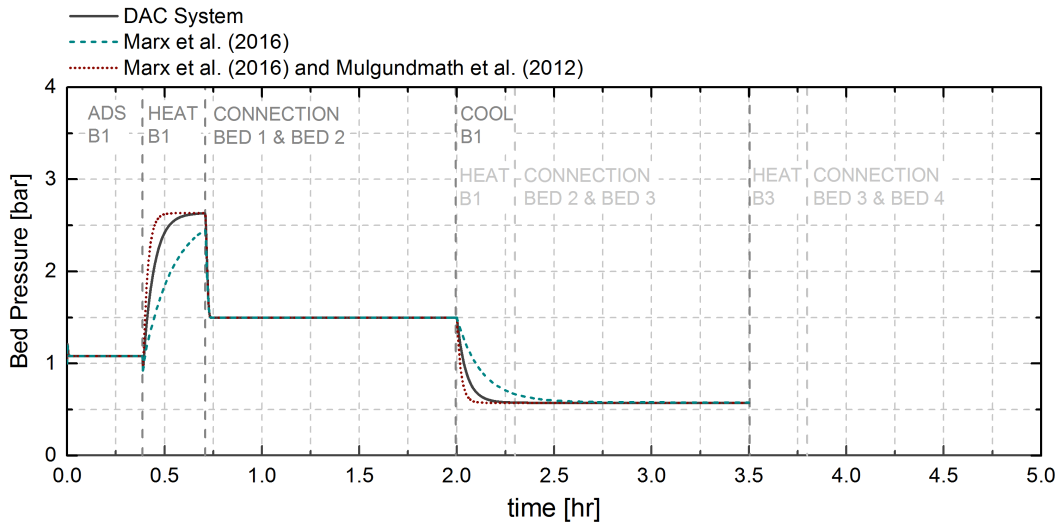

Figure 5.10. Bed 1 pressure profile at the product end of the column, z=1, over a cycle approaching a cyclic steady state (Run 1). Abbreviations: ADS, adsorption step; HEAT, heating step; B1, Bed 1; B2, Bed 2; B3, Bed 3.

and compare it with the ones of Marx et al. (2016). When using the experimental values given by Marx et al. (2016), the heating and cooling steps can reach a steady state slower than the parameters considered in this study. However, by considering a higher heat transfer coefficient between the sorbent bed and the wall (95 J m^{-2} K^{-1} (Mulgundmath et al., 2012)) and a 220 J m^{-2} s^{-1} K^{-1} (Marx et al., 2016) heat transfer coefficient between the wall and the heat exchanging fluid, a steady state in concentration and pressure can be reached faster than the other two cases reported (see Figures 5.10 and 5.11).

Heating up the columns requires time. However, the connection between the beds is more complicated since the beds operate at different temperatures, which create a temperature gradient and thus a concentration gradient. The pressure equilibrium between the two beds is reached within the first few seconds of being connected. However, the fluid concentration steady state is reached after around 14 hr of continuous connection between the two beds (see Figure 5.12) due to the temperature gradient and the self diffusion of the binary mixture.

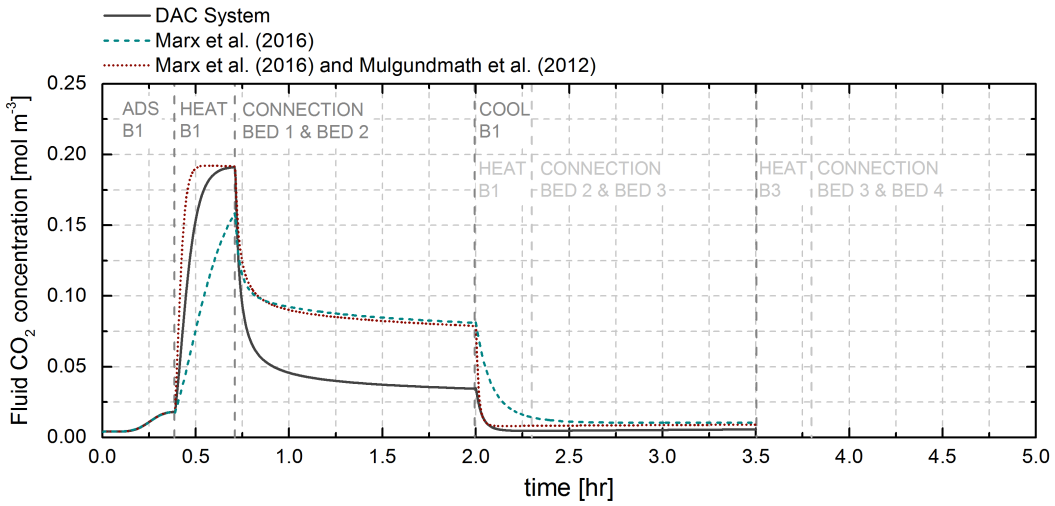

Figure 5.11. Bed 1 CO_2 concentration profiles at the product end of the column, z=1, over a cycle approaching a cyclic steady state (Run 1). Abbreviations: ADS, adsorption step; HEAT, heating step; B1, Bed 1; B2, Bed 2; B3, Bed 3.

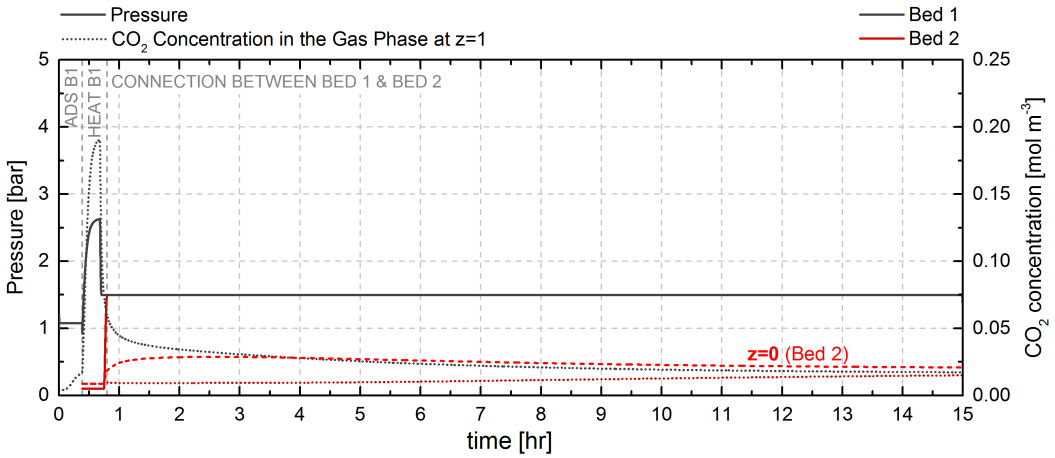

Figure 5.12. Pressure and CO_2 concentration profiles at the product end, z=1, of Bed 1 and Bed 2 approaching cyclic steady state. CO_2 fluid concentration profile at position z=0 of Bed 2 is also illustrated for comparison. Abbreviations: ADS, adsorption step; HEAT, heating step; B1, Bed 1.

The connection-between-two-beds time step has to be decreased such that the productivity or else the capture rate of the process, i.e. the amount of CO_2 that is produced by a unit mass of sorbent in a unit time ($kgCO_2\ kg_{ads}{}^{-1}\ hr^{-1}$), will increase. Therefore, it is of great importance to investigate the possibility of reducing the duration of this step or to identify factors that can increase the process productivity. Among other factors, the investigation whether an efficient adsorbed amount of the key component has been adsorbed before approaching a steady state has to be studied.

As stated by Joss et al. (2015) the adsorption/desorption steps of a TSA system are governed by heat transfer, which is inherently complex. From Figure 5.13a, it can be seen that the N_2 does not adsorb very much, as it breaks through almost immediately; however, some does adsorb, as evidenced by the moderate temperature increase throughout the bed. The CO_2, on the other hand, adsorbs significantly more, and breaks through much later. However, due to the dilute existence of CO_2 in the feed stream, the adsorbing CO_2 creates a front of a very

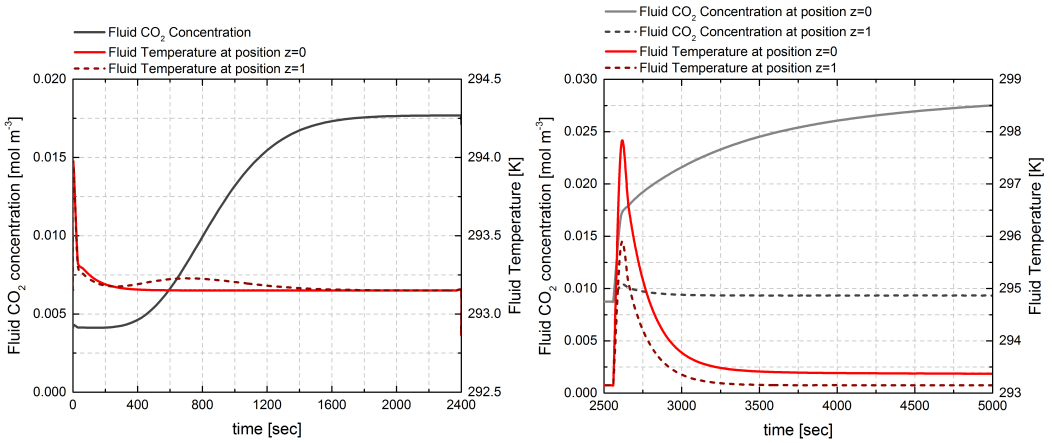

(a) adsorption in Bed 1 **(b)** adsorption in Bed 2

Figure 5.13. Temperature and CO_2 concentration profiles at the inlet, z=0, and outlet, z=1, of column for the case of: *(a)* adsorption in Bed 1 and *(b)* adsorption in Bed 2.

small temperature as it advances through the column. Thus, the adsorption step, due to the dilute nature of the most strongly adsorable species performs near isothermal conditions. A comparison of Figure 5.13a with Figure 5.13b illustrates that the temperature effect on the second bed is higher than the first bed. This is due to the higher concentration of the more strongly adsorbable species in the feed stream of Bed 2. The figure also illustrates that the temperature excursions happen at the same time at positions z=0 and z=1 of Bed 2. This can be explained by the instantaneous pressure equilibration, which creates a strong concentration gradient between the two beds such that the feed stream reaches the other end of Bed 2 instantaneously. It is expected that at a greater CO_2 concentration the adsorption kinetics of CO_2 will not only be dependent on the equilibrium parameters, but they will also be strongly affected by the temperature gradients between the beds. This effect has been extensively investigated by others (Hu et al., 2014; Joss et al., 2015).

The uneven concentration of Bed 2, as illustrated in Figure 5.13b, can explain the difference in the temperatures at the entrance (z=0) and exit (z=1) of Bed 2. Also, the step increase in the CO_2 concentration and fluid temperature in the first seconds of the connection between Bed 1 and Bed 2 step is because of the pressure gradient between the beds, which reaches a steady state instantaneously. The continuous CO_2 uptake of Bed 2 from Bed 1 is due to the temperature gradient between the beds and can be explained by the small temperature difference between the positions '0' and '1' of Bed 2. The temperature at the position z=0 is slightly higher since Bed 1 discharges its stream into Bed 2 at that position.

Figure 5.14 illustrates the fluid and adsorbed CO_2 profiles at different positions of Bed 1 and Bed 2 during the connection step. Since the dynamic behaviour of the connected beds is complex and steady states are expected to be reached after relatively long times, compromises between the steady state and the process capture rate have to be made. Figure 5.14 shows that the adsorbed CO_2 concentration in different positions of Bed 2 approaches the average adsorbed concentration, which happens to be at z=0.5 and >10 hr. At positions z=1 of Bed 1 and z=0 of Bed 2 the initial pressure difference between the two beds generates a concentration gradient, which exists from the first moment of the connection and lasts for few seconds. Steady state is reached after 15 hr of connection due to the dilute nature of CO_2 in each bed, the small concentration gradient due to the temperature gradient, and

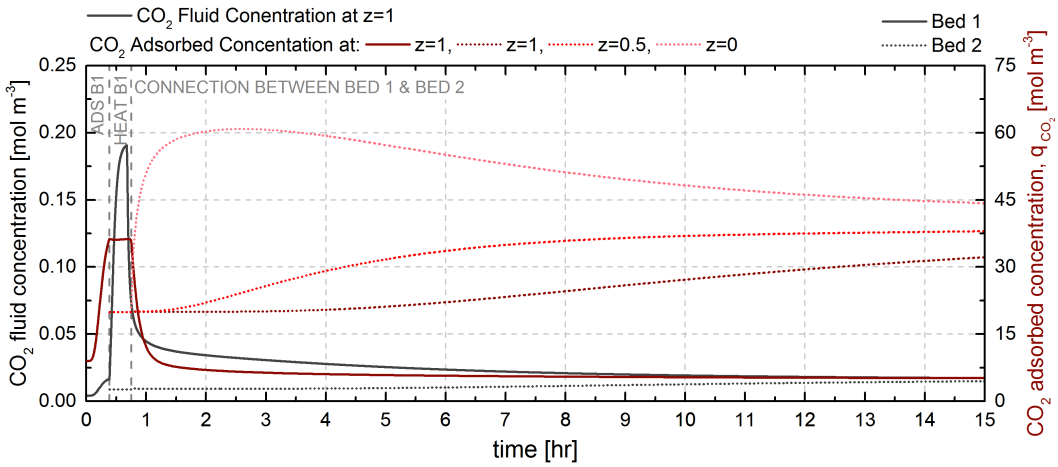

Figure 5.14. Fluid (gray curves) and adsorbed (red curves) CO_2 concentration profiles in Bed 1 and Bed 2 approaching cyclic steady state. Abbreviations: ADS, adsorption step; HEAT, heating step; B1, Bed 1.

the very slow self-diffusion of each gas from one bed to the other. It is also remarkable that after four hours of the process, the adsorbed CO_2 concentration of Bed 2 at z=0 decreases monotonically and the adsorbed concentration at other positions increases following similar trends. This phenomenon can be explained from the concentration wave that is created along the bed.

An important feature in the present DAC system is the compression and purification of CO_2 in the storage bed. Figure 5.15 presents the maximum adsorbed concentration in the inlet of the unit (at z=0). Figure 5.7 considers that each connection between Bed k and Bed k+1 takes around 2 hr. Figure 5.15 compares this case with longer operational times of each connection in order to increase the stored amount of CO_2. It was observed that longer operational times >20 hr result in greater average adsorbed amounts in the storage bed (31.4 molCO_2 m^{-3}). However, >20 hr for each connection between the beds result in a 65 hr total operational time[3] and results in a significantly low productivity.

In order to decrease the operational times, the following measures can be considered:

(i) Since by connecting two beds together (Bed k–1 and Bed k) the adsorbed amounts are concentrated in the inlet (z=0) of Bed k, Bed k should then discharge from the position z=0 into the next bed, Bed k+1. By applying these modifications to the process presented in Figure 5.3, resulted in the schematic illustrated in Figure 5.16. The modifications are marked in red.

(ii) Shorter lengths and higher diameters may decrease the required operational time of each connection. For this reason, Figure 5.17 considers different ratios of the length of the column (L) over the diameter of the column (D). It is shown that when D>L (see Figure 5.17a), the adsorbed amount trend is steeper. The maximum amount is reached faster at the position z=0 and is higher than that obtained by L>D. Figure 5.17b investigates different ratio of D/L. A ratio of D/L=2 requires less operational time for the connection steps and results in a higher CO_2 adsorbed amount in the storage

[3]Since there are three connection steps in each cycle (3×20 hr) plus the operating times as presented in Figure 5.7 (5 hr), the total operational time of the process becomes 65 hr.

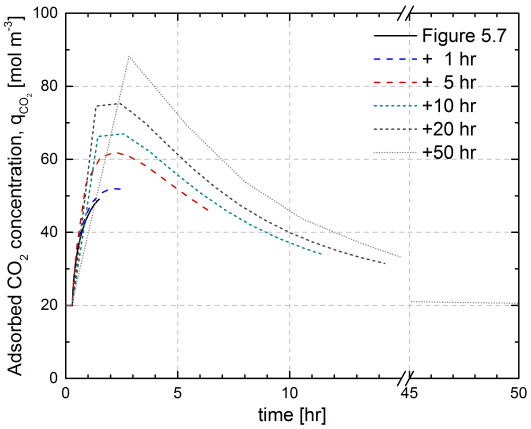

Figure 5.15. Adsorbed CO_2 concentration profiles in Bed 4 at 20 °C at different operational times.

Figure 5.7 considers that each connection between Bed k and Bed k+1 takes around 2 hr. The other cases are 3 hr (+1 hr), 7 hr (+5 hr), 12 hr (+10 hr), 22 hr (+20 hr), and 52 hr (+50 hr) operational times of each connection. The operational times for the rest of the steps of the process are the same as those illustrated in Figure 5.7. Therefore, the total operational times are (8, 20, 35, 65, and 155) hr, respectively.

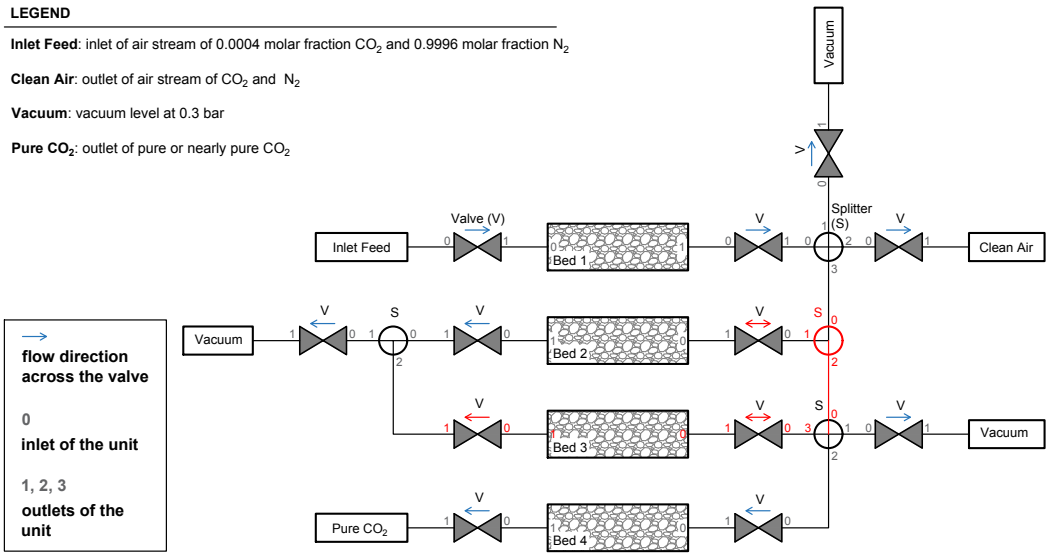

Figure 5.16. A new schematic representation of the direct air capture process in CySim. Abbreviations: V, valve; S, splitter; '0', inlet of the unit; '1', '2', and '3', outlets of the unit. Flow direction always follows from the '0' index to the either '1' or '2' or '3' index.

The modifications compared to Figure 5.3 are denoted with red colour.

bed (31.4 molCO_2 m^{-3}). This amount is the same with the one obtained by having $L>D$ and >20 hr operation of each connection step.

(iii) A smaller mass of the storage bed will lead to a higher equilibrium pressure after the connection between Bed 3 and Bed 4 and may increase the stored CO_2 amount. As Figure 5.18a shows, by keeping D/L=2 and reducing the mass of Bed 4 by a third or a tenth, a faster operational time for the connection step is required and higher average concentrations (around 40 molCO_2 m^{-3}) can be achieved (see).

(iv) Smaller masses in each bed will also increase the productivity of the process as the equilibrium-between-two-beds steps will require less time. This is investigated in

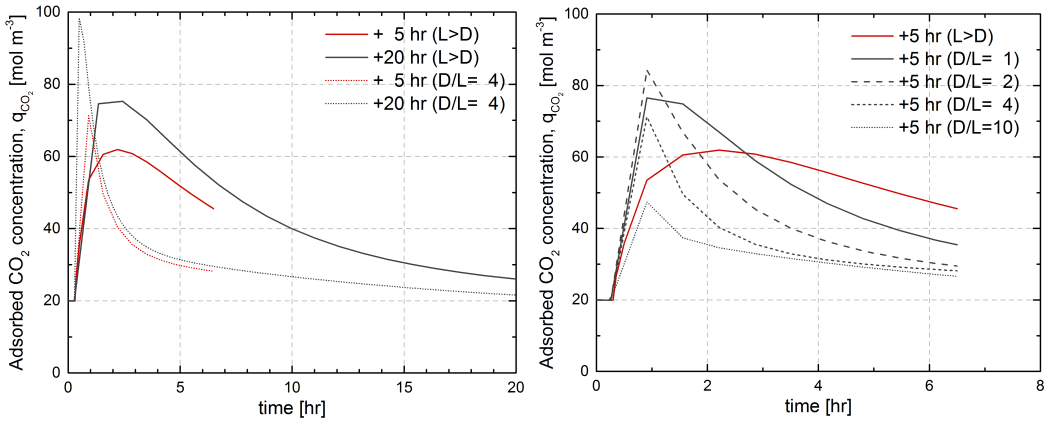

(a) $L>D$ versus $D>L$ **(b)** $D>L$

Figure 5.17. Adsorbed CO_2 concentration profiles at the inlet, z=0, of Bed 4 at 20 °C at different operational times considering different ratios of column length (L) over diameter (D): *(a)* $L>D$ and $D>L$ and *(b)* D/L=(1, 2, 4, or 10).

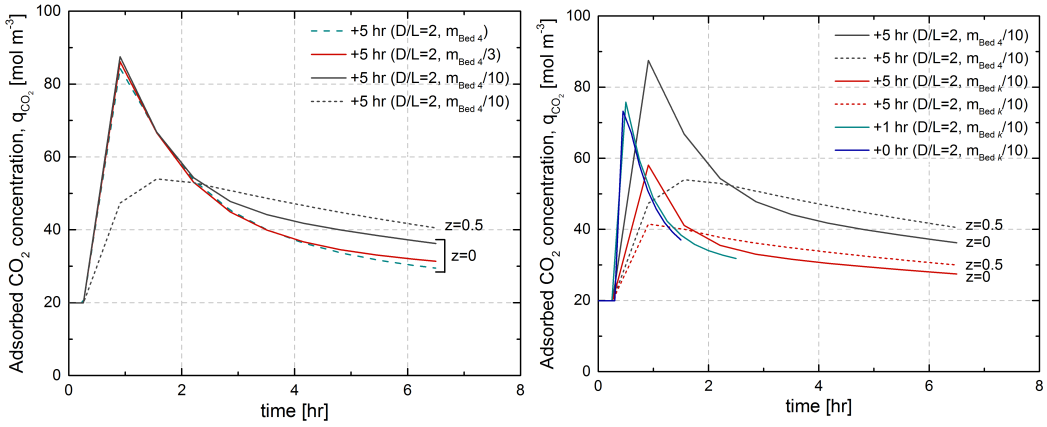

(a) smaller mass in Bed 4 **(b)** smaller mass in each bed

Figure 5.18. Adsorbed CO_2 concentration profiles at the inlet, z=0, of Bed 4 at 20 °C at different operational times considering less mass of adsorbent in each bed: *(a)* $m_{bed,4}/3$ and $m_{bed,4}/10$ and *(b)* $m_{bed,k}/10$.

Figure 5.18b. By reducing the mass of each bed by a tenth, the final amount that is stored reduces from around 40 to around 34 molCO_2 m^{-3}. However, the operational times is significantly reduced and consequently the productivity increases. The total operational time, therefore, can be reduced from 20 hr (noted here as +5 hr) to 5 hr (noted here as +0 hr).

Concluding, shorter beds (D/L=2) and reduced masses ($m_{bed,k}/10$) reduce the process operational time. Therefore, a further consideration on the optimal operational time of the process based on the average adsorbed amounts is investigated in Figure 5.19. It shows that similar adsorbed concentrations can be achieved by reducing the operational time of the connection between the beds. The total operational time can be reduced by a fifth (4 hr) and the average adsorbed amount is maintained at around 34 molCO_2 m^{-3}. This indicates that steady state times can be significantly reduced by considering effective masses and D to L ratios.

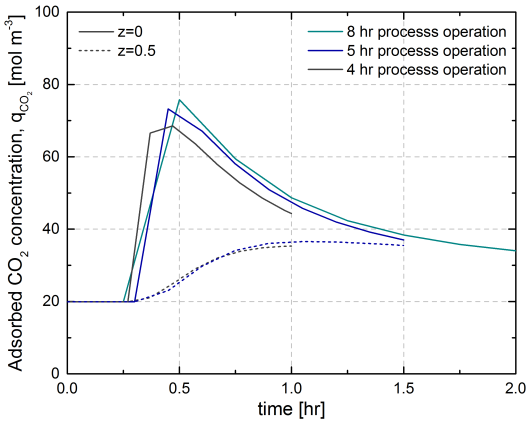

Figure 5.19. Adsorbed CO_2 concentration profiles at z=0 and z=0.5 of Bed 4 at 20 °C at different operational times.

5.5 Extending the DAC Cycle Simulation and Investigating the Performance of DAC

The results reported previously for the DAC cycle simulation refer to the first cycle of the process. Since more than one cycles could not be generated with CySim, in order to have a qualitative understanding of the performance of the DAC system, it is assumed that steady states are reached in each step of the process and the total operational time of a single cycle is 4 hr. This is a valid approximation as it has been shown using CySim that by selecting optimal masses and D to L ratios, steady state times in each step of the process can be significantly reduced resulting in 4 hr total operational time of a single cycle. The process, as described in Chapter 3, is able to capture 4 molCO_2 per kg of adsorbent in Bed 4 at run 60 (see Figure 3.26b), if the beds are filled with zeolite 13X. Therefore, the concentrations at each step of the process may follow the equilibrium ones as obtained from the equilibrium model in Chapter 3 and therefore the masses in each bed are: $m_{bed,1}$=0.1 kg, $m_{bed,2}$=0.02 kg, $m_{bed,3}$=0.005 kg, and $m_{bed,4}$=0.03 kg. Since 4 molCO_2 kg^{-1} of Bed 4 can be captured at run 60, 60 cycles will require approximately 240 hr to complete. This yields to a productivity of 0.0007 kgCO_2 $kg_{bed,4}{}^{-1}$ hr^{-1} or else 6.43 kgCO_2 $kg_{bed,4}{}^{-1}$ yr^{-1}. One must keep in mind that for a separation process to be viable, the plant must yield reasonable productivity (Joss et al., 2015). Thus, to increase the productivity of the process, more than one series of beds, including the adsorption bed and the compression and purification beds, must discharge into the same storage bed. Also, an optimised adsorbent material, other than zeolite 13X, may reduce the cycles of the process, yield to higher purity in the storage bed, and as a consequence, increase the process capture rate.

Since DAC is not only defending against energy and cost restrictions, the feasibility to process such a huge amount of air has to be considered. Therefore, Carbon Engineering and Climeworks developed an approach to have many blocks of smaller air contactors, such as 12' tall and 40' long (Holmes and Keith, 2012; Holmes et al., 2013), to maximise the surface air available for the adsorption of atmospheric CO_2 and to optimise the air turbulence and mixing. Climeworks states that its world's first commercial direct air capture plant in Hinwil, Switzerland, can remove 900 tCO_2 from ambient air per year, which requires 90 m^2 of land only for the eighteen air contactors. If each of the present DAC unit stores

100 tCO_2 per year and Bed 4 density is 900 kg m^3 (as ε_p=0.25), the bed should be filled with 15.5 tn of 13X. This is equivalent to a bed having an 3.5 m diameter and 1.8 m length. As previously discussed, small masses decreases the process operational time. Therefore, either very small air capture prototypes have to be designed or multi-series of Bed 1 and the beds that consist the compression and purification train have to discharge in the same storage bed. By assuming that the ratio between the masses of the storage bed and Bed 1 is 0.3 and the Bed 1 density is 600 kg m^3 (as ε=0.5), the total adsorbed amount that the air contactors have to be filled with is 51.7 tn of 13X. This is equivalent to a 11.25 m^2 of land and around 7.5 m (L) $\times$ 7.5 m (H) $\times$ 1.5 m (W) of air contactors. Then, a total of 10.3 tn of 13X in Bed 2 and 2.6 tn of 13X in Bed 3 are also required. Also, to have a cycle completed in 4 hr, 510K contactors have to be built. This number is unprofitable.

Otherwise, if the mass scaling factor $m_{4,\mathrm{scale}}$ [kg] follows:

$$m_{4,\mathrm{scale}} = i\, m_{4,\mathrm{d}}, \qquad \text{where} \quad i = 10^j \quad \text{and} \quad j = 1, 2, 3, 4..., \tag{5.44}$$

the total operational time $t_{\mathrm{T,scale}}$ [hr] may scale as:

$$t_{\mathrm{T,scale}} = 5^j\, t_{\mathrm{T,d}}\, N_{\mathrm{C}}. \tag{5.45}$$

Here, $m_{4,\mathrm{d}}$ [kg] denotes the designed mass of the storage bed as considered in the dynamic model (0.03 kg), $t_{\mathrm{T,d}}$ [hr] is the designed total operational time (4 hr), and N_{C} is the number of cycles (=60).

If the scaling factor j=0, then the capacity of the air capture unit is 0.53 gCO_2 per day. Considering the scaling factor, the capacity becomes:

$$\mathrm{SC}_{13\mathrm{X}} = 96\, \frac{m_{4,\mathrm{scale}}}{t_{\mathrm{T,scale}}} = 96\, \frac{10^j\, 0.03}{5^j\, 240}, \tag{5.46}$$

where $\mathrm{SC}_{13\mathrm{X}}$ is the scaled capacity in [$molCO_2$ day^{-1}]. Specifically, if a scaling factor of j=10 is selected, the capture capacity of the unit may reach 541 gCO_2 per day. Climeworks stated that their first prototype can reach a capacity of 135 $kgCO_2$ day^{-1}. This capture capacity can be achieved here with a scaling factor of j=18. Since the capacity of their material is stated to be <1 mol kg^{-1} (Wurzbacher et al., 2011), much faster adsorption kinetics have been achieved. If the number of runs here can be reduced to 6, e.g. by adding more beds, the capture capacity becomes 5.3 gCO_2 day^{-1}. Then, around 173 $kgCO_2$ day^{-1} can be captured if a scaling factor of j=15 is selected. This means that each cycle has to be completed within minutes or even seconds in order to have an efficient capture rate. Alternatively, having more than one series of beds discharging into the same storage bed, faster capture rates can be achieved.

6 Development of a Proof-of-Concept Experimental Apparatus

> *Il ne fallait jamais faire des expériences pour confirmer ses idées, mais simplement pour les contrôler.*
> *We must never make experiments to confirm our ideas, but simply to control them.*
>
> **— Claude Bernard**
> (French physiologist)

6.1 Introduction

The aim of this study is to develop an efficient unit, a prototype, capable of capturing CO_2 and releasing a compressed and purified CO_2 stream at conditions suitable for CO_2 storage. Therefore, after the examination of the adsorption equilibrium and non-equilibrium of the DAC system, the optimisation of the process, and the theoretical and experimental investigation of possible used adsorbent materials, the design and development of the experimental system follows. The steps that were considered in the development of the system are presented in Figure 6.1. The current status of the DAC development is the prototyping. An experimental apparatus is designed and realised not only to validate the results obtained from the previous analysis but also to prove the concept of the capture, compression, and purification of an extremely dilute CO_2 by using low grade heat.

This chapter mainly focuses on describing: *(i)* the design of the apparatus with emphasis on the volume of each bed and the maximal design pressure and purity in the storage bed, *(ii)* the process and instrumentation diagram (P&ID), *(iii)* the main instruments of the system for data collection and monitoring and their suppliers, *(iv)* the description of the experimental system, and finally *(v)* the operation of the system. Since the validity of an experiment is directly affected by its construction and execution, attention to the experimental design is extremely important.

6.2 Design and Considerations for the Experimental Apparatus

The use of zeolite 13X, AQSOA-Z02 and/or Y-S3-50 adsorbents were considered for the initial design. Therefore, a drying system had to be placed prior to the separation of CO_2 due to the competitive adsorption of CO_2 and H_2O as investigated in Chapter 4. For the design of the drying system, the design of the first adsorption bed had to be prioritised. However, this is restricted to: *(i)* the relative mass of the storage bed, *(ii)* the designed purity, *(iii)* the

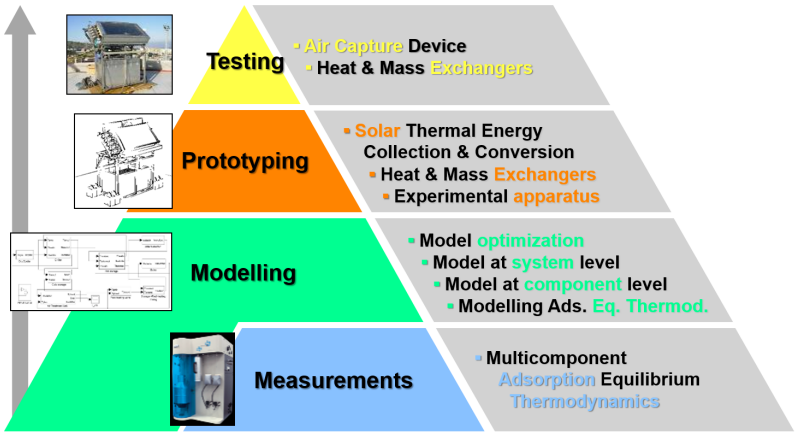

Figure 6.1. Steps of development of the Direct Air Capture prototype.

number of beds in the system, and *(iv)* the limitations imposed by the design requirements. The *(iv)* is due to the shape and mass of each bed, especially the last compression and purification bed (Bed N_B–1), and the connections required between the inlet and outlet. Figure 6.2 illustrates the design of Bed 1.

Cold plate coolers (CP-036HT Peltier – thermoelectric cold plate) from TE Technology, Inc. (2010) have been selected for heating up and cooling down the beds. The structure and the dimensions of the heat plate imposed limitations on the design of the beds. Therefore, the beds have a larger surface/diameter and less mass of adsorbent, which is achieved by a reduction in height, for better heat transfer. A cylindrical structure has been selected for a homogeneous flow distribution in the bed. It was also easier to construct the bed using the cutting and shaping machines available in the University of Edinburgh workshop. The beds were made from aluminium due to its reasonably high heat transfer. Since the bed wall thickness affects the heat transfer rate, particular attention to its design was taken.

For this initial design, the number of beds is fixed to four. Therefore, the maximum masses, and consequently the dimensions of each bed are:

Bed 1: 30.0 g of material, considering the use of zeolite 13X pellets. Therefore, a 1200 kg m^{-3} pellet density, a 0.37 void fraction of the bed, and a 4 mm diameter of the pellets, as obtained from Oreggioni et al. (2015), are considered. Thus, the dimensions of the bed can be estimated. For Bed 1, the dimensions are 64 mm diameter (D) and 8.2 mm height (H). Optional aluminium plates of 1.5 mm width (W) can be placed at the bottom of the bed to reduce its height and therefore its volume.

Bed 2: 5.8 g of material, considering the use of zeolite 13X pellets. The dimensions of the bed are D=40 mm and H=5.2 mm. The limitation of the height is imposed by the diameter of the pellets.

Bed 3: 2.5 g of material, considering the use of zeolite 13X pellets. The dimensions of the bed are D=26 mm and H=5.2 mm. Special attention had to be taken due to the small size of the bed. The limitations of the height and the diameter of the bed are imposed by the number of inlets and outlets of the bed, since the NTP unions had to be placed at the top of the surface of the bed, as illustrated in Figure 6.2.

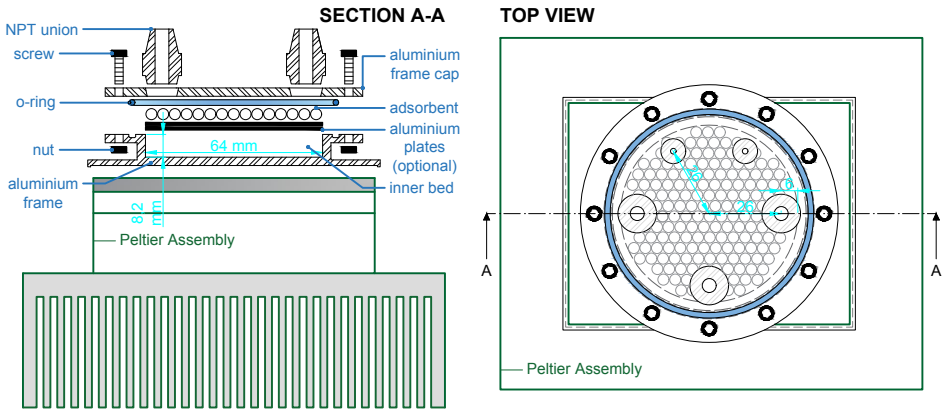

Figure 6.2. The top view and section A–A view of the circular packed Bed 1 of 64 mm diameter and 8.2 mm height, which is composed by: optional aluminium plates to be placed at the bottom of the bed, adsorbent pellets, aluminium frame cap, plastic o-ring and screws to seal the bed, and NPT unions for the connections of the inlet and outlets of the bed.

Bed 4: 51.1 g of material, considering the use of zeolite 13X pellets. The dimensions of the bed are D=70 mm and H=12 mm. Particular attention had to be taken since the designed pressure is considered to be >40 bar. Therefore, the limitation of the thickness of the walls of the bed had to be taken into consideration.

Optional aluminium plates of W=1.5 mm were prepared for all the beds and therefore, the volume can be readjusted. The analytical drawings of each bed are given in Appendix D.

For the design of the drying system, a relative humidity of 50% has been considered. The volume of the desiccant can be obtained by fixing the mass of Bed 1, the composition of CO_2 in the inlet stream, the flow rate of the fluid, and the H_2O adsorption capacity of silica gel and zeolite 5A. Hence, four drying columns have to be constructed, each one having H=0.5 m and D=1 in. Silica gel is used at the first half of the column as it is a great desiccant at high humidity content. Zeolite 5A is used at the second half of the column as it is a good desiccant at lower humidity content. Besides, zeolite 5A is employed as it has lower CO_2 adsorption capacity compared to other zeolites, such as 13X as reported by Wang and LeVan (2009). Therefore, humidity sensors prior and after the drier are required. In addition, a CO_2 sensor is also beneficial after the drying system, prior the entrance of the capture system.

6.2.1 Process and Instrumentation Diagram (P&ID)

The P&ID is presented in Figure 6.3 and highlights the major pieces of equipment, i.e. the drying system and the series of four connected beds, along with the stream information. The primary pipelines are denoted with a dark blue color and the secondary lines with a light blue color. An A4 P&ID drawing is provided in Appendix D.

A compressed air at 4–6 bar pressure and in 400 ppm CO_2, which is available from the university network, is used. This requires the use of a filter/regulator to filter out all the impurities, such as moisture, oil droplets, *etc*., prior entering the drying system. This is mainly due to the oil impurities that can cause degradation of the adsorbent in the drying columns. The pressure, temperature, and humidity are monitored before and after drying. CO_2 gas meters are placed before the inlet and after the outlet of Bed 1 to record the CO_2

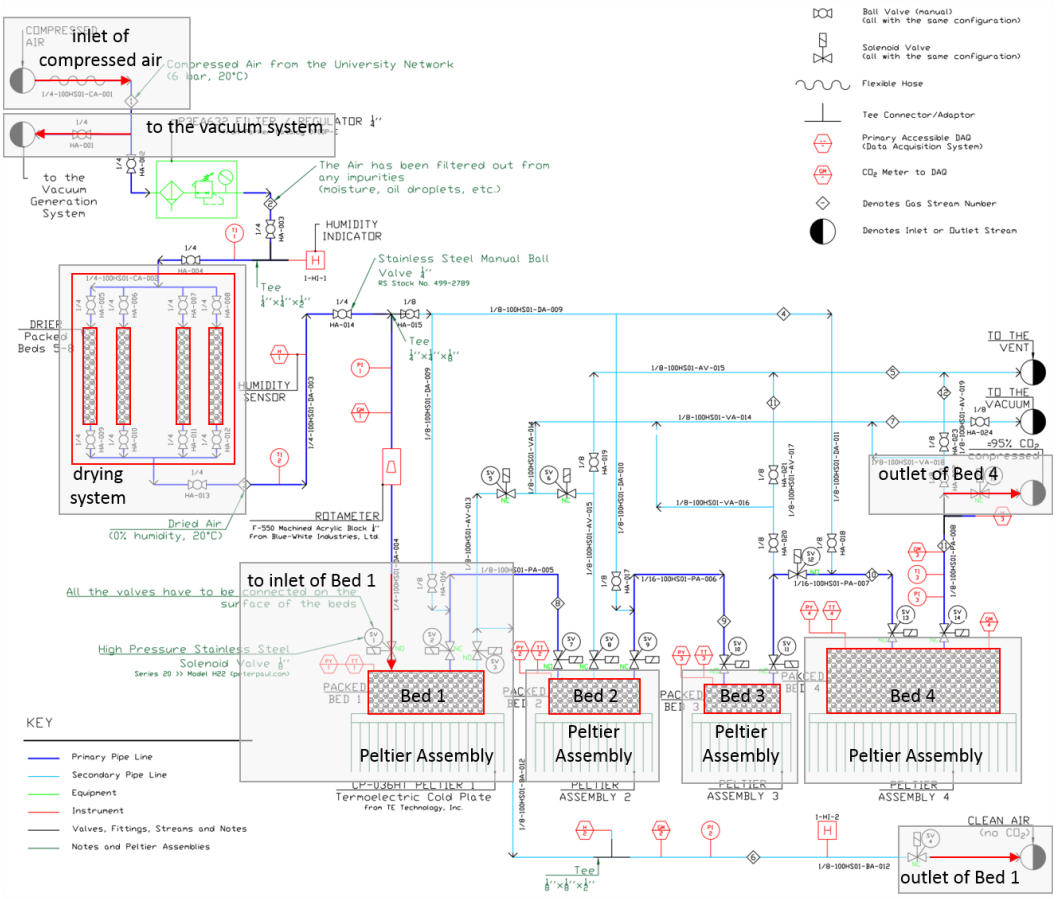

Figure 6.3. P&ID of the Direct Air Capture experimental apparatus highlighting the preliminary drying system, the Bed 1 inlet of the dried air and outlet of the clean air, the series of the four connected beds, and the Bed 4 outlet of the compressed air.

concentration. A rotameter is also placed prior to the inlet of Bed 1 to regulate the flow rate entering the bed. The pressure and humidity are also reported in the outlet of the clean air, in the exit of Bed 1.

The distance between each bed is reduced to the minimum distance possible, which is determined by the construction, in order to eliminate the void volume of the beds. Therefore, solenoid valves and NTP unions are connected to the surface of each bed. Pressure transducers and thermocouples are also connected on the surface of the beds, through NTP units, for pressure and temperature monitoring. All the columns, beds and pipelines are connected to the vacuum system and to the vent for the preliminary regeneration of the beds. Another CO_2 sensor is connected to the storage bed to record the required purity in the bed. Finally, pressure, temperature, humidity, and CO_2 concentration are also monitored in the outlet of the storage bed.

A 3D model of the process was designed using the software Solid Edge and is presented in Figure 6.4. All the parts composed the system are placed on a 1.3 m (H) x 1.3 m (L) x 0.6 m (W) trolley/cart, as illustrated in Figure 6.4a, to give an idea of the dimensions of the experimental apparatus and to help eliminating problems arising during the development of the system. Figure 6.4b also shows the series of the four beds that are connected close to each other to eliminate the piping and consequently, the void volume of the beds.

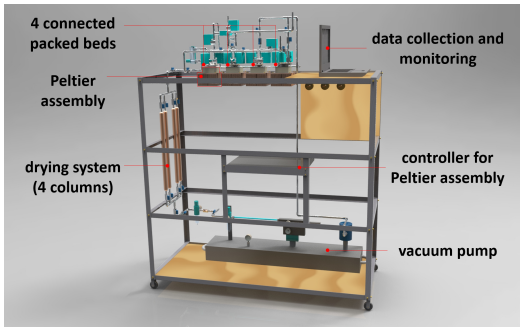

(a) the whole system

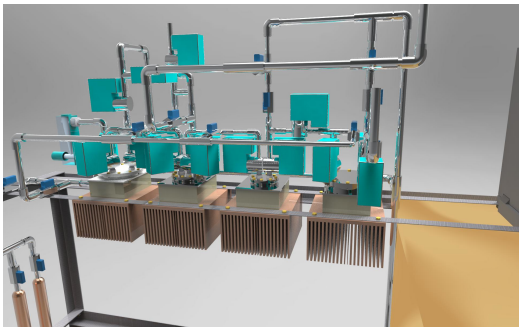

(b) a series of four connceted beds

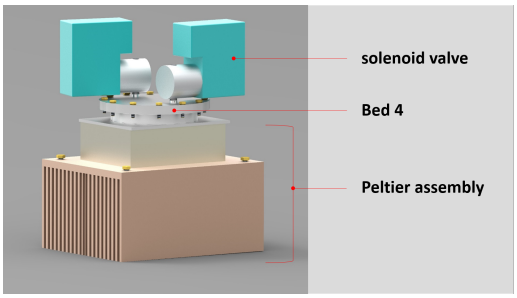

(c) Bed 4

Figure 6.4. A 3D model of the Direct Air Capture system as designed in Solid Edge: the drying system, the series of four connected beds, the Peltier assemblies, the controller to operate the Peltiers, and the vacuum pump.

6.2.2 Experimental Apparatus

A detailed description of that apparatus is given here. Compressed humid air at around 4 bar, as provided from the university network, enters the system through a flexible tube. Then, the compressed air flows through a filter/regulator (0...4 bar) to filter out any impurities, such as moisture, particles, oil droplets, *etc.*, and to control the pressure of the process. A thermocouple (type T Pt100 probe) has been placed before the drying system to measure the temperature of the H_2O adsorption in the four drying columns. The drying system, which is placed before Bed 1, consists of four columns of D=1 in and L=0.5 m. Once the dried air exits the columns, a humidity sensor (HC2A-SM probe) integrated with a temperature sensor (Pt100), a 1 1/2" dial pressure gauge (0...2 bar), and a CO_2 sensor (MinIR) are placed in-line for the collection of humidity and temperature, pressure, and CO_2 inlet concentration data, respectively. In addition, an air rotameter (Model FL-2011) is also placed prior to the inlet of Bed 1 to control the air flow. Details about the instrument specifications and accuracies are presented in Table 6.1.

Once the air is dried, it is then passed through Bed 1, at the position SV1 (solenoid valve 1) and exists it at the position SV3 (see P&ID in Figure 6.3). In the outlet line of Bed 1, a 1 1/2" dial pressure gauge (0...2 bar), a humidity sensor (HC2A-SM probe) integrated with a temperature sensor (Pt100), and a CO_2 sensor (Model 906) are placed for the collection of pressure, humidity and temperature, and CO_2 outlet concentration, respectively. Information about the instruments are listed in Table 6.1 and pictures of the experimental apparatus are presented in Figure 6.5. Each bed has a thermocouple (Pt100) and pressure transmitter (A-10) for the collection of data. Bed 4 is expected to be connected to a CO_2 sensor for

Table 6.1. Specifications and accuracy of the instruments used in the experimental apparatus.

Product		Description	Range of Application	Accuracy	Output Signal	Reference
Pt100	**1**	⋆ Type T stainless steel ungrounded thermocouple of 1.5 mm diameter and 50 mm length probe	0...350 °C	1 °C or 0.75%	Analog Output 4...20 mA (2-wire)	Omega Engineering Ltd
		⋆ Surface mount RTD Pt100 sensor with 0.9...2 sec response time	–73...260 °C	±0.15..0.35 °C (at 0...100 °C)	Analog Output 4...20 mA (4-wire)	
		⋆ RTD Pt100 probe with pot seal and spring strain relief of 1.5 mm diameter and 20 mm length probe	–50...300 °C	±0.15..0.35 °C (at 0...100 °C)	Analog Output 4...20 mA (2-wire)	
Pressure Transmitter A-10 WIKA	**2**	⋆ A-10 gauge with 1/8 NPT circular connector, –20...100 °C permissible medium temperature range	0...4 bar (for Bed 1) 0...10 bar (for Bed 2) 0...16 bar (for Bed 3) 0...25 bar (for Bed 4)	$\leq \pm 0.3\%$ non-linearity	Analog Output 4...20 mA (2-wire)	JWF Process Solutions Ltd
Humidity sensor HC2A-SM	**3**	⋆ ROTRONIC HYGROMER HT-1 with 12 sec response time ⋆ Integrated Pt100 1/3 Class B	0...100 %RH –50...100 °C	±0.5 %RH ±0.1 K	Analog Output 0..1 V	Rotronic Instruments Ltd
CO_2 sensor MinIR	**4**	⋆ Low power carbon dioxide sensor with 10...180 sec response time and operating conditions of 0.95...10 bar, 0...50 °C and 0...95 %RH	0...5%	±70 ppm ±5% of reading < 1% of FS non-linearity	USB Lead to the sensor	Gas Sensing Solutions
CO_2 sensor Model 906	**5**	⋆ Inline CO_2 Analyzer with 15...20 sec response time with an inlet flow of 5...1000 cc min^{-1}	0...5,000 ppm	±1% of reading or 0.2% CO_2 for 0...100% range	Analog Output 4...20 mA	Quantek Instruments Inc.
Air filter/regulator	**6**	⋆ Modular filter regulator Rc1/4 port with autodrain and 1 1/2" dial pressure gauge with Operating temperature range of –5...60 °C	0...4 bar			RS Components Ltd
Air rotameter	**7**	⋆ Model FL-2011 acrylic air flow meter and regulator	0.1...1.0 L min^{-1}	±5 %FS (up to 4,000 L min^{-1})		Omega Engineering Ltd
Pressure indicator	**8**	⋆ 1 1/2" dial pressure gauge with center back mount 1/8 NPT fitting	0...2 bar 0...42 bar	±2...3 %FS ±2...3 %FS		Omega Engineering Ltd
Peltier CP-036HT	**9**	⋆ CP-036HT Peltier thermoelectric cold plate (–26...100 °C requires 0...78 watts)	–10...100 °C			TE Technology Inc.
Controller LDD/TEC 19" Rack Enclosure	**10**	⋆ LTR-1200 (1 x TEC-1122). Basic: rack, interfaces, display, fans. TEC-1122-SV-Pt100 and 2 x temperature sensor cable ⋆ LTR-1200 (1 x TEC-1122, 1 x TEC-1123). Basic: rack, interfaces, display, fans. Power supply system: 3 x 12V/360W (TEC-1123) and 1 x 24V/400W (TEC-1122). TEC-1122-SV-Pt100, 1 x TEC-1123-HV-Pt100, and 4 x temperature sensor cable				Meerstetter Engineering GMBH
Mini vacuum pump	**11**	⋆ Mini pumpset DO 10 VTS 6 M	230...50 Hz			Vacuum Technologies Ltd
Vacuum regulator	**12**	⋆ Membrane-piston regulator with capacity 2...10 cum h^{-1} and room temperature –10...80 °C	1...800 mbar			
Suction Filter	**13**	⋆ FC 10 suction filter with paper cartridge with fluid temperature –20...60 °C, filter degree 5÷7 μ and max capacity of 15 cum h^{-1} ⋆ FB 10 suction filter with metal cartridge with fluid temperature –20...50 °C, filter degree 44 μ and max capacity of 10 cum h^{-1}	0.5...2,000 mbar 0.5...3,000 mbar			

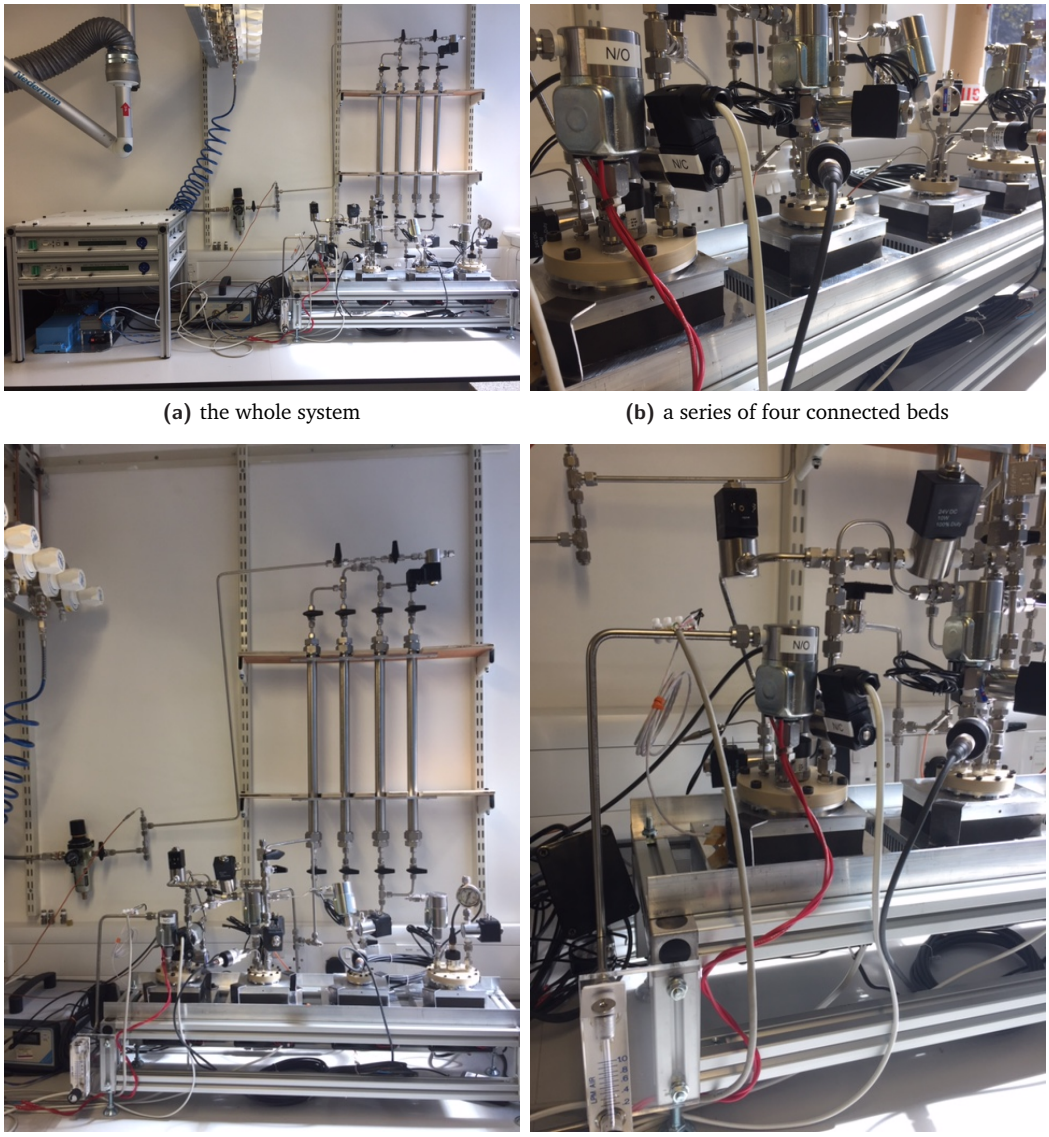

(a) the whole system

(b) a series of four connected beds

(c) the drying system and four beds

(d) Bed 1 and Bed 2

Figure 6.5. Pictures of the Experimental Apparatus.

the collection of the CO_2 concentration in Bed 4 in the end of each process cycle and final regeneration and discharge in the end of the complete process operation. Drawings that show the specific location of the instruments at the top of each bed are given in Appendix D.

In addition to the connections described, a mini vacuum pump (Mini pumpset DO 10 VTS 6 M) is connected with all the parts of the process, for the elimination of excess gases in the system prior to the process operation and for the optional vacuum steps in Bed 1 and Bed 2. Also, controllers (LDD/TEC 19" Rack Enclosure) are used to operate and control the temperature of the Peltier thermoelectric cold plates (CP-036HT). To operate both the Peltier and the controller, a surface mount RTD Pt100 sensor and a RTD Pt100 probe are connected at the surface of the bed and at the Peltier plate, respectively. Information about these parts are given in Table 6.1.

All the reported parts of the DAC apparatus are illustrated in Figure 6.6. The index number of each component in Table 6.1 is used to identify these components in Figure 6.6.

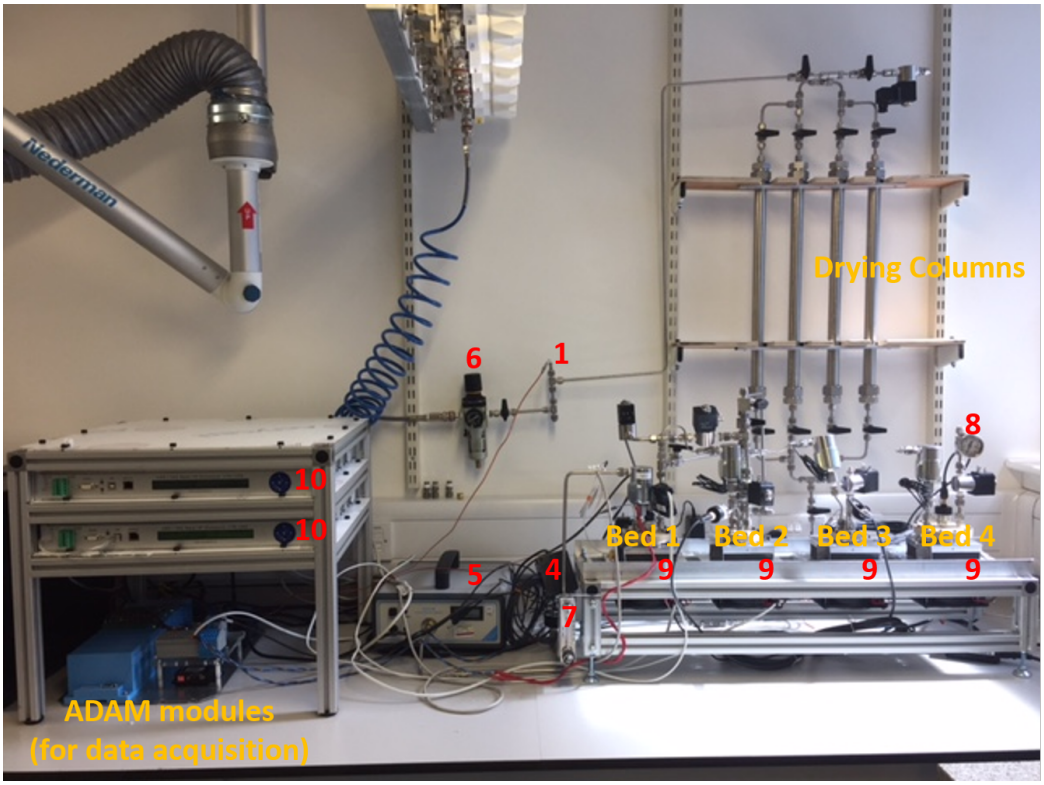

(a) the whole system

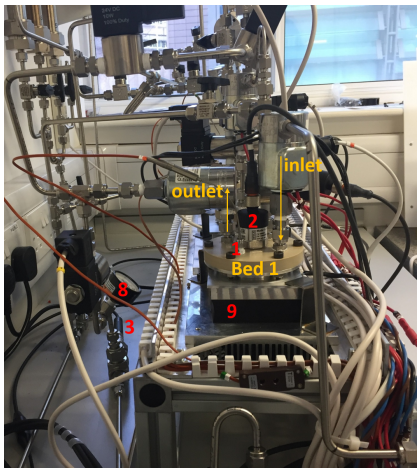

(b) Bed 1

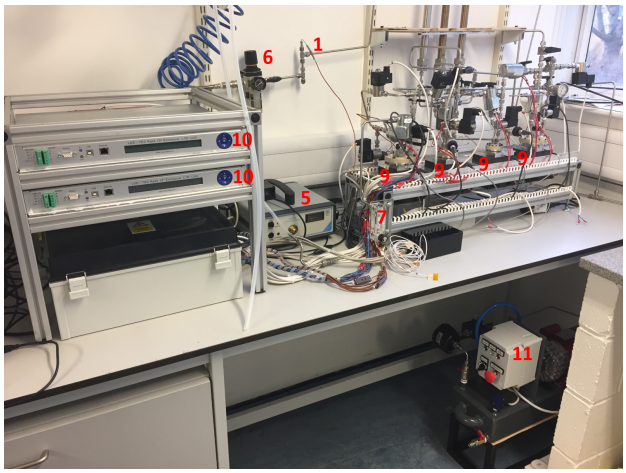

(c) including the vacuum pump

Figure 6.6. Pictures of the Experimental Apparatus including identification numbers as given by Table 6.1.

6.3 Valve Sequence

Tables 6.2 and 6.3 give the manual and solenoid valve sequences, respectively, following the process that has been analytical discussed in Chapter 3 and the P&ID of Figure 6.3. Table 6.3 also includes the required sequence for the Peltier assemblies for all the four beds including heating and cooling steps. Both the tables also include the evacuation of all the lines and the beds and the preliminary regeneration steps in order to remove the excess undesired

Table 6.2. Specifications and accuracy of the instruments used in the experimental apparatus.

Process	Steps	Notes	Valves																							
			HA-001	HA-002	HA-003	HA-004	HA-005	HA-006	HA-007	HA-008	HA-009	HA-010	HA-011	HA-012	HA-013	HA-014	HA-015	HA-016	HA-017	HA-018	HA-019	HA-020	HA-021	HA-022	HA-023	HA-024
Drying	1	Drying of ALL lines, beds & pieces of equipment	CV	OV	OV	OV	OV	OV	OV	OV	OV	OV	OV	OV	OV	OV	OV	OV	OV	OV	OV	OV	CV	CV	CV	CV
	2	End of the process	—	—	—	—	—	—	—	—	—	—	—	—	—	—	CV	CV	CV	CV	CV	CV	CV	—	—	—
		Notes: **1–2**, no power is needed to operate these valves.																								
Starting	1	Heating up ALL beds to T_{high}	OV	—	—	—	—	—	—	—	—	—	—	—	—	—	—	—	—	—	—	—	—	—	—	—
	2	Evacuation of the beds	—	—	—	—	—	—	—	—	—	—	—	—	—	—	—	—	—	—	—	OV	—	OV	—	OV
	3	Cooling down ALL beds to T_{low}	—	—	—	—	—	—	—	—	—	—	—	—	—	—	—	—	—	—	—	CV	—	CV	—	CV
		Notes: **1–3**, no power is needed to operate these valves.																								
Adsorption / Compression / Purification	1	Adsorption in Bed 1	—	—	—	—	—	—	—	—	—	—	—	—	—	—	—	—	—	—	—	—	—	—	—	—
		Sidestep between Steps 1 & 2	—	—	—	—	—	—	—	—	—	—	—	—	—	—	—	—	—	—	—	—	—	—	—	—
	2	Instantaneous vacuum of Bed 1	—	—	—	—	—	—	—	—	—	—	—	—	—	—	—	—	—	—	—	—	—	—	—	OV
		Sidestep between Steps 2 & 3	—	—	—	—	—	—	—	—	—	—	—	—	—	—	—	—	—	—	—	—	—	—	—	—
	3	Heating up to T_{high} of Bed 1	—	—	—	—	—	—	—	—	—	—	—	—	—	—	—	—	—	—	—	—	—	—	—	CV
	4	Equilibration between Beds 1 & 2	—	—	—	—	—	—	—	—	—	—	—	—	—	—	—	—	—	—	—	—	—	—	—	—
		Sidestep between Steps 4 & 5	—	—	—	—	—	—	—	—	—	—	—	—	—	—	—	—	—	—	—	—	—	—	—	—
	5	Instantaneous vacuum of Bed 2	—	—	—	—	—	—	—	—	—	—	—	—	—	—	—	—	—	—	—	—	—	—	—	OV
		Sidestep between Steps 5 & 6	—	—	—	—	—	—	—	—	—	—	—	—	—	—	—	—	—	—	—	—	—	—	—	—
	6	Heating up to T_{high} of Bed 2	—	—	—	—	—	—	—	—	—	—	—	—	—	—	—	—	—	—	—	—	—	—	—	CV
	7	Equilibration between Beds 2 & 3	—	—	—	—	—	—	—	—	—	—	—	—	—	—	—	—	—	—	—	—	—	—	—	—
	8	Heating up to T_{high} of Bed 3	—	—	—	—	—	—	—	—	—	—	—	—	—	—	—	—	—	—	—	—	—	—	—	—
	9	Equilibration between Beds 3 & 4	—	—	—	—	—	—	—	—	—	—	—	—	—	—	—	—	—	—	—	—	—	—	—	—
		Collection of purified stream in Bed 4	—	—	—	—	—	—	—	—	—	—	—	—	—	—	—	—	—	—	—	—	—	—	—	—
	10	Cooling down ALL beds to T_{low}	—	—	—	—	—	—	—	—	—	—	—	—	—	—	—	—	—	—	—	—	—	—	—	—
		Repeat steps 1–10 for $N_{\text{C}} - 1$ times	—	—	—	—	—	—	—	—	—	—	—	—	—	—	—	—	—	—	—	—	—	—	—	—
		Notes: **1–10**, no power is needed to operate these valves.																								
Collection	1	Heating up Bed 4 to T_{high}	CV	—	—	—	—	—	—	—	—	—	—	—	—	—	—	—	—	—	—	—	—	—	—	—
	2	Discharge purified stream	—	—	—	—	—	—	—	—	—	—	—	—	—	—	—	—	—	—	—	—	—	—	—	—
	3	Collection of purified stream	—	—	—	—	—	—	—	—	—	—	—	—	—	—	—	—	—	—	—	—	—	—	—	—
		Notes: **1–2**, no power is needed to operate these valves.																								

Abbreviations:
CD, Closed Valve; **OP**, Open Valve.
■, close the recommended valves and then heat up or cool down.

Table 6.3. Specifications and accuracy of the instruments used in the experimental apparatus.

Process	Steps	Notes	Valves																Peltier Assembly			
			SV1	SV2	SV3	SV4	SV5	SV6	SV7	SV8	SV9	SV10	SV11	SV12	SV13	SV14	SV15	SV16	P1	P2	P3	P4
Drying	1	Drying of ALL lines, beds & pieces of equipment	OV	CV	OV	OV	CV	CV	OV	OV	CV	OV	OV	CV	OV	OV	OV	CV	OFF	OFF	OFF	OFF
	2	End of the process	CV	—	CV	CV	—	—	CV	CV	—	CV	CV	—	CV	CV	CV	—	—	—	—	—
		Notes: **1**, power is needed to open **SV(4, 8, 11, 14, 15)** and to close **SV12**; **2**, power is needed to close **SV(1, 3, 7, 10, 12, 13)**.																				
Starting	1	Heating up ALL beds to T_{high}	—	—	—	—	—	—	—	—	—	—	—	—	—	—	—	OV	HU	HU	HU	HU
	2	Evacuation of the beds	—	—	OV	—	OV	OV	OV	OV	—	OV	OV	—	OV	OV	—	—	—	—	—	—
	3	Cooling down ALL beds to T_{low}	—	—	CV	—	CV	CV	CV	CV	—	CV	CV	—	CV	CV	—	—	CD	CD	CD	CD
		Notes: **1**, power is needed to close **SV(1, 3, 7, 10, 12, 13)** and to open **SV16**; **2**, power is needed to close **SV(1, 12)** and to open **SV(5, 6, 8, 11, 14, 16)**; **3**, power is needed to close **SV(1, 3, 7, 10, 12, 13)**.																				
Adsorption / Compression / Purification	1	Adsorption in Bed 1	OV	—	OV	OV	—	—	—	—	—	—	—	—	—	—	—	—	—	OFF	OFF	OFF
		Sidestep between Steps 1 & 2	CV	—	CV	CV	—	—	—	—	—	—	—	—	—	—	—	—	—	—	—	—
	2	Instantaneous vacuum of Bed 1	—	—	OV	—	OV	—	—	—	—	—	—	—	—	—	—	OV	—	—	—	—
		Sidestep between Steps 2 & 3	—	—	CV	—	—	—	—	—	—	—	—	—	—	—	—	—	HU	—	—	—
	3	Heating up to T_{high} of Bed 1	—	—	—	—	CV	—	—	—	—	—	—	—	—	—	—	CV	—	—	—	—
	4	Equilibration between Beds 1 & 2	—	OV	—	—	—	—	OV	—	—	—	—	—	—	—	—	—	—	CD	—	—
		Sidestep between Steps 4 & 5	—	CV	—	—	—	—	CV	—	—	—	—	—	—	—	—	—	OFF	—	—	—
	5	Instantaneous vacuum of Bed 2	—	—	—	—	—	OV	—	OV	—	—	—	—	—	—	—	OV	—	—	—	—
		Sidestep between Steps 5 & 6	—	—	—	—	—	CV	—	—	—	—	—	—	—	—	—	—	—	HU	—	—
	6	Heating up to T_{high} of Bed 2	—	—	—	—	—	—	—	CV	—	—	—	—	—	—	—	CV	—	—	—	—
	7	Equilibration between Beds 2 & 3	—	—	—	—	—	—	—	—	OV	OV	—	—	—	—	—	—	—	—	CD	—
	8	Heating up to T_{high} of Bed 3	—	—	—	—	—	—	—	—	CV	CV	—	—	—	—	—	—	—	OFF	HU	—
	9	Equilibration between Beds 3 & 4	—	—	—	—	—	—	—	—	—	—	OV	OV	OV	—	—	—	—	—	—	CD
		Collection of purified stream in Bed 4	—	—	—	—	—	—	—	—	—	CV	CV	CV	—	—	—	—	—	—	OFF	OFF
	10	Cooling down ALL beds to T_{low}	—	—	—	—	—	—	—	—	—	—	—	—	—	—	—	—	CD	CD	CD	CD
		Repeat steps 1–10 for $N_{\text{C}} - 1$ times	—	—	—	—	—	—	—	—	—	—	—	—	—	—	—	—	—	—	—	—
		Notes: **1**, power is needed to open **SV4** and to close **SV(7, 10, 12, 13)**, and then to close **SV(1, 3, 7, 10, 12, 13)**; **2**, power is needed to close **SV(1, 7, 10, 12, 13)** and to open **SV(5, 16)**, and then to close **SV(1, 3, 7, 10, 12, 13)**, and to open **SV(5, 16)**; **3**, power is needed to close **SV(1, 3, 7, 10, 12, 13)**; **4**, power is needed to close **SV(1, 3, 10, 12, 13)** and to open **SV2**, and then to close **SV(1, 3, 7, 10, 12, 13)**; **5**, power is needed to close **SV(1, 3, 7, 10, 12, 13)** and to open **SV(6, 8, 16)**, and then to close **SV(1, 3, 7, 10, 12, 13)** and to open **SV(8, 16)**; **6**, power is needed to close **SV(1, 3, 7, 10, 12, 13)**; **7**, power is needed to close **SV(1, 3, 7, 12, 13)** and to open **SV9**; **8**, power is needed to close **SV(1, 3, 7, 10, 12, 13)**; **9**, power is needed to close **SV(1, 3, 7, 10)** and to open **SV11**, and then to close **SV(1, 3, 7, 10, 12, 13)**; **10**, power is needed to close **SV(1, 3, 7, 10, 12, 13)**.																					
Collection	1	Heating up Bed 4 to T_{high}	—	—	—	—	—	—	—	—	—	—	—	—	—	—	—	—	—	—	—	HU
	2	Discharge purified stream	—	—	—	—	—	—	—	—	—	—	—	—	—	OV	OV	—	—	—	—	OFF
	3	Collection of purified stream	—	—	—	—	—	—	—	—	—	—	—	—	—	CV	CV	—	—	—	—	—
		Notes: **1**, power is needed to close **SV(1, 3, 7, 10, 12, 13)**; **2**, power is needed to close **SV(1, 3, 7, 10, 12, 13)** and to open **SV(14, 15)**; **3**, power is needed to close **SV(1, 3, 7, 10, 12, 13)**.																				

Abbreviations:
CD, Closed Valve; **OP**, Open Valve; **HU**, Peltier Assembly heats up the beds to T_{high}; **CD**, Peltier Assembly cools down the beds to T_{low}; **OFF**, Set Peltier Assembly off.
SV#, Normally Closed Solenoid Valve; **SV#**, Normally Open Solenoid Valve.
■, the valve opens only for few seconds for instantaneous evacuation; ■, close the recommended valves and then heat up or cool down; ■, cooling down to T_{low} step could also be performed at previous steps.

gases inside the system prior to the beginning of first process cycle (see 'drying' and 'starting' process in Tables 6.2 and 6.3).

The ten-step process in the 'adsorption/compression/purification' process of Tables 6.2 and 6.3 has to be repeated for N_C–1 times according to the required number of cycles of the process. Finally, the 'collection' process refers to the collection of the purified stream as it is discharged from the storage bed. For the collection of the purified stream, a small tank with a pressure transducer may be connected at the exit of Bed 4 (see Figure 6.3). The solenoid valves highlighted with a blue colour in Table 6.3 represent the normally open solenoid valves, which need electricity only for closing. The normally open, instead of the normally closed, solenoid valves were selected to avoid the temperature increase on the surface of the beds during each adsorption step, since when electricity is needed to operate the valves, it will cause an increase of the valve temperature. This will cause an increase of the bed temperature which is not favour during adsorption.

6.4 Future Improvements of the Design and the Performance of the DAC System

6.4.1 Improvements based on Pressure Drop Considerations

As previously discussed, the pressure drop is expected to be a great part of the total specific energy consumption due to the massive amount of air that has to be flow through the system. Let us simply assume that 10 tCO_2 need to be passed through the adsorption bed and that the CO_2 concentration in the inlet is 400 ppm. By assuming an ideal gas then the volume of the processed air can be calculated from the ideal gas equation of state. At atmospheric conditions, 1.367×10^7 m^3 of air per 10 tCO_2 have to be processed. Thus, the big issue here is the pressure drop through the bed and the required energy to balance pressure drop. As stated in Chapter 4, Section 4.2, it is feasible to improve the structure of the beds such that the energy requirements due to the pressure drop across the bed become far less significant. It has been shown that the specific energy use of a fan to capture 10 tCO_2 in a packed bed is 18.9 MJ mol^{-1} (50 MW power). In comparison, 24.5 kJ mol^{-1} (64.5 kW power) is needed in a structured packing.

6.4.2 Improvements of the Design of the DAC System

Heating and cooling cycles of the Peltier assembly are illustrated in Figure 6.7. The first part, A, is the cooling step at around 25 °C, which takes <1 hour to reach, starting from an initial wall temperature at around 14 °C. Then, the first heating step at 30 °C is illustrated, which takes about half an hour. The second heating step at 60 °C is reached within 20 mins. Therefore, the required heating and cooling times of the bed wall using the Peltier assembly are reasonable considering that due to kinetic and dispersive phenomena, cyclic steady state time steps are expected to require more time. The Peltier assembly is able to reach 60 °C within 1 hour of heating. Although, these cycles have to be maintained for a certain period in order to achieve the desired temperature inside the beds and the steady state conditions. That is something that has to be investigated once the complete data acquisition of the DAC system is ready. In addition, with the proper isolation around the beds and the

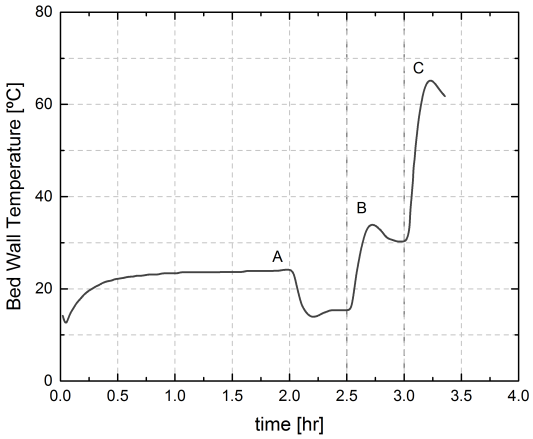

Figure 6.7. Bed wall temperature heating and cooling using Peltier assembly. Points: A, cooling and maintain at around 25 °C; B, first heating step at 30 °C; and C, heating step at 60 °C.

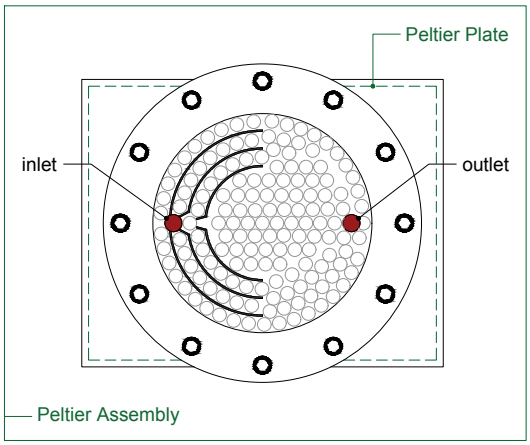

Figure 6.8. Alternative design for Bed 1. Red circles indicate the inlet and outlet of the bed as it is placed above the Peltier assembly and the top surface is removed: top view. Metallic thin elements have been placed around the inlet to enhance mass transfer.

Peltier elements and different current input to the Peltiers, higher bed wall temperatures are expected to be reached.

Since there are no experiments performed yet with the DAC system, the following recommendations on design and performance improvements are theoretical. At first, the inlet and outlet of the first bed have been designed at the top surface. Generally, packed beds are designed with the inlet on one side of the circular plane surface and the outlet on the other. Also, the biggest dimension is the length of the bed and not the diameter. Here, the actual length of the bed is the height of the bed and the biggest dimension is the diameter of the bed. This selection, as previously explained, is due to design requirements to increase the heat transfer between the heat plate and the bed wall. Since the Peltier plate has been selected, the inlet and outlet of the adsorption beds were placed at the top and a mono-layer of adsorbent pellets was designed in order to increase the heat and mass transfer. However, by placing thin metallic plates (0.4 mm) as illustrated in Figure 6.8 inside Bed 1, the heat and mass transfer inside the bed may be increased. Experiments with and without the plates will be needed in order to demonstrate this concept.

A sensitive part of the system is the packing of the adsorbent material inside the beds. The material cannot be regenerated inside the beds as very high temperatures, such as 200–300 °C, cannot be reached by the Peltier assembly. Since the material has to be regenerated in another station, it has to be carefully moved and placed inside the beds. A continuous flow of N_2 or an inner gas during the process of packing may reduce the amount of H_2O that can be adsorbed. Also, once the material is packed, the top lid has to be placed and the thermocouple has to be sealed first. Then, the bolts have to be screwed one at the opposite direction of the previous one.

Experimental data is needed in order to prove the concept of the separation of CO_2 from air and the compression and purification. Once the experimental data is collected, then more improvements on the design of the prototype can be suggested and the kinetic model can be built in order to more accurately describe the actual adsorption kinetics of the DAC process. Finally, the scaling-up performance and limitations can be obtained.

Conclusions and Perspectives

7

The world's unrivalled economic growth and prosperity have driven a period of unprecedented change; new needs, new requirements, new vulnerabilities, and subsequently new technologies. The challenge is to transition to technologies that simultaneously address the worlds' most fundamental demands, such as efficient systems, energy and economic competitiveness, and environmental responsibility. Carefully targeted research, development, demonstration, and deployment are essential to achieving improvements in cost and performance of a new technology. Advanced technologies can have significant impact on the next generation of challenges. Of these, deep reductions in GHG emissions have been proved to be essential.

Direct air capture technology takes a competitive advantage in the global shift to a zero-carbon world as it is the only current available option that can remove the thousand tonnes of CO_2 that have been emitted into the atmosphere since the beginning of the industrial era. However, the dilute nature of CO_2 in the atmosphere challenges researches as to how to find to find an efficient way to separate the air and to purify and compress the captured CO_2 to levels competitive to geological storage to, for instance, enhance the oil and gas recovery. Separating CO_2 from air is proved to be feasible. Although, challenges such as the reduction of the process energy consumption, the low capital and operational costs competitive to other carbon capture technologies, and the feasibility to process such a huge amount of air have to be addressed. Once the energy and economical costs become affordable and all the challenges and issues related with the deployment of air capture are clarified and resolved, air capture may play a significant role in controlling CO_2 emissions.

7.1 The Design and Development of an Air Capture Process

Here, an air capture process able to remove carbon dioxide directly from the atmosphere and compress and purify it through multiple adsorption/desorption stages by TSA has been presented. The process can be used as an intermittent process and/or a continuous process by small process modifications; however, the continuous process steps have not been considered for the purpose of this study. Commercial zeolite 13X has been extensively considered in the literature as a competitive adsorbent to separate CO_2 over N_2 even from extremely dilute streams. Here, the use of zeolite 13X as a benchmark physisorbent for air capture has been initially studied. Guidelines to process design as a result of process optimisation by considering the process steps and parameters, operational conditions, and adsorptive properties of the solid, are suggested. Specific energy consumptions at <2 MJ mol$CO_2{}^{-1}$ and final purities at $>95\%$ have been thermodynamically proved.

Since the adsorbent plays a significant role in the performance of a separation process by adsorption, a theoretical investigation on the physical properties of the adsorbent and an experimental investigation on two competitive materials for air capture have also been examined. Since the inlet feed stream is extremely diluted, large volumes of the stream have

to be processed in order to adsorb or remove a significant amount of the trace impurity. By considering the extremely high flow rates, pressure drops have to be eliminated to prevent high power consumptions. Therefore, high bulk void fractions especially in the adsorption contactor are essential. In addition, when water is present in the feed stream, air capture requires the pretreatment of the processed air prior to adsorption since physiorbents are largely more favourable to H_2O uptake than that of CO_2. Since physisorbents reduce the energy required for regeneration, solids that adsorb H_2O at high partial pressures and CO_2 at extremely low partial pressures in the feed stream can be superior. Type III or type V water adsorption isotherms can be more appropriate for air capture in order to avoid the adsorption of H_2O at lower partial pressures. Since water adsorption on AQSOA-Z02 follows the type V isotherm, pure CO_2 and N_2 adsorption and their co-adsorption have been studied experimentally. Although, H_2O uptake has been found to be higher than that of CO_2, another novel adsorbent, Y-S3-50, has been considered. The high uptake of CO_2 over N_2, competitive to zeolite 13X, seemed to be very promising; however, high H_2O uptakes have been recently reported from other researchers. Therefore, more research is still needed in order to design the suitable physisorbent for air capture.

The design of an optimal coupled material and adsorption process requires an accurate description of the mass and heat transfer through the bed and between the fluid and the porous adsorbent particles. By employing an in-house cyclic simulation, CySim, the dynamic investigation of the current air capture process has been studied. A process capture rate of 6.43 $kgCO_2\ kg_{ads}^{-1}\ yr^{-1}$ has been obtained. Nevertheless, better capture rates may be obtained by considering: *(i)* a higher number of beds in the compression and purification train of the process, such that the number of cycles of the process will be reduced significantly achieving the same or even higher purities, *(ii)* an adsorbent with greater selectivity and adsorption capacity that can increase the amount of captured, compressed, and purified CO_2 in the storage bed, *(iii)* an optimised design of the air separation unit, such as the deployment of many blocks of smaller air contactors that can maximise the surface air available for the adsorption of atmospheric CO_2 and optimise the air turbulence and mixing, and (iv) the deployment of more than one series of beds to discharge in the same storage bed.

Based on the theoretical equilibrium results as obtained from the optimisation of the process and material parameters, an experimental system has been developed to prove the separation, compression, and purification concept of the presented DAC process. Further tests on the apparatus and optimised designs are required before deciding on the optimal prototype.

7.2 Process Evaluation, Design Limitations, and Performance

It has been shown that the energy cost to separate CO_2 from air is expected to be less than 2 MJ $molCO_2^{-1}$, which is consistent with the calculations presented here and with the separative work, as obtained by employing the value function (Ruthven, 2014). The energy use is reduced as the CO_2 concentration in the feed stream increases. Thus, to separate CO_2 from closed atmospheres, such as marine and space crafts, less energy is required in comparison to capturing CO_2 from point sources such as fossil fuel power plants.

Table 7.1. Specifications and performance of air capture.

Property	Requirement	Reference
Solar energy available [a]	4.7–8.1 MJ m^{-2} day^{-1}	Santori et al., 2012
Minimum required purity	95%	Markewitz et al., 2012
Maximum level of impurities	y_{H_2O}<0.05%; $y_{N_2}+y_{O_2}+y_{Ar}$<4%	Markewitz et al., 2012
Recovery	50%	—
Specific energy demand [b]	< 45.4 MJ $kgCO_2{}^{-1}$	—
Surface area for 1 $GtCO_2$ capture	< 50 000–87 000 km^2	—
Capture Rate	> 380–660 tCO_2 ha^{-1} yr^{-1}	—
Pressure	> supercritical (73.8 bar for pure CO_2)	Mazzoccoli et al., 2014

[a] Assuming 50% of solar energy collection efficiency.
[b] Optimistic value obtained from the calculations of the value function (Ruthven, 2014; Ruthven et al., 2015).

For instance, approximate 120 kJ mol^{-1} is consumed by the post-combustion capture of CO_2 from the flue gas stream of a gas-fired power plant for urea production (Courtesy of Mitsubishi Heavy Industries Ltd.) in Malaysia (IPCC, 2005). This is around one order of magnitude lower than the energy required by a DAC system and one order of magnitude higher than the theoretical minimum work of DAC. Bringing the energy cost of DAC down to more affordable energy levels is stated as not unrealistic, although, it is challenging. Further research and development is needed in order to optimise DAC technologies so that they are available for deployment when urgently required.

The purity and pressure of CO_2 typically recovered from an amine-based chemical absorption process are as follows (Sander and Mariz, 1992)

(i) CO_2 purity is 99.9% by volume or more (under water saturated conditions).

(ii) CO_2 pressure is 50 kPa (gauge).

DAC prototypes are now able to deliver a purified stream of >97% at 5 kPa (Climeworks LLC, 2017). The DAC system here is able to provide such high purities, by considering specific adsorptive parameters, at much higher pressures, >20 bar. One must keep in mind that energy is also required to compress the purified stream at around 73.8 bar. Table 7.1 is repeated here to display the requirements of a DAC process. As previously discussed, by assuming that the energy of the DAC process is provided by solar energy, then the capture rate is 380–660 tCO_2 ha^{-1} yr^{-1}.

From previous investigations on a six-bed DAC process, after 50 runs of the process, around 2.32 $molCO_2$ or 0.102 $kgCO_2$ per kg of adsorbent in the first bed at 95% purity can be recovered after processing 6695 mol or 194 kg of air consisting of 400 ppm of CO_2. Therefore, for removing 3 $GtCO_2$ from the atmosphere, the extreme amount of 5700 Gt of air have to be treated annually. This is equivalent to the volume of a cube with edges of 167×10^3 km in length, whose surface area would be almost 55 times larger than that of the earth. It would appear that air capture is not going to be a feasible approach for tackling climate change unless the fast processing of air can be achieved. Let us assume that an ideal air capture system is developed, which is able to remove CO_2 from the air with 100% recovery. The amount of air that has to be treated in order to capture 3 $GtCO_2$ yr^{-1} is then 4936 Gt of air, very similar to the present DAC system. The questions here are: how many DAC devices will be needed globally; how much air each device can process and at what productivity; what is the most efficient way to process the air; if solar or wind energy are employed, which energy source and what locations are the most suitable ones; what is the energy rate available and what is the required land use?

Most estimates suggest that capturing, but not compressing, a stream of CO_2 from a coal-fired power plant will cost closer to about 30–60 US$ tCO_2^{-1} (IPCC, 2005; Ansolobehere et al., 2007; Rochelle, 2009). As stated in the literature, CO_2 abatement costs for DAC are high, ideally quoted between 100–200 US$ tCO_2^{-1} (Jones, 2008), once direct air capture systems are manufactured at scale. In order to capture 3.3 $GtCO_2$ yr^{-1}, an investment amounting to $330–660 bn yr^{-1} is required, which is equivalent to the total charitable donations of $390 bn yr^{-1} in 2016 (Giving USA, 2017).

At present, DAC plants would be extremely resource-intensive. After all, no one has built a large-scale plant yet; only a few laboratory plants and prototypes are in operation. In order to be effective, however, the plants would have to be constructed on an industrial scale. They would have to be of gigantic proportions, not to mention need incredible amounts of sorbent.

It is of the utmost importance that a research and development effort must be launched with the aim of finding out the best way to conduct air capture and what the cost would be. However, progress has been very slow as no one involved in this subject has found a way to raise the money necessary to move at the needed speed. The development of a viable, cost effective, and environmentally acceptable means of capturing CO_2 from the atmosphere will take decades. Research and development is urgently needed in order to have the technology available in few decades from now and be consistent with a <2 °C target.

7.3 Future Improvements of the Performance

The current study covers the early stages of development of a temperature swing adsorption process for the removal of CO_2 directly from the atmospheric air. The design of the process steps, the operational conditions, the design of the structured beds, and the adsorptive and physical parameters of the adsorbent have been investigated. However, these design guidelines have to be further investigated including all the dynamic parameters of the process, including heat and mass transfer phenomena inside the adsorbent. Also, the energy consumption of an air pre-drying unit has to be considered in the overall process energy consumption, unless a physisorbent with a higher selectivity of CO_2 over H_2O has been designed. Measures to improve the dynamic model have to be taken in order to achieve a representation of the dynamic behaviour of the specific DAC system. As discovered in this study, the process capture rate is significantly affected by the self-diffusion of the gases from one bed to the other due to the temperature gradient. Future improvements of the process performance have to employ ways to increase the productivity of the process, such as more than one series of beds, including the adsorption bed and the compression and purification beds, will discharge into the same storage bed.

The proposed system has been built in order to experimentally prove the concept of the CO_2 capture, compression, and purification. Directions to the proper design of the prototype must be further investigated by considering: *(i)* better heating and cooling options, such as heat channels inside a monolithic structure for the first bed, *(ii)* optimal bed designs, and *(iii)* the most suitable structured adsorbents.

The field of air capture is still in its infancy, but a more detailed analysis of various process designs and additional, low-cost processes are clearly needed, which provides many opportunities for engineers to play a crucial role in the development of the field.

A Thermodynamic Criteria for Equilibrium and the Approach to Steady State for Two Beds Closed Separator

A.1 Thermodynamic Criteria for Equilibrium Separation in a Closed Separator

Thermodynamic equilibrium between two or more phases or two or more regions requires the existence of thermal, mechanical, and chemical equilibrium. Thermal equilibrium is achieved if all phases and regions of the closed separator are at the same constant temperature. Mechanical equilibrium requires equality of pressure in all phases and regions of the separator. The transfer of species between two or more phases or regions achieves the chemical equilibrium. The criteria for equilibrium here will directly allow the calculation of different concentrations of a given species in different phases (Sirkar, 2014). This calculation presumes the existence of thermal and mechanical equilibrium. If the region is subjected to an external force field, the criterion for equilibrium separation is affected by the external potential field (Sirkar, 2014).

A.2 Equality of Chemical Potential at Equilibrium Between Gas and Adsorbed Phases

Equilibrium thermodynamics state that the chemical potential of a component (μ_i), which is the driving force for adsorption of a gas (Ruthven, 1984), should be the same for all phases that constitute the system (the gas and adsorbed phases). However, the equilibrium condition for equality of chemical potential in the solid and gas phases applies only to adsorbates (Myers and Monson, 2014). The chemical potential of a gas in a mixture is governed by (Myers and Monson, 2014)

$$\mu_i\left(T,\psi,x\right)=\mu_i^0\left(T,\psi\right)+RT\ln x_i, \qquad (\text{const. } T), \tag{A.1}$$

where μ_i is the chemical potential, μ_i^0 refers to the chemical potential in the standard state at the same temperature (T) and grand potential (ψ) as the mixture, and $x_i=\frac{f_i}{f_i^0}$. The chemical potential μ_i is the derivative of the Gibbs energy ($\mathrm{d}G$) with respect to the mole number in question, n_i:

$$\mu_i=\left(\frac{\mathrm{d}G}{\mathrm{d}n_i}\right)_{T,p,n_{j\neq i}}, \tag{A.2}$$

where n_j are the number of moles of the other components. Although it is not the easiest way in practice, a general approach of finding the equilibrium condition is by finding when

the Gibbs energy of the mixture is a minimum (Walas, 1985). At a given temperature and pressure, the stable phase will be the one with the lower Gibbs free energy. The equality in chemical potential is verified in Eq. (A.3a) to Eq. (A.3f) by minimising the Gibbs free energy of the total system at constant temperature and pressure as

$$\mathrm{d}G^{\mathrm{t}} = \mathrm{d}G^{\mathrm{a}} + \mathrm{d}G^{\mathrm{g}} + \mathrm{d}G^{\mathrm{s}}, \tag{A.3a}$$

$$\mathrm{d}G^{\mathrm{a}} = -S^{\mathrm{a}}\,\mathrm{d}T + \sum_i \mu_i^{\mathrm{a}}\,\mathrm{d}n_i^{\mathrm{a}}, \tag{A.3b}$$

$$\mathrm{d}G^{\mathrm{g}} = -S^{\mathrm{g}}\,\mathrm{d}T + V^{\mathrm{g}}\,\mathrm{d}P + \sum_i \mu_i^{\mathrm{g}}\mathrm{d}n_i^{\mathrm{g}}, \tag{A.3c}$$

$$\mathrm{d}G^{\mathrm{s}} = \mathrm{d}\mu^{\mathrm{s}} = -S^{\mathrm{s}}\,\mathrm{d}T + V^{\mathrm{s}}\,\mathrm{d}P. \tag{A.3d}$$

By minimizing G^{t} at constant T and p under the constraint of

$$n_i^{\mathrm{t}} = n_i^{\mathrm{a}} + n_i^{\mathrm{g}} = \text{constant}. \tag{A.3e}$$

If we consider that an amount of material $\mathrm{d}n_i$ moves from phase a to phase g so as $\mathrm{d}n_i^{\mathrm{g}} = \mathrm{d}n_i$ and $\mathrm{d}n_i^{\mathrm{a}} = -\mathrm{d}n_i$ then, $\mathrm{d}G^{\mathrm{t}}$ becomes

$$\mathrm{d}G^{\mathrm{t}} = \sum_i \mu_i^{\mathrm{a}}\,\mathrm{d}n_i^{\mathrm{a}} + \sum_i \mu_i^{\mathrm{g}}\,\mathrm{d}n_i^{\mathrm{g}} = \sum_i (\mu_i^{\mathrm{g}} - \mu_i^{\mathrm{a}})\,\mathrm{d}n_i = 0. \tag{A.3f}$$

A.3 The Approach to the Steady State Between Two Beds Operating at Different Temperatures

For the specific case of two packed-beds that are connected together, the following initial conditions for the two-bed's systems have to be considered: *(i)* different volume, *(ii)* different constant operation temperature, *(iii)* different initial pressure, and *(iv)* different initial concentration of the *i*th species in each bed. The considered imposed force fields (driving forces) in developing separation in this closed two-beds' system are the pressure, the temperature, and the concentration gradients. Once the two beds are connected together, the following effects occur:

(i) Non-equilibrium pressure gradient exerts bulk motion of molecules from high to low pressure regions.

(ii) Molecules diffuse from high concentration regions to low concentration regions.

(iii) The existence of a temperature gradient exerts unequal forces on molecules of different kinds such that the lighter gas species concentrates in the hotter region and the heavier gas species concentrates in the cooler region, known as thermal diffusion or Soret effect (Bird et al., 1960; Sirkar, 2014).

Under the assumption of a quasi-steady state, the concentration gradient due to temperature and concentration difference between the two beds have to be defined as pressure equilibration is expected to be reached rapidly.

A.3.1 Concentration Gradient/Self-Diffusion of Binary Mixture

The molar flux of species 1, N_1, is defined as the sum of the molar diffusive and convective fluxes of species 1 as

$$N_1 = J_1 + C_t\, y_1\, \upsilon_M, \tag{A.4}$$

where J_1 is the molar diffusive flux of species 1 due to concentration gradient, C_t describes the total concentration of the binary mixture, y_1 is the molar fraction of species 1, and υ_M is the mixture molar-averaged velocity. If there is no bulk flow (convection effect or bodily transport) of species 1 then

$$N_1 = J_1, \tag{A.5a}$$

$$\sum_{i=1}^{N_c} J_i = 0, \tag{A.5b}$$

$$J_1 = -J_2. \tag{A.5c}$$

Thus, in a binary mixture, the diffusion fluxes J_1 and J_2 are equal and oppositely directed. This phenomenon is known as equimolar counterdiffusion.

Fick's first law of diffusion states that in a binary mixture of gas 1 and gas 2 the diffusion flux of species 1 is proportional to its concentration gradient as

$$J_1 = -C_t\, D_{12} \nabla y_1, \tag{A.6}$$

where D_{12} is the diffusion coefficient and can be estimated by using an equation given by Bird et al. (1960). By considering that molar flux happens only in the z-direction, then Eq. (A.6) becomes

$$J_1 = -C_t\, D_{12}\, \frac{\mathrm{d}y_1}{\mathrm{d}z}. \tag{A.7}$$

For binary diffusion in a two bulb diffusion cell and under the assumption of quasi-steady state, the equilibrium diffusion time (relaxation time) can be calculated as shown by Duncan and Toor (1962). For nitrogen/carbon dioxide binary mixture, D_{12}=0.168 cm^2 s^{-1} (Duncan and Toor, 1962).

A.3.2 The Approach to the Steady State in Gaseous Thermal Diffusion of Binary Mixture

The forces exerted on gas species 1 in a binary mixture of 1 and 2 subjected to a temperature gradient, $F|_{\text{mol of 1}}$ [kg m^2 mol^{-1} s^{-2}], is governed by (Bird et al., 1960)

$$F|_{\text{mol of 1}} = -\frac{R\,T\,D_1^{\mathrm{T}}}{D_{12}\,C_1\,M_1} \nabla \ln T = F_{\mathrm{T1}}, \tag{A.8}$$

where D_1^{T} [kg m^{-1} s^{-1}] is the thermal diffusion coefficient of species 1 in a binary mixture of 1 and 2, D_{12} [m^2 s^{-1}] is the ordinary diffusion coefficient, C_1 [mol m^{-3}] denotes the number of molecules of species 1 per unit of volume, and M_1 [kg mol^{-1}] is the molar mass of species 1. An approximation for the coefficient D_{12} is given by Srivastava and Madan

(1953). A thermal diffusion ratio k_{T} has been defined (Bird et al., 1960; Brodkey and Hershey, 1988) as

$$k_{\mathrm{T}} = \frac{\rho_{\mathrm{t}}\, D_1^{\mathrm{T}}}{C_{\mathrm{t}}^2\, M_1\, M_2\, D_{12}}, \tag{A.9}$$

where $D_1^{\mathrm{T}} = D_2^{\mathrm{T}}$ as species 1 goes towards the hotter region, species 2 moves towards the cooler region. If the thermal diffusion ratio k_{T} for a given species 1 is positive, then, from Eqs. (A.8) and (A.9), it is concluded that species 1 moves due to the temperature gradient from the hotter region to the colder region, building up its concentration in the colder bulb. At equilibrium, or else at steady state, the temperature-gradient-driven flux of species 1 is balanced by that due to the concentration-gradient-driven flux in the opposite direction, since the two generated forces from the opposite direction must balance each other (Sirkar, 2014). The force on a mol of species 1 due to the temperature gradient in a binary mixture of species 1 and 2 is given by

$$J_i^{\mathrm{T}} = \frac{F_{\mathrm{T}1}}{f_1^{\mathrm{d}}}\, C_1 = -\left(\frac{R\,T}{D_{12}}\right) \frac{D_1^{\mathrm{T}}}{C_1\, M_1}\, (\nabla \ln T)\, \frac{C_1}{f_1^{\mathrm{d}}} = -\frac{D_1^{\mathrm{T}}}{M_1}\, (\nabla \ln T)\,, \tag{A.10}$$

where J_i^{T} [mol m^{-2} s^{-1}] denotes the temperature-gradient-driven molar flux, f_1^{d} [kg mol^{-1} s] represents the frictional coefficient of species 1 ($= R\,T/D_{12}$) and there is no bulk velocity. This flux is opposed by the diffusive flux J_1 of species 1 from a concentration gradient given by Bird et al. (1960) and Lawson and Yang (1973) as

$$J_1^{\mathrm{T}} = -\frac{D_1^{\mathrm{T}}}{M_1}\, (\nabla \ln T) = -J_1 = \frac{C_{\mathrm{t}}^2\, M_1\, M_2\, D_{12}}{\rho_{\mathrm{t}}\, M_1} \nabla x_1 \tag{A.11}$$

where C_{t} [mol m^{-3}] represents the total molecules of the binary mixture of species 1 and 2 per unit volume and x_1 is the molar fraction of species 1. Attention must be paid to every term as these considerations are applied only in the bulk gas phase of each bed. By assuming that species 1 and 2 move only in one coordinate direction and by considering Eq. (A.9) (Bird et al., 1960; Lawson and Yang, 1973)

$$-\frac{D_1^{\mathrm{T}}\, \rho_{\mathrm{t}}}{C_{\mathrm{t}}^2\, M_1\, M_2\, D_{12}} \frac{\mathrm{d}T}{T} = \mathrm{d}x_1 = -k_{\mathrm{T}}\, \frac{\mathrm{d}T}{T}. \tag{A.12}$$

The relation between the concentrations of the molecular species in a binary gas mixture and the temperature gradient is given in the Chapman-Enskog equation[1] (Grew, 1947; Srivastava and Madan, 1953). k_{T} can be expressed in terms of thermal diffusion constant a_{T} as $k_{\mathrm{T}} = -a_{\mathrm{T}}\, x_1\, (1 - x_1)$ as described by Lonsdale and Mason (1957) and Bird et al. (1960). Then Eq. (A.12) becomes

$$a_{\mathrm{T}}\, \frac{\mathrm{d}T}{T} = \frac{\mathrm{d}x_1}{x_1\, (1 - x_1)}, \tag{A.13}$$

which is also given by Shashkov et al. (1979). Integrating between region 1 (Bed 1) at T_1 and region 2 (Bed 2) at T_2 and considering the product $x_1\, (1 - x_1)$ to be a constant[2], Eq. (A.13) yields

$$a_{\mathrm{T}} \overline{x_1}\, \left(\overline{1 - x_1}\right) \ln \frac{T_1}{T_2} = x_1|_{T_1} - x_1|_{T_2} = x_{11} - x_{12} \tag{A.14}$$

[1] $\nabla c_1 = -\nabla c_2 = -k_{\mathrm{T}}\, \nabla \ln T$ (Grew, 1947)
where c_1 and c_2 denote the concentration of species 1 and 2, respectively.

[2] Separation generated by thermal diffusion is rather low; therefore the product $x_1\, (1 - x_1)$ is considered to be a constant at an average value of $\overline{x_1}\, \left(\overline{1 - x_1}\right)$ (Sirkar, 2014).

In order to calculate $(x_{11} - x_{12})$, the expression $a_{\mathrm{T}}\overline{x_1}\left(\overline{1-x_1}\right)$, which is equal to $-k_{\mathrm{T}}$, has to be calculated or estimated. Estimated values of k_{T} for the binary mixture of CO_2 and N_2 are given by Bastick et al. (1939). For illustration, a rough estimate of k_{T} for temperatures below 143 °C is 0.0119 (Bastick et al., 1939). Thus, in the case of T_1=95 °C (Bed 1) and T_2=20 °C (Bed 2), the $(x_{11} - x_{12})$ value is -0.0027, indicating about a 0.3% higher concentration of the heavier species CO_2 in the cool region (T_2 – Bed 2).

By considering the separation factor, $q(\infty)$

$$q(\infty) = x_1(\infty)/x_2(\infty), \tag{A.15}$$

then (Lonsdale and Mason, 1957)

$$\begin{aligned}
\frac{1}{q(\infty)} = \frac{x_2(\infty)}{x_1(\infty)} &= \frac{x_1(0)}{x_1(\infty)}\left[1 + \frac{V_1}{V_2}\frac{T_2}{T_1}\left(1 - \frac{x_1(\infty)}{x_1(0)}\right)\right] \\
x_2(\infty) &= x_1(0)\left[1 + \frac{V_1}{V_2}\frac{T_2}{T_1}\left(\frac{x_1(0) - x_1(\infty)}{x_1(0)}\right)\right] \\
x_2(\infty) - x_1(0) &= \frac{V_1}{V_2}\frac{T_2}{T_1}\left(x_1(0) - x_1(\infty)\right) \\
\frac{x_2(\infty) - x_1(0)}{x_1(0) - x_1(\infty)} &= \frac{V_1}{V_2}\frac{T_2}{T_1}.
\end{aligned} \tag{A.16}$$

Alternatively, from (Grew, 1947)

$$s = s'\left(1 + \frac{V_1}{V_2}\frac{T_2}{T_1} + \theta\right), \tag{A.17}$$

where $s = c_2(\infty) - c_1(\infty)$, $s' = c_2(\infty) - c_2(0)$, $c_1 = \frac{P}{RT_1}$, and $c_2 = \frac{P}{RT_2}$. θ is a function of the volumes of the connecting tube and of the temperatures. Here, θ is considered as negligible. Then Eq. (A.17) becomes

$$\begin{aligned}
c_2(\infty) - c_1(\infty) &= \left(c_2(\infty) - c_2(0)\right)\left(1 + \frac{V_1}{V_2}\frac{T_2}{T_1}\right) \\
P(\infty)\,T_2\left(\frac{1}{T_2} - \frac{1}{T_1}\right) &= \left(P(\infty) - P_2(0)\right)\left[1 + \frac{V_1}{V_2}\frac{T_2}{T_1}\right].
\end{aligned} \tag{A.18}$$

Eq. (A.16) or (A.18) can be considered in the system of equations given in Chapter 3, Section 3.3, to calculate the different molar fractions in each bed and the equilibrium pressure.

Benchmark Adsorbent Material: Zeolite 13X

B

B.1 CO_2 and N_2 single equilibrium adsorption on zeolite 13X regressed with mono-site Langmuir Equation

The benchmark case has been developed to confirm that the proposed process is thermodynamically feasible. The present case is restricted to the simple case of binary adsorption of trace impurity CO_2 (species (1) in the mixture) and secondary gas N_2 (species (2) in the mixture) on a commercial sorbent zeolite 13X. For this reason, data on pure-component CO_2 and N_2 adsorption on zeolite 13X from Xiao et al. (2008) had been used.

The success of multi-component adsorption relies heavily upon the accuracy of single-gas adsorption (Siperstein and Myers, 2001). For this reason, the following linear form of Langmuir isotherm was used for a better regression at low range of pressures and consequently more accurate predictions on Henry's regions[1]

$$\frac{1}{q_i} = \frac{1}{q_s} + \frac{1}{b_i\, q_s}\,\frac{1}{p_i}. \tag{B.1}$$

The Langmuir isotherm parameters, $b_{0,i}$, ΔH_i, and $q_{s,i}$, for each adsorbate gas i were extracted by simultaneous non-linear regression of the experimental isotherm data measured at different temperatures. To be thermodynamically consistent, the multi-component model assumes that an adsorbent has a fixed number of adsorption sites ($q_{s,i}$). $q_{s,i}$ was obtained from the regression of the more strongly adsorbed compound at the lowest measured temperature and was fixed as the same at all the rest of the measured temperatures and less adsorable gases.

The Henry constant, K, reported here as b, is temperature dependent through the van't Hoff equation: $\ln K = -\frac{\Delta H}{RT} + \frac{\Delta S}{R}$, where K is the equilibrium constant, ΔH is the standard enthalpy change and ΔS is the standard entropy change. Thus, $\ln K$ has a linear relationship with $-1/T$ if ΔH remains constant. By plotting $\ln K$ versus $-1/T$ at different measured temperatures, ΔH can be calculated from the slop and b_0 from the intercept that is equal to $\frac{\Delta S}{R}$.

Adsorption isotherms of carbon dioxide, nitrogen, and oxygen on zeolite 13X, which are collected for the results obtained from the dual-site Langmuir (Eq. (B.2)) fitting of the collected experimental data from Xiao et al. (2008), are plotted against the mono-site Langmuir equation in Figures B.1a and B.1b, respectively. Solid lines represent the mono-site Langmuir fitting and symbols illustrate the 'fake data' reproduced from the results from the data regression using the dual-site Langmuir for both gases at 298.15 K and 353.15 K. The results obtained from the regression are summarised in Table B.1.

[1] A correct fitting at low-pressure region is essential to describe multi-component data.

Table B.1. Mono-Site Langmuir isotherm parameters of pure CO_2, N_2, and O_2 on zeolite 13X.

Parameter	Unit	CO_2		N_2		O_2	
		298 K	353 K	298 K	353 K	298 K	353 K
q_s	mol kg^{-1}	4.00	4.00	4.00	4.00	4.00	4.00
b	kPa^{-1}	0.144	0.019	0.0004	0.0002	0.000008	0.000007
K_H	mol kg^{-1} kPa^{-1}	0.577	0.078	0.0016	0.0006	4.00	4.00
$\left(10^{-7}\right)$ b_0	kPa^{-1}	3.76	3.76	9.74	9.74	41.59	41.59
$(-)$ ΔH	kJ mol^{-1}	31.86	31.86	14.92	14.92	1.71	1.71

Note: Data obtained from Xiao et al., 2008 and regressed using the linear form of Langmuir isotherm.

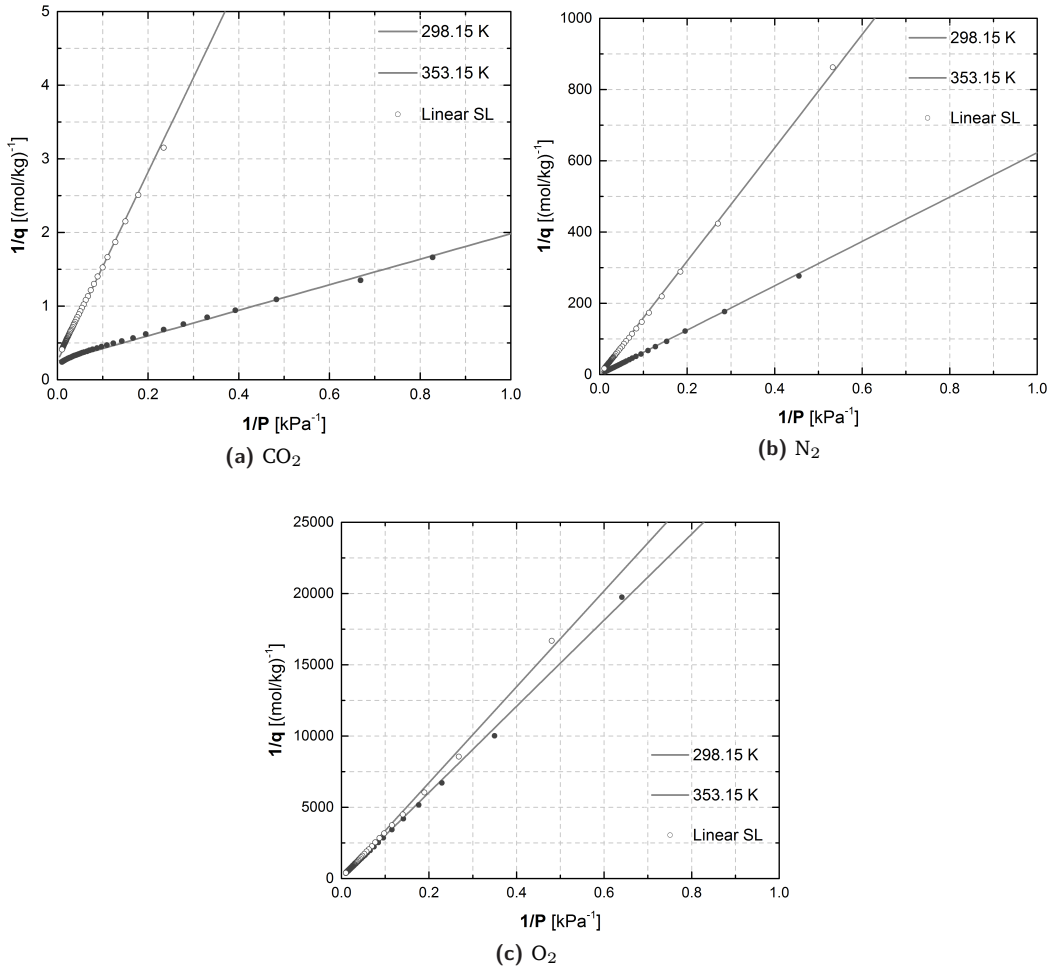

Figure B.1. Single component adsorption equilibrium isotherms of: (*a*) carbon dioxide, (*b*) nitrogen, and *(c)* oxygen on zeolite 13X at: 298.15 K (•) and 353.15 K (○). The solid lines represent the regression with the linear Langmuir equation.

The amount adsorbed following the dual-site Langmuir isotherm is calculated from

$$q = q_{s(1)} \frac{b_{0(1)}\, e^{\frac{-\Delta H_{(1)}}{RT}}\, p}{1 + b_{0(1)}\, e^{\frac{-\Delta H_{(1)}}{RT}}\, p} + q_{s(2)} \frac{b_{0(2)}\, e^{\frac{-\Delta H_{(2)}}{RT}}\, p}{1 + b_{0(2)}\, e^{\frac{-\Delta H_{(2)}}{RT}}\, p}, \tag{B.2}$$

where the subscripts (1) and (2) represent the adsorption sites.

Figures B.1a and B.1b prove that at all pressures, CO_2 is adsorbed strongly on zeolite 13X compared to N_2 and O_2. Carbon dioxide, nitrogen, and oxygen isotherms are type I isotherms, as has been established by Brunauer et al. (1940) and identified by IUPAC into

five classical types (Cortés, 1985; Thommes et al., 2015), indicating adsorption of gases in micropores.

Using the extended Langmuir equation for multi-component mixtures (Eq. 3.10 in Chapter 3, Section 3.3) in conjunction with the definition of selectivity given in Eq. (3.22 in Chapter 3, Section 3.3), it can be shown that the adsorbent selectivity of species (1) over species (2) is constant for the entire range of partial pressures (Yang, 2003) and follows

$$S_{1,2} = \frac{q_{s_1} b_1}{q_{s_2} b_2} = \frac{b_1}{b_2} \left(= \frac{K_1}{K_2} \right), \tag{B.3}$$

where the product ($q_{s_1}\, b_1$) corresponds to the initial slope of the isotherm, or else Henry's constant (K), for species i. The selectivity of CO_2 over N_2 at 298.15 K and 353.15 K is 360 and 95, respectively. The oxygen is the least strongly adsorbed compound compared to carbon dioxide and nitrogen and thus it is not considered in this analysis. The decrease of the selectivity with temperature, pressure, and the mole fraction of the preferentially adsorbed species is typical behaviour for binary adsorption (Myers, 2006).

Another important factor in the adsorption separation is the change in the adsorbed amounts of the two components upon cycling the pressure. This factor is known as working capacity[2] of the adsorbent material that typically refers to the strongly adsorbed species. The ratio of the working capacities of the two components give an idea about the adsorption performance for a particular state, which is defined as

$$W = \frac{\Delta q_1}{\Delta q_2}. \tag{B.4}$$

The adsorption performance W of CO_2 and N_2 on zeolite 13X for the adsorption step (A) at 298 K and the heating step (B) at 373 K, is plotted against a range of temperature and feed composition. These ranges are from 270 K to 320 K and from 100 ppm to 0.1% CO_2 in the feed stream of CO_2 and N_2 for the cases of 50 kPa and 101.325 kPa feed pressure as depicted in Figure B.2. Significant temperature difference between the two steps, higher feed concentration of component (1), and higher pressure in step (A) result in a higher working capacity, and subsequently greater performance of the sorbent. Working capacities of zeolite 13X for high pressure steps can be found in Balahmar et al. (2016).

B.2 Internal CO_2, N_2, and O_2 single equilibrium adsorption on zeolite 13X regressed with dual-site Langmuir Equation

Single equilibrium adsorption measurements of CO_2 and N_2 on zeolite 13X were also obtained from the Carbon Capture group at the University of Edinburgh. The regressed data using dual-site Langmuir isotherm at (283.15, 303.15, 323.15 and 343.15) K are illustrated in Figures B.3a and B.3b and the parameters are given in Table B.2.

These regressed data have not been used further in this study.

[2]The working capacity for TSA separations is defined as the difference between the adsorbed amounts at the adsorption (low temperature and pressure) and the desorption (high temperature and pressure) (Yang, 2003).

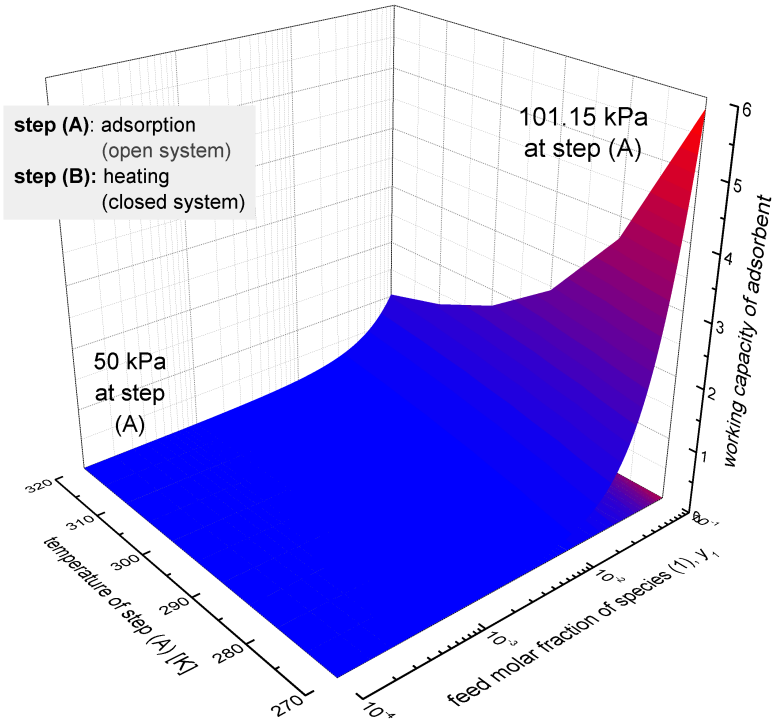

Figure B.2. Working capacity of zeolite 13X over a range of temperature and feed molar fraction of species (1) at step (A) (adsorption until saturation) at 50 kPa (surface display) and 101.325 kPa and step (B) (heating of isolated bed at 373.15 K).

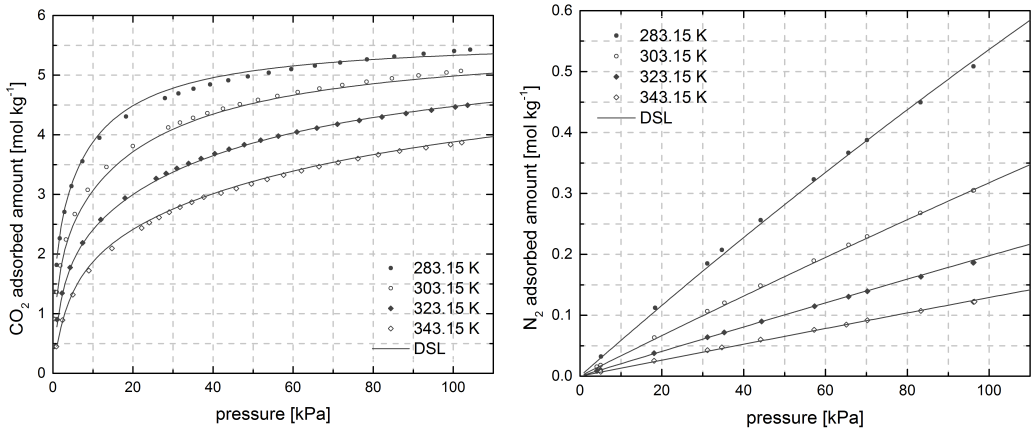

(a) CO_2 **(b)** N_2

Figure B.3. In-house single component adsorption equilibrium isotherms of: (*a*) carbon dioxide and (*b*) nitrogen on zeolite 13X at: 298.15 K (•) and 353.15 K (○). The solid lines represent the regression with the nonlinear Langmuir equation.

Table B.2. Dual-Site Langmuir isotherm parameters for CO_2, N_2, and O_2.

	$q_{s(1)}$ [mol kg^{-1}]	$q_{s(2)}$ [mol kg^{-1}]	$b_0^{(1)}$ [kPa^{-1}]	$b_0^{(2)}$ [kPa^{-1}]	$\Delta H^{(1)}$ [kJ mol^{-1}]	$\Delta H^{(2)}$ [kJ mol^{-1}]
CO_2	3.44	2.20	3.11 $\left(10^{-6}\right)$	31.88 $\left(10^{-6}\right)$	$(-)$ 30.81	$(-)$ 32.98
N_2	3.44	2.20	0.20 $\left(10^{-6}\right)$	0.20 $\left(10^{-6}\right)$	$(-)$ 20.20	$(-)$ 20.20
[a] **O_2**	3.44	2.20	3.32 $\left(10^{-6}\right)$	3.32 $\left(10^{-6}\right)$	$(-)$ 1.05	$(-)$ 1.05

[a] Data are obtained from Xiao et al. (2008).

Process Analysis and Design

C

C.1 The Case of Direct Air Capture: Supplementary Information on Mass and Energy Balances

In Chapter 3, Section 3.4, material and energy balances are analytically discussed for a specified case of DAC. The following Figures C.1 to C.3, present the number of moles and pressure profiles at equilibrium obtained during the connection between two beds. The process parameters, operational conditions, and physical and adsorptive properties of zeolite 13X are given in Tables 3.4 and 3.5 (in Section 3.4, Chapter 3). Figure C.1 compares the equilibrium number of moles and pressure during the connection step between Bed 3 and Bed 4. Dotted lines represent the initial values in Bed 3. Those correspond to the equilibrium values obtained from the heating step of Bed 3 prior to the connection with Bed 4 step. The analytical steps of the process are presented in Tables 3.2 and 3.3 (in Section 3.2, Chapter 3). Bed 3 operates at high temperature and Bed 4 operates at low temperature. The equilibrium pressure profile follows the N_2 equilibrium concentration profiles inside the two bed and reaches the same value for both beds at each cycle of the process. Pressure increases cycle after cycle until it reaches a maximum and then decreases until the concentrations inside the beds reach a steady state. A maximum pressure in both beds is obtained at around 60 cycles of the process. After 60 cycles, the pressure decreases since N_2 is moving from Bed 4 to Bed 3. The amount of CO_2 stored in Bed 4 at a steady state is around 9 times higher than that of N_2 stored in the same bed. Also, the amount of CO_2 in the storage bed is much greater than that in Bed 3 since not only Bed 3 operates at higher temperature but also the mass of Bed 4 is higher allowing more material to be stored.

Figure C.2 presents the equilibrium number of moles and pressure during the connection of Bed 2 and Bed 3. Again, the dotted lines represent the initial values. For Bed 2, the initial values are those obtained from the heating step at equilibrium and for Bed 3 are obtained from the cooling step at equilibrium. The process step sequence is presented in Table 3.3 of Chapter 3. Again, the pressure profiles are the same for each bed and the equilibrium pressure profile follows the equilibrium profile of the N_2 concentrations in both beds. At each cycle of the process, the equilibrium number of moles of species i in Bed 3 at the end of the connection-with-Bed-4 step is the same with the equilibrium number of moles of species i in Bed 3 at the cooling-of-Bed-3 step (see Figures C.1b and C.2a). Most of the CO_2 passes from Bed 2 to Bed 3 and then from Bed 3 to Bed 4 until cycle 100. Further operation of the process will not significantly increase the purity of the process; instead, it will result in an unreasonable energy consumption. Figure C.2b shows that the concentration of CO_2 is built up also in Bed 2 and becomes higher that that of N_2 after 110 cycles of the process. However, during the connection between Bed 1 and Bed 2 (see Figure C.3) N_2 concentration is always higher than CO_2 concentration. This is due to the fact that Bed 1 is always open to atmospheric air at the beginning of each cycle.

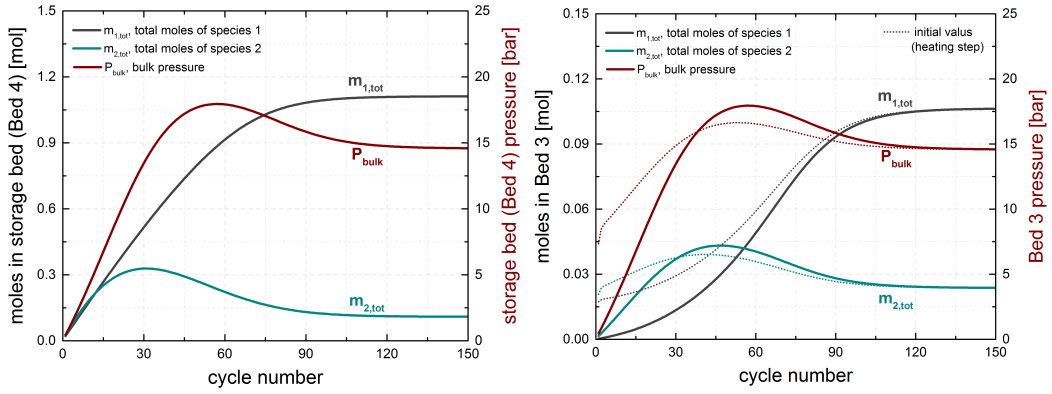

(a) P-moles in Bed 4 (**adsorption**) **(b)** P-moles in Bed 3 (**desorption**)

Figure C.1. Total moles of CO_2 stored (gray curve, $m_{1,\mathrm{tot}}$), total moles of N_2 stored (green curve, $m_{2,\mathrm{tot}}$), and bulk pressure (dark red curve) profiles at equilibrium during the connection between Bed 3 and Bed 4 at each operational cycle. (**a**) Bed 4 operates at T_{low} (adsorption) and (**b**) Bed 3 operates at T_{high} (desorption). Dotted curves represent initial values.

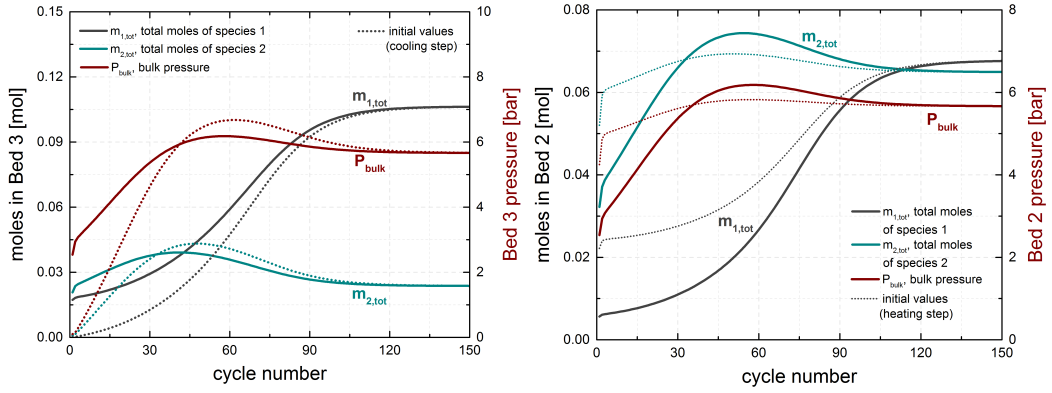

(a) P-moles in Bed 3 (**adsorption**) **(b)** P-moles in Bed 2 (**desorption**)

Figure C.2. Total moles of CO_2 stored (gray curve, $m_{1,\mathrm{tot}}$), total moles of N_2 stored (green curve, $m_{2,\mathrm{tot}}$), and bulk pressure (dark red curve) profiles during the connection between Bed 2 and Bed 3 at each operational cycle. (**a**) Bed 3 operates at T_{low} (adsorption) and (**b**) Bed 2 operates at T_{high} (desorption). Dotted curves represent initial values.

Pressure and concentration profiles at each step of the operation of each bed are illustrated in Figures C.4 to C.7. These include steps of cooling, adsorption in Bed k (or else connection with Bed k–1), vacuum (optional), heating, and desorption of Bed k (or else connection with Bed k+1). These graphs provide a better understanding of what is happening in the pressure and CO_2 and N_2 concentrations inside each bed at each operational step. They also provide necessary information for the examination of mass balances.

Section 3.4, Chapter 3, considers the contribution of three different types of energy consumed in the process: *(i)* heat at 95 °C, *(ii)* cold at 20 °C, and *(iii)* electricity for the optional vacuum steps in the first beds (in this case Beds 1 and 2). Here, the energy consumption from the operation of a fan to flow air through the adsorption contactor is considered. To calculate this electric energy consumption, the following considerations are taken into account:

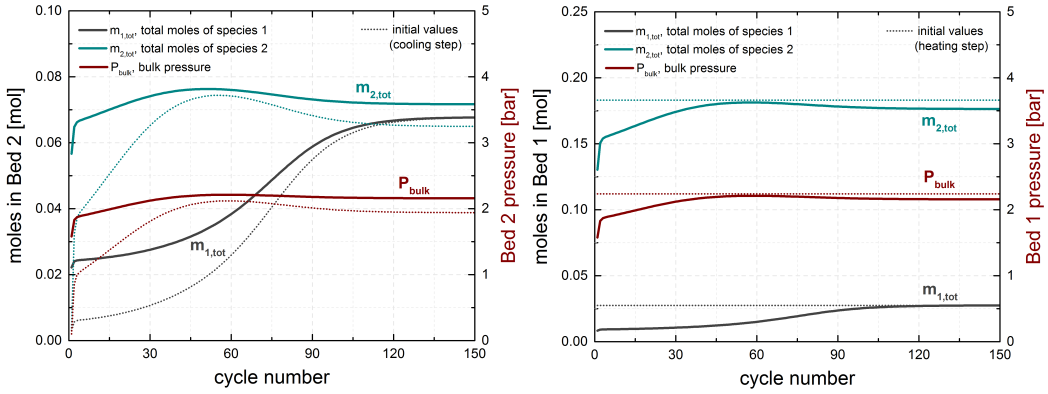

(a) P-moles in Bed 2 (**adsorption**) **(b)** P-moles in Bed 1 (**desorption**)

Figure C.3. Total moles of CO_2 stored (gray curve, $m_{1,\mathrm{tot}}$), total moles of N_2 stored (green curve, $m_{2,\mathrm{tot}}$), and bulk pressure (dark red curve) profiles during the connection between Bed 1 and Bed 2 at each operational cycle. (**a**) Bed 2 operates at T_{low} (adsorption) and (**b**) Bed 1 operates at T_{high} (desorption). Dotted curves represent initial values.

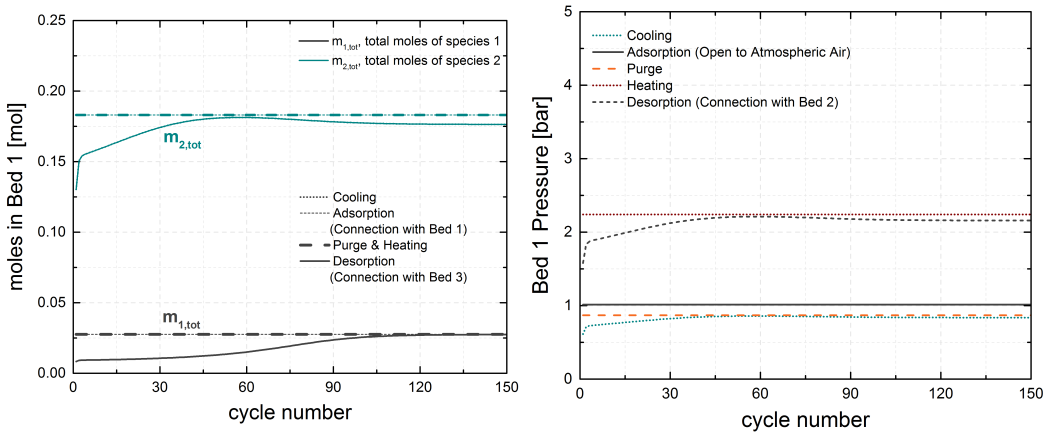

(a) moles in Bed 1 (**adsorption**) **(b)** pressure in Bed 1 (**desorption**)

Figure C.4. (**a**) Total moles of CO_2 (gray curve, $m_{1,\mathrm{tot}}$) and N_2 (green curve, $m_{2,\mathrm{tot}}$) stored, and (**b**) pressure profiles at each step of the operation of Bed 1 at each operational cycle.

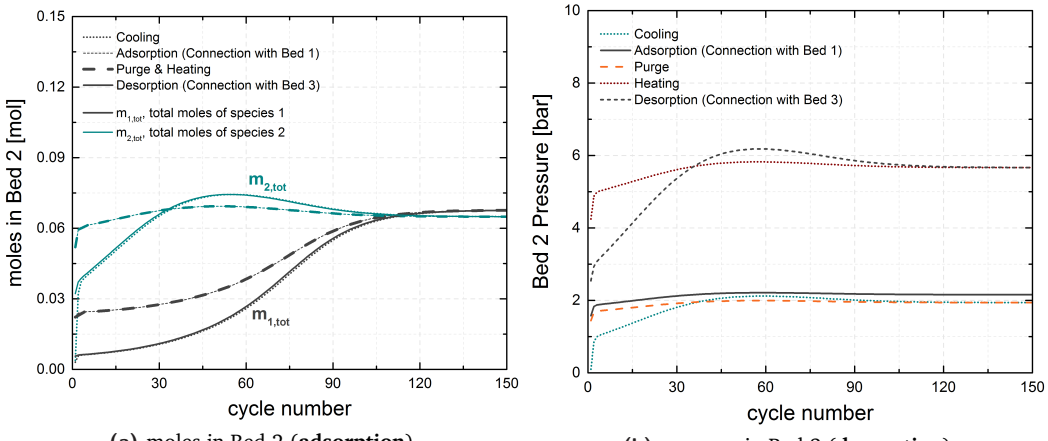

(a) moles in Bed 2 (**adsorption**) **(b)** pressure in Bed 2 (**desorption**)

Figure C.5. (**a**) Total moles of CO_2 (gray curve, $m_{1,\mathrm{tot}}$) and N_2 (green curve, $m_{2,\mathrm{tot}}$) stored, and (**b**) pressure profiles at each step of the operation of Bed 2 at each operational cycle.

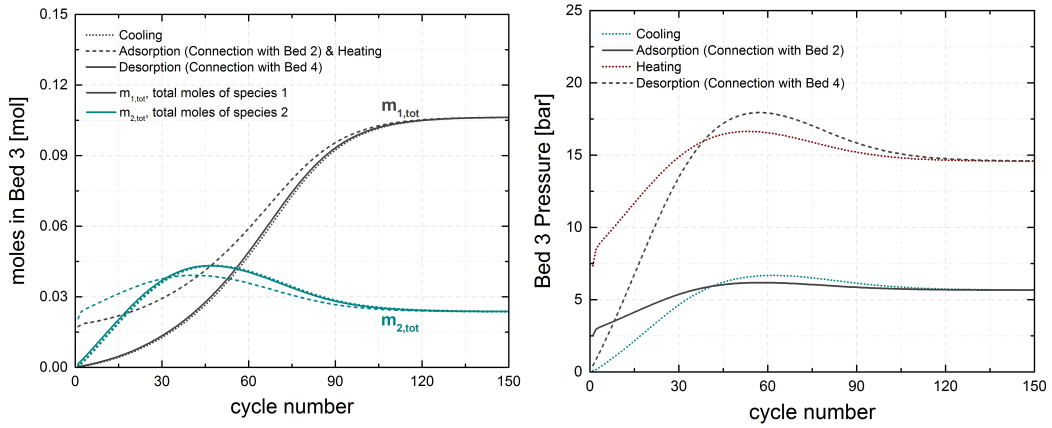

(a) moles in Bed 3 (**adsorption**)

(b) pressure in Bed 3 (**desorption**)

Figure C.6. (**a**) Total moles of CO_2 (gray curve, $m_{1,\mathrm{tot}}$) and N_2 (green curve, $m_{2,\mathrm{tot}}$) stored, and (**b**) pressure profiles at each step of the operation of Bed 3 at each operational cycle.

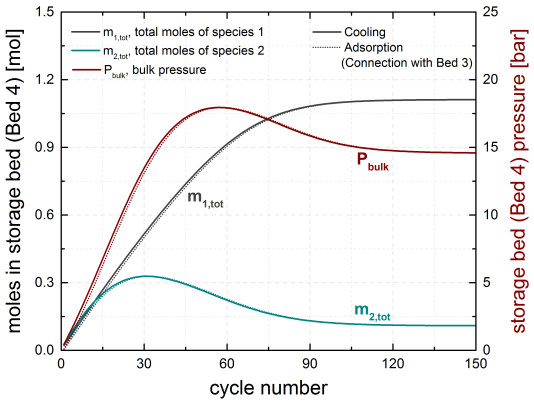

Figure C.7. Total moles of CO_2 stored (gray curve, $m_{1,\mathrm{tot}}$), total moles of N_2 stored (green curve, $m_{2,\mathrm{tot}}$), and pressure profiles at each step of the operation of Bed 4 at each operational cycle.

(i) The pressure drop across Bed 1 is calculated from the pressure drop in a squared structured packing. Therefore, it is governed by:

$$\Delta P = L \, \frac{16}{0.562} \, \frac{\eta_{\mathrm{f}} \, \upsilon}{b^2}, \tag{C.1}$$

where L [m] denotes the length of the adsorption contactor, b [m] is the width of the squared structured packing, η_{f} [kPa s] is the fluid viscosity, and υ [m s^{-1}] defines the interstitial flow velocity.

(ii) L=0.2 m, b=10 mm, η_{f}=18.3 10^{-6} Pa s, and υ=15 m s^{-1}.

(iii) The electric energy consumption of the fan is calculated from:

$$W_{\mathrm{el}} = \frac{n \, R \, T}{\vartheta_{\mathrm{f}}} \ln\left(\frac{P_1}{P_2}\right), \tag{C.2}$$

where ϑ_{f} is the overall fan efficiency, and P_1 and P_2 [kPa] are the pressure in the inlet and the outlet of the adsorption contactor, respectively.

(iv) $P_2 = P_{\mathrm{atm}}$, $P_1 = P_{\mathrm{atm}} + \Delta P$, and ϑ_{f}=1.

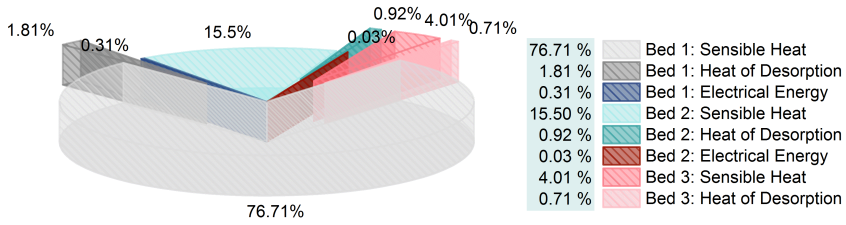

Figure C.8. Percentage of specific energy consumptions due to the heat of desorption, sensible heat, and electrical energy consumed at the end of the process for each Bed.

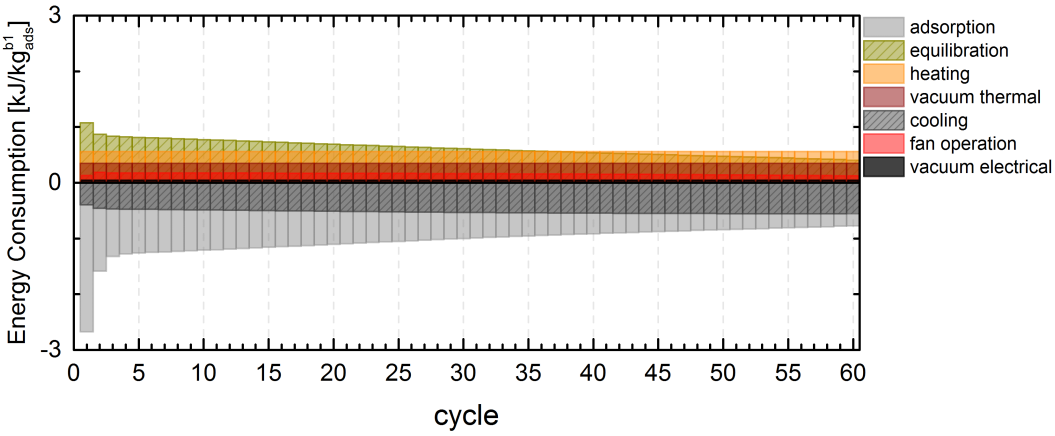

Figure C.9. Total specific energy consumption due to thermal heating, thermal cooling, and electrical energy for the operation of Bed 1. Sensible heat is not included.

The total specific sensible heat required by the process is 5.33 MJ_{th} $molCO_2{}^{-1}$. The adsorbent material is the main contributor accounting for 96.55% of the total energy for sensible heating. As illustrated in Figure C.8, 76.71% of total specific sensible heat is required by Bed 1 and only 15.5% and 4.01% are required from Bed 2 and Bed 3 respectively. 5.52 MJ_{th} $molCO_2{}^{-1}$ of thermal energy was consumed by the process in the form of heating. The total specific electrical energy consumption for the operation of the fan and the optional vacuum steps of Bed 1 and Bed 2 is only 0.02 MJ_{el} $molCO_2{}^{-1}$. The total specific electrical energy consumption for the operation of the fan is 0.01 MJ_{el} $molCO_2{}^{-1}$.

Figure C.9 considers the total specific energy consumption due to thermal heating, thermal cooling, and electrical energy for the operation of Bed 1. Here, sensible heat is not included in this figure.

C.2 Sensitivity Analysis: Calculations and Supplementary Information

C.2.1 2^5 Full Factorial Design – Calculations

A sensitivity analysis is performed considering five key parameters affecting the performance of the system in terms of process and adsorbent material. These parameters are reported in Chapter 3, Section 3.5, and in Table C.1. For sake of simplicity, these key parameters are reported here as P1 (number of cycles), P2 (mass ratio of the beds), P3 (adsorbent saturation capacity), P4 (selectivity of trace gas over the main gas in the binary feed stream)

Table C.1. Factors and levels investigated for full factorial design.

	Parameter	Low Level (–)	High Level (+)
P1	Number of cycles, N_{C}	30	50
P2	[a] Mass ratio, $m_{\mathrm{bed},i}/m_{\mathrm{bed},i+1}$	4	5
P3	Saturation capacity, q_{s}	4	5
P4	Selectivity of (A) over (B), $S_{\mathrm{A/B}}$	400	600
P5	Number of beds, N_{B}	4	5

[a] The subscript i refers to the number of bed, $i = 1, ..., N_{\mathrm{B}} - 1$.

Note: For sake of simplicity, masses of Bed 1 ($m_{\mathrm{bed},1}$) and storage bed ($m_{\mathrm{bed},N_{\mathrm{B}}}$) are fixed at 1 kg and 0.3 kg, respectively, and the isosteric heat of adsorption of species (A), ΔH_{A}, and (B), ΔH_{B}, are fixed at –35 kJ mol^{-1} and –15 kJ mol^{-1}, respectively. Here, (A) denotes the most strongly adsorbed compound and (B) the less strongly adsorbed compound.

and P5 (number of beds of the process). The 2^5 full factorial design requires 25 cycles and the results obtained from the corresponding values, lower level ($-$) and higher level ($+$), of the five parameters of Table C.1 are listed in Table C.2.

To estimate the mean effects of each parameter and their high order interactions on the factors: specific energy, purity, pressure, and recovery are calculated using the Yate's algorithm. The results from this method are presented in Tables C.3 and C.4. The values of column (I) are obtained from adding the pairs of the results of the performance parameters (one at a time) together to fill the first 16 entries, while the last 16 entries are obtained by subtracting the top number from the bottom number of each pair (Freni et al., 2008). The entries in columns (II) to (V) are obtained analogously from columns (I) to (IV). Finally the effects on each factor are calculated by dividing the values of column (V) by 2^4, except the mean value (in Run 1) which is divided by 2^5. This first estimated is the grand average (mean) of all the runs.

The investigated effects of input variables obtained from full factorial design have also been confirmed using Minitab® software. From Minitab, the factorial plots for the output response on specific energy and purity have been extracted and are presented in Figures C.10 and C.11, respectively. These figures present the main effects and their interactions where the colour-squared interactions represent the most important parameters on the output response. The parallel interactions have no significant effects where the crossed interactions, or interactions that are converging together have the most significant effects. When the interactions are crossed, then those single parameters have to be considered together.

Figure C.10a shows that the number of cycles has a significant effect on energy. The parameters of the adsorbent material, such as the adsorption capacity and the selectivity, have a positive effect on energy. By increasing the number of beds and the number of cycles, a negative effect on energy is expected as a significant amount of energy is caused by the sensible heat. Two-level interactions are also significant on energy. In Figure C.10b, the main two-level interactions are highlighted. As stated above, crossing lines and converging lines have the most significant effects while parallel lines have minor effects. The number of beds have a significant interaction in combination with the mass ratio between the beds and the number of cycles. This is an indication that the number of beds have a significant effect on the energy of the system.

Figure C.11a illustrates that selectivity has the main positive effect on purity. The number of beds and cycles also have a major positive effect on purity. The two-level interactions

Table C.2. The 2^5 full factorial design and performance parameters.

Run	P1	P2	P3	P4	P5	P1	P2	P3	P4	P5	Specific Energy [MJ mol^{-1}]	Purity [molar ratio]	Pressure [bar]	Recovery [%]
1	-	-	-	-	-	30	4	4	400	4	2.46	0.88	23.02	73.47
2	+	-	-	-	-	50	4	4	400	4	3.95	0.90	19.50	70.39
3	-	+	-	-	-	30	5	4	400	4	2.34	0.86	24.48	79.28
4	+	+	-	-	-	50	5	4	400	4	3.73	0.90	19.96	75.84
5	-	-	+	-	-	30	4	5	400	4	2.02	0.88	25.35	73.64
6	+	-	+	-	-	50	4	5	400	4	3.23	0.91	21.52	70.52
7	-	+	+	-	-	30	5	5	400	4	1.92	0.87	27.12	79.46
8	+	+	+	-	-	50	5	5	400	4	3.04	0.91	22.00	75.97
9	-	-	-	+	-	30	4	4	800	4	2.36	0.92	18.48	70.44
10	+	-	-	+	-	50	4	4	800	4	3.84	0.93	15.63	68.89
11	-	+	-	+	-	30	5	4	800	4	2.23	0.91	19.68	76.22
12	+	+	-	+	-	50	5	4	800	4	3.62	0.93	16.02	74.63
13	-	-	+	+	-	30	4	5	800	4	1.93	0.92	20.91	70.63
14	+	-	+	+	-	50	4	5	800	4	3.13	0.94	17.69	69.04
15	-	+	+	+	-	30	5	5	800	4	1.82	0.92	22.45	76.43
16	+	+	+	+	-	50	5	5	800	4	2.95	0.94	18.10	74.79
17	-	-	-	-	+	30	4	4	400	5	2.51	0.90	18.71	75.88
18	+	-	-	-	+	50	4	4	400	5	3.85	0.91	27.14	69.35
19	-	+	-	-	+	30	5	4	400	5	3.24	0.89	1.94	77.90
20	+	+	-	-	+	50	5	4	400	5	3.80	0.93	12.37	77.49
21	-	-	+	-	+	30	4	5	400	5	2.06	0.90	20.75	76.05
22	+	-	+	-	+	50	4	5	400	5	3.16	0.92	30.30	69.43
23	-	+	+	-	+	30	5	5	400	5	2.66	0.89	1.91	78.09
24	+	+	+	-	+	50	5	5	400	5	3.11	0.93	13.45	77.65
25	-	-	-	+	+	30	4	4	800	5	2.40	0.94	16.04	71.99
26	+	-	-	+	+	50	4	4	800	5	3.79	0.94	22.68	67.57
27	-	+	-	+	+	30	5	4	800	5	3.04	0.94	2.04	76.83
28	+	+	-	+	+	50	5	4	800	5	3.68	0.95	10.84	75.47
29	-	-	+	+	+	30	4	5	800	5	1.97	0.94	18.27	72.18
30	+	-	+	+	+	50	4	5	800	5	3.10	0.94	25.78	67.65
31	-	+	+	+	+	30	5	5	800	5	2.48	0.94	2.05	77.07
32	+	+	+	+	+	50	5	5	800	5	3.00	0.96	12.08	75.66

Table C.3. Estimated effects for specific energy consumption and purity from the 2^5 full factorial design, by Yate's analysis.

Run	Identification Code (ID)	Specific Energy [MJ/mol]	I	II	III	IV	V	Effects on Energy [MJ/mol]	Purity [%]	I	II	III	IV	V	Effects on Purity [%]
1	Mean	2.46	6.41	12.48	22.69	44.57	92.42	2.89	0.88	1.78	3.54	7.11	14.52	29.34	0.92
2	P1	3.95	6.07	10.21	21.88	47.85	17.54	1.10	0.90	1.76	3.57	7.41	14.82	0.34	0.02
3	P2	2.34	5.25	12.05	24.39	10.41	0.90	0.06	0.86	1.79	3.69	7.27	0.20	0.00	0.00
4	P1 P2	3.73	4.96	9.83	23.46	7.13	-3.14	-0.20	0.90	1.78	3.72	7.55	0.14	0.12	0.01
5	P3	2.02	6.20	13.40	5.21	-1.27	-9.26	-0.58	0.88	1.85	3.63	0.13	-0.04	0.08	0.01
6	P1 P3	3.23	5.85	10.99	5.20	2.17	-1.82	-0.11	0.91	1.84	3.64	0.07	0.04	0.04	0.00
7	P2 P3	1.92	5.06	12.91	3.45	-0.35	-0.14	-0.01	0.87	1.86	3.77	0.11	0.04	0.02	0.00
8	P1 P2 P3	3.04	4.77	10.55	3.68	-2.79	0.30	0.02	0.91	1.86	3.78	0.03	0.08	-0.02	0.00
9	P4	2.36	6.36	2.88	-0.63	-4.49	-1.74	-0.11	0.92	1.81	0.06	-0.03	0.06	0.58	0.04
10	P1 P4	3.84	7.04	2.33	-0.64	-4.77	0.22	0.01	0.93	1.82	0.07	-0.01	0.02	-0.14	-0.01
11	P2 P4	2.23	5.22	2.87	1.23	-1.09	-0.30	-0.02	0.91	1.82	0.03	0.01	0.02	0.04	0.00
12	P1 P2 P4	3.62	5.77	2.33	0.94	-0.73	0.10	0.01	0.93	1.82	0.04	0.03	0.02	-0.04	0.00
13	P3 P4	1.93	6.19	1.90	-0.19	0.11	0.10	0.01	0.92	1.88	0.05	0.03	0.02	0.00	0.00
14	P1 P3 P4	3.13	6.72	1.55	-0.16	-0.25	-0.02	0.00	0.94	1.89	0.06	0.01	0.00	0.00	0.00
15	P2 P3 P4	1.82	5.07	2.03	-1.43	0.03	0.02	0.00	0.92	1.88	0.01	0.05	-0.02	0.02	0.00
16	P1 P2 P3 P4	2.95	5.48	1.65	-1.36	0.27	0.02	0.00	0.94	1.90	0.02	0.03	0.00	0.02	0.00
17	P5	2.51	1.49	-0.34	-2.27	-0.81	3.28	0.21	0.90	0.02	-0.02	0.03	0.30	0.30	0.02
18	P1 P5	3.85	1.39	-0.29	-2.22	-0.93	-3.28	-0.21	0.91	0.04	-0.01	0.03	0.28	-0.06	0.00
19	P2 P5	3.24	1.21	-0.35	-2.41	-0.01	3.44	0.22	0.89	0.03	-0.01	0.01	-0.06	0.08	0.01
20	P1 P2 P5	3.80	1.12	-0.29	-2.36	0.23	-2.44	-0.15	0.93	0.04	0.00	0.01	-0.08	0.04	0.00
21	P3 P5	2.06	1.48	0.68	-0.55	-0.01	-0.28	-0.02	0.90	0.01	0.01	0.01	0.02	-0.04	0.00
22	P1 P3 P5	3.16	1.39	0.55	-0.54	-0.29	0.36	0.02	0.92	0.02	0.00	0.01	0.02	0.00	0.00
23	P2 P3 P5	2.66	1.20	0.53	-0.35	0.03	-0.36	-0.02	0.89	0.02	0.01	0.01	-0.02	-0.02	0.00
24	P1 P2 P3 P5	3.11	1.13	0.41	-0.38	0.07	0.24	0.02	0.93	0.02	0.02	0.01	-0.02	0.02	0.00
25	P4 P5	2.40	1.34	-0.10	0.05	0.05	-0.12	-0.01	0.94	0.01	0.02	0.01	0.00	-0.02	0.00
26	P1 P4 P5	3.79	0.56	-0.09	0.06	0.05	0.24	0.02	0.94	0.04	0.01	0.01	0.00	-0.02	0.00
27	P2 P4 P5	3.04	1.10	-0.09	-0.13	0.01	-0.28	-0.02	0.94	0.02	0.01	-0.01	0.00	0.00	0.00
28	P1 P2 P4 P5	3.68	0.45	-0.07	-0.12	-0.03	0.04	0.00	0.95	0.04	0.00	0.01	0.00	0.00	0.00
29	P3 P4 P5	1.97	1.39	-0.78	0.01	0.01	0.00	0.00	0.94	0.00	0.03	-0.01	0.00	0.00	0.00
30	P1 P3 P4 P5	3.10	0.64	-0.65	0.02	0.01	-0.04	0.00	0.94	0.01	0.02	-0.01	0.02	0.00	0.00
31	P2 P3 P4 P5	2.48	1.13	-0.75	0.13	0.01	0.00	0.00	0.94	0.00	0.01	-0.01	0.00	0.02	0.00
32	P1 P2 P3 P4 P5	3.00	0.52	-0.61	0.14	0.01	0.00	0.00	0.96	0.02	0.02	0.01	0.02	0.02	0.00

Table C.4. Estimated effects for pressure and recovery from the 2^5 full factorial design, by Yate's analysis.

Run	Identification Code(ID)	Pressure [bar]	I	II	III	IV	V	Effects on Pressure [bar]	Recovery [%]	I	II	III	IV	V	Effects on Recovery [%]
1	Mean	23.02	42.52	86.96	182.95	331.91	568.26	17.76	73.47	143.86	298.98	598.57	1179.64	2365.90	73.93
2	P1	19.50	44.44	95.99	148.96	236.35	41.86	2.62	70.39	155.12	299.59	581.07	1186.26	-45.22	-2.83
3	P2	24.48	46.87	69.81	126.57	-31.07	-115.28	-7.21	79.28	144.16	290.18	601.84	-19.50	91.66	5.73
4	P1 P2	19.96	49.12	79.15	109.78	72.93	4.44	0.28	75.84	155.43	290.89	584.42	-25.72	17.66	1.10
5	P3	25.35	34.11	60.16	-16.99	7.71	31.20	1.95	73.64	139.33	300.62	-13.13	45.60	2.62	0.16
6	P1 P3	21.52	35.70	66.41	-14.08	-122.99	2.36	0.15	70.52	150.85	301.22	-6.37	46.06	-0.46	-0.03
7	P2 P3	27.12	38.60	51.60	39.95	-4.23	-7.54	-0.47	79.46	139.67	291.86	-14.00	-0.82	0.30	0.02
8	P1 P2 P3	22.00	40.55	58.18	32.98	8.67	-0.26	-0.02	75.97	151.22	292.56	-11.72	18.48	0.10	0.01
9	P4	18.48	45.85	-8.04	4.17	18.37	-50.78	-3.17	70.44	145.23	-6.52	22.53	1.32	-34.92	-2.18
10	P1 P4	15.63	14.31	-8.95	3.54	12.83	-4.06	-0.25	68.89	155.39	-6.61	23.07	1.30	9.04	0.57
11	P2 P4	19.68	51.05	-6.51	-67.23	-1.97	10.84	0.68	76.22	145.48	-3.14	20.42	-0.18	5.76	0.36
12	P1 P2 P4	16.02	15.36	-7.57	-55.76	4.33	1.04	0.07	74.63	155.74	-3.23	25.64	-0.28	-5.48	-0.34
13	P3 P4	20.91	38.72	18.86	-2.29	0.69	0.64	0.04	70.63	139.56	-6.94	-0.73	0.04	0.20	0.01
14	P1 P3 P4	17.69	12.88	21.09	-1.94	-8.23	-0.28	-0.02	69.04	152.30	-7.06	-0.09	0.26	-0.04	0.00
15	P2 P3 P4	22.45	44.05	15.44	3.99	-0.61	0.10	0.01	76.43	139.83	-5.78	12.30	-0.02	0.08	0.00
16	P1 P2 P3 P4	18.10	14.13	17.54	4.68	0.35	0.34	0.02	74.79	152.73	-5.94	6.18	0.12	0.00	0.00
17	P5	18.71	-3.52	1.92	9.03	-33.99	-95.56	-5.97	75.88	-3.08	11.26	0.61	-17.50	6.62	0.41
18	P1 P5	27.14	-4.52	2.25	9.34	-16.79	104.00	6.50	69.35	-3.44	11.27	0.71	-17.42	-6.22	-0.39
19	P2 P5	1.94	-3.83	1.59	6.25	2.91	-130.70	-8.17	77.90	-3.12	11.52	0.60	6.76	0.46	0.03
20	P1 P2 P5	12.37	-5.12	1.95	6.58	-6.97	12.90	0.81	77.49	-3.49	11.55	0.70	2.28	19.30	1.21
21	P3 P5	20.75	-2.85	-31.54	-0.91	-0.63	-5.54	-0.35	76.05	-1.55	10.16	-0.09	0.54	-0.02	0.00
22	P1 P3 P5	30.30	-3.66	-35.69	-1.06	11.47	6.30	0.39	69.43	-1.59	10.26	-0.09	5.22	-0.10	-0.01
23	P2 P3 P5	1.91	-3.22	-25.84	2.23	0.35	-8.92	-0.56	78.09	-1.59	12.74	-0.12	0.64	0.22	0.01
24	P1 P2 P3 P5	13.45	-4.35	-29.92	2.10	0.69	0.96	0.06	77.65	-1.64	12.90	-0.16	-6.12	0.14	0.01
25	P4 P5	16.04	8.43	-1.00	0.33	0.31	17.20	1.08	71.99	-6.53	-0.36	0.01	0.10	0.08	0.01
26	P1 P4 P5	22.68	10.43	-1.29	0.36	0.33	-9.88	-0.62	67.57	-0.41	-0.37	0.03	0.10	-4.48	-0.28
27	P2 P4 P5	2.04	9.55	-0.81	-4.15	-0.15	12.10	0.76	76.83	-6.62	-0.04	0.10	0.00	4.68	0.29
28	P1 P2 P4 P5	10.84	11.54	-1.13	-4.08	-0.13	0.34	0.02	75.47	-0.44	-0.05	0.16	-0.04	-6.76	-0.42
29	P3 P4 P5	18.27	6.64	2.00	-0.29	0.03	0.02	0.00	72.18	-4.42	6.12	-0.01	0.02	0.00	0.00
30	P1 P3 P4 P5	25.78	8.80	1.99	-0.32	0.07	0.02	0.00	67.65	-1.36	6.18	-0.01	0.06	-0.04	0.00
31	P2 P3 P4 P5	2.05	7.51	2.16	-0.01	-0.03	0.04	0.00	77.07	-4.53	3.06	0.06	0.00	0.04	0.00
32	P1 P2 P3 P4 P5	12.08	10.03	2.52	0.36	0.37	0.40	0.03	75.66	-1.41	3.12	0.06	0.00	0.00	0.00

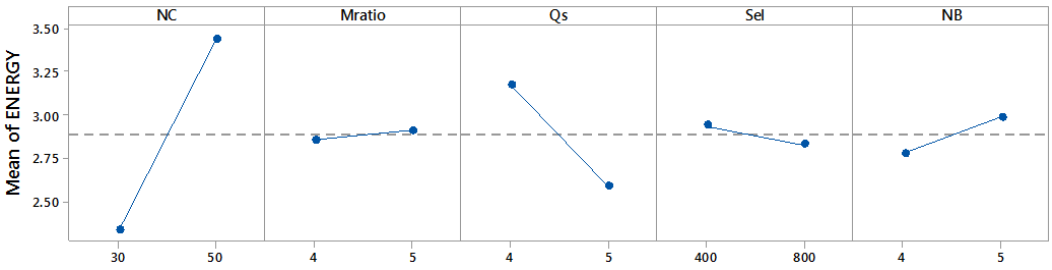

(a) main effects plot for energy

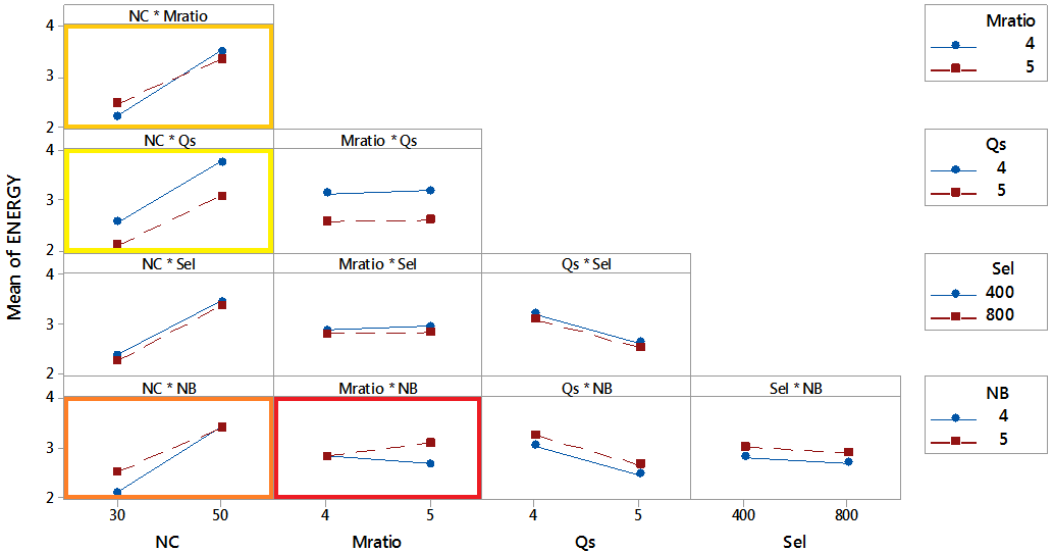

(b) interaction plot for energy

Figure C.10. Factorial plots for the main effects and their interactions on the specific energy as obtained from Minitab® software. Abbreviations: NC, number of cycles; Mratio, mass ratio between the beds; Qs, adsorption capacity; Sel, selectivity; and NB, number of beds.

Note: The stronger interactions are colour-squared. Colour discrimination shows how significant the interaction is on energy: red (stronger interaction) – yellow (weaker interaction).

between the main effects are given in Figure C.11b. The number of cycles in combination with selectivity and number of cycles have major effects on purity. This result is inferred for this process as both the pressure and purity in the last bed is built up cycle after cycle until it reaches a plateau.

The main effects on pressure and recovery are given in Table C.4. In general, the mass of the storage bed has a significant effect on pressure. By fixing the mass of the storage bed at 0.3 kg for the process that consist of 4 beds or 5 beds, the major effect on pressure has not be considered. The mass ratio and number of beds have a negative significant effect on pressure and the interaction of the number of cycles and number of beds has a positive interaction effect. Although, the mass ratio has a major positive effect on recovery, both the number of cycles and selectivity are negative effects. For the process optimisation, the targeted objectives are the specific energy consumption and purity in the storage bed. The masses are fixed from the optimiser, although the pressure and recovery can be constrained. For this reason, their results after sensitivity analysis are not analysed more extensively.

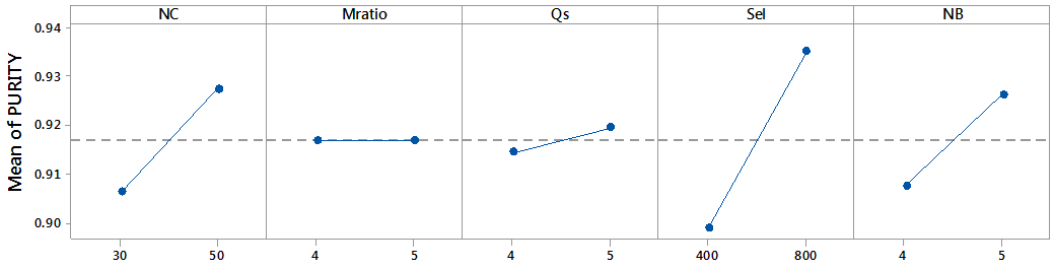

(a) main effects plot for purity

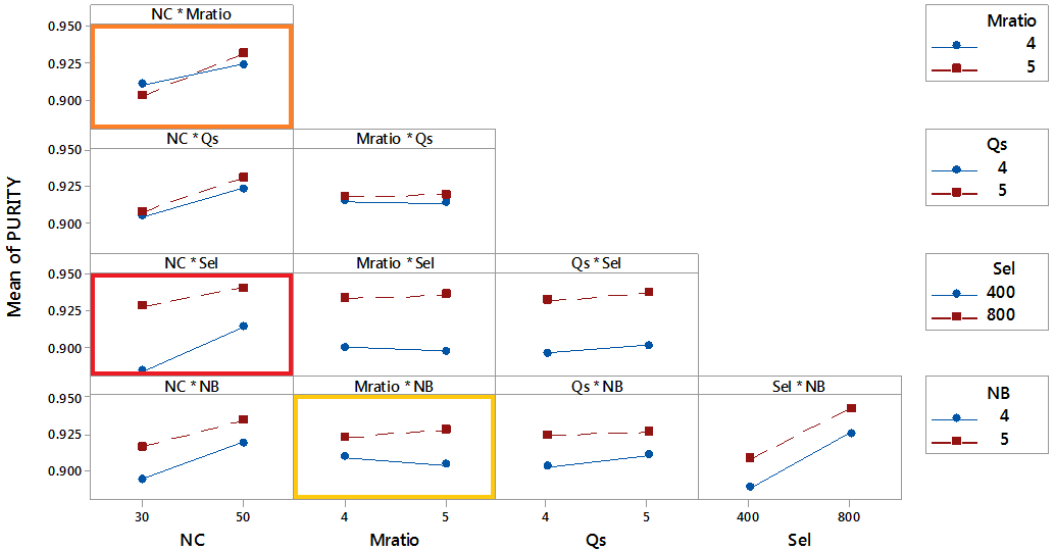

(b) interaction plot for purity

Figure C.11. Factorial plots for the main effects and their interactions on the final purity as obtained from Minitab® software. Abbreviations: NC, number of cycles; Mratio, mass ratio between the beds; Qs, adsorption capacity; Sel, selectivity; and NB, number of beds.

Note: The stronger interactions are colour-squared. Colour discrimination shows how significant the interaction is on energy: red (stronger interaction) – yellow (weaker interaction).

C.2.2 2^6 Full Factorial Design

In this stage of design and before performing the multi-objective optimisation strategies, the results from the sensitivity analysis are significant for giving guidance on same parameters that have a major effect on system's performance, especially in terms of energy consumption and purity in the storage bed. They also provide a better understanding on how to address the optimisation problem. Although 2^6 FFD is more time consuming, it may give a better understanding on the performance of the system. Table C.5 illustrates the effects that are taken into account for this analysis considering 20% change (low and high levels) of an intermediate value. By adding an additional factor to the sensitivity analysis (the heat of adsorption of species (B)) and slightly changing the low and high levels of the design, a better understanding of the effects and their interactions is obtained and discussed below.

Figure C.12 represents the results of the main effects and their interactions on the specific energy of the process. By adding the heat of adsorption of species (B) (component in excess), the number of cycles, and selectivity become less important. However, the number of beds and the mass ratio between the beds become the most significant effects. It is clear that by

Table C.5. Factors and levels investigated for 2^6 full factorial design.

	Parameter	Low Level	Int. Level	High Level
NB	Number of beds, N_B	4	5	6
NC	Number of cycles, N_C	40	—	60
Mratio	[a] Mass ratio, $m_{bed,i}/m_{bed,i+1}$	4	—	6
Sel	Selectivity of (A) over (B), $S_{A/B}$	400	—	600
Qs	Saturation capacity, q_s [MJ mol^{-1}]	4	—	6
DH_B	Heat of adsorption of species (B), ΔH_B [kJ mol^{-1}]	–18	—	–12

[a] The subscript i refers to the number of bed, $i = 1, ..., N_B - 1$.

Note: For sake of simplicity, masses of Bed 1 ($m_{bed,1}$) and storage bed (m_{bed,N_B}) are fixed at 1 kg and 0.3 kg, respectively, and isosteric heat of adsorption of species (A), ΔH_A, is fixed at –35 kJ mol^{-1}. Here, (A) denotes the most strongly adsorbed compound and (B) the less strongly adsorbed one.

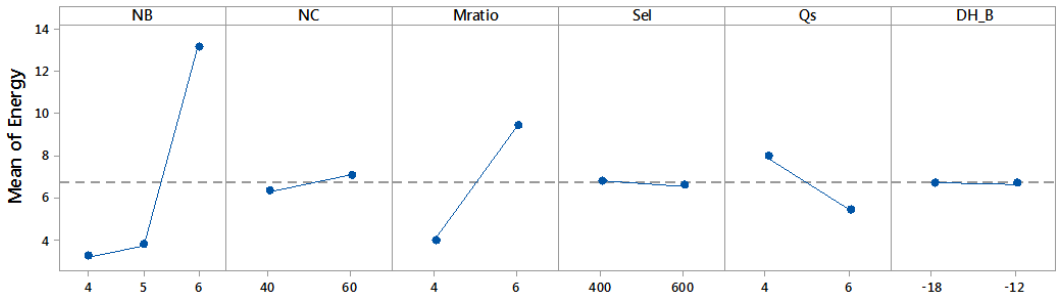

(a) main effects plot for energy

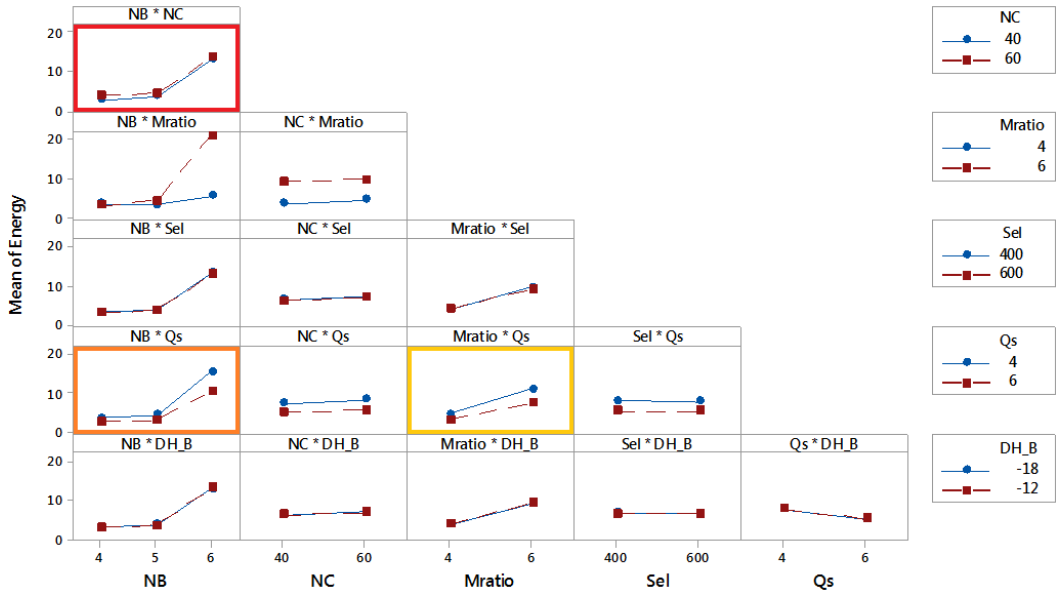

(b) interaction plot for energy

Figure C.12. Factorial plots for the main effects and their interactions on the specific energy as obtained from Minitab® software. Abbreviations: NB, number of beds; NC, number of cycles; Mratio, mass ratio between the beds; Sel, selectivity; Qs, adsorption capacity; and DH_B, heat of adsorption of species (B).

Note: The stronger interactions are colour-squared. Colour discrimination shows how significant the interaction is on energy: red (stronger interaction) – yellow (weaker interaction).

adding different factors, the effects, which are correlated, give different results. In addition, by comparing the two-level interactions, the number of beds in combination with the number of cycles and the adsorption capacity have the most important interaction effect.

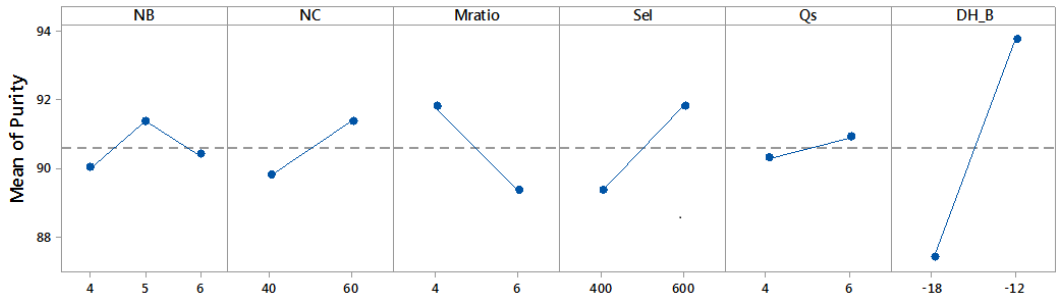

(a) main effects plot for purity

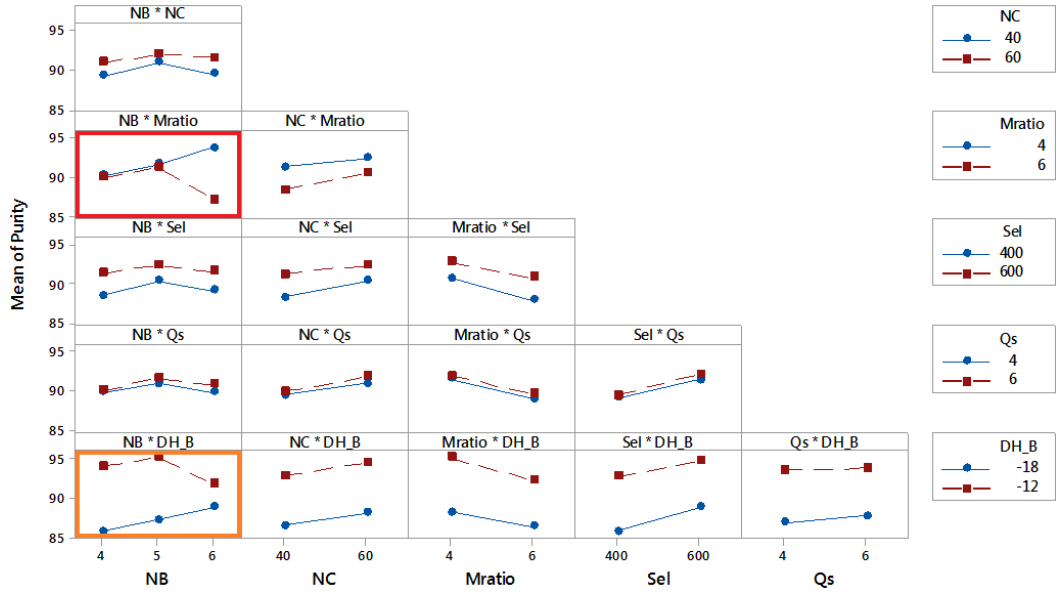

(b) interaction plot for purity

Figure C.13. Factorial plots for the main effects and their interactions on the purity in the last bed as obtained from Minitab® software. Abbreviations: NB, number of beds; NC, number of cycles; Mratio, mass ratio between the beds; Sel, selectivity; Qs, adsorption capacity; and DH_B, heat of adsorption of species (B).

Note: The stronger interactions are colour-squared. Colour discrimination shows how significant the interaction is on purity: red (stronger interaction) – yellow (weaker interaction).

Figure C.13 illustrates the main effects and their interactions on the purity in the storage bed. It is clear that the heat of adsorption (isosteric heat) of species (B) has the strongest effect on purity. That can be explained from the fact that the adsorption isotherm of this component is lower, which subsequently leads to lower adsorption capacity (even if selectivity of component (A) over (B) is constant). The selectivity has also a positive effect on purity. What it is more interesting though is that the number of beds, mass ratio between the beds, and heat of adsorption of species (B) have a significant effect on system's performance and therefore must be considered as input parameters for optimisation.

Figures C.14 and C.15 illustrate the factorial plots of the main effects and their interactions on the pressure in the storage bed at the last cycle of the process and the recovery of the process, respectively. Figures C.14a and C.14b show that the most important effects on the pressure in the storage bed are the number of beds of the process, mass ratio between the beds, and heat of adsorption of species (B) and their interactions with all having a negative

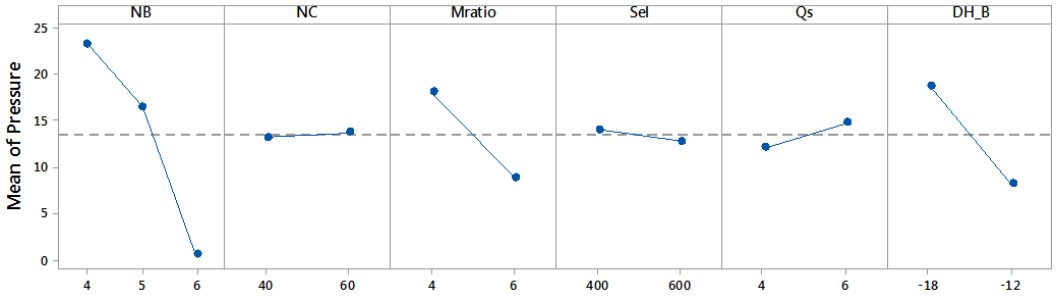

(a) main effects plot for pressure

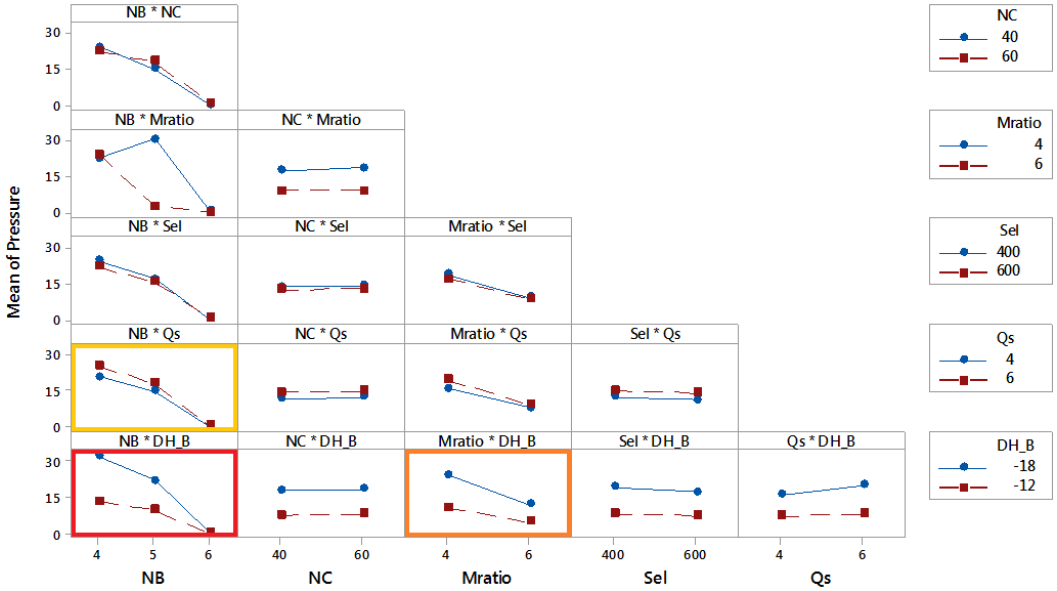

(b) interaction plot for pressure

Figure C.14. Factorial plots for the main effects and their interactions on the pressure in the storage bed as obtained from Minitab® software. Abbreviations: NB, number of beds; NC, number of cycles; Mratio, mass ratio between the beds; Sel, selectivity; Qs, adsorption capacity; and DH_B, heat of adsorption of species (B).

Note: The stronger interactions are colour-squared. Colour discrimination shows how significant the interaction is on energy: red (stronger interaction) – yellow (weaker interaction).

effect on pressure. The negative effect of the increased number of beds on purity has to do with not only the mass ratio between the beds, but also with the fixed mass of the storage bed at 0.3 kg. A smaller mass of the storage bed, for instance, increases the pressure in the bed. This is a parameter to be optimised using a multi-objective optimisation algorithm. Figures C.15a and C.15b present the main effects and their interactions on the recovery of the process. Again, the number of beds has a major negative effect on recovery so as its interaction with the mass ratio between the beds.

Since the optimisation strategy focuses on two objectives, the specific energy consumption and the purity in the storage bed, the results of the sensitivity analysis on these factors are more important. The following outcomes have to be considered:

(i) The number of beds can have a positive or negative effect on the specific energy and pressure of the process depending on the mass of adsorbent in each bed (as sensible

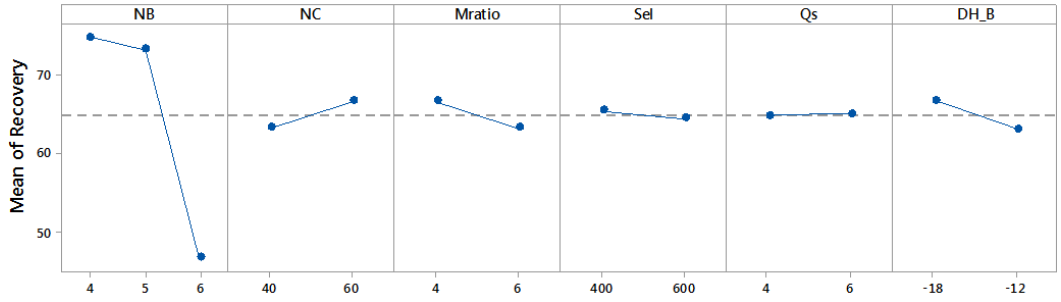

(a) main effects plot for recovery

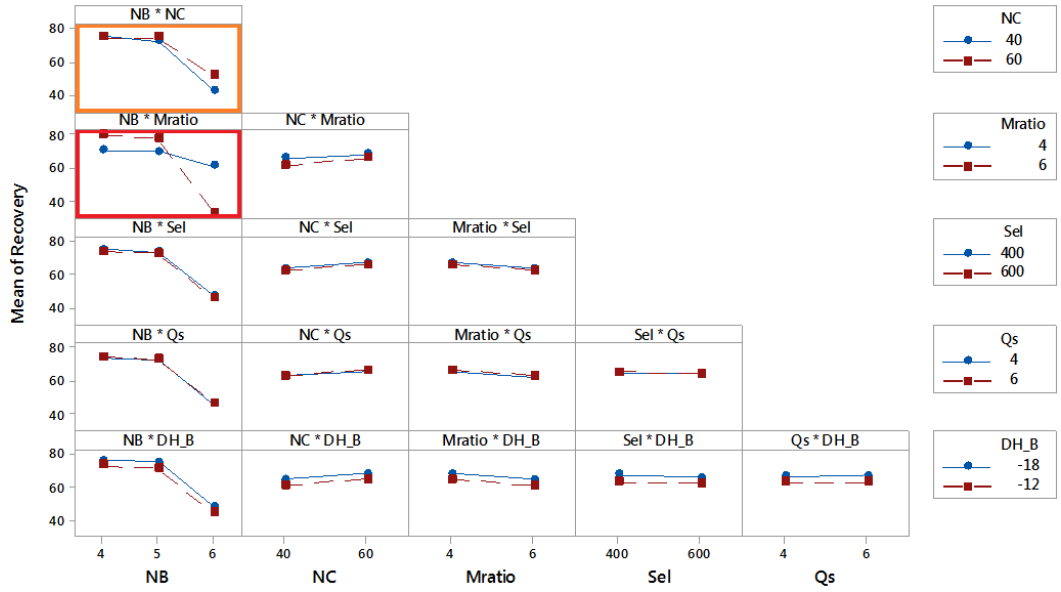

(b) interaction plot for recovery

Figure C.15. Factorial plots for the main effects and their interactions on the recovery of the process as obtained from Minitab® software. Abbreviations: NB, number of beds; NC, number of cycles; Mratio, mass ratio between the beds; Sel, selectivity; Qs, adsorption capacity; and DH_B, heat of adsorption of species (B).

Note: The stronger interactions are colour-squared. Colour discrimination shows how significant the interaction is on energy: red (stronger interaction) – yellow (weaker interaction).

heat has a significant contribution to the specific thermal energy consumption) and the mass ratio between the beds.

(ii) The number of cycles has an expected unfavourable effect on the specific energy consumption and a positive effect on purity. It can be a parameter for optimisation in order to increase the performance of the system.

(iii) Selectivity is not an important parameter on the specific energy but it has a major positive effect on process' purity.

(iv) The adsorption capacity affects negatively the specific energy use of the process and positively affects the purity. An adsorbent material characterised by higher adsorption capacity rather than higher selectivity of the key component (A) over (B) is more effective for the performance of the process and thus it has to be preferred.

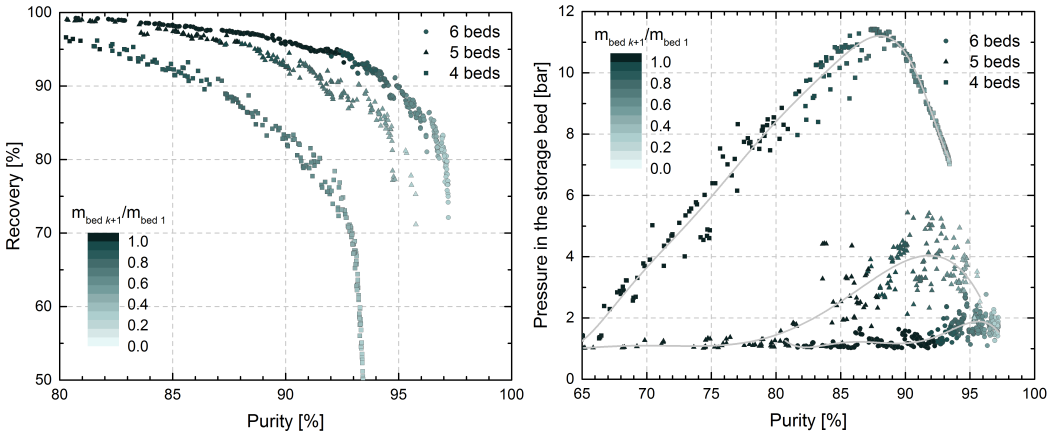

(a) recovery vs purity

(b) pressure vs purity

Figure C.16. Correlation between *(a)* recovery and purity and *(b)* pressure and purity for the case of 4, 5, and 6 beds, 400 ppm y_{A}, $S_{T_{\mathrm{low}}}$=900, X=5, q_{s}=4 mol kg^{-1}, and 50 cycles.

(v) Another parameter that is relevant to the adsorbent material is the heat of adsorption of species (B). This parameter has a significant effect on the purity of the process and an unexpected positive effect on the pressure and the recovery.

However, how the parameters are correlated and a better understanding on how they interact with each other and affect the process performance may be obtained from process optimisation.

C.3 Multi-Objective Optimisation Analysis: Supplementary Information

Figure C.16 illustrates the correlation between the process recovery and the pressure in the storage bed with the purity in the storage bed and the mass of the storage bed for the case of 4, 5, and 6 beds and y_{A}=400 ppm, $S_{T_{\mathrm{low}}}$=900, X=5 $\left(=\frac{S_{T_{\mathrm{low}}}}{S_{T_{\mathrm{high}}}}\right)$, q_{s}=4 mol kg^{-1}, and 50 cycles of the process. Generally, by adding more compression beds to the process, both the purity and recovery increase. Figure C.16b shows that the number of beds have a negative effect on pressure in the storage bed. The design has been constrained to a pressure >1 bar and recovery >10%. By increasing the lower limit of pressure to 2, 5, and 10 bar for the case of 6 beds, the resulting Pareto fronts are illustrated in Figure C.17a and the resulting correlation of pressure, purity, and mass of the storage bed is highlighted in Figure C.17b.

C.4 Process Design: Supplementary Information

Figure C.18 represents the non-linear correlation between the mass of the storage bed, the mass ratio $m_{\mathrm{bed},i}/m_{\mathrm{bed},N_{\mathrm{B}}}$ (where $i = 1, ..., N_{\mathrm{B}}-1$) and the purity for the case of 6 beds and y_{A}=400 ppm, $S_{T_{\mathrm{low}}}$=900, X=5, q_{s}=4 mol kg^{-1}, and N_{R}=50. These results were obtained from the performance of the 6 beds with a constrained storage pressure in the final bed at 2, 5, and 10 bar. The multi-objective optimiser was forced to converge at higher values of pressure in the storage bed and as a result the design rules are slightly different.

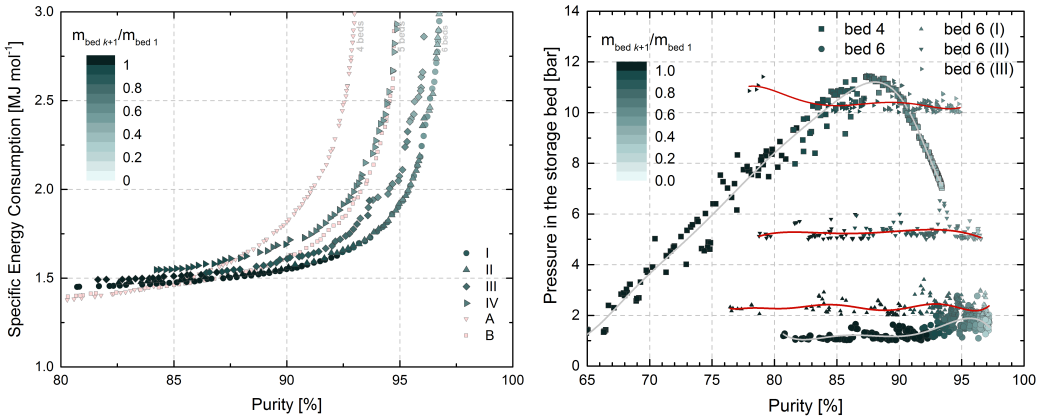

(a) 6 beds – abbreviations for constrained storage pressure: I, 1 bar; II, 2 bar; III, 5 bar; and IV, 10 bar.

(b) 6 beds – abbreviations for constrained storage pressure: I, 2 bar; II, 5 bar; and III, 10 bar.

Figure C.17. Process analysis and design for the case of 6 beds, 400 ppm y_{A}, $S_{T_{\mathrm{low}}}$=900, X=5, q_{s}=4 mol kg^{-1}, 50 cycles and 2, 5, and 10 bar lower limit/constraint of pressure.

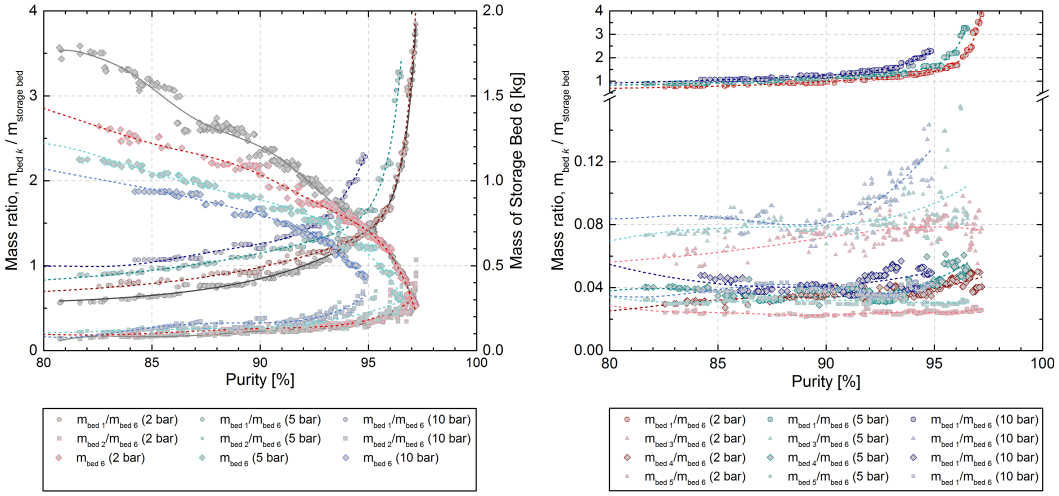

Figure C.18. Correlation between purity, mass of storage bed and mass ratio of each bed over the mass of the storage bed for the case of six beds, y_{A}=400 ppm, $S_{T_{\mathrm{low}}}$=900, X=5, q_{s}=4 mol kg^{-1}, N_{R}=50 and 2, 5, and 10 bar lower limit/constraint of storage pressure.

Drawings of Experimental Set-up

D

Here, the following design drawings of the DAC experimental apparatus are provided:

(i) Figure D.1 provides the process and instrumentation diagram of the system.

(ii) Figure D.2 illustrates the design of the adsorption bed, Bed 1.

(iii) Figure D.3 shows the design of Bed 2, in the compression and purification train.

(iv) Figure D.4 provides the design of Bed 3, in the compression and purification train.

(v) Figure D.5 illustrates the design of the storage bed, Bed 4.

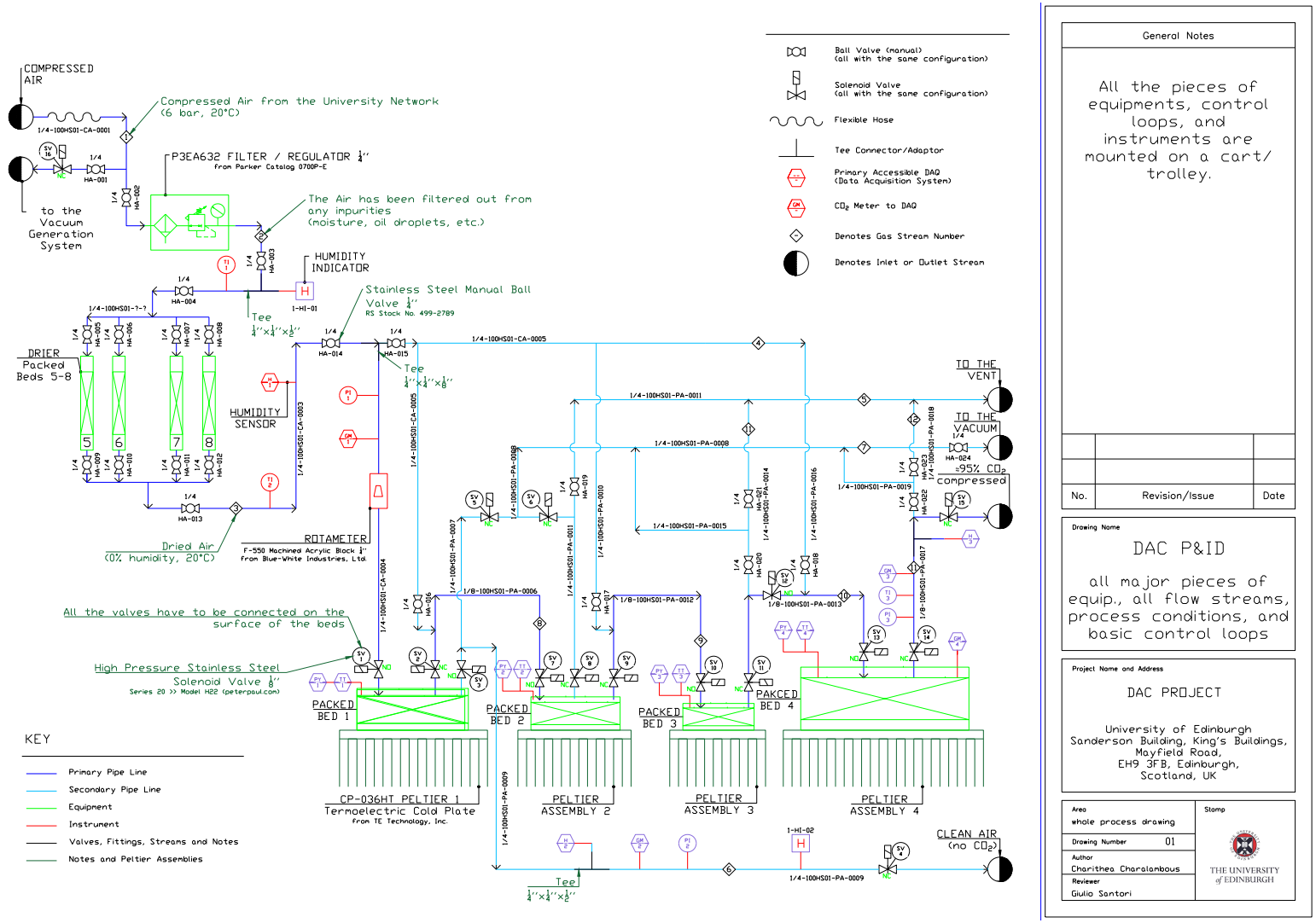

Figure D.1. Process and Instrumentation Diagram for the Direct Air Capture Experimental Apparatus by the Carbon Capture Group at the University of Edinburgh.

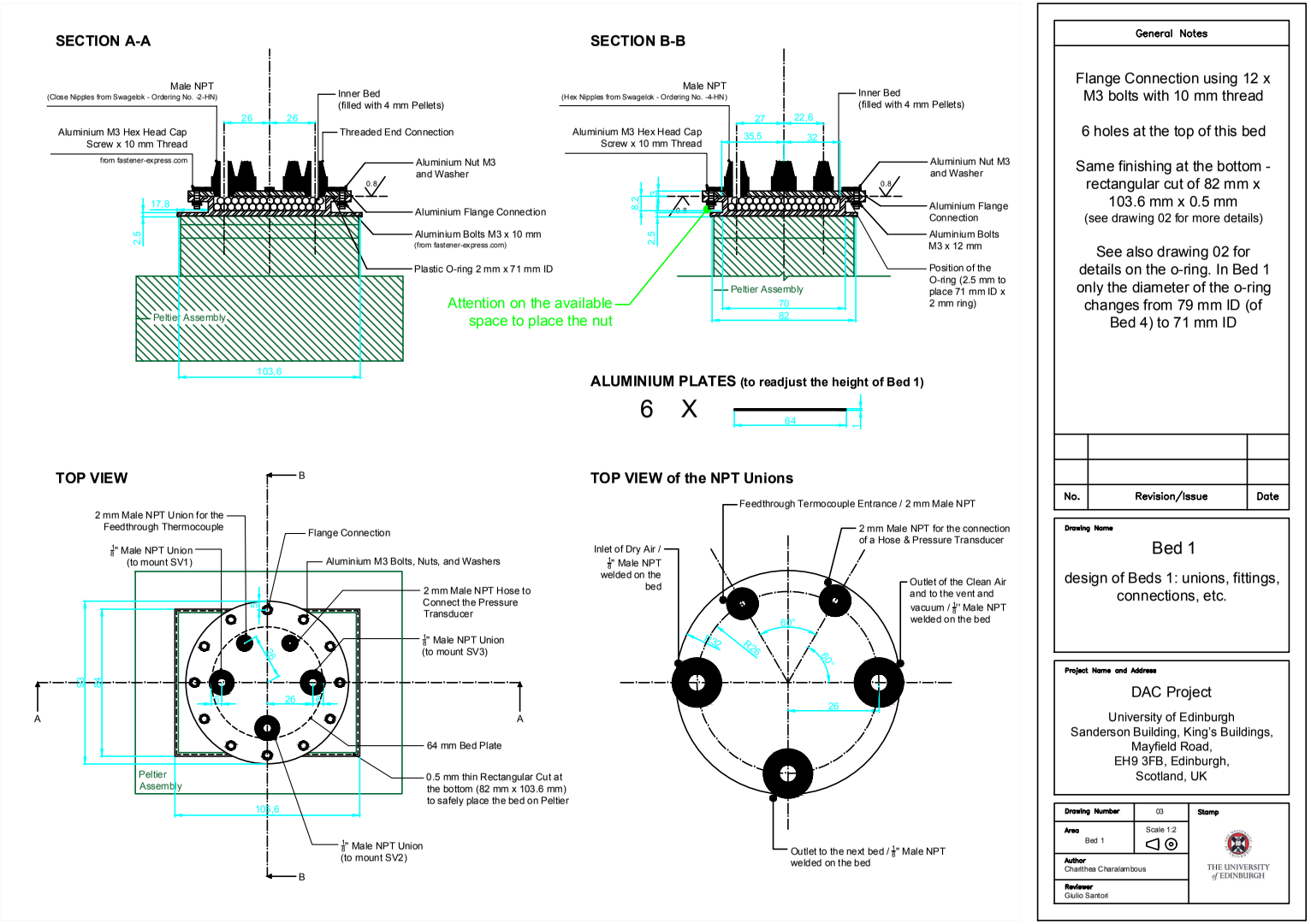

Figure D.2. Bed 1 design drawings of the Direct Air Capture Experimental Apparatus by the Carbon Capture Group at the University of Edinburgh.

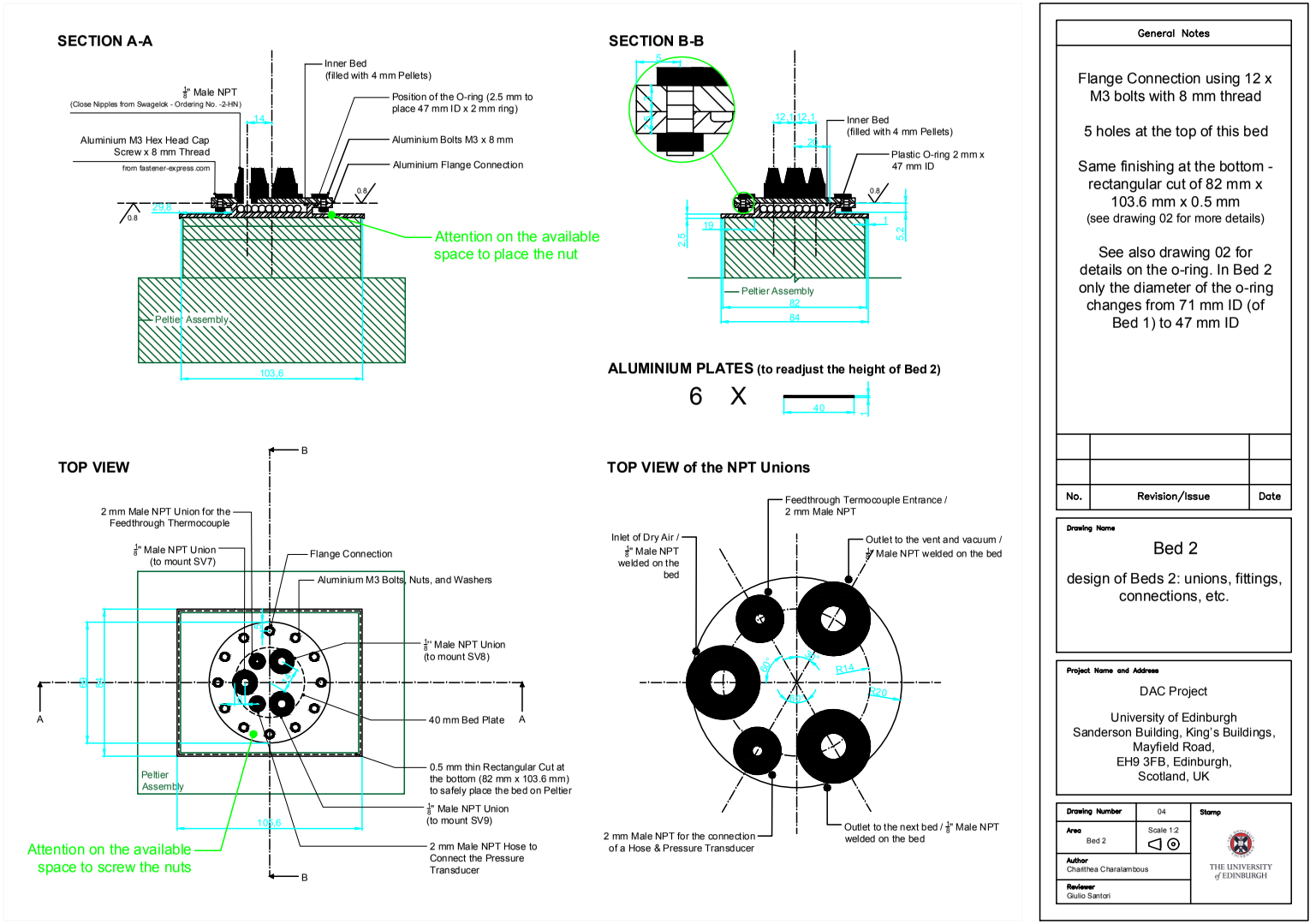

Figure D.3. Bed 2 design drawings of the Direct Air Capture Experimental Apparatus by the Carbon Capture Group at the University of Edinburgh.

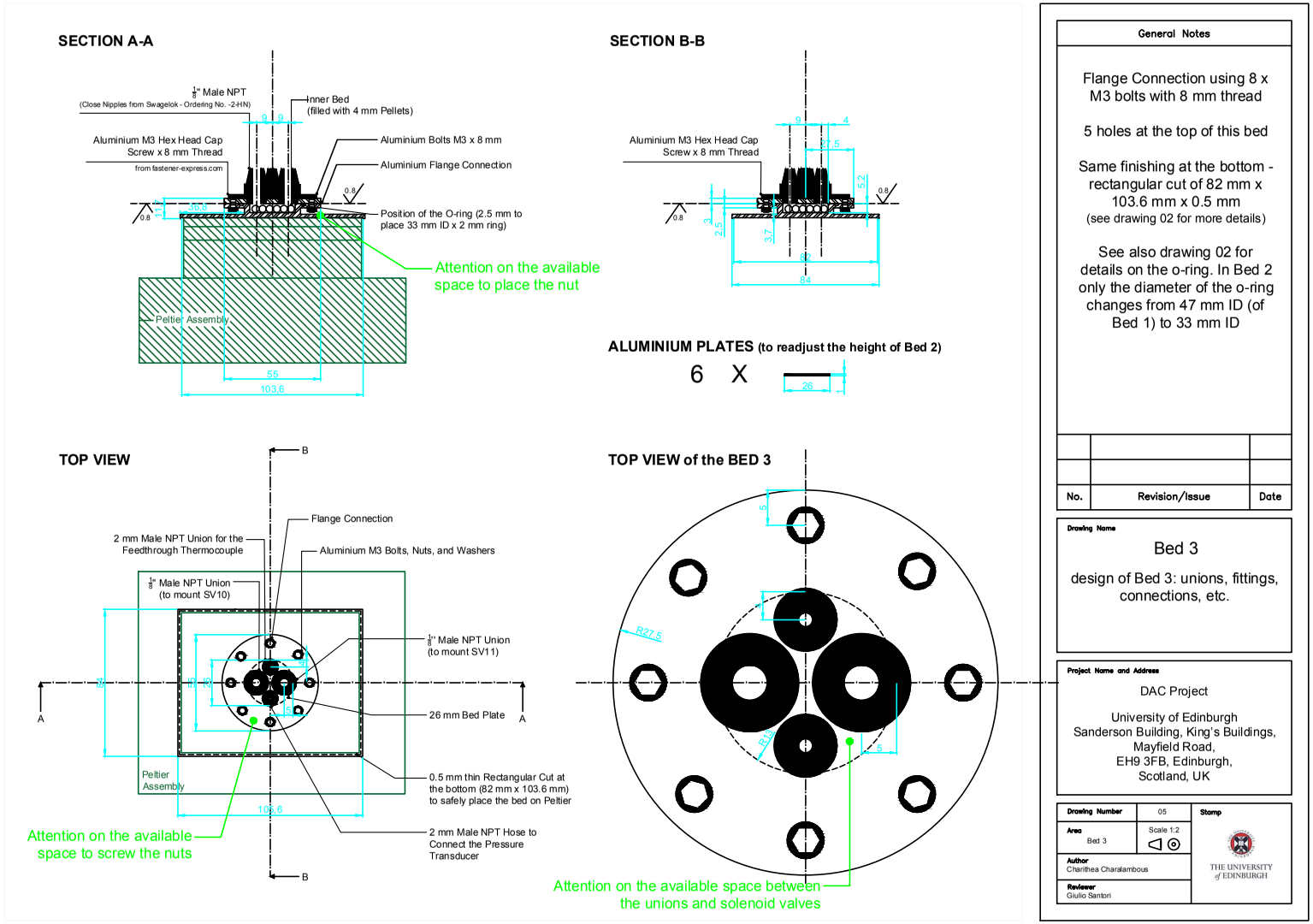

Figure D.4. Bed 3 design drawings of the Direct Air Capture Experimental Apparatus by the Carbon Capture Group at the University of Edinburgh.

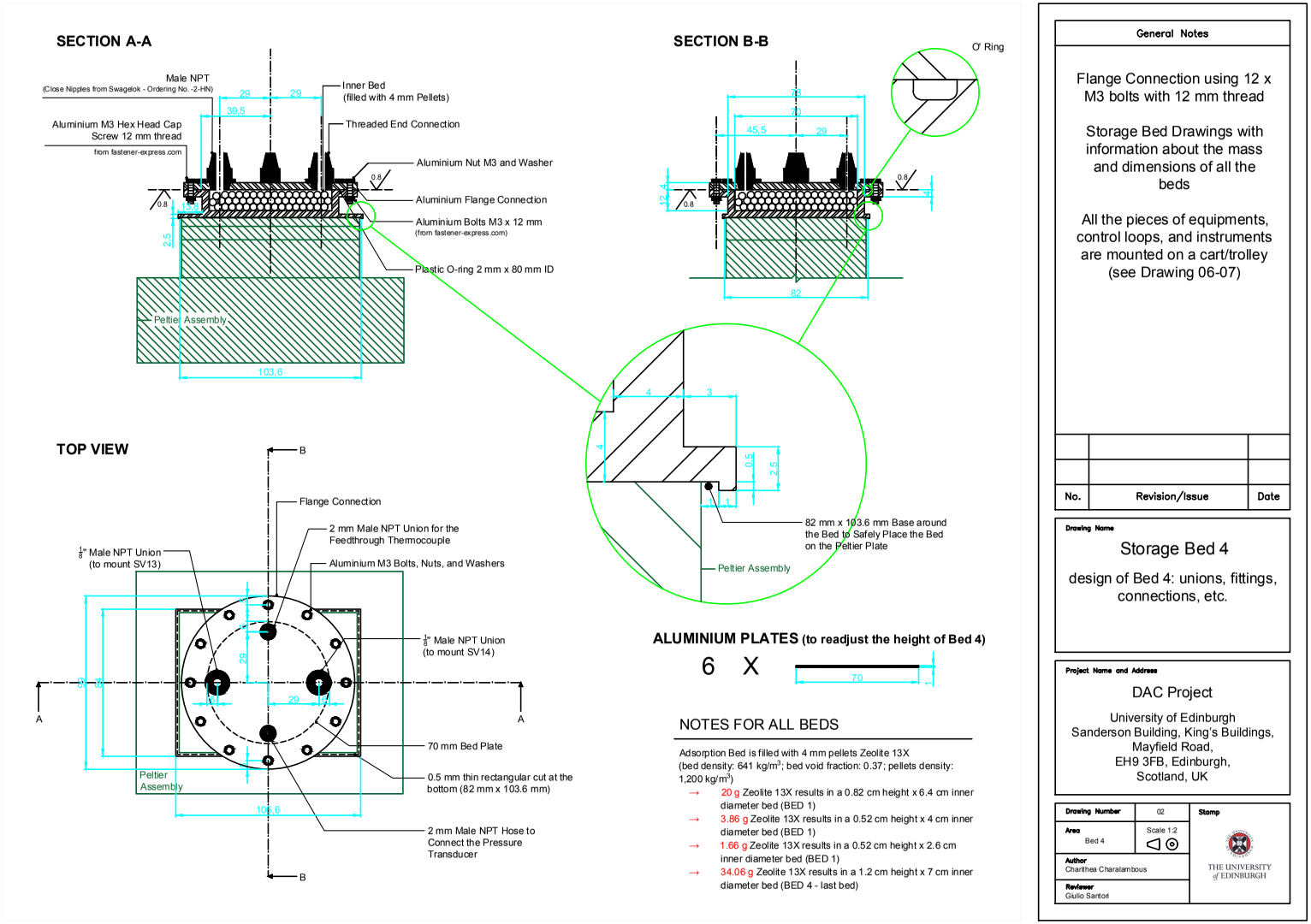

Figure D.5. Bed 4 design drawings of the Direct Air Capture Experimental Apparatus by the Carbon Capture Group at the University of Edinburgh.

Bibliography

Ahn, Hyungwoong and Chang-Ha Lee (2003). “Adsorption dynamics of water in layered bed for air-drying tsa process”. In: *AIChE J.* 49.6, pp. 1601–1609 (cit. on p. 34).

Akhtar, Farid, Linnéa Andersson, Steven Ogunwumi, Niklas Hedin, and Lennart Bergström (2014). “Structuring adsorbents and catalysts by processing of porous powders”. In: *J. Eur. Ceram. Soc.* 34.7, pp. 1643–1666 (cit. on pp. 78, 83).

Alkhabbaz, Mustafa A., Praveen Bollini, Guo Shiou Foo, Carsten Sievers, and Christopher W. Jones (2014). “Important Roles of Enthalpic and Entropic Contributions to CO_2 Capture from Simulated Flue Gas and Ambient Air Using Mesoporous Silica Grafted Amines”. In: *J. Am. Chem. Soc.* 136.38, pp. 13170–13173 (cit. on p. 26).

Ansolobehere, S., J. Beer, J. Deutch, et al. (2007). *The Future of Coal: Options for a Carbon-Constrained World, an interdisciplinary MIT study*. Tech. rep. Cambridge, MA: Massachusetts Institute of Technology, p. 175 (cit. on p. 156).

Arora, Vivek K. and Alvaro Montenegro (2011). “Small temperature benefits provided by realistic afforestation efforts”. In: *Nature Geosci.* 4.8, pp. 514–518 (cit. on p. 5).

Atilhan, M., S. Ejaz, J. Zhou, et al. (2010). “Characterization of Deepwater Natural Gas Samples. Part 1: 78 % Methane Mixture with Heavy Components”. In: *J. Chem. Eng. Data* 55.11, pp. 4907–4911 (cit. on p. 104).

Atkins, Peter and Julio de Paula (2006). “Statistical thermodynamics 2: applications”. In: *Atkins’ Physical Chemistry*. Eighth Ed. New York: W. H. Freeman and Company. Chap. 17, pp. 589–619 (cit. on p. 59).

Baciocchi, Renato, Giuseppe Storti, and Marco Mazzotti (2006). “Process design and energy requirements for the capture of carbon dioxide from air”. In: *Chemical Engineering and Processing: Process Intensification* 45.12, pp. 1047–1058 (cit. on p. 20).

Bai, Runsheng, Jingguang Deng, and Ralph T. Yang (2003). “Improved Multisite Langmuir Model for Mixture Adsorption Using Multiregion Adsorption Theory”. In: *Langmuir* 19.7, pp. 2776–2781 (cit. on p. 37).

Balahmar, Norah, Alexander M. Lowbridge, and Robert Mokaya (2016). “Templating of carbon in zeolites under pressure: synthesis of pelletized zeolite templated carbons with improved porosity and packing density for superior gas (CO_2 and H_2) uptake properties”. In: *J. Mater. Chem. A* 4.37, pp. 14254–14266 (cit. on pp. 51, 72, 123, 167).

Banaszkiewicz, Tomasz and Maciej Chorowski (2015). “Analysis of the applicability of adsorption oxygen generators in the field of industry and power engineering”. In: *Journal of Power Technologies* 95, pp. 1–5 (cit. on p. 34).

Barta, D. J. and D. L. Henninger (1994). “Regenerative life support systems — Why do we need them?” In: *Advances in Space Research* 14.11, pp. 403–410 (cit. on p. 57).

Bastick, R. E., H. R. Heath, and T. L. Ibbs (1939). “The Molecular Fields of Carbon Dioxide and Nitrous Oxide”. In: *Source: Proceedings of the Royal Society of London. Series A, Mathematical and Physical Sciences* 173.955, pp. 543–554 (cit. on pp. 44, 163).

Beck, Joakim, Daniel Friedrich, Stefano Brandani, and Eric S. Fraga (2015). “Multi-Objective Optimisation using Surrogate Models for the Design of VPSA Systems”. In: *Comput. Chem. Eng.* 82, pp. 318–329 (cit. on pp. 117, 120–122).

Belmabkhout, Youssef, Rodrigo Serna-Guerrero, and Abdelhamid Sayari (2010). “Amine-bearing mesoporous silica for CO_2 removal from dry and humid air”. In: *Chem. Eng. Sci.* 65.11, pp. 3695–3698 (cit. on p. 28).

Bezerra, Diôgo P., Ronan S. Oliveira, Rodrigo S. Vieira, Célio L. Cavalcante, and Diana C. S. Azevedo (2011). “Adsorption of CO_2 on nitrogen-enriched activated carbon and zeolite 13X”. In: *Adsorption* 17.1, pp. 235–246 (cit. on p. 89).

Bird, Robert Byron, Warren E. Stewart, and Edwin N. Lightfoot (1960). *Transport phenomena*. New York, London: John Wiley & Sons, Inc., p. 780 (cit. on pp. 44, 160–162).

Bird, Robert Byron, Warren E. Stewart, and Edwin N. Lightfoot (2007). *Transport phenomena*. Second Ed. New York, London: John Wiley & Sons, Inc., p. 905 (cit. on pp. 124, 125).

Blum, Harold A., Leroy F. Stutzman, and Wayne S. Dodds (1952). “Gas Absorption - Absorption of Carbon Dioxide from Air by Sodium and Potassium Hydroxides.” In: *Ind. Eng. Chem.* 44.12, pp. 2969–2974 (cit. on p. 19).

Bolis, Vera (2013). “Fundamentals in Adsorption at the Solid-Gas Interface. Concepts and Thermodynamics”. In: *Calorimetry and Thermal Methods in Catalysis*. Ed. by Aline Auroux. Heidelberg: Springer. Chap. 1, pp. 3–50 (cit. on p. 59).

Bolster, Carl H. and George M. Hornberger (2007). “On the use of linearized Langmuir equations”. In: *Soil Sci. Soc. Am. J.* 71.6, p. 1796 (cit. on p. 98).

Bonaccorsi, Lucio, Luigi Calabrese, Serena Alioto, Paolo Bruzzaniti, and Edoardo Proverbio (2017). “Surface silanation of alumina-silica zeolites for adsorption heat pumping”. In: *Renew. Energy* 110, pp. 79–86 (cit. on pp. 77, 88, 107).

Boot-Handford, Matthew E., Juan C. Abanades, Edward J. Anthony, et al. (2014). “Carbon capture and storage update”. In: *Energy Environ. Sci.* 7.1, p. 130 (cit. on p. 9).

Borel, Lucien and Daniel Favrat (2010). *Thermodynamics and energy systems analysis: from energy to exergy*. EFPL Press, p. 795 (cit. on p. 28).

Box, George E. P., J. Stuart Hunter, and William Gordon Hunter (2005). *Statistics for experimenters: design, innovation, and discovery*. Second Ed. New Jersey: John Wiley & Sons, Inc., p. 633 (cit. on p. 58).

Brandani, Federico and Douglas M. Ruthven (2004). “The Effect of Water on the Adsorption of CO_2 and C_3H_8 on Type X Zeolites”. In: *Ind. Eng. Chem. Res.* 43.26, pp. 8339–8344 (cit. on p. 76).

Brandani, Stefano (2012). “Carbon Dioxide Capture from Air: A Simple Analysis”. English. In: *Energ. Environ.* 23.2, pp. 319–328 (cit. on pp. 8, 10, 11, 25).

Brandani, Stefano, Enzo Mangano, and Lev Sarkisov (2016). “Net, excess and absolute adsorption and adsorption of helium”. In: *Adsorption* 22.2, pp. 261–276 (cit. on pp. 88, 89, 91).

Brodkey, Robert S. and Harry C. Hershey (1988). *Transport phenomena: a unified approach.* Volume I. Ohio: Brodkey Publishing, p. 391 (cit. on pp. 44, 162).

Broughton, D. B. (1948). “Adsorption Isotherms for Binary Gas Mixtures”. In: *Ind. Eng. Chem.* 40.8, pp. 1506–1508 (cit. on p. 42).

Brunauer, Stephen, Lola S. Deming, W. Edwards Deming, and Edward Teller (1940). “On a Theory of the van der Waals Adsorption of Gases”. In: *J. Am. Chem. Soc.* 62.7, pp. 1723–1732 (cit. on p. 166).

Brunetti, A., F. Scura, G. Barbieri, and E. Drioli (2010). “Membrane technologies for CO_2 separation”. In: *J. Membr. Sci.* 359, pp. 115–125 (cit. on p. 8).

Canadell, Josep G. and Michael R. Raupach (2008). “Managing Forests for Climate Change Mitigation”. In: *Science* 320.5882, pp. 1456–1457 (cit. on p. 5).

Cavenati, Simone, Carlos A. Grande, and Alírio E. Rodrigues (2005). “Upgrade of Methane from Landfill Gas by Pressure Swing Adsorption”. In: *Energy Fuels* 19.6, pp. 2545–2555 (cit. on p. 118).

Cavenati, Simone, Carlos A. Grande, and Alírio E. Rodrigues (2006). “Separation of mixtures by layered pressure swing adsorption for upgrade of natural gas”. In: *Chem. Eng. Sci.* 61.12, pp. 3893–3906 (cit. on p. 123).

Chaikittisilp, Watcharop, Hyung-Ju Kim, and Christopher W. Jones (2011a). “Mesoporous Alumina-Supported Amines as Potential Steam-Stable Adsorbents for Capturing CO_2 from Simulated Flue Gas and Ambient Air”. In: *Energy Fuels* 25.11, pp. 5528–5537 (cit. on p. 26).

Chaikittisilp, Watcharop, Ratayakorn Khunsupat, Thomas T. Chen, and Christopher W. Jones (2011b). “Poly(allylamine)–Mesoporous Silica Composite Materials for CO_2 Capture from Simulated Flue Gas or Ambient Air”. In: *Ind. Eng. Chem. Res.* 50.24, pp. 14203–14210 (cit. on pp. 26, 69).

Chaikittisilp, Watcharop, Jonathan D. Lunn, Daniel F. Shantz, and Christopher W. Jones (2011c). “Poly(L-lysine) Brush-Mesoporous Silica Hybrid Material as a Biomolecule-Based Adsorbent for CO_2 Capture from Simulated Flue Gas and Air”. In: *Chem. Eur. J.* 17.38, pp. 10556–10561 (cit. on p. 26).

Chakraborty, Anutosh and Baichuan Sun (2014). “An adsorption isotherm equation for multi-types adsorption with thermodynamic correctness”. In: *Appl. Therm. Eng.* 72.2, pp. 190–199 (cit. on p. 33).

Charalambous, C., M.-C. Ferrari, G. Santori, and S. Brandani (2016). *Thermally-driven adsorption, concentration and purification of highly dilute gases*. Work presented at the Heat Powered Cycle Conference, Nottingham, UK (cit. on pp. 27, 38, 41).

Chen, Chen and Massimo Tavoni (2013). “Direct air capture of CO_2 and climate stabilization: A model based assessment”. In: *Clim. Change* 118.1, pp. 59–72 (cit. on p. 7).

Chichilnisky, Graciela, Peter Eisenberger, Roger W. Cohen, et al. (2009). “Global Warming and Carbon-Negative Technology: Prospects for a Lower-Cost Route to a Lower-Risk Atmosphere”. In: *Energy Environ.* 20.6, pp. 973–984 (cit. on p. 5).

Choi, S., J. H. Drese, P. Eisenberger, and C. W. Jones (2009a). “A New Paradigm of Anthropogenic CO_2 Reduction: Adsorptive Fixation of CO_2 From the Ambient Air as a Carbon Negative Technology”. In: *AIChE Annu. Meet.* Nashville (cit. on p. 25).

Choi, S., J. H. Drese, R. R. Chance, P. M. Eisenberger, and C. W. Jones (2011a). *Application of amine-tethered solid sorbents to CO_2 fixation from air* (cit. on p. 26).

Choi, Sunho, Jeffrey H. Drese, and Christopher W. Jones (2009b). “Adsorbent materials for carbon dioxide capture from large anthropogenic point sources.” In: *ChemSusChem* 2.9, pp. 796–854 (cit. on pp. 9, 22, 25).

Choi, Sunho, McMahan L. Gray, and Christopher W. Jones (2011b). “Amine-Tethered Solid Adsorbents Coupling High Adsorption Capacity and Regenerability for CO_2 Capture From Ambient Air”. In: *ChemSusChem* 4.5, pp. 628–635 (cit. on p. 26).

Choi, Sunho, Jeffrey H. Drese, Peter M. Eisenberger, and Christopher W. Jones (2011c). “Application of amine-tethered solid sorbents for direct CO_2 capture from the ambient air.” In: *Environ. Sci. Technol.* 45.6, pp. 2420–2427 (cit. on pp. 9, 22, 26).

Choi, Sunho, Taku Watanabe, Tae-Hyun Bae, David S. Sholl, and Christopher W. Jones (2012). “Modification of the Mg/DOBDC MOF with Amines to Enhance CO_2 Adsorption from Ultradilute Gases”. In: *J. Phys. Chem. Lett.* 3.9, pp. 1136–1141 (cit. on p. 26).

Cortés, Joaquín (1985). “Gas-solid adsorption isotherms”. In: *Adv. Colloid Interface Sci.* 22.2-4, pp. 151–176 (cit. on p. 167).

Couck, Sarah, Julien Cousin-Saint-Remi, Stijn Van der Perre, et al. (2018). “3D-printed SAPO-34 monoliths for gas separation”. In: *Micropor. Mesopor. Mat.* 255, pp. 185–191 (cit. on p. 99).

Creutzig, Felix, N. H. Ravindranath, Göran Berndes, et al. (2015). “Bioenergy and climate change mitigation: an assessment”. In: *Global Change Biol. Bioenergy* 7.5, pp. 916–944 (cit. on p. 5).

Cristancho, Diego E., Ivan D. Mantilla, Saquib Ejaz, et al. (2010). “Force transmission error analysis for a high-pressure single-sinker magnetic suspension densimeter”. In: *Int. J. Thermophys.* Vol. 31. 4-5. Springer US, pp. 698–709 (cit. on p. 104).

Curtin, Teresa, Michael J. Zaworotko, David G. Madden, et al. (2017). “Flue-gas and direct-air capture of CO_2 by porous metal–organic materials”. In: *Phil. Trans. R. Soc. A* 375, p. 11 (cit. on p. 28).

Dahlquist, Erik and Andrew Jones (2005). “Presentation of a dry black liquor gasification process with direct causticization”. In: *Tappi J.* 4.5, pp. 15–19 (cit. on p. 23).

Dahmus, Jeffrey B. and Timothy G. Gutowski (2007). “What Gets Recycled: An Information Theory Based Model for Product Recycling”. In: *Environ. Sci. Technol.* 41.21, pp. 7543–7550 (cit. on p. 12).

Dantas, T. L. P, F. M. T Luna, I. J Silva Jr, et al. (2011). “Modeling of the fixed - bed adsorption of carbon dioxide and a carbon dioxide - nitrogen mixture on zeolite 13X”. In: *Braz. J. Chem. Eng.* 28.3, pp. 533–544 (cit. on p. 123).

Darunte, Lalit A., Aloysius D. Oetomo, Krista S. Walton, David S. Sholl, and Christopher W. Jones (2016). “Direct Air Capture of CO_2 Using Amine Functionalized MIL-101(Cr)”. In: *ACS Sustainable Chem. Eng.* 4.10, pp. 5761–5768 (cit. on p. 26).

Deb, Kalyanmoy, Samir Agrawal, Amrit Pratap, and T. Meyarivan (2000). “A Fast Elitist Non-dominated Sorting Genetic Algorithm for Multi-objective Optimisation: NSGA-II”. In: *Proceedings of the 6th International Conference on Parallel Problem Solving from Nature*. Ed. by Marc. Schoenauer, Kalyanmoy Deb, Giinter Rudolph, et al. Paris: Springer, pp. 849–858 (cit. on p. 61).

Di Nicola, G., M. Pacetti, F. Polonara, G. Santori, and R. Stryjek (2008). “Development and optimization of a method for analyzing biodiesel mixtures with non-aqueous reversed phase liquid chromatography”. In: *J. Chromatogr. A* 1190.1, pp. 120–126 (cit. on p. 58).

Diagne, Doudou, Motonobu Goto, and Tsutomu Hirose (1996). “Numerical analysis of a dual refluxed PSA process during simultaneous removal and concentration of carbon dioxide dilute gas from air”. In: *J. Chem. Technol. Biotechnol.* 65.1, pp. 29–38 (cit. on p. 9).

Didas, Stephanie A., Ambarish R. Kulkarni, David S. Sholl, and Christopher W. Jones (2012). “Role of Amine Structure on Carbon Dioxide Adsorption from Ultradilute Gas Streams such as Ambient Air”. In: *ChemSusChem* 5.10, pp. 2058–2064 (cit. on p. 26).

Do, D. Duong (1998). *Adsorption Analysis: Equilibria and Kinetics*. Second Ed. Imperial College Press, pp. 1–892 (cit. on pp. 17, 34, 75, 76, 93, 94, 109, 111).

Dreisbach, F., H. W. Lösch, and P. Harting (2002). “Highest Pressure Adsorption Equilibria Data: Measurement with Magnetic Suspension Balance and Analysis with a New Adsorbent/Adsorbate-Volume”. In: *Adsorption* 8.2, pp. 95–109 (cit. on pp. 89, 91).

Dreisbach, F., R. Seif, and H. W. Lösch (2003). “Adsorption equilibria of CO/H_2 with a magnetic suspension balance: Purely gravimetric measurement”. In: *J. Therm. Anal. Calorim.* 71.1, pp. 73–82 (cit. on p. 91).

Drioli, Enrico and Giuseppe Barbieri (2011). *Membrane Engineering for the Treatment of Gases: Gas-Separation Problems with Membranes*. Royal Society of Chemistry, p. 298 (cit. on p. 9).

Dubey, M K, H Ziock, G Rueff, et al. (2002). “Extraction of carbon dioxide from the atmosphere through engineering chemical sinkage”. In: *Fuel Chem. Division Preprints* 47.1, pp. 81–84 (cit. on p. 19).

Duffie, John A. and William A. Beckman (2013). *Solar engineering of thermal processes*. Fourth Ed. Hoboken, New Jersey: John Wiley & Sons, Inc., p. 910 (cit. on p. 51).

Duncan, J. B. and H. L. Toor (1962). “An experimental study of three component gas diffusion”. In: *AIChE Journal* 8.1, pp. 38–41 (cit. on p. 161).

Dunne, J. A., M. Rao, S. Sircar, R. J. Gorte, and A. L. Myers (1996). “Calorimetric Heats of Adsorption and Adsorption Isotherms. 2. O_2, N_2, Ar, CO_2, CH_4, C_2H_2, and SF_6 on NaX, H-ZSM-5, and Na-ZSM-5 Zeolites”. In: *Langmuir* 12.24, pp. 5896–5904 (cit. on p. 87).

Dupont, Elise, Rembrandt Koppelaar, and Hervé Jeanmart (2018). “Global available wind energy with physical and energy return on investment constraints”. In: *Applied Energy* 209, pp. 322–338 (cit. on p. 13).

EIA (2017). *International Energy Outlook 2016*. Tech. rep. U.S. Energy Information Administration, p. 276 (cit. on pp. 1, 2).

Eisenberger, Peter (2015). *Rotating multi-monolith bed movement system for removing CO_2 from the atmosphere* (cit. on p. 25).

Eisenberger, Peter and Graciela Chichilnisky (2014). *System and method for removing carbon dioxide from an atmosphere and global thermostat using the same* (cit. on p. 25).

Elfving, Jere, Cyril Bajamundi, and Juho Kauppinen (2017). “Characterization and Performance of Direct Air Capture Sorbent”. In: *International COnference on Greenhouse Gas Control Technologies*. Vol. 114. Switzerland, pp. 6087–6101 (cit. on p. 28).

ElSherif, Dina and James C. Knox (2005). “International Space Station Carbon Dioxide Removal Assembly (ISS CDRA) Concepts and Advancements”. In: *International Conference on Environmental Systems*. Rome, pp. 1–5 (cit. on pp. 8, 57, 87).

Ferrari, M.-C., D. Friedrich, G. Santori, and S. Brandani (2013). *Design of a small scale air capture system*. Work presented at the FOA11: 11th International Symposium on the Fundamentals of Adsorption, Baltimore, MD, United States (cit. on pp. 27, 41).

Freni, A., G. Maggio, S. Vasta, et al. (2008). “Optimization of a solar-powered adsorptive ice-maker by a mathematical method”. In: *Solar Energy* 82.11, pp. 965–976 (cit. on pp. 58, 174).

Friedlingstein, P., R. M. Andrew, J. Rogelj, et al. (2014). “Persistent growth of CO_2 emissions and implications for reaching climate targets”. In: *Nature Geosci.* 7.10, pp. 709–715 (cit. on p. 3).

Friedrich, Daniel, Maria-Chiara Ferrari, and Stefano Brandani (2013). “Efficient Simulation and Acceleration of Convergence for a Dual Piston Pressure Swing Adsorption System”. In: *Ind. Eng. Chem. Res.* 52.26, pp. 8897–8905 (cit. on p. 120).

Friedrich, Daniel, Enzo Mangano, and Stefano Brandani (2015). “Automatic estimation of kinetic and isotherm parameters from ZLC experiments”. In: *Chem. Eng. Sci.* 126, pp. 616–624 (cit. on p. 120).

Fuss, Sabine, Josep G. Canadell, Glen P. Peters, et al. (2014). “Betting on negative emissions”. In: *Nature Clim. Change* 4.10, pp. 850–853 (cit. on pp. 4, 13, 16).

GEA and IIASA (2012). *Global Energy Assessment: Toward a Sustainable Future*. Ed. by Thomas B. Johansson, Anand Patwardhan, Nebojsa Nakicenovic, and Luis Gomez-Echeverri. Cambridge, New York, Laxenburg: Cambridge University Press, p. 93 (cit. on p. 5).

Gebald, C., J. A. Wurzbacher, and A. Steinfeld (2012). *Amine containing fibrous structure for adsorption of CO_2 from atmospheric air* (cit. on pp. 26, 27).

Gebald, Christoph, Jan Andre Wurzbacher, Philippe Tingaut, Tanja Zimmermann, and Aldo Steinfeld (2011). “Amine-based nanofibrillated cellulose as adsorbent for CO_2 capture from air.” In: *Environ. Sci. Technol.* 45.20, pp. 9101–9108 (cit. on p. 27).

Gebald, Christoph, Jan A. Wurzbacher, Philippe Tingaut, and Aldo Steinfeld (2013). “Stability of Amine-Functionalized Cellulose during Temperature-Vacuum-Swing Cycling for CO_2 Capture from Air”. In: *Environ. Sci. Technol.* 47.17, pp. 10063–10070 (cit. on p. 27).

Gebald, Christoph, Jan A. Wurzbacher, Andreas Borgschulte, Tanja Zimmermann, and Aldo Steinfeld (2014). “Single-Component and Binary CO_2 and H_2O Adsorption of Amine-Functionalized Cellulose”. In: *Environ. Sci. Technol.* 48.4, pp. 2497–2504 (cit. on p. 27).

Gholami, M. and M. R. Talaie (2010). “Investigation of Simplifying Assumptions in Mathematical Modeling of Natural Gas Dehydration Using Adsorption Process and Introduction of a New Accurate LDF Model”. In: *Ind. Eng. Chem. Res.* 49.2, pp. 838–846 (cit. on p. 115).

Gibson, J. A. Arran, Enzo Mangano, Elenica Shiko, et al. (2016). “Adsorption Materials and Processes for Carbon Capture from Gas-Fired Power Plants: AMPGas”. In: *Ind. Eng. Chem. Res.* 55.13, pp. 3840–3851 (cit. on pp. 28, 50).

Giesy, Timothy J., Yu Wang, and M. Douglas LeVan (2012). “Measurement of Mass Transfer Rates in Adsorbents: New Combined-Technique Frequency Response Apparatus and Application to CO_2 in 13X Zeolite”. In: *Ind. Eng. Chem. Res* 51, pp. 11509–11517 (cit. on p. 113).

Giving USA (2017). *Giving USA 2017: The Annual Report on Philanthropy for the Year 2016* (cit. on pp. 13, 156).

Glueckauf, E. (1955). “Theory of chromatography. Part 10: Formula for diffusion into spheres and their application to chromatography”. In: *Trans. Faraday Soc.* 51, pp. 1540–1551 (cit. on p. 117).

Goeppert, Alain, Miklos Czaun, Robert B. May, et al. (2011). “Carbon dioxide capture from the air using a polyamine based regenerable solid adsorbent”. In: *J. Am. Chem. Soc.* 133.50, pp. 20164–7 (cit. on p. 28).

Goeppert, Alain, Hang Zhang, Miklos Czaun, et al. (2014). “Easily regenerable solid adsorbents based on polyamines for carbon dioxide capture from the air”. In: *ChemSusChem* 7.5, pp. 1386–1397 (cit. on p. 70).

Goldsworthy, M. J. (2014). “Measurements of water vapour sorption isotherms for RD silica gel, AQSOA-Z01, AQSOA-Z02, AQSOA-Z05 and CECA zeolite 3A”. In: *Micropor. Mesopor. Mat.* 196, pp. 59–67 (cit. on p. 87).

Goos, Elke, Uwe Riedel, Li Zhao, and Ludger Blum (2011). “Phase diagrams of CO_2 and CO_2–N_2 gas mixtures and their application in compression processes”. In: *Energy Procedia* 4, pp. 3778–3785 (cit. on p. 8).

Grande, Carlos A. (2012). “Advances in Pressure Swing Adsorption for Gas Separation”. In: *ISRN Chemical Engineering* 2012, pp. 1–13 (cit. on p. 34).

Grew, K. E. (1947). “Thermal Diffusion in Mixtures of the Inert Gases”. In: *Proceedings of the Royal Society of London A: Mathematical, Physical and Engineering Sciences*. Vol. 189. 1018, pp. 402–414 (cit. on pp. 162, 163).

Gummer, John, Nick Chater, Samuel Fankhauser, et al. (2016). *UK climate action following the Paris Agreement*. Tech. rep. London, p. 59 (cit. on pp. 5, 16).

Harlick, Peter J. E. and F. Handan Tezel (2004). “An experimental adsorbent screening study for CO_2 removal from N_2”. In: *Micropor. Mesopor. Mat.* 76.1-3, pp. 71–79 (cit. on p. 87).

He, Hongkun, Wenwen Li, Mingjiang Zhong, et al. (2013). “Reversible CO_2 capture with porous polymers using the humidity swing”. In: *Energy Environ. Sci.* 6.2, pp. 488–493 (cit. on p. 24).

Hefti, Max, Dorian Marx, Lisa Joss, and Marco Mazzotti (2015). “Adsorption equilibrium of binary mixtures of carbon dioxide and nitrogen on zeolites ZSM-5 and 13X”. In: *Micropor. Mesopor. Mat.* 215, pp. 215–228 (cit. on pp. 50, 87).

Heidel, Kenton, David Keith, Arvinder Singh, and Geoff Holmes (2011). “Process design and costing of an air-contactor for air-capture”. In: *Energy Procedia* 4, pp. 2861–2868 (cit. on p. 22).

Hinduja, M. J., S. Sundaresan, and R. Jackson (1980). “A crossflow model of dispersion in packed bed reactors”. In: *AIChE J.* 26.2, pp. 274–281 (cit. on p. 115).

Holmes, Geoffrey and David W. Keith (2012). “An air-liquid contactor for large-scale capture of CO_2 from air.” In: *Phil. Trans. R. Soc. A* 370.1974, pp. 4380–403 (cit. on pp. 20, 22, 136).

Holmes, Geoffrey, Kevin Nold, Tylor Walsh, et al. (2013). “Outdoor Prototype Results for Direct Atmospheric Capture of Carbon Dioxide”. In: *Energy Procedia* 37, pp. 6079–6095 (cit. on pp. 22, 136).

Hoover, Roger P. and Phillip C. Wankat (2002). “Gas compression using temperature swing adsorption”. In: *Separ. Sci. Technol.* 37.14, pp. 3187–3199 (cit. on pp. 41, 43).

House, Kurt Zenz, Antonio C. Baclig, Manya Ranjan, et al. (2011). “Economic and energetic analysis of capturing CO_2 from ambient air.” In: *Proceedings of the National Academy of Sciences of the United States of America* 108.51, pp. 20428–33 (cit. on pp. 8, 10–12, 20).

Hu, Xiayi, Enzo Mangano, Daniel Friedrich, Hyungwoong Ahn, and Stefano Brandani (2014). “Diffusion mechanism of CO_2 in 13X zeolite beads”. In: *Adsorption* 20.1, pp. 121–135 (cit. on pp. 51, 106, 113, 117, 123, 124, 132).

Hwang, Kye Soon, Jae Ho Jun, and Won Kook Lee (1995). “Fixed-bed adsorption for bulk component system. Non-equilibrium, non-isothermal and non-adiabatic model”. In: *Chem. Eng. Sci.* 50.5, pp. 813–825 (cit. on p. 113).

Inman, Mason (2008). “Carbon is forever”. In: *Nature Reports Climate Change* 02.0812, pp. 156–158 (cit. on p. 1).

IPCC (2005). *IPCC Special Report on Carbon Dioxide Capture and Storage*. Ed. by Bert Metz, Ogunlade Davidson, Heleen de Coninck, Manuela Loos, and Leo Meyer. Cambridge: Cambridge University Press, p. 431 (cit. on pp. 79, 155, 156).

IPCC (2014). *Climate Change 2014: Synthesis Report. Contribution of Working Groups I, II and III to the Fifth Assessment Report of the Intergovernmental Panel on Climate Change*. Tech. rep. Geneva, Switzerland: IPCC, p. 151 (cit. on pp. 5, 16).

IPCC (2015). *Climate Change 2014: Mitigation of Climate Change*. Ed. by Ottmar Edenhofer, Ramón Pichs-Madruga, Youba Sokona, et al. IPCC Working Group III Contribution AR5. Geneva, Switzerland, p. 141 (cit. on pp. 3, 5).

Jacobson, Mark Z., Mark A. Delucchi, Zack A. F. Bauer, et al. (2017). “100% Clean and Renewable Wind, Water, and Sunlight All-Sector Energy Roadmaps for 139 Countries of the World”. In: *Joule* 1, pp. 1–14 (cit. on p. 13).

Jones, Christopher W. (2011). “CO_2 Capture from Dilute Gases as a Component of Modern Global Carbon Management”. In: *Annu. Rev. Chem. Biomol. Eng.* 2.1, pp. 31–52 (cit. on pp. 19, 22, 23).

Jones, Christopher W. (2013). *Removing Carbon Dioxide from the Atmosphere: Scientific, Technological and Societal Challenges*. Tech. rep. Georgia: Georgia Institute of Technology, p. 4 (cit. on p. 15).

Jones, Nicola (2008). “Sucking carbon out of the air”. In: *Nature* (cit. on pp. 13, 20, 156).

Joos, F., J. L. Sarmiento, and U. Siegenthaler (1991). “Estimates of the effect of Southern Ocean iron fertilization on atmospheric CO_2 concentrations”. In: *Nature* 349.6312, pp. 772–775 (cit. on p. 5).

Joos, Lennart, Joseph A. Swisher, and Berend Smit (2013). “Molecular Simulation Study of the Competitive Adsorption of H_2O and CO_2 in Zeolite 13X”. In: *Langmuir* 29.51, pp. 15936–15942 (cit. on p. 87).

Joss, Lisa, Matteo Gazzani, Max Hefti, Dorian Marx, and Marco Mazzotti (2015). “Temperature Swing Adsorption for the Recovery of the Heavy Component: An Equilibrium-Based Shortcut Model”. In: *Ind. Eng. Chem. Res.* 54.11, pp. 3027–3038 (cit. on pp. 9, 131, 132, 136).

Kapoor, A., J. A. Ritter, and Ralph T. Yang (1990). “An extended Langmuir model for adsorption of gas mixtures on heterogeneous surfaces”. In: *Langmuir* 6.3, pp. 660–664 (cit. on p. 42).

Kayal, Sibnath, Sun Baichuan, and Bidyut Baran Saha (2016). “Adsorption characteristics of AQSOA zeolites and water for adsorption chillers”. In: *Int. J. Heat Mass Tran.* 92, pp. 1120–1127 (cit. on p. 88).

Keating, Michael (1993). *The Earth Summit's Agenda for Change: A Plain Language Version of Agenda 21 and the Other Rio Agreements*. Second Ed. Geneva, Switzerland: Centre for Our Common Future, p. 70 (cit. on p. 2).

Keith, David and Maryam Mahmoudkhani (2012). *Carbon dioxide capture* (cit. on pp. 22, 23).

Keith, David W. (2009). "Why capture CO_2 from the atmosphere?" In: *Science* 325.5948, pp. 1654–5 (cit. on p. 6).

Keith, David W., Minh Ha-Duong, and Joshuah K. Stolaroff (2006). "Climate Strategy with CO_2 Capture from the Air". In: *Clim. Change* 74.1-3, pp. 17–45 (cit. on pp. 6, 20).

Keith, David W., Kenton Heidel, and Robert Cherry (2010). "Capturing CO_2 from the atmosphere: rationale and process design considerations". In: *Geo-Engineering Climate Change: Environmental Necessity of Pandora's Box?* Ed. by Brian Launder and J. Michael T. Thompson. Cambridge University Press. Chap. 6, pp. 107–126 (cit. on pp. 22, 23).

Kemball, C., E. K. Rideal, and E. A. Guggenheim (1948). "Thermodynamics of monolayers". In: *Trans. Faraday Soc.* 44, p. 948 (cit. on p. 42).

Khalighi, Mona, Shamsuzzaman Farooq, and Iftekhar A Karimi (2012). "Nonisothermal Pore Diffusion Model for a Kinetically Controlled Pressure Swing Adsorption Process". In: *Ind. Eng. Chem. Res.* 51.32, pp. 10659–10670 (cit. on pp. 115, 118).

Kheshgi, Haroon S. (1995). "Sequestering atmospheric carbon dioxide by increasing ocean alkalinity". In: *Energy* 20.9, pp. 915–922 (cit. on p. 5).

Konak, Abdullah, David W. Coit, and Alice E. Smith (2006). "Multi-objective optimization using genetic algorithms: A tutorial". In: *Reliab. Eng. & Syst. Safe* 91.9, pp. 992–1007 (cit. on p. 61).

Kriegler, Elmar, Keywan Riahi, Nico Bauer, et al. (2015). "Making or breaking climate targets: The AMPERE study on staged accession scenarios for climate policy". In: *Technol. Forecase. Soc.* 90, pp. 24–44 (cit. on pp. 6, 7).

Kulkarni, Ambarish R. and David S. Sholl (2012). "Analysis of Equilibrium-Based TSA Processes for Direct Capture of CO_2 from Air". In: *Ind. Eng. Chem. Res.* 51.25, pp. 8631–8645 (cit. on pp. 25, 26).

Kumar, Ravi (1989). "Adsorption column blowdown: adiabatic equilibrium model for bulk binary gas mixtures". In: *Ind. Eng. Chem. Res.* 28.11, pp. 1677–1683 (cit. on pp. 42, 47).

Kunzig, Robert and Wallace Broecker (2009). "Carbon scrubbers: taking CO_2 out of the air". In: *New Scientist* 201.2690, pp. 34–37 (cit. on p. 21).

Lackner, K. S. and A. Wright (2010). *Laminar scrubber apparatus for capturing carbon dioxide from air and methods of use* (cit. on p. 24).

Lackner, Klaus S. (2003). "A Guide to CO_2 Sequestration". In: *Science* 300.5626, pp. 1677–1678 (cit. on p. 19).

Lackner, Klaus S. (2009). "Capture of carbon dioxide from ambient air". In: *Eur. Phys. J. Special Topics* 176.1, pp. 93–106 (cit. on pp. 6, 14, 20, 25, 87).

Lackner, Klaus S. and Sarah Brennan (2009). "Envisioning carbon capture and storage: expanded possibilities due to air capture, leakage insurance, and C-14 monitoring". In: *Climatic Change* 96.3, pp. 357–378 (cit. on p. 24).

Lackner, Klaus S. and Ping Liu (2008). *Removal of carbon dioxide from air* (cit. on p. 24).

Lackner, Klaus S., Grimes Patrick, and Ziock Hans-Joachim (1999). "Carbon Dioxide Extraction from air: Is it an option?" In: *Proceeding of the 24th Annual Technical Conference on Coal Utilization and Fuel Systems, Clearwater, Florida*, pp. 885–896 (cit. on p. 19).

Lackner, Klaus S., Sarah Brennan, Jürg M. Matter, et al. (2012). "The urgency of the development of CO_2 capture from ambient air." In: *Proceedings of the National Academy of Sciences of the United States of America* 109.33, pp. 13156–62 (cit. on pp. 8, 12).

Langmuir, Irving (1918). “The adsorption of gases on plane surfaces of glass, mica and platinum”. In: *J. Am. Chem. Soc.* 40.9, pp. 1361–1403 (cit. on pp. 36, 42).

Lawson, M. L. and Wen-Jei Yang (1973). “The stability of a layer of binary gas mixture heated below”. In: *J. Fluid Mech.* 57.01, pp. 103–110 (cit. on p. 162).

Le Treut, H., R. Somerville, U. Cubasch, et al. (2007). *Climate Change 2007: Mitigation of Climate Change*. Ed. by S. Solomon, D. Qin, M. Manning, et al. Cambridge University Press (cit. on p. 1).

Lee, K. B. and S. Sircar (2008). “Removal and recovery of compressed CO_2 from flue gas by a novel thermal swing chemisorption process”. In: *AIChE J.* 54.9, pp. 2293–2302 (cit. on p. 87).

Lee, Tae Soo, Jung Hyuk Cho, and Suk Hwan Chi (2015). “Carbon dioxide removal using carbon monolith as electric swing adsorption to improve indoor air quality”. In: *Build. Environ.* 92, pp. 209–221 (cit. on p. 8).

Lemmon, Eric W., Marcia L. Huber, and Mark O. McLinden (2013). *NIST Standard Reference Database 23: Reference Fluid Thermodynamic and Transport Properties-REFPROP, Version 9.1, National Institute of Standards and Technology* (cit. on pp. 51, 72, 103).

LeVan, M. Douglas, Giorgio Carta, and M. Carmen Yon (1998). “Adsorption and Ion Exchange”. In: *Perry’s chemical engineers’ handbook*. Ed. by Robert H. Perry, Don W. Green, and James O. Maloney. Seventh Ed. New York: McGraw-Hill. Chap. 16, pp. 1–66 (cit. on pp. 14, 33, 34, 46, 50, 76, 116, 117).

Li, Gang, Ranjeet Singh, Dan Li, et al. (2009). “Synthesis of biomorphic zeolite honeycomb monoliths with 16 000 cells per square inch”. In: *J. Mater. Chem.* 19.44, p. 8372 (cit. on p. 76).

Li, Wen, Sunho Choi, Jeffrey H. Drese, et al. (2010a). “Steam-Stripping for Regeneration of Supported Amine-Based CO_2 Adsorbents”. In: *ChemSusChem* 3.8, pp. 899–903 (cit. on p. 26).

Li, Wen, Praveen Bollini, Stephanie A. Didas, et al. (2010b). “Structural Changes of Silica Mesocellular Foam Supported Amine-Functionalized CO_2 Adsorbents Upon Exposure to Steam”. In: *ACS Appl. Mater. Interfaces* 2.11, pp. 3363–3372 (cit. on p. 26).

Lonsdale, Harold K. and Edward A. Mason (1957). “Thermal Diffusion and the Approach to the Steady State in H_2–CO_2 and He–CO_2”. In: *J. Phys. Chem.* 61.11, pp. 1544–1551 (cit. on pp. 162, 163).

Lopes, Filipe V. S., Carlos A. Grande, Ana M. Ribeiro, et al. (2009). “Adsorption of H_2, CO_2 , CH_4, CO, N_2 and H_2O in Activated Carbon and Zeolite for Hydrogen Production”. In: *Sep. Sci .Technol.* 44.5, pp. 1045–1073 (cit. on pp. 117, 123).

Lüthi, Dieter, Martine Le Floch, Bernhard Bereiter, et al. (2008). “High-resolution carbon dioxide concentration record 650,000–800,000 years before present”. In: *Nature* 453.7193, pp. 379–382 (cit. on p. 2).

Macdonald, I. F., M. S. El-Sayed, K. Mow, and F. A. L. Dullien (1979). “Flow through Porous Media-the Ergun Equation Revisited”. In: *Ind. Eng. Chem. Fundamen.* 18.3, pp. 199–208 (cit. on p. 115).

MacKay, David J. C. (2009). *Sustainable Energy — without the hot air*. Cambridge, UK: UIT Cambridge Ltd., p. 383 (cit. on p. 6).

Mahmoudkhani, M., K. R. Heidel, J. C. Ferreira, D. W. Keith, and R. S. Cherry (2009). “Low energy packed tower and caustic recovery for direct capture of CO_2 from air”. In: *Energy Procedia* 1.1, pp. 1535–1542 (cit. on p. 23).

Mahmoudkhani, Maryam and David W. Keith (2009). “Low-energy sodium hydroxide recovery for CO_2 capture from atmospheric air—Thermodynamic analysis”. In: *Int. J. Greenhouse Gas Control* 3.4, pp. 376–384 (cit. on p. 23).

Mangano, E., S. Brandani, M. C. Ferrari, et al. (2013). “Efficient and Rapid Screening of Novel Adsorbents for Carbon Capture in the UK IGSCC Project”. In: *Energy Procedia* 37, pp. 40–47 (cit. on p. 50).

Markewitz, Peter, Wilhelm Kuckshinrichs, Walter Leitner, et al. (2012). “Worldwide innovations in the development of carbon capture technologies and the utilization of CO_2”. In: *Energy Environ. Sci.* 5.6, pp. 7281–7305 (cit. on pp. 8, 13, 155).

Marx, Dorian, Lisa Joss, Max Hefti, and Marco Mazzotti (2016). “Temperature Swing Adsorption for Postcombustion CO_2 Capture: Single- and Multicolumn Experiments and Simulations”. In: *Ind. Eng. Chem. Res.* 55.5, pp. 1401–1412 (cit. on pp. 128, 130).

Mason, Jarad A., Kenji Sumida, Zoey R. Herm, Rajamani Krishna, and Jeffrey. R. Long (2011). “Evaluating metal–organic frameworks for post-combustion carbon dioxide capture via temperature swing adsorption”. In: *Energy Environ. Sci.* 4.8, p. 3030 (cit. on p. 34).

Mattox, E. M., J. C. Knox, and D. M. Bardot (2013). “Carbon dioxide removal system for closed loop atmosphere revitalization, candidate sorbents screening and test results”. In: *Acta Astronautica* 86, pp. 39–46 (cit. on pp. 8, 57).

May, Eric F., Reid C. Miller, and Zhengjun Shan (2001). “Densities and Dew Points of Vapor Mixtures of Methane + Propane and Methane + Propane + Hexane Using a Dual-Sinker Densimeter”. In: *J. Chem. Eng. Data* 46.5, pp. 1160–1166 (cit. on p. 89).

Mazzoccoli, Michela, Barbara Bosio, Elisabetta Arato, and Stefano Brandani (2014). “Comparison of equations-of-state with P–ρ–T experimental data of binary mixtures rich in CO_2 under the conditions of pipeline transport”. In: *J. Supercrit. Fluids* 95, pp. 474–490 (cit. on pp. 13, 30, 155).

Mc Intyre, J. A., C. E. Holland, and J. A. Ritter (2002). “High Enrichment and Recovery of Dilute Hydrocarbons by Dual-Reflux Pressure-Swing Adsorption”. In: *Ind. Eng. Chem. Res* 41.14, pp. 3499–3504 (cit. on p. 9).

McDonald, Thomas M., Woo Ram Lee, Jarad A. Mason, et al. (2012). “Capture of carbon dioxide from air and flue gas in the alkylamine-appended metal-organic framework mmen-Mg_2(dobpdc)”. In: *J. Am. Chem. Soc.* 134.16, pp. 7056–65 (cit. on p. 28).

McLinden, Mark O. and Cornelia Lösch-Will (2007). “Apparatus for wide-ranging, high-accuracy fluid (p,ρ,T) measurements based on a compact two-sinker densimeter”. In: *J. Chem. Thermodynamics* 39.4, pp. 507–530 (cit. on p. 89).

Meier, Anton, Enrico Bonaldi, Gian Mario Cella, Wojciech Lipinski, and Daniel Wuillemin (2006). “Solar chemical reactor technology for industrial production of lime”. In: *Solar Energy* 80.10, pp. 1355–1362 (cit. on p. 23).

Meinshausen, M., S. C. B. Raper, and T. M. L. Wigley (2011). “Emulating coupled atmosphere-ocean and carbon cycle models with a simpler model, MAGICC6 – Part 1: Model description and calibration”. In: *Atmos. Chem. Phys.* 11, pp. 1417–1456 (cit. on p. 3).

Meinshausen, Malte, Louise Jeffery, Johannes Guetschow, et al. (2015). “National post-2020 greenhouse gas targets and diversity-aware leadership”. In: *Nature Clim. Change* 5.12, pp. 1098–1106 (cit. on p. 3).

Mérel, J., M. Clausse, and F. Meunier (2006). “Carbon dioxide capture by indirect thermal swing adsorption using 13X zeolite”. In: *Environ. Prog.* 25.4, pp. 327–333 (cit. on pp. 113, 126).

Mulgundmath, V. P., R. A. Jones, F. H. Tezel, and J. Thibault (2012). “Fixed bed adsorption for the removal of carbon dioxide from nitrogen: Breakthrough behaviour and modelling for heat and mass transfer”. In: *Sep. Purif. Technol.* 85, pp. 17–27 (cit. on pp. 123, 125, 130).

Mulloth, Lila M., Dave L. Affleck, Micha Rosen, et al. (2004). “Air-Cooled Design of a Temperature-Swing Adsorption Compressor for Closed-Loop Air Revitalization Systems”. English. In: *International Conference on Environmental Systems*, pp. 2004–01–2374 (cit. on p. 57).

Myers, Alan L. (1968). “Adsorption of gas mixtures. A thermodynamic approach.” In: *Ind. Eng. Chem.* 60.5, pp. 45–49 (cit. on p. 49).

Myers, Alan L. (2006). *Thermodynamics of adsorption*. Ed. by Trevor M. Letcher. Cambridge: Royal Society of Chemistry. Chap. 21, pp. 243–253 (cit. on pp. 46, 167).

Myers, Alan L. and Peter A. Monson (2014). "Physical adsorption of gases: the case for absolute adsorption as the basis for thermodynamic analysis". In: *Adsorption* 20.4, pp. 591–622 (cit. on pp. 43, 50, 91, 95, 97, 159).

Myers, Alan L. and John M. Prausnitz (1965). "Thermodynamics of mixed-gas adsorption". In: *AIChE J.* 11.1, pp. 121–127 (cit. on pp. 49, 50).

Nakao, Shin-Ichi and Motoyuki Suzuki (1983). "Mass transfer coefficient in cyclic adsorption and desorption." In: *J. Chem. Eng. Jpn.* 16.2, pp. 114–119 (cit. on p. 117).

Nastaj, Józef and Bogdan Ambrożek (2009). "Modeling of Drying of Gases Using Solid Desiccants". In: *Drying Technol.* 27.12, pp. 1344–1352 (cit. on p. 34).

NewClimate Institute, Ecofys, and Climate Analytics (2016). "The ten most important short-term steps to limit warming to 1.5°C". In: *Climate Action Tracker*, pp. 1–44 (cit. on pp. 3–5).

Nikulshina, V. and A. Steinfeld (2009). "CO_2 capture from air via CaO-carbonation using a solar-driven fluidized bed reactor—Effect of temperature and water vapor concentration". In: *Chem. Eng. J.* 155.3, pp. 867–873 (cit. on pp. 23, 24).

Nikulshina, V., D. Hirsch, M. Mazzotti, and A. Steinfeld (2006). "CO_2 capture from air and co-production of H_2 via the $Ca(OH)_2$–$CaCO_3$ cycle using concentrated solar power–Thermodynamic analysis". In: *Energy* 31.12, pp. 1715–1725 (cit. on pp. 22, 23).

Nikulshina, V., M. E. Gálvez, and A. Steinfeld (2007). "Kinetic analysis of the carbonation reactions for the capture of CO_2 from air via the $Ca(OH)_2$–$CaCO_3$–CaO solar thermochemical cycle". In: *Chem. Eng. J.* 129.1-3, pp. 75–83 (cit. on p. 23).

Nikulshina, V., N. Ayesa, M. E. Gálvez, and A. Steinfeld (2008). "Feasibility of Na-based thermochemical cycles for the capture of CO_2 from air—Thermodynamic and thermogravimetric analyses". In: *Chem. Eng. J.* 140.1-3, pp. 62–70 (cit. on p. 23).

Nikulshina, V., C. Gebald, and A. Steinfeld (2009). "CO_2 capture from atmospheric air via consecutive CaO-carbonation and $CaCO_3$-calcination cycles in a fluidized-bed solar reactor". In: *Chem. Eng. J.* 146.2, pp. 244–248 (cit. on pp. 23, 24).

Oreggioni, Gabriel D., Stefano Brandani, Mauro Luberti, et al. (2015). "CO_2 capture from syngas by an adsorption process at a biomass gasification CHP plant: Its comparison with amine-based CO_2 capture". In: *Int. J. Greenhouse Gas Control* 35, pp. 71–81 (cit. on pp. 51, 106, 123, 140).

Otani, Y., C. Kanaoka, C. Usui, S. Matsui, and H. Emi (1986). "Adsorption of mercury vapor on particles." In: *Environ. Sci. Technol.* 20.7, pp. 735–8 (cit. on p. 9).

Park, Yong-Jin, Sang-Jin Lee, Jong-Ho Moon, Dae-Ki Choi, and Chang-Ha Lee (2006). "Adsorption Equilibria of O_2 , N_2 , and Ar on Carbon Molecular Sieve and Zeolites 10X, 13X, and LiX". In: *J. Chem. Eng. Data* 51.3, pp. 1001–1008 (cit. on p. 70).

Pigorini, Giuseppe and M. Douglas LeVan (1997). "Equilibrium Theory for Pressure Swing Adsorption. 3. Separation and Purification in Two-Component Adsorption". In: *Ind. Eng. Chem. Res.* 36.6, pp. 2306–2319 (cit. on p. 39).

Pillai, Renjith S., Sunil A. Peter, and Raksh V. Jasra (2008). "Adsorption of carbon dioxide, methane, nitrogen, oxygen and argon in NaETS-4". In: *Micropor. Mesopor. Mat.* 113.1, pp. 268–276 (cit. on p. 105).

Pini, Ronny (2014). "Interpretation of net and excess adsorption isotherms in microporous adsorbents". In: *Micropor. Mesopor. Mat.* 187, pp. 40–52 (cit. on p. 93).

Poling, Bruce E., John M. Prausnitz, and John P. O'Connell (2001). *The Properties of Gases and Liquids*. Fifth Ed. McGraw-Hill, p. 768 (cit. on p. 125).

Powlson, David S., Clare M. Stirling, M. L. Jat, et al. (2014). “Limited potential of no-till agriculture for climate change mitigation”. In: *Nature Clim. Change* 4.8, pp. 678–683 (cit. on p. 5).

Pratt, Henry R. C. (1967). *Countercurrent Separation Processes*. Amsterdam: Elservier (cit. on p. 10).

Pulin, A. L., A. A. Fomkin, V. A. Sinitsyn, and A. A. Pribylov (2001). “Adsorption and adsorption-induced deformation of NaX zeolite under high pressures of carbon dioxide”. In: *Russ. Chem. B+* 50.1, pp. 60–62 (cit. on p. 87).

PwC (2015). *EU Emissions Target and Implications for Business*. Ed. by Jonathan Grant, Robert Milnes, Oliver Muller, et al. London: PricewaterhouseCoopers LLP, p. 4 (cit. on p. 3).

Pye, Steve, Francis G N Li, James Price, and Birgit Fais (2017). “Achieving net-zero emissions through the reframing of UK national targets in the post-Paris Agreement era”. In: *Nature Energy* 2.3, p. 17024 (cit. on p. 3).

Ranjan, Manya and Howard J. Herzog (2011). “Feasibility of air capture”. In: *Energy Procedia* 4, pp. 2869–2876 (cit. on pp. 5, 6).

Rao, M. B. and S. Sircar (1999). “Thermodynamic Consistency for Binary Gas Adsorption Equilibria”. In: *Langmuir* 15, pp. 7258–7267 (cit. on p. 97).

Rege, Salil U., Ralph T. Yang, and Mark A. Buzanowski (2000). “Sorbents for air prepurification in air separation”. In: *Chem. Eng. Sci* 55.21, pp. 4827–4838 (cit. on pp. 9, 22, 50).

Rezaei, F. and P. Webley (2010). “Structured adsorbents in gas separation processes”. In: *Sep. Purif. Technol.* 70.3, pp. 243–256 (cit. on p. 76).

Rezaei, Fateme and Paul Webley (2009). “Optimum structured adsorbents for gas separation processes”. In: *Chem. Eng. Sci* 64.24, pp. 5182–5191 (cit. on pp. 51, 72).

Riahi, Keywan, Elmar Kriegler, Nils Johnson, et al. (2015). “Locked into Copenhagen pledges — Implications of short-term emission targets for the cost and feasibility of long-term climate goals”. In: *Technol. Forecast. Soc.* 90, pp. 8–23 (cit. on pp. 6, 7).

Rochelle, Gary T. (2009). “Amine Scrubbing for CO_2 Capture”. In: *Science* 325.5948, pp. 1652–1654 (cit. on p. 156).

Rodriguez-Illera, Marta, Moniek A. Boon, Remko M. Boom, and Anja E. M. Janssen (2015). “Comparison of structured adsorbents for the adsorptive isolation of food ingredients from large streams”. In: *Chem. Eng. Res. Des.* 98.2, pp. 240–251 (cit. on p. 78).

Rogelj, Joeri, Michiel Schaeffer, Malte Meinshausen, et al. (2015). “Zero emission targets as long-term global goals for climate protection”. In: *Environ. Res. Lett.* 10.105007, pp. 1–11 (cit. on p. 3).

Rogelj, Joeri, Michel Den Elzen, Niklas Höhne, et al. (2016). “Paris Agreement climate proposals need a boost to keep warming well below 2 °C”. In: *Nature* 534, pp. 631–639 (cit. on p. 3).

Rosen, Micha S., Lila M. Mulloth, Dave L. Affleck, Yuan Wang, and M. Douglas LeVan (2005). “Development and Testing of a Temperature-Swing Adsorption Compressor for Carbon Dioxide in Closed-Loop Air Revitalization Systems”. English. In: *International Conference on Environmental Systems*, pp. 2005–01–2941 (cit. on p. 57).

Rother, J. and T. Fieback (2013). “Multicomponent adsorption measurements on activated carbon, zeolite molecular sieve and metal–organic framework”. In: *Adsorption* 19.5, pp. 1065–1074 (cit. on p. 87).

Rouquerol, Françoise, Jean Rouquerol, and Kenneth Sing (1999). *Adsorption by powders and porous solids*. San Diego: Academic Press, p. 467 (cit. on p. 33).

Ruthven, D.M., S. Farooq, and S. Brandani (2015). “Work of separation in CO_2 capture: Applicability of the value function”. In: *Chem. Eng. Sci.* 126, pp. 604–607 (cit. on pp. 13, 155).

Ruthven, Douglas M. (2014). “CO_2 capture: Value functions, separative work and process economics”. In: *Chem. Eng. Sci.* 114, pp. 128–133 (cit. on pp. 10–13, 28, 154, 155).

Ruthven, Douglas M., Shamsuzzaman Farroq, and Kent S. Knaebel (1994). *Pressure Swing Adsorption*. New York: VCH Publishers, Inc., p. 353 (cit. on pp. 35, 110).

Ruthven, M. Douglas (1984). *Principles of Adsorption and Adsorption Processes*. John Wiley & Sons, pp. 1–453 (cit. on pp. 17, 33–36, 42, 76, 86, 109, 113, 124, 126, 159).

Saidi, Kais and Sami Hammami (2015). "The impact of CO_2 emissions and economic growth on energy consumption in 58 countries". In: *Energy Reports* 1, pp. 62–70 (cit. on p. 1).

Saleh, Bahaa and Martin Wendland (2005). "Measurement of Vapor Pressures and Saturated Liquid Densities of Pure Fluids with a New Apparatus". In: *J. Chem. Eng. Data* 50.2, pp. 429–437 (cit. on p. 93).

Samari, Mohammad (2014). "CO_2 Capture from Dilute Sources via Lime-Based Sorbents". PhD thesis. University of Ottawa, p. 84 (cit. on p. 24).

Sander, M. T. and C. L. Mariz (1992). "The Fluor Daniel® econamine FG process: Past experience and present day focus". In: *Energy Convers. Manage.* 33.5-8, pp. 341–348 (cit. on p. 155).

Santori, G., A. Frazzica, A. Freni, et al. (2013). "Optimization and testing on an adsorption dishwasher". In: *Energy* 50, pp. 170–176 (cit. on pp. 45, 51, 58, 88, 123).

Santori, Giulio and Mauro Luberti (2016). "Thermodynamics of thermally-driven adsorption compression". In: *Sustain. Mat. Technol.* 10, pp. 1–9 (cit. on p. 41).

Santori, Giulio, Alessio Sapienza, and Angelo Freni (2012). "A dynamic multi-level model for adsorptive solar cooling". In: *Renew. Energy* 43, pp. 301–312 (cit. on pp. 13, 51, 155).

Santori, Giulio, Mauro Luberti, and Hyungwoong Ahn (2014). "Ideal adsorbed solution theory solved with direct search minimisation". In: *Comput. Chem. Eng.* 71, pp. 235–240 (cit. on p. 95).

Santori, Giulio, Mauro Luberti, and Stefano Brandani (2015). "Common tangent plane in mixed-gas adsorption". In: *Fluid Phase Equilibr.* 392, pp. 49–55 (cit. on pp. 49, 95).

Santori, Giulio, Charithea Charalambous, Maria-Chiara Ferrari, and Stefano Brandani (2018). "Adsorption artificial tree for atmospheric carbon dioxide capture, purification and compression". In: *Energy* (cit. on pp. 25–27).

Sanz-Peez, Eloy S., Christopher R. Murdock, Stephanie A. Didas, and Christopher W. Jones (2016). "Direct Capture of CO_2 from Ambient Air". In: *Chem. Rev* 116, pp. 11840–11876 (cit. on pp. 28, 76).

Sapienza, Alessio, Salvatore Santamaria, Andrea Frazzica, and Angelo Freni (2011). "Influence of the management strategy and operating conditions on the performance of an adsorption chiller". In: *Energy* 36.9, pp. 5532–5538 (cit. on p. 88).

Satish, Usha, Mark J. Mendell, Krishnamurthy Shekhar, et al. (2012). "Is CO_2 an Indoor Pollutant? Direct Effects of Low-to-Moderate CO_2 Concentrations on Human Decision-Making Performance". In: *Environ. Health Perspect.* 120.12, pp. 1671–1677 (cit. on p. 57).

Sattler, Klaus, Hans Jacob Feindt, and Klaus Sattler (1995). *Thermal separation processes: principles and design*. Weinheim: VCH, p. 545 (cit. on p. 127).

Sayari, Abdelhamid, Qing Liu, and Prashant Mishra (2016). "Enhanced Adsorption Efficiency through Materials Design for Direct Air Capture over Supported Polyethylenimine". In: *ChemSusChem* 9.19, pp. 2796–2803 (cit. on p. 28).

Schaeffer, Michiel, Laila Gohar, Elmar Kriegler, et al. (2015). "Mid- and long-term climate projections for fragmented and delayed-action scenarios". In: *Technol. Forecast Soc. Change* 90.Part A, pp. 257–268 (cit. on p. 5).

Schneider, Erich and Darshan Sachde (2013). "The Cost of Recovering Uranium from Seawater by a Braided Polymer Adsorbent System". In: *Sci. Global Secur.* 21.2, pp. 134–163 (cit. on p. 12).

Schuiling, R. D. and P. Krijgsman (2006). "Enhanced Weathering: An Effective and Cheap Tool to Sequester CO_2". In: *Clim. Change* 74, pp. 349–354 (cit. on p. 5).

Shashkov, A. G., A. F. Zolotukhina, T. N. Abramenko, B. P. Mathur, and S. C. Saxena (1979). "Thermal diffusion factors for binary gas systems: Ar-N_2, Ar-CO_2, He-H_2, He-N_2O, Kr-N_2O and He-NH_3". In: *J. Physics B: Atomic and Mole. Phys.* 12.21, pp. 3619–3630 (cit. on p. 162).

Shekhah, Osama, Youssef Belmabkhout, Karim Adil, et al. (2015). "A facile solvent-free synthesis route for the assembly of a highly CO_2 selective and H_2S tolerant NiSIFSIX metal–organic framework". In: *Chem. Commun.* 51.51, pp. 13565–13712 (cit. on p. 28).

Sherman, Steven R. (2009). "Nuclear powered CO_2 capture from the atmosphere". In: *Environ. Prog. Sustain. Energy* 28.1, pp. 52–59 (cit. on p. 22).

Shi, Xiaoyang, Hang Xiao, Klaus S. Lackner, and Xi Chen (2016). "Capture CO_2 from Ambient Air Using Nanoconfined Ion Hydration". In: *Angew. Chem. Int. Ed.* 55.12, pp. 4026–4029 (cit. on p. 28).

Simon, A.J., Naluahi B. Kaahaaina, S. Julio Friedmann, and Roger D. Aines (2011). "Systems analysis and cost estimates for large scale capture of carbon dioxide from air". In: *Energy Procedia* 4, pp. 2893–2900 (cit. on pp. 13, 20).

Sing, Kenneth S. W., Douglas H. Everett, R. A. W. Haul, et al. (1985). "Reporting physisorption data for gas/solid systems with special reference to the determination of surface area and porosity". In: *Pure Appl. Chem.* 57.4, pp. 603–619 (cit. on pp. 36, 87).

Siperstein, Flor R. and Alan L. Myers (2001). "Mixed-gas adsorption". In: *AIChE J.* 47.5, pp. 1141–1159 (cit. on pp. 45, 50, 165).

Sircar, S., T.C. C. Golden, and M.B. B. Rao (1996). "Activated carbon for gas separation and storage". In: *Carbon* 34.1, pp. 1–12 (cit. on pp. 9, 34, 76).

Sircar, Shivaji (1995). "Influence of adsorbate size and adsorbent heterogeneity of IAST". In: *AIChE J.* 41.5, pp. 1135–1145 (cit. on p. 45).

Sircar, Shivaji and Alan L. Myers (2003). "Gas Separation by Zeolites". In: *Handbook of Zeolite Science and Technology*. Ed. by Scott M. Auerbach, Kathleen A. Carrado, and Prabir K. Dutta. New York, Basel: Marcel Dekker, Inc. Chap. 22 (cit. on p. 83).

Sircar, Shivaji (2003). "Adsorption Technology for Gas Separation". In: *Proceedings of the Third Pacific Basin Conference on Adsorption Science and Technology*. Ed. by Chang-Ha Lee. River Edge, London: World Scientific Publishing Co. Pte. Ltd., pp. 72–78 (cit. on pp. 33, 34).

Sirkar, Kamalesh K. (2014). *Separation of molecules, macromolecules and particles: principles, phenomena and processes*. Cambridge: Cambridge Series in Chemical Engineering, p. 889 (cit. on pp. 43, 44, 159, 160, 162).

Smith, Laurence H., Perry L. McCarty, and Peter K. Kitanidis (1998). "Spreadsheet method for evaluation of biochemical reaction rate coefficients and their uncertainties by weighted nonlinear least-squares analysis of the integrated monod equation". In: *Appl. Environ. Microb.* 64.6, pp. 2044–50 (cit. on p. 98).

Smith, Pete, Steven J Davis, Felix Creutzig, et al. (2016). "Biophysical and economic limits to negative CO_2 emissions". In: *Nature Clim. Change* 6.1, pp. 42–50 (cit. on pp. 5–7, 13).

Socolow, Robert, Michael Desmond, Roger Aines, et al. (2011). *Direct Air Capture of CO_2 from Chemicals: A Technology Assessment for the APS Panel on Public Affairs*. Tech. rep., pp. 1–91 (cit. on pp. 5, 20).

Song, Q.-H., Z.-H. Tan, Y.-P. Zhang, et al. (2014). "Do the rubber plantations in tropical China act as large carbon sinks?" In: *iForest* 7.1, pp. 42–47 (cit. on p. 13).

Spector, N.A. and B.F. Dodge (1946). "Removal of carbon dioxide from atmospheric air". In: *Trans. Am. Inst. Chem. Eng.* 42.56, pp. 827–848 (cit. on p. 19).

Srivastava, B. N. and M. P. Madan (1953). "Thermal Diffusion of Gas Mixtures and Forces between Unlike Molecules". In: *Proceedings of the Physical Society. Section A*. Vol. 66. 3. IOP Publishing, pp. 278–287 (cit. on pp. 44, 161, 162).

Steinberg, Meyer and Vi Duong Dang (1977). “Production of synthetic methanol from air and water using controlled thermonuclear reactor power-I. technology and energy requirement”. In: *Energy Conv.* 17.2-3, pp. 97–112 (cit. on p. 19).

Stern, Nicholas (2006). *Stern Review on the Economics of Climate Change*. Tech. rep. 2, pp. 1–10 (cit. on p. 1).

Stolaroff, Joshuah, David Keith, and Greg Lowry (2006). “A pilot-scale prototype contactor for CO_2 capture from ambient air: cost and energy requirements”. In: *8th Greenhouse Gas Control Technologies Conference*. Trondheim, Norway, pp. 1–6 (cit. on p. 20).

Stolaroff, Joshuah K., David W. Keith, and Gregory V. Lowry (2008). “Carbon Dioxide Capture from Atmospheric Air Using Sodium Hydroxide Spray”. In: *Environ. Sci. Technol.* 42.8, pp. 2728–2735 (cit. on pp. 22, 23).

Stuckert, Nicholas R. and Ralph T. Yang (2011). “CO_2 capture from the atmosphere and simultaneous concentration using zeolites and amine-grafted SBA-15”. In: *Environ. Sci. Technol.* 45.23, pp. 10257–10264 (cit. on pp. 27, 28).

Sumida, Kenji, David L. Rogow, Jarad A. Mason, et al. (2012). “Carbon Dioxide Capture in Metal–Organic Frameworks”. In: *Chem. Rev.* 112.2, pp. 724–781 (cit. on p. 1).

Tepe, J. B. and B. F. Dodge (1943). *Absorption of Carbon Dioxide by Sodium Hydroxide Solutions in a Packed Column*. Vol. 39. Publications from the School of Engineering, pp. 255–276 (cit. on p. 19).

Thommes, Matthias, Katsumi Kaneko, Alexander V Neimark, et al. (2015). “IUPAC Technical Report Physisorption of gases, with special reference to the evaluation of surface area and pore size distribution (IUPAC Technical Report)”. In: *Pure Appl. Chem* (cit. on pp. 36, 167).

Towler, Gavin P. and Ray K. Sinnott (2013). *Chemical engineering design: principles, practice, and economics of plant and process design*. Second Ed. Oxford: Butterworth-Heinemann, p. 1303 (cit. on p. 58).

UKCCC (2017). *UK Climate Change Risk Assessment 2017*. Tech. rep. London: UK Committee on Climate Change, p. 79 (cit. on p. 3).

Vemula, Rama Rao, Mayuresh V Kothare, and Shivaji Sircar (2017). “Lumped heat and mass transfer coefficient for simulation of a pressure swing adsorption process”. In: *Sep. Sci. Technol.* 52.1, pp. 35–41 (cit. on p. 113).

Vidic, Radisav D. and Douglas P. Siler (2001). “Vapor-phase elemental mercury adsorption by activated carbon impregnated with chloride and chelating agents”. In: *Carbon* 39.1, pp. 3–14 (cit. on p. 9).

Vilarrasa-García, E., J. A. Cecilia, M. Bastos-Neto, et al. (2015). “CO_2/CH_4 adsorption separation process using pore expanded mesoporous silicas functionalizated by APTES grafting”. In: *Adsorption* 21.8, pp. 565–575 (cit. on p. 89).

Voss, Christian (2005). “Applications of Pressure Swing Adsorption Technology”. In: *Adsorption* 11.S1, pp. 527–529 (cit. on p. 34).

Wakao, N. and T. Funazkri (1978). “Effect of fluid dispersion coefficients on particle-to-fluid mass transfer coefficients in packed beds”. In: *Chem. Eng. Sci.* 33.10, pp. 1375–1384 (cit. on p. 124).

Walas, Stanley M. (1985). *Phase Equilibria in Chemical Engineering*. Butterworth-Heinemann, p. 671 (cit. on p. 160).

Wang, Tao, Klaus S. Lackner, and Allen Wright (2011). “Moisture swing sorbent for carbon dioxide capture from ambient air.” In: *Environ. Sci. Technol.* 45.15, pp. 6670–5 (cit. on pp. 24, 25, 80).

Wang, Xiaoxing, Xiaoliang Ma, Viviane Schwartz, et al. (2012). “A solid molecular basket sorbent for CO_2 capture from gas streams with low CO_2 concentration under ambient conditions”. In: *Phys. Chem. Chem. Phys.* 14.4, pp. 1485–1492 (cit. on p. 28).

Wang, Yu and M. Douglas LeVan (2009). “Adsorption Equilibrium of Carbon Dioxide and Water Vapor on Zeolites 5A and 13X and Silica Gel: Pure Components”. In: *J. Chem. Eng. Data* 54.10, pp. 2839–2844 (cit. on p. 141).

Wankat, Phillip C. (1986). “Packed Bed Adsorption Operations”. In: *Large-Scale Adsorption and Chromatography*. CRC Press. Chap. 3, pp. 69–77 (cit. on p. 9).

Weireld, G. De, M. Frère, and R. Jadot (1999). “Automated determination of high-temperature and high-pressure gas adsorption isotherms using a magnetic suspension balance”. In: *Meas. Sci. Technol.* 10.2, pp. 117–126 (cit. on p. 91).

Wilcox, Jennifer, Reza Haghpanah, Erik C. Rupp, Jiajun He, and Kyoungjin Lee (2014). “Advancing Adsorption and Membrane Separation Processes for the Gigaton Carbon Capture Challenge”. In: *Annu. Rev. Chem. Biomol. Eng.* 5.1, pp. 479–505 (cit. on pp. 75, 107).

Wilcox, Jennifer, Peter C. Psarras, and Simona Liguori (2017). “Assessment of reasonable opportunities for direct air capture”. In: *Environ. Res. Lett.* 12.6, p. 065001 (cit. on p. 28).

Woolf, Dominic, James E. Amonette, F. Alayne Street-Perrott, Johannes Lehmann, and Stephen Joseph (2010). “Sustainable biochar to mitigate global climate change.” In: *Nature Commun.* 1, p. 56 (cit. on p. 5).

Wright, A. B., K. S. Lackner, B. Wright, et al. (2012). *Removal of carbon dioxide from air* (cit. on p. 24).

Wright, A. B., K. S. Lackner, E. Leon-Guerrero, et al. (2017). *Capture of carbon dioxide (CO_2) from air* (cit. on p. 24).

Wu, Jihuai, Zhang Lan, Jianming Lin, et al. (2017). “Counter electrodes in dye-sensitized solar cells”. In: *Chem. Soc. Rev.* 46.46, pp. 5975–6023 (cit. on p. 14).

Wurzbacher, Jan A. (2015). “Development of a temperature-vacuum swing process for CO_2 capture from ambient air”. PhD thesis. ETH Zürich, p. 175 (cit. on p. 26).

Wurzbacher, Jan Andre, Christoph Gebald, and Aldo Steinfeld (2011). “Separation of CO_2 from air by temperature-vacuum swing adsorption using diamine-functionalized silica gel”. In: *Energy Environ. Sci.* 4.9, p. 3584 (cit. on pp. 26, 27, 69, 137).

Wurzbacher, Jan Andre, Christoph Gebald, Nicolas Piatkowski, and Aldo Steinfeld (2012). “Concurrent separation of CO_2 and H_2O from air by a temperature-vacuum swing adsorption/desorption cycle.” In: *Environ. Sci. Technol.* 46.16, pp. 9191–9198 (cit. on pp. 26, 27).

Wurzbacher, Jan Andre, Christoph Gebald, Samuel Brunner, and Aldo Steinfeld (2016). “Heat and mass transfer of temperature-vacuum swing desorption for CO_2 capture from air”. In: *Chem. Eng. J.* 283, pp. 1329–1338 (cit. on p. 27).

Xiao, Penny, Jun Zhang, Paul Webley, et al. (2008). “Capture of CO_2 from flue gas streams with zeolite 13X by vacuum-pressure swing adsorption”. In: *Adsorption* 14.4-5, pp. 575–582 (cit. on pp. 50, 71, 106, 123, 165, 166, 168).

Yang, Ralph T. (1987). *Gas separation by adsorption processes*. Stoneham, United States of America: Butterworths Publishers, p. 352 (cit. on p. 116).

Yang, Ralph T. (2003). *Adsorbents: Fundamentals and Applications*. Hoboken, New Jersey: John Wiley & Sons, Inc., p. 410 (cit. on p. 167).

Yang, Ralph T. (1997). *Gas Separation by Adsorption Processes*. Chemical Engineering. Imperial College Press (cit. on p. 42).

Zeman, Frank (2007). “Energy and Material Balance of CO_2 Capture from Ambient Air”. In: *Environ. Sci. Technol.* 41.21, pp. 7558–7563 (cit. on pp. 20, 22).

Zeman, Frank (2008). “Experimental results for capturing CO_2 from the atmosphere”. In: *AIChE J.* 54.5, pp. 1396–1399 (cit. on pp. 20, 22).

Zeman, Frank (2014). “Reducing the Cost of Ca-Based Direct Air Capture of CO_2”. In: *Environ. Sci. Technol.* 48.19, pp. 11730–11735 (cit. on p. 20).

Zeman, Frank S. and Klaus S. Lackner (2004). “Capturing Carbon Dioxide Directly from the Atmosphere”. In: *World Resource Review* 16.2, pp. 157–172 (cit. on p. 19).

Zhang, Wenbin, Hao Liu, Chenggong Sun, Trevor C. Drage, and Colin E. Snape (2014). “Capturing CO_2 from ambient air using a polyethyleneimine-silica adsorbent in fluidized beds”. In: *Chem. Eng. Sci.* 116, pp. 306–316 (cit. on p. 28).

Zhao, Ruikai, Shuai Deng, Yinan Liu, et al. (2017). “Carbon pump: Fundamental theory and applications”. In: *Energy* 119, pp. 1131–1143 (cit. on p. 11).

Webpages

Carbon Engineering Ltd (2017). *Direct Air Capture*. URL: `http://carbonengineering.com/air-capture/` (visited on Dec. 19, 2014) (cit. on p. 23).

Climeworks LLC (2017). *CO_2 Capture Process - climeworks*. URL: `http://www.climeworks.com/capture{\_}process.html` (visited on Dec. 19, 2014) (cit. on pp. 26, 27, 155).

European Commission (2017). *EU climate action*. URL: `https://ec.europa.eu/clima/citizens/eu{\_}en` (visited on Aug. 27, 2017) (cit. on p. 3).

Global Thermostat (2017). *A carbon negative solution*. URL: `http://globalthermostat.com/` (visited on Oct. 9, 2017) (cit. on p. 26).

Mitsubishi Plastics Inc. (1962). *Industrial Materials Zeolite AQSOA ™*. URL: `https://www.m-chemical.co.jp/en/products/departments/mcc/aquachem/` (cit. on pp. 77, 88).

Mitsubishi Plastics Inc., Business Development Dep. Industrial Materials Division (2009). *Zeolitic Water Vapor Adsorbent AQSOA ™*. URL: `http://www.mpi.co.jp/infopdf/AQSOA.pdf` (cit. on pp. 87, 88).

NASA (2011). *Weather, Climate and Composition Science from AIRS*. URL: `https://airs.jpl.nasa.gov/weather_and_climate_sciences/overview` (visited on Mar. 10, 2017) (cit. on p. 1).

NASA (2017). *NASA Global Climate Change: Vital Signs of the Planet: Carbon Dioxide*. URL: `https://climate.nasa.gov/vital-signs/carbon-dioxide/` (visited on Aug. 26, 2017) (cit. on p. 1).

Quantachrome Instruments (2013). *Material Characterization Instrumentation - Surface Area, Density, Pore Size*. URL: `http://www.quantachrome.com` (visited on Jan. 13, 2017) (cit. on p. 93).

Rubotherm Präzisionsmesstechnik GmbH. *Analytical Measuring Instruments*. URL: `http://www.rubotherm.com` (visited on July 4, 2017) (cit. on p. 90).

Scripps Institution of Oceanography (2017). *Keeling Curve Lessons*. URL: `http://scrippsco2.ucsd.edu/history_legacy/keeling_curve_lessons` (visited on Mar. 10, 2017) (cit. on p. 1).

United Nations (2012). *United Nations Conference on Sustainable Development*. URL: `https://sustainabledevelopment.un.org/rio20` (visited on Aug. 26, 2017) (cit. on p. 2).

List of Publications

Conferences

C. Charalambous, G. Santori, M.-C. Ferrari and S. Brandani (2017). *Removing carbon dioxide from the atmosphere*. Work presented at the School of Engineering Conference, University of Edinburgh, Edinburgh, UK.

C. Charalambous, G. Santori, M.-C. Ferrari and S. Brandani (2016). *Thermally-driven adsorption, concentration and purification of highly dilute gases*. Work presented at the Heat Powered Cycle Conference, Nottingham, UK.

C. Charalambous, G. Santori, M.-C. Ferrari and S. Brandani (2015). *Thermally driven process for atmospheric CO_2 capture*. Work presented at the Scottish Carbon Capture and Storage Conference, Edinburgh, UK.

Journal Articles

G. Santori, C. Charalambous, M.-C. Ferrari and S. Brandani (2018). "Adsorption artificial tree for atmospheric carbon dioxide capture, purification and compression". In: *Energy*, 162, pp. 1158–1168.

C. Charalambous, G. Santori, E. Vilarrasa-Garcia, M. Bastos-Neto, C. L. Cavalcante Jr. and S. Brandani (2018). "Pure and binary adsorption of carbon dioxide and nitrogen on AQSOA®-FAM-Z02". In: *J. Chem. Eng. Data*, 63.3, pp. 661–670.

G. R. M. Dowson, D. G. Reed, J.-M. Bellas, C. Charalambous and P. Styring (2016). "Fast and selective separation of carbon dioxide from dilute streams by pressure swing adsorption using solid ionic liquids". In: *Faraday Discuss.*, 192, pp. 511–527.

Journal of chemical & engineering data

Cite This: J. Chem. Eng. Data 2018, 63, 661−670

Article

pubs.acs.org/jced

Pure and Binary Adsorption of Carbon Dioxide and Nitrogen on AQSOA FAM Z02

Charithea Charalambous,[†] Giulio Santori,*[,†] Enrique Vilarrasa-Garcia,[‡] Moises Bastos-Neto,[‡] Célio L. Cavalcante, Jr.,[‡] and Stefano Brandani[†]

[†]The University of Edinburgh, School of Engineering, Institute for Materials and Processes, Sanderson Building, The King's Buildings, Mayfield Road, EH9 3FB, Edinburgh, Scotland, U.K.

[‡]Universidade Federal do Ceará, Departamento de Engenharia Quimica, Grupo de Pesquisa em Separações por Adsorção, Campus do Pici, Bl. 709, 60455-760 - Fortaleza, CE Brasil

ABSTRACT: Adsorption equilibria of CO_2, N_2, and the CO_2/N_2 binary system on AQSOA FAM Z02 grains were measured over a temperature range of 295 to 348 K and over a wide range in pressure from 0.2 to 20 bar using a gravimetric method. CO_2 and N_2 single-component experimental equilibrium measurements were regressed using the Toth equation. CO_2 adsorption on AQSOA FAM Z02 reported higher loadings compared to N_2 adsorption at all measured temperatures, with an adsorption capacity of 6.1 mmol g^{-1}. The adsorption of the CO_2/N_2 binary mixture at different gas-phase compositions (0.15/0.85, 0.50/0.50, and 0.80/0.20 mole fractions) was studied. The experimental data were compared with the prediction of ideal adsorbed solution theory (IAST), which also included the nonidealities in the bulk gas phase. The IAST model has shown agreement with the experimental data with <4% average relative error in the absolute adsorbed amount.

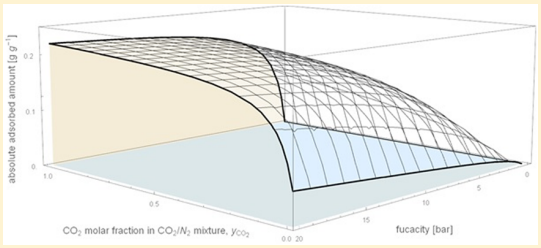

1. INTRODUCTION

The capture of carbon dioxide by adsorptive processes is based on the preferential adsorption of carbon dioxide on porous adsorbents from dilute gas streams. Several reviews have compared the features of different solid adsorbents for carbon capture such as activated carbons, zeolites, metal organic frameworks, silica, and polymers of intrinsic porosity.[1−3] The optimal performance of any adsorption separation process is enabled by materials with large CO_2 working capacities and selectivity over the additional components in the mixture and ideally long lifetime cycles.[4] In industrial processes, zeolite 13X is frequently used as an adsorbent due to its high adsorption capacity[5,6] and high CO_2 selectivity over other gases.[7−9] However, when H_2O is present in the mixture, in applications such as CO_2 capture from flue gases and CO_2 removal in closed-circuit breathing systems, it adsorbs near its pure-component isotherm,[10] making zeolite 13X an unfavorable sorbent for carbon dioxide removal applications. Alternatively, the initial stream has to undergo preliminary drying, which removes nearly 99.9% of water from the mixture before further treatment. Consequently, the drying step adds a cost to the gas-separation process, and it is most likely not feasible on large-scale applications.[11]

Ideally, an adsorbent with a hydrophobic nature or with a relatively low uptake from low to moderate levels of humidity, which follows an unfavorable adsorption isotherm or the type III and V isotherms according to the IUPAC classification of adsorption isotherms,[12] can be superior for carbon dioxide separation and purification processes.

The functional adsorbent material zeolite (FAM Z-series), commercialized by Mitsubishi Plastics Inc., shows the most advantageous adsorption isotherms when placed in contact with water.[13] AQSOA-FAM-Z02, based on the SAPO-34 zeotype with a CHA structure, hereafter referred to in this article as AQSOA-Z02, shows very suitable adsorption characteristics—a type V adsorption isotherm as investigated by Goldsworthy[14] and by Wei Benjamin Teo et al.[15]—in recovering CO_2 from a gas mixture containing H_2O. Because of the stepwise uptake of water, the partial pressure of water has to exceed a threshold value before water can be adsorbed. This is a feature of AQSOA-Z02 that makes it more favorable than other benchmarking materials such as zeolite 13X, which instead shows a type I isotherm for water with a very steep trend at low pressure.

A low-humidity content feed can be found in applications such as CO_2 removal from atmospheric air[16] and from closed cabin atmospheres[17] to sustain the quality of the breathed air. Therefore, CO_2 exists in the feed stream in parts per million (ppm) while N_2 and O_2 are the main components of the fluid. In order to study the separation of CO_2 for these applications, at least the adsorption of CO_2, N_2, and H_2O on the selected adsorbent is required. Hence, a study on the adsorption equilibrium of carbon dioxide, nitrogen, and carbon dioxide−nitrogen mixtures on AQSOA-Z02 was carried out with a gravimetric apparatus from vacuum to high pressures. The Toth isotherm

Received: September 30, 2017
Accepted: January 24, 2018
Published: February 6, 2018

model and the ideal adsorbed solution theory (IAST) in conjunction with the Toth model were applied to describe single-component and mixture equilibria. Consequently, this step adds a cost to the gas-separation process.

2. EXPERIMENTAL METHODS

Materials. The adsorption of carbon dioxide, nitrogen, and carbon dioxide−nitrogen binary systems of (i) 15 mol % CO_2 and 85 mol % N_2, (ii) 50 mol % CO_2 and 50 mol % N_2, and (iii) 80 mol % CO_2 and 20 mol % N_2 on AQSOA-FAM-Z02 is reported. The adsorbent is a CHA-type (silico)aluminophosphate in the form of loose grain sizes ranging from 0.25 to 0.45 mm.[18,19] The physical properties of the adsorbent material are given in Table 1. CO_2 (99.6%) and N_2 (99.995%) were obtained from White Martins-Praxair (Brazil).

Table 1. Physical and Surface Properties of AQSOA FAM Z02

material property	value	reference
crystal size [μm]	5−10	20
specific surface area [$m^2\ g^{-1}$]	650−770	20
mean pore diameter [nm]	0.38	13
pellet particle density (ρ_{pellet}) [$g\ cm^{-3}$]	1.081[a]	
skeleton density (ρ_{sk}) [$g\ cm^{-3}$]	2.256[a]	
micropore volume (V_{micro}) [$cm^3\ g^{-1}$]	0.279[a]	
macropore volume (V_{macro}) [$cm^3\ g^{-1}$]	0.203[a]	

[a]Data measured in the Adsorption Laboratory of the University of Edinburgh. Micropore volume measurement confirmed data disclosed in ref 21. Macropore volume is calculated from experimental quantities as $V_{macro} = (1/\rho_{pellet}) - V_{micro} - (1/\rho_{sk})$.

Material Skeleton Density and Porosity. A Quantachrome UltraPyc 1200e He pycnometer was used to determine the skeleton density or nonaccessible specific volume of the sample.[22] A NIST certified stainless steel sphere of volume 7.07 cm^3 was used to calibrate the volume of the cell. The cell was calibrated with and without the sphere prior to the collection of data.

Once the sample was regenerated at 473 K under vacuum for 2 h, in an outgassing station of an Autosorb iQ, 4.37 g of the sample was loaded into the cell. A purge step was carried out for 3 min to evacuate the pores of the sample and the cell. After the purge step, 10 volume measurements were carried out, and the results of the last 5 runs were collected and averaged to calculate the skeleton density, which is given in Table 1.

An Autosorb Poremaster mercury porosimeter was used to measure the volume of the macropore of the sample. The regenerated sample (1.03 g) was loaded into a porosimeter cell, and the procedure, as described by Brandani et al.,[22] was followed for the investigation of the pellet density and macropore volume. From these results, the micropore volume was calculated. The outcomes are summarized in Table 1.

Gravimetric Apparatus. The adsorption experiments were performed using a Rubotherm (Bochum, Germany) magnetic suspension microbalance equipped with a gas mixture dosing unit.

The sample was exposed to the measuring atmosphere while the balance was located outside this atmosphere under ambient conditions, which was achieved using a magnetic suspension coupling, as described by Weireld et al.[23] Pure-component experiments were performed using the two-position mode of the permanent magnet, the so-called zero point position and measuring point position. The mass at the zero-point position was calibrated and tared for more accurate weight measurements, and the data at both positions were used to correct the buoyancy effect. A comprehensive description of the experimental apparatus and the measurement procedure is given by Dreisbach et al.[24]

Around 0.5 g of adsorbent was outgassed at 473 K until no mass variation in the system was observed and then cooled to experimental temperature while the gas pressure was increased stepwise until a 20 bar maximal pressure was reached. The mass variation at equilibrium was recorded for each pressure step. Pure-component measurements were performed using the gravimetric setup described by Bezerra et al.[25]

The three-position mode automatic magnetic suspension microbalance, consisting of the zero point position, measuring point 1, and measuring point 2 positions, with an automatic gas mixture dosing system,[26] was used for binary mixture adsorption equilibria measurements and density determination, where a titanium sinker was added to the sample container as demonstrated in previous reports.[27,28] By lifting up the sample holder (measuring point 1 position), the sorption measurement was collected, and by raising and weighing the Ti sinker (measuring point 2 position), the density of the fluid phase was determined.

A procedure similar to that used for the regeneration of the adsorbent in the two-position magnetic suspension balance was also implemented on the three-position balance prior to the recorded data. The peripherals and magnetic suspension coupling were operated automatically using MessPro software (Rubotherm) for the collection of adsorbed mass and density at each pressure step under isothermal conditions.

Data Analysis. Since adsorption data were obtained gravimetrically, balance reading $m_{Bal}(p, T)$ has to be corrected due to the buoyancy effects acting on the adsorbent and components of the balance holding the sample by

$$m_{Bal,Corr}(p, T) = \Delta m_{spec}(p, T) + (V_s + V_{sc})\rho(p, T) \quad (1)$$

where $m_{Bal,Corr}$ [g] denotes the mass of adsorbate after buoyancy correction, V_s [cm^3] represents the specific volume of the adsorbent sample displacing the atmosphere, V_{sc} [cm^3] represents the volume of the balance suspended components, ρ [$g\ cm^{-3}$] denotes the density of the atmosphere surrounding the sample, p [bar] is the pressure, and T [K] is the temperature.

Δm_{spec} [g] indicates the specific mass change of the sample due to adsorption. This was governed by

$$\Delta m_{spec}(p, T) = m_{Bal,Corr}(p, T) - m_{sc}(p, T) - m_s(p, T) \quad (2)$$

where m_{sc} [g] is the mass of the sample container in vacuum obtained from a blank measurement without sample and m_s [g] denotes the mass of reactivated sample calculated in the loading and reactivation of the sample step with an inert gas. Information about the blank measurement and the loading and reactivation of sample steps can be found in Weireld et al.[23] V_{sc} in eq 1 does not depend on pressure and was measured in a calibration experiment without a sample.[24]

By considering V_s as equal to the skeleton volume (V_{sk}), the surface excess adsorbed amount was evaluated. However, to model adsorption processes, the absolute adsorption has to be determined as stated by Brandani et al.[22] and Myers and Monson.[29] The difference between the absolute and excess adsorption was governed by

$$q^{abs} = q^{exc} + \frac{\rho_g V_{ads}}{m_s M_w} \quad (3)$$

DOI: 10.1021/acs.jced.7b00864
J. Chem. Eng. Data 2018, 63, 661−670

where q^{abs} [mol kg^{-1}] represents the absolute adsorbed amount, q^{exc} [mol kg^{-1}] denotes the excess adsorbed amount, ρ_g [g cm^{-3}] is the density of the gas phase, V_{ads} is the pore volume participating in the adsorption [cm^3], equivalent to the micropore volume in the present work, and M_w [kg mol^{-1}] is the molecular mass of the gas.

By considering the volume of the adsorbed layer, V_s in eq 1 becomes the volume of the solid including micropores, which cannot be measured directly in the same experimental setup. This value can be obtained experimentally by measuring the volume of the skeleton and the volume of the micropores (V_{micro}) independently. V_{sk} was measured in the same gravimetric system by carrying out experiments with an inert gas. In this work, helium was used for V_{sk} determination. Another alternative to examining the nonaccessible volume of the sample was implemented using a helium pycnometer (HeP), as has been previously described. The volume of the adsorbed layer or else V_{micro} was calculated from

$$V_{micro} = V_s - V_{sk} = (V_{pellet} - V_{macro})_{HgP} - (V_{sk})_{HeP} \quad (4)$$

where the volume of the pellet V_{pellet} [cm^3] and the volume of the macropores V_{macro} [cm^3] were obtained by means of mercury intrusion porosimetry (HgP) .

Error Analysis. The parameters that theoretically affect the sorption measurements followed

$$q^{abs} = f(m_{Bal}, m_{sc+s}, m_s, \dot{v}_i, P, T, V_{micro}) \quad (5)$$

where $\dot{v}_i$ [mL min^{-1}] denotes the measured volumetric flow rate of species i in the fluid gas.

To determine the effect of each parameter on the uncertainty in the absolute adsorbed amount, the partial differentials of the independent errors were calculated by

$$\delta V_{sc+s} = f(m_{Bal}, m_{sc+s}, \rho) = \left[\left(\left(\frac{\partial V_{sc+s}}{\partial m_{Bal}}\right)\delta m_{Bal}\right)^2 + \left(\left(\frac{\partial V_{sc+s}}{\partial m_{sc+s}}\right)\delta m_{sc+s}\right)^2 + \left(\left(\frac{\partial V_{sc+s}}{\partial \rho}\right)\delta\rho\right)^2\right]^{0.5} \quad (6)$$

$$\delta\rho = f(P, T, y) = \left[\left(\left(\frac{\partial \rho}{\partial P}\right)\delta P\right)^2 + \left(\left(\frac{\partial \rho}{\partial T}\right)\delta T\right)^2 + \sum_{i=1}^{2}\left(\left(\frac{\partial \rho}{\partial y}\right)\delta y\right)^2\right]^{0.5} \quad (7)$$

$$\delta\Delta m_{spec} = f(m_{Bal}, m_s) = \left[\left(\left(\frac{\partial \Delta m_{spec}}{\partial m_{Bal}}\right)\delta m_{Bal}\right)^2 + \left(\left(\frac{\partial \Delta m_{spec}}{\partial m_s}\right)\delta m_s\right)^2\right]^{0.5} \quad (8)$$

Here, V_{sc+s} [cm^3] is the volume of the sample container and the solid, and y_i denotes the molar fraction of species i in the fluid gas. Equation 7 is considered for multicomponent adsorption measurements. For pure-component mixtures, the term δy_i is excluded.

Therefore, the dependent errors in excess and absolute adsorbed amounts were calculated as follows

$$\delta q^{exc} = f(\Delta m_{spec}, \rho, V_{sc+s}, m_s) = \left(\frac{\partial q^{exc}}{\partial \Delta m_{spec}}\right)\delta\Delta m_{spec} + \left(\frac{\partial q^{exc}}{\partial \rho}\right)\delta\rho + \left(\frac{\partial q^{exc}}{\partial V_{sc+s}}\right)\delta V_{sc+s} + \left(\frac{\partial q^{exc}}{\partial m_s}\right)\delta m_s \quad (9)$$

$$\delta q^{abs} = f(q^{exc}, \rho, V_{micro}) = \left(\frac{\partial q^{abs}}{\partial q^{exc}}\right)\delta q^{exc} + \left(\frac{\partial q^{abs}}{\partial \rho}\right)\delta\rho + \left(\frac{\partial q^{abs}}{\partial V_{micro}}\right)\delta V_{micro} \quad (10)$$

Table 2 represents the uncertainties in the characteristic data. The accuracy of the gas dosing system and the uncertainty in density measurements were considered only for the multicomponent adsorption equilibrium measurements. The uncertainty in the density measurement over the whole temperature and pressure range of the apparatus was given by Rubotherm GmbH.[30] This followed

$$\frac{\Delta\rho}{\rho} \leq \pm[0.02\% + 0.01\ \text{kg m}^{-3}] \quad (11)$$

At very low densities, the relative part of eq 11 (0.02%) is negligible compared to the absolute part (0.01 kg m^{-3}). The absolute part would in fact result in a very high relative error, especially for densities below 10 kg m^{-3} as discussed in ref 33.

3. ANALYTICAL ISOTHERM MODEL AND DATA FIT

Pure-Component Data Fit. The reported pure CO_2 and N_2 adsorption equilibrium data on AQSOA-FAM-Z02 were regressed using the semiempirical Toth isotherm model. The Toth isotherm was selected since the Toth equation is valid at the low and high ends of the pressure range. This is because the equation agrees with Henry's law at low pressure and has a

Table 2. Uncertainties in Measurements

property	parameter value	reference
standard deviation of mass reading [mg]	±0.02	30
standard deviation of mass of the solid [g]	±0.001	31
standard uncertainty in temperature [K][a]	±2	
accuracy of pressure measurements [%][a]	±1	
accuracy of gas dosing [% FS]	±0.04[b]	30
uncertainty in density measurement	±(0.02% + 0.01 kg m^{-3})	30
uncertainty in micropore volume [cm^3 g^{-1}]	±0.001[c]	32

[a]The temperature is measured beneath the sample in the measuring cell using a platinum resistance probe (Pt-100). Pressure measurements are also carried out in the measuring cell. The full pressure range of the balance used for single-component measurements is 200 bar. The balance used for multicomponent adsorption is equipped with two sensors: one up to 10 bar and a second up to 40 bar. [b]Full scale error is considered to be 100 mL min^{-1}. [c]Considering ±0.2% volume accuracy in the gas pycnometer and ±9 × 10^{-5} cm^3 volume resolution in the mercury porosimeter as obtained from the supplier, Quantachrome Instruments.

DOI: 10.1021/acs.jced.7b00864
J. Chem. Eng. Data 2018, 63, 661−670

Table 3. Experimental CO_2 Adsorption Equilibrium Data

298 K		323 K		348 K	
f [bar]	q^{abs} [mol kg^{-1}]	f [bar]	q^{abs} [mol kg^{-1}]	f [bar]	q^{abs} [mol kg^{-1}]
0.005	0.058	0.200	0.482	0.200	0.220
0.010	0.102	0.579	1.124	0.499	0.542
0.021	0.182	0.996	1.652	0.997	0.992
0.028	0.239	1.492	2.058	1.493	1.366
0.039	0.309	1.985	2.371	1.988	1.600
0.048	0.368	2.966	2.811	2.983	1.994
0.058	0.429	4.915	3.332	4.946	2.511
0.068	0.489	6.842	3.655	6.866	2.856
0.079	0.547	10.546	4.047	10.647	3.306
0.087	0.592	14.152	4.281	14.346	3.563
0.099	0.650	18.501	4.516	18.843	3.855
0.199	1.062				
0.299	1.382				
0.398	1.639				
0.500	1.865				
0.600	2.056				
0.699	2.219				
0.799	2.364				
0.900	2.499				
0.993	2.609				
1.489	3.081				
1.980	3.367				
2.965	3.752				
4.896	4.170				
6.758	4.421				
10.443	4.728				
13.905	4.916				
18.046	5.068				

Table 4. Experimental N_2 Adsorption Equilibrium Data

298 K		323 K		348 K	
f [bar]	q^{abs} [mol kg^{-1}]	f [bar]	q^{abs} [mol kg^{-1}]	f [bar]	q^{abs} [mol kg^{-1}]
0.200	0.066	0.200	0.035	0.200	0.026
0.500	0.138	0.500	0.081	0.510	0.0.66
1.010	0.245	1.010	0.149	1.000	0.106
1.500	0.341	1.510	0.209	1.500	0.151
2.029	0.441	2.000	0.268	2.021	0.197
2.998	0.610	3.030	0.385	3.021	0.295
4.995	0.863	5.010	0.581	5.003	0.443
7.041	1.092	6.999	0.741	7.036	0.577
11.047	1.432	11.019	1.030	11.034	0.802
15.019	1.690	14.999	1.260	15.036	0.984
19.940	1.910	20.010	1.470	20.060	1.170

finite limit when the pressure is sufficiently high.[34] The Toth equation was governed by

$$q = q_s \frac{b(T)f}{[1 + (b(T)f)^t]^{1/t}} \quad (12)$$

where q [mol kg^{-1}] represents the amount adsorbed, q_s [mol kg^{-1}] denotes the monolayer adsorption capacity, $b(T)$ [bar^{-1}] and t are temperature-dependent parameters, and f [bar] is the fugacity of the adsorbate in the gas phase. Parameters b and t are specific for adsorbate−adsorbent pairs, where parameter t characterizes the system's structural heterogeneity in adsorbent micropores. For $t = 1$, the isotherm reduces to the fundamental Langmuir adsorption isotherm equation, and further away from unity, the system is supposed to be more heterogeneous.[35]

A knowledge of the adsorption equilibrium and isosteric heat of adsorption is essential for the proper design and operation of any gas-phase adsorption process. The differential adsorption enthalpy (or isosteric heat of adsorption) $\Delta\bar{h}$ [kJ mol^{-1}] for pure fluids can be determined by solving the Clausius−Clapeyron relation:

$$-\frac{\Delta\bar{h}}{R_g T^2} = \left(\frac{\partial \ln f}{\partial T}\right)_q \quad (13)$$

A temperature-dependent expression for the fugacity f is obtained by inversion of the Toth isotherm and by expressing the heterogeneity constant t and the adsorption affinity b with temperature-

DOI: 10.1021/acs.jced.7b00864
J. Chem. Eng. Data 2018, 63, 661−670

Table 5. Parameters of CO_2 and N_2 Pure Component Data Regressed with the Toth Equation

		298.15 K		323.15 K		348.15 K	
parameter	unit	value	uncertainty	value	uncertainty	value	uncertainty
CO_2							
saturation capacity, q_s	mol kg^{-1}	6.06	±0.159		±0.2790		±0.1650
Henry's law constant, K_H	mol kg^{-1} bar^{-1}	10.77	±0.128	4.09	±0.0750	1.92	±0.0420
heterogeneity constant, t		0.62	±0.018	0.63	±0.0310	0.63	±0.0400
pre-exponential factor, b_0	(10^{-5}) bar^{-1}	1.06	±0.078		±0.1160		±0.1430
monolayer heat of adsorption, E	(−) kJ mol^{-1}	29.78	±0.182		±0.2950		±0.3950
N_2							
saturation capacity, q_s	mol kg^{-1}	6.06	±0.136		±0.1370		±0.2100
Henry's law constant, K_H	mol kg^{-1} bar^{-1}	0.34	±0.019	0.18	±0.0001	0.13	±0.0002
heterogeneity constant, t		0.58	±0.016	0.62	±0.0150	0.59	±0.0200
pre-exponential factor, b_0	(10^{-5}) bar^{-1}	6.44	±0.317		±0.0200		±0.0740
monolayer heat of adsorption, E	(−) kJ mol^{-1}	16.69	±0.121		±0.0900		±0.0750

dependent correlations. The adsorption affinity b follows the form

$$b = b_0 \exp\left(\frac{E}{R_g T}\right) \tag{14}$$

where b_0 [bar^{-1}] is the pre-exponential factor, E [kJ mol^{-1}] is the monolayer heat of adsorption, R_g [kJ mol^{-1} K^{-1}] is the universal gas constant. By using the general expression for the heterogeneity coefficient t, the following is the differential enthalpy from the Toth isotherm:

$$-\frac{\Delta\bar{h}}{R_g T^2} = \frac{E}{R_g T^2} + \left(\frac{dt}{dT}\right)\left[\frac{1}{t}\left(\frac{\ln(q/q_s)}{1-(q/q_s)^t}\right) + \frac{1}{t^2}\ln((q_s/q)^t - 1)\right] \tag{15}$$

When the heterogeneity coefficient t is temperature-independent, the differential enthalpy reduces to the monolayer heat of adsorption. The parameters obtained from the regression of single-component data, i.e., q_s, b_0, E, and t, allow the precise prediction of the mixture adsorption equilibria. Even small errors in the single-component adsorption isotherm fitting can result in large errors in the description of multicomponent adsorption, especially in the low-coverage pressure range.

Multicomponent Data Fitting. Multicomponent adsorption equilibrium data was predicted using the ideal adsorbed solution theory (IAST).[29] The bulk gas phase was assumed to be nonideal; therefore, the subsequent system of equations for N_C components was

$$P_{bulk} y_i \varphi_i = f_i^0 x_i \tag{16}$$

$$\psi_i = \int_0^{f_i^0} \frac{n_i^0(f_i)}{f_i}\, df_i \tag{17}$$

$$1 - \sum_{i=1}^{N_c} x_i = 0 \tag{18}$$

$$\frac{1}{n_t} = \sum_{i=1}^{N_c} \frac{m_i}{n_i^0(f_i^0) M_{w_i}} = 0 \tag{19}$$

P_{bulk} [bar] denotes the bulk pressure, y_i and x_i are the concentrations of species i in the bulk gas phase and adsorbed phase, respectively, φ_i is the fugacity coefficient of the ith component, f_i^0 [bar] and n_i^0 [mol kg^{-1}] are the pure-component fugacity in the adsorbed phase and the pure amount of adsorbed of species i at the same temperature and reduced grand potential ψ_i [mol kg^{-1}] of the mixture, respectively, n_t [mol kg^{-1}] denotes the total amount adsorbed, and m_i is the mass fraction of species i in the adsorbed phase.

IAST states that each component in the adsorbed phase has the same reduced grand potential at equilibrium;[36] therefore,

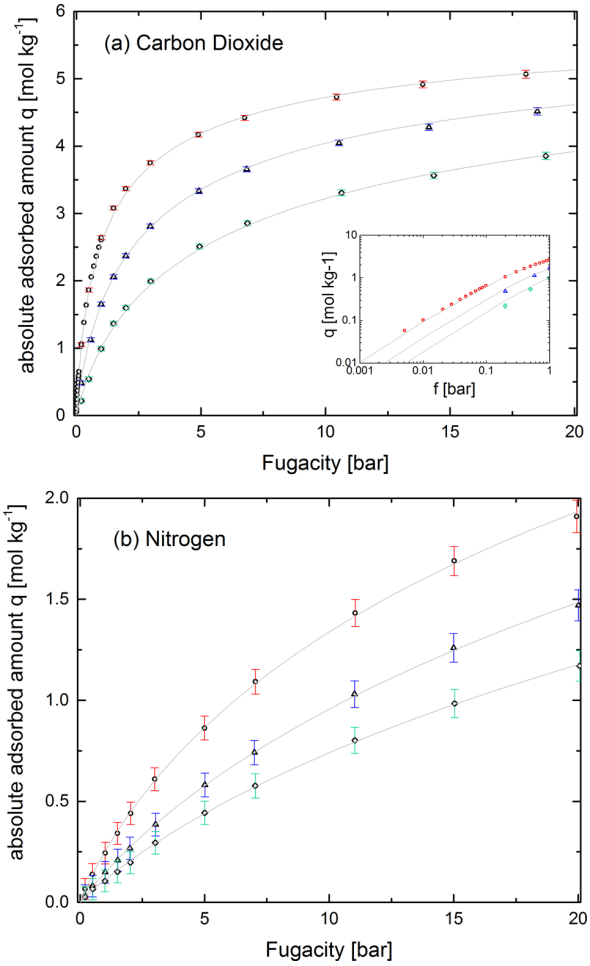

Figure 1. Single-component adsorption equilibrium isotherms of (a) carbon dioxide and (b) nitrogen on AQSOA-FAM-Z02 at 298.15 K (○), 323.15 K (△), and 348.15 K (◇). The solid lines represent the best fit with the Toth equation.

DOI: 10.1021/acs.jced.7b00864
J. Chem. Eng. Data 2018, 63, 661−670

Table 6. Experimental Adsorption Equilibrium Data of the CO_2/N_2 Binary Mixture on AQSOA-FAM-Z02

0.15/0.85 CO_2/N_2 mole fraction				0.5/0.5 CO_2/N_2 mole fraction				0.8/0.2 CO_2/N_2 mole fraction			
T	f	ρ_{exp}	q^{abs}	T	f	ρ_{exp}	q^{abs}	T	f	ρ_{exp}	q^{abs}
[K]	[bar]	[g cm^{-3}]	[g g^{-1}]	[K]	[bar]	[g cm^{-3}]	[g g^{-1}]	[K]	[bar]	[g cm^{-3}]	[g g^{-1}]
295	1.97	0.0024	0.071	295	1.47	0.0021	0.1	297	4.87	0.0081	0.173
295	2.97	0.0037	0.086	295	1.96	0.0028	0.114	297	6.78	0.0116	0.187
295	4.94	0.0061	0.106	295	2.94	0.0043	0.134	297	8.65	0.0150	0.196
295	6.92	0.0086	0.119	295	4.91	0.0072	0.157	297	10.51	0.0186	0.202
295	10.87	0.0135	0.136	295	6.85	0.0101	0.171	297	14.10	0.0258	0.211
295	14.78	0.0184	0.148	295	10.71	0.0161	0.187	297	18.41	0.0351	0.219
295	19.61	0.0246	0.158	295	14.46	0.0222	0.197				
				295	19.05	0.0299	0.206				
323	1.97	0.0022	0.036	323	1.47	0.0019	0.053	323	2.03	0.0029	0.079
323	2.97	0.0033	0.045	323	1.96	0.0025	0.064	323	2.94	0.0043	0.101
323	4.95	0.0055	0.060	323	2.96	0.0039	0.081	323	4.90	0.0073	0.127
323	6.93	0.0078	0.072	323	4.92	0.0065	0.104	323	6.82	0.0104	0.144
323	10.92	0.0122	0.089	323	6.88	0.0092	0.12	323	8.72	0.0136	0.156
323	14.85	0.0167	0.101	323	10.78	0.0146	0.139	323	10.63	0.0168	0.165
323	19.73	0.0223	0.113	323	14.60	0.0201	0.151	323	14.31	0.0233	0.177
				323	19.29	0.0271	0.161	323	18.81	0.0316	0.191
348	1.97	0.0021	0.023	348	1.47	0.0017	0.027	348	2.03	0.0027	0.051
348	2.97	0.0031	0.03	348	1.97	0.0023	0.034	348	2.95	0.004	0.067
348	4.96	0.0052	0.04	348	2.96	0.0035	0.048	348	4.91	0.0068	0.091
348	6.95	0.0073	0.049	348	4.94	0.006	0.068	348	6.84	0.0097	0.108
348	10.95	0.0114	0.062	348	6.9	0.0085	0.083	348	10.71	0.0155	0.131
348	14.93	0.0156	0.074	348	10.83	0.0136	0.105	348	14.45	0.0213	0.144
348	19.81	0.0208	0.083	348	14.69	0.0185	0.119	348	19.05	0.0289	0.163
				348	19.45	0.0248	0.131				

$$\psi = \psi_1 = \cdots = \psi_{N_C} \tag{20}$$

For the case of a binary mixture, the Toth model has an analytical expression for the reduced grand potential, but the pure-component hypothetical fugacity had to be determined from a numerical method. The Toth expression for the reduced grand potential is given by

$$\psi_i = f_i^0 q_s b_i \, {}_2F_1\left(\frac{1}{t_i}; \frac{1}{t_i}; \left(1 + \frac{1}{t_i}\right); -(f_i^0 b_i)^{t_i}\right) \tag{21}$$

where ${}_2F_1$ is the Gauss hypergeometric function ${}_2F_1$.[37]

4. RESULTS AND DISCUSSION

Pure-Component Adsorption Equilibria. Pure CO_2 and N_2 component data on AQSOA-FAM-Z02 was measured at (298.15, 323.15, and 348.15) K and the pressure range from 0.2 to 20 bar. All measured and treated CO_2 and N_2 equilibrium data are presented in Tables 3 and 4. The best-fitting parameters of single-component data were obtained by performing a weighted fit to the definition of the sum of squares due to error (SSE). To apply this method, weights were added to the definition of the sum of residuals divided by the sum of weights to normalize the objective function as follows

$$f(q_s, b, t) = \frac{\sum_{i=1}^{N_{data}} [w_i(q_{exp} - q_{theor}(q_s, b, t))]^2}{\sum_{i-1}^{m} w_i} \tag{22}$$

where $w_i = (i + 1)^{-1}$ is the ith weighting factor, q_{exp} [g g^{-1}] is the ith experimental absolute adsorbed amount, q_{theor} [g g^{-1}] is the ith model-predicted adsorbed amount obtained from the Toth equation, and N_{data} denotes the number of pressure steps (observations) at each isotherm.

The objective function $f(q_s, b, t)$ was then minimized using the nonlinear conjugate gradient model, and parameters b_0 and E were calculated from eq 14.

The regressed parameters of the proposed model for describing pure adsorption isotherms and their estimated uncertainties are presented in Table 5. Experimentally collected adsorption isotherms of carbon dioxide and nitrogen on AQSOA-FAM-Z02 were plotted against the Toth equation and are illustrated in Figure 1.

A correct fitting in the low-pressure region (Henry's region) essential to describing multicomponent data as the integration of the reduced grand potential is sensitive to low surface coverage.[29] For this reason, more data for the strongly adsorbed component were measured at low pressure and at the lowest temperature (see Figure 1a). The isotherms are described well for all temperatures for all systems. At all pressures, carbon dioxide was the most strongly adsorbed gas. Both carbon dioxide and nitrogen isotherms are type I isotherms, indicating the adsorption of gases in micropores.

Similar CO_2 and N_2 adsorption isotherms on AQSOA-FAM-Z02 were recently reported from Couck et al.[38] for AQSOA-FAM-Z02 powder, where 5.6 mol kg^{-1} of pure CO_2 is adsorbed at 303 K and 20 bar. This is slightly higher than the CO_2 uptake on AQSOA-Z02 pellets under the same conditions of 5 mol kg^{-1}. N_2 uptakes are instead essentially identical in AQSOA-Z02 powder and pellet.

Binary Mixture Adsorption Equilibria. In order to characterize the coadsorption behavior of CO_2/N_2, binary adsorption equilibrium gravimetric experiments of CO_2/N_2 were carried out. Experiments for the coadsorption of CO_2/N_2 mixtures on AQSOA-FAM-Z02 were performed at temperatures from 295 to 348 K and pressure ranges from the lowest available pressure allowed from the experimental apparatus, 1.5−2 bar up to 20 bar.

DOI: 10.1021/acs.jced.7b00864
J. Chem. Eng. Data 2018, 63, 661−670

Balance readings in [g], pressure in [bar], temperature in [K], and density in [g cm^{-3}] are listed in Table 6 along with all measured and treated binary data. Predicted results were obtained from the IAST model using the parameters obtained from the single-component measurements. Figure 2a–c illustrates the

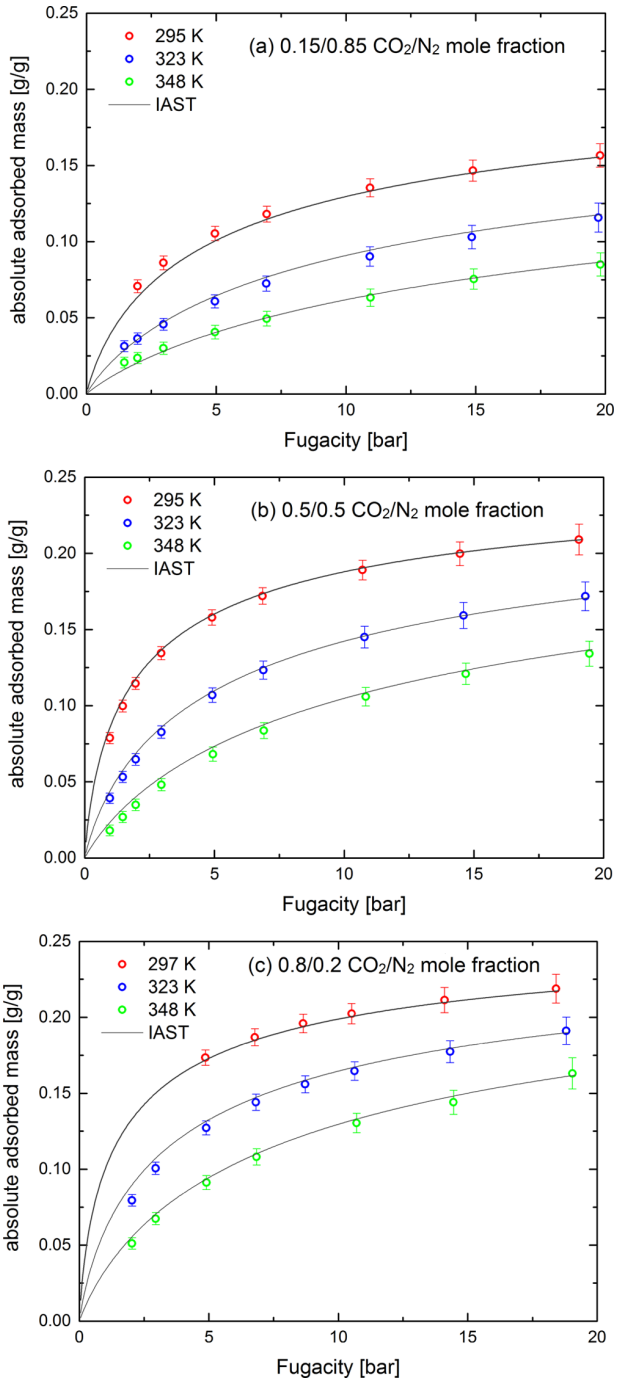

Figure 2. Predicted (lines) and experimental (symbols) binary adsorption equilibria of CO_2/N_2 on AQSOA-FAM-Z02 at (295 to 348) K. Errors were calculated according to Table 2.

measured and predicted binary adsorption isotherms at temperatures of (295 to 348) K.

As expected from the single-component results, CO_2 was the strongly adsorbed component. Therefore, the measured CO_2/N_2 equilibrium compositions were shifted toward higher values as the feed was enriched in CO_2. In addition, the capacities for binary CO_2 adsorption were lower than for pure CO_2. For the sake of simplicity, the CO_2 concentration in the feed stream was plotted against the predicted CO_2 concentration in the adsorbed phase (as obtained from the IAST model) at 323 and 348 K and is illustrated in Figure 3. According to Figure 3, the

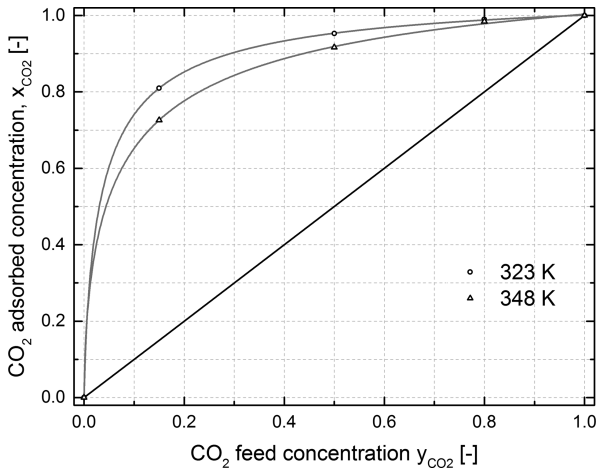

Figure 3. CO_2 concentration in the gas phase (y_{CO_2}) against the predicted CO_2 concentration in the adsorbed phase (x_{CO_2}) on AQSOA-FAM-Z02 at 323 and 348 K.

concentration of CO_2 in the adsorbed phase is high over an extended range of CO_2 partial pressures. For instance, a 5% CO_2 feed stream gives >60% concentrated CO_2 in the adsorbed phase at temperatures below 323 K.

The relative errors (RE %) in the measured absolute adsorbed amount of the CO_2/N_2 mixture on AQSOA-FAM-Z02, defined in eq 23, are shown in Figure 4

$$\mathrm{RE\%} = \left(\frac{q_{\mathrm{exp}} - q_{\mathrm{theor}}}{q_{\mathrm{exp}}} \right) \times 100 \tag{23}$$

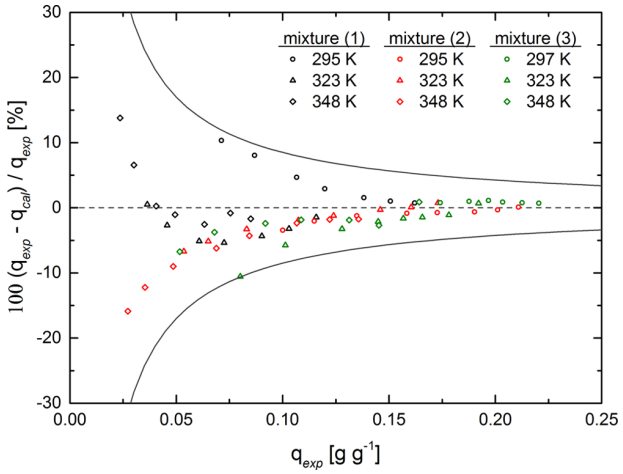

Figure 4. Percent difference between the experimental absolute adsorbed amount and estimated values from IAST: ——, estimated uncertainties in the current measurements; mixture 1 (0.15/0.85 CO_2/N_2 mole fraction); mixture 2 (0.50/0.50 CO_2/N_2 mole fraction); and mixture 3 (0.80/0.20 CO_2/N_2 mole fraction).

DOI: 10.1021/acs.jced.7b00864
J. Chem. Eng. Data 2018, 63, 661–670

The average relative error (ARE %) in the measured absolute adsorbed amount is

$$\text{ARE \%} = \frac{100}{N_{\text{data}}} \sum_{i=1}^{N_{\text{data}}} \frac{q_{\text{exp}} - q_{\text{theor}}}{q_{\text{exp}}} \quad (24)$$

where subscripts exp and theor denote the experimental and estimated values, respectively. The density of the mixture at each measured pressure step and temperature was also obtained theoretically by means of REFPROP[39] to provide a comparison with the experimental data. The RE % in density measurements followed eq 23, and the results are illustrated in Figure 5. Figure 5

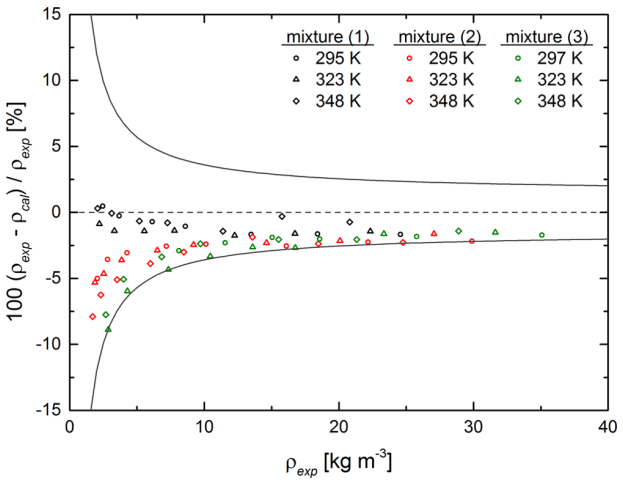

Figure 5. Percent difference between the experimental density and estimated values from REFPROP: ——, estimated uncertainties in the current measurements; mixture 1 (0.15/0.85 CO_2/N_2 mole fraction); mixture 2 (0.50/0.50 CO_2/N_2 mole fraction); and mixture 3 (0.80/0.20 CO_2/N_2 mole fraction).

also shows the estimated uncertainty in the density measurements, which was found to be ±1.5% + 0.21 kg m^{-3}. The maximum RE % in density was obtained at lower pressures. The deviation in density measurements is mainly due to the uncertainty in pressure, temperature, molar composition analysis, and mass and volume measurements of the sinker and the adsorbent. Minor errors, such as the force transmission error caused by the magnetic behavior of the cell, the suspension coupling, and the measured fluid, as highlighted by Cristancho et al.[40] and Atilhan et al.,[41] were not taken into consideration in this study.

Since the fit quality of the pure-component isotherms is reasonable, as a <2% RE % at each measured point was obtained, the discrepancy between the measured and predicted absolute adsorbed amounts (Figure 4) can be explained by the deviation in density measurements (Figure 5). The absolute part of the estimated uncertainty in the density measurements (0.21 kg m^{-3}) explains the higher percent differences at lower density levels.

The ARE % in the measured amount adsorbed was <4% for each tested CO_2/N_2 mixture at each reported temperature. The estimated uncertainty in the absolute adsorbent amount was found to be ±0.0085 g g^{-1} as illustrated in Figure 4. Therefore, the adsorption data of mixtures can be reasonable described over the entire composition range using the IAST model.

Adsorption selectivity is one of the most important parameters for separation applications. Equilibrium selectivity of CO_2 over N_2 was defined from

$$S_{CO_2/N_2} = \frac{x_{CO_2}/x_{N_2}}{y_{CO_2}/y_{N_2}} \quad (25)$$

Selectivity values are listed in Table 7. The selectivity was increased with the increase in the CO_2 concentration in the feed stream and the reduction in temperature. Accordingly, the highest estimated selectivity was achieved for the 80 mol % CO_2 and 20 mol % N_2 mixture and the lowest reported temperature.

5. CONCLUSIONS

Pure-component adsorption and coadsorption equilibria measurements have been carried out for CO_2, N_2, and their mixtures on AQSOA-FAM-Z02 using a gravimetric apparatus. Single gas isotherms were obtained at pressures of between 0.2 and 20 bar at (298, 323, and 348) K and were regressed with the Toth isotherm model. CO_2 was found to be the most strongly adsorbed compound with a reported adsorption capacity of 6.1 mmol g^{-1}. Binary adsorption equilibria measurements were performed at pressures from 1.5 to 20 bar for different gas compositions at different temperatures. The IAST model in conjunction with the Toth equation was used to predict the adsorbed amount of each gas in the CO_2/N_2 mixture and to characterize the coadsorption behavior of the mixture. Results showed the preferential adsorption of carbon dioxide over nitrogen even at lower concentrations of CO_2. The adsorption loadings for binary CO_2 were lower than for pure CO_2, which indicates that CO_2 and N_2 adsorbed competitively for the concentration range investigated.

The predictions of binary equilibria with the IAST model showed relatively good agreement with the experimental data, giving a <4% ARE % in the measured absolute adsorbed amounts. The discrepancy between experimental and predicted adsorption equilibrium data in low-pressure regions had been explained by the analysis of measurement uncertainties.

Table 7. Estimated Binary Mixture of CO_2 and N_2 Adsorption Equilibrium Data Using IAST

mixture	T [K]	CO_2 [mmol g^{-1}]	N_2 [mmol g^{-1}]	x_{CO_2} [a]	q_{tot} [g g^{-1}] [b]	selectivity
15 mol % CO_2–85 mol % N_2	295	0.922	0.137	0.870	0.044	38
	323	0.430	0.101	0.809	0.022	24
	348	0.218	0.083	0.725	0.012	15
50 mol % CO_2–50 mol % N_2	295	1.929	0.049	0.975	0.086	39
	323	1.103	0.044	0.962	0.050	25
	348	0.578	0.041	0.934	0.026	14
80 mol % CO_2–20 mol % N_2	295	2.217	0.016	0.993	0.098	138
	323	1.462	0.015	0.990	0.065	97
	348	0.864	0.014	0.984	0.038	61

[a]Denotes the molar fraction of CO_2 in the adsorbed phase. [b]Denotes the total absolute adsorbed amount of the mixture.

DOI: 10.1021/acs.jced.7b00864
J. Chem. Eng. Data 2018, 63, 661–670

AUTHOR INFORMATION

Corresponding Author

*E-mail: g.santori@ed.ac.uk. Tel: +44 (0)131 6519043.

ORCID

Giulio Santori: 0000-0003-2156-6647

Célio L. Cavalcante Jr.: 0000-0001-9409-3292

Funding

The research leading to these results was financially supported by EU IRSES (grant no. 295156), the Offshore Gas Separation Project (OFFGAS), and EU project Atmospheric Carbon Capture (ACCA, grant agreement no. 630863).

Notes

The authors declare no competing financial interest.

ABBREVIATIONS

ARE%, average relative error; IAST, ideal adsorbed solution theory; RE%, relative error; SSE, sum of squares due to error

REFERENCES

(1) Boot-Handford, M.; Abanades, C.; Anthony, E.; Blunt, M. J.; Brandani, S.; Mac Dowell, N.; Fernández, J. R.; Ferrari, M.-C.; Gross, R.; Hallett, J. P.; Haszeldine, S.; Heptonstall, P.; Lyngfelt, A.; Makuch, Z.; Mangano, E.; Porter, R. T. J.; Pourkashanian, M.; Rochelle, G. T.; Shah, N.; Yao, J.; Fennell, P. Carbon Capture and Storage Update. *Energy Environ. Sci.* **2014**, *7*, 130−189.

(2) Samanta, A.; Zhao, A.; Shimizu, G. K. H.; Sarkar, P.; Gupta, R. Post-Combustion CO2 Capture Using Solid Sorbents: A Review. *Ind. Eng. Chem. Res.* **2012**, *51*, 1438−1463.

(3) Choi, S.; Drese, J. H.; Jones, C. W. Adsorbent Materials for Carbon Dioxide Capture from Large Anthropogenic Point Sources. *ChemSusChem* **2009**, *2*, 796−854.

(4) Ruthven, D. M. *Principles of Adsorption and Adsorption Processes*; John Wiley & Sons: New York, 1984.

(5) Pulin, A. L.; Fomkin, A. A.; Sinitsyn, V. A.; Pribylov, A. A. Adsorption and Adsorption-Induced Deformation of NaX Zeolite under High Pressures of Carbon Dioxide. *Russ. Chem. Bull.* **2001**, *50*, 60−62.

(6) Rother, J.; Fieback, T. Multicomponent Adsorption Measurements on Activated Carbon, Zeolite Molecular Sieve and Metal−organic Framework. *Adsorption* **2013**, *19*, 1065−1074.

(7) Dunne, J. A.; Rao, M.; Sircar, S.; Gorte, R. J.; Myers, A. L. Calorimetric Heats of Adsorption and Adsorption Isotherms. 2. O_2, N_2, Ar, CO_2, CH_4, C_2H_6, and SF_6 on NaX, H-ZSM-5, and Na-ZSM-5 Zeolites. *Langmuir* **1996**, *12*, 5896−5904.

(8) Hefti, M.; Marx, D.; Joss, L.; Mazzotti, M. Adsorption Equilibrium of Binary Mixtures of Carbon Dioxide and Nitrogen on Zeolites ZSM-5 and 13X. *Microporous Mesoporous Mater.* **2015**, *215*, 215−228.

(9) Harlick, P. J. E.; Tezel, F. H. An Experimental Adsorbent Screening Study for CO_2 Removal from N_2. *Microporous Mesoporous Mater.* **2004**, *76*, 71−79.

(10) Joos, L.; Swisher, J. A.; Smit, B. Molecular Simulation Study of the Competitive Adsorption of H_2O and CO_2 in Zeolite 13X. *Langmuir* **2013**, *29*, 15936−15942.

(11) Lee, K. B.; Sircar, S. Removal and recovery of compressed CO_2 from flue gas by a novel thermal swing chemisorption process. *AIChE J.* **2008**, *54*, 2293−2302.

(12) Sing, K. S. W.; Everett, D. H.; Haul, R. A. W.; Moscou, L.; Pierotti, R. A.; Rou- querol, J.; Siemieniewska, T. Reporting physisorption data for gas/solid systems with special reference to the determination of sur- face area and porosity. *Pure Appl. Chem.* **1985**, *57*, 603−619.

(13) Mitsubishi Plastics Inc., Business Development Dep. Industrial Materials Division, Zeolitic Water Vapor Adsorbent AQSOA; 2008; pp 1−4; http://www.mpi.co.jp/infopdf/AQSOA.pdf.

(14) Goldsworthy, M. J. Measurements of Water Vapour Sorption Isotherms for RD Silica Gel, AQSOA-Z01, AQSOA-Z02, AQSOA-Z05 and CECA Zeolite 3A. *Microporous Mesoporous Mater.* **2014**, *196*, 59−67.

(15) Wei Benjamin Teo, H.; Chakraborty, A.; Fan, W. Improved adsorption characteristics data for AQSOA types zeolites and water systems under static and dynamic conditions. *Microporous Mesoporous Mater.* **2017**, *242*, 109−117.

(16) Lackner, K. S. Capture of carbon dioxide from ambient air. *Eur. Phys. J.: Spec. Top.* **2009**, *176*, 93−106.

(17) ElSherif, D.; Knox, J. C. *International Space Station Carbon Dioxide Removal Assembly (ISS CDRA) Concepts and Advancements*; International Conference on Environmental Systems; Rome, 2005; pp 1−5.

(18) Sapienza, A.; Santamaria, S.; Frazzica, A.; Freni, A. Influence of the Management Strategy and Operating Conditions on the Performance of an Adsorption Chiller. *Energy* **2011**, *36*, 5532−5538.

(19) Santori, G.; Frazzica, A.; Freni, A.; Galieni, M.; Bonaccorsi, L.; Polonara, F.; Restuccia, G. Optimization and testing on an adsorption dishwasher. *Energy* **2013**, *50*, 170−176.

(20) Mitsubishi Plastics Inc., Industrial Materials Zeolite AQSOA; 1962; http://www.mpi.co.jp/english. (accessed Aug 29, 2017).

(21) Kayal, S.; Baichuan, S.; Saha, B. B. Adsorption Characteristics of AQSOA Zeolites and Water for Adsorption Chillers. *Int. J. Heat Mass Transfer* **2016**, *92*, 1120−1127.

(22) Brandani, S.; Mangano, E.; Sarkisov, L. Net, excess and absolute adsorption and adsorption of helium. *Adsorption* **2016**, *22*, 261−276.

(23) Weireld, G. D.; Frère, M.; Jadot, R. Automated determination of high-temperature and high-pressure gas adsorption isotherms using a magnetic suspension balance. *Meas. Sci. Technol.* **1999**, *10*, 117−126.

(24) Dreisbach, F.; Lösch, H. W.; Harting, P. Highest Pressure Adsorption Equilibria Data: Measurement with Magnetic Suspension Balance and Analysis with a New Adsorbent/Adsorbate-Volume. *Adsorption* **2002**, *8* (2), 95−109.

(25) Bezerra, D. P.; Oliveira, R. S.; Vieira, R. S.; Cavalcante, C. L.; Azevedo, D. C. S. Adsorption of CO_2 on Nitrogen-Enriched Activated Carbon and Zeolite 13X. *Adsorption* **2011**, *17*, 235−246.

(26) Vilarrasa-García, E.; Cecilia, J. A.; Bastos-Neto, M.; Cavalcante, C. L.; Azevedo, D. C. S.; Rodriguez-Castellón, E. CO_2/CH_4 Adsorption Separation Process Using Pore Expanded Mesoporous Silicas Functionalizated by APTES Grafting. *Adsorption* **2015**, *21*, 565−575.

(27) May, E. F.; Miller, R. C.; Shan, Z. Densities and Dew Points of Vapor Mixtures of Methane + Propane and Methane + Propane + Hexane Using a Dual-Sinker Densimeter. *J. Chem. Eng. Data* **2001**, *46*, 1160−1166.

(28) McLinden, M. O.; Lösch-Will, C. Apparatus for wide-ranging, high-accuracy fluid (p,ρ,T) measurements based on a compact two-sinker densimeter. *J. Chem. Thermodyn.* **2007**, *39*, 507−530.

(29) Myers, A. L.; Monson, P. A. Physical adsorption of gases: the case for absolute adsorption as the basis for thermodynamic analysis. *Adsorption* **2014**, *20*, 591−622.

(30) Vilarrasa-García, E.; Cecilia, J. A.; Rodríguez Aguado, E.; Jiménez-Jiménez, J.; Cavalcante, C. L.; Azevedo, D. C. S.; Rodríguez-Castellón, E. Amino-modified pillared adsorbent from water-treatment solid wastes applied to CO2/N2 separation. *Adsorption* **2017**, *23*, 405−421.

(31) Pini, R. Interpretation of Net and Excess Adsorption Isotherms in Microporous Adsorbents. *Microporous Mesoporous Mater.* **2014**, *187*, 40−52.

(32) Lowell, S.; Shields, J. E.; Thomas, M. A.; Thommes, M. *Characterization of Porous Solids and Powders: Surface Area, Pore Size and Density*; Kluwer Academic Publishers: 2004.

(33) Saleh, B.; Wendland, M. Measurement of Vapor Pressures and Saturated Liquid Densities of Pure Fluids with a New Apparatus. *J. Chem. Eng. Data* **2005**, *50*, 429−437.

(34) Do, D. D. *Adsorption Analysis: Equilibria and Kinetics*, 2nd ed.; Imperial College Press, 1998; pp 1−892.

DOI: 10.1021/acs.jced.7b00864
J. Chem. Eng. Data 2018, 63, 661−670

(35) Wang, Y.; LeVan, M. D. Adsorption Equilibrium of Carbon Dioxide and Water Vapor on Zeolites 5A and 13X and Silica Gel: Pure Components. *J. Chem. Eng. Data* **2009**, *54*, 2839−2844.
(36) Santori, G.; Luberti, M.; Brandani, S. Common tangent plane in mixed-gas adsorption. *Fluid Phase Equilib.* **2015**, *392*, 49−55.
(37) Santori, G.; Luberti, M.; Ahn, H. Ideal adsorbed solution theory solved with direct search minimisation. *Comput. Chem. Eng.* **2014**, *71*, 235−240.
(38) Couck, S.; Cousin-Saint-Remi, J.; Van der Perre, S.; Baron, G. V.; Minas, C.; Ruch, P.; Denayer, J. F. 3D-printed SAPO-34 monoliths for gas separation. *Microporous Mesoporous Mater.* **2018**, *255*, 185−191.
(39) Lemmon, E. W.; Huber, M. L.; McLinden, M. O. *NIST Standard Reference Database 23: Reference Fluid Thermodynamic and Transport Properties-REFPROP*, Version 9.1; National Institute of Standards and Technology, 2013; https://www.nist.gov/srd/refprop. (accessed Jan 08, 2018).
(40) Cristancho, D. E.; Mantilla, I. D.; Ejaz, S.; Hall, K. R.; Iglesias-Silva, G. A.; Atilhan, M. Force transmission error analysis for a high-pressure single-sinker magnetic suspension densimeter. *Int. J. Thermophys.* **2010**, *31*, 698−709.
(41) Atilhan, M.; Ejaz, S.; Zhou, J.; Cristancho, D.; Mantilla, I.; Holste, J.; Hall, K. R. Characterization of Deepwater Natural Gas Samples. Part 1:78% Methane Mixture with Heavy Components. *J. Chem. Eng. Data* **2010**, *55*, 4907−4911.

DOI: 10.1021/acs.jced.7b00864
J. Chem. Eng. Data 2018, 63, 661−670

List of Figures

List of Tables

Glossary

Abbreviations

Ar	argon
AR	afforestation and reforestration
ARSs	air revitalisation systems
BECCS	bioenergy (energy from biomass) with carbon capture and storage
CCS	carbon capture and storage
CDRA	carbon dioxide removal assembly
CO_2	carbon dioxide
CO_2eq	CO_2 equivalent
CPT	compression and purification train
CySim	in-house cycle simulator software
DAC	direct air capture of CO_2 from ambient air
DSL	dual-site Langmuir
EDL	extended dual-site Langmuir
ESA	electric swing adsorption
ESL	extended single Langmuir
EW	enhanced weathering of minerals
FFD	full factorial design
GGR	greenhouse gas removal
GHG	greenhouse gas
H_2O	water
HeP	Quantachrome UltraPyc 1200e He pycnometer
HgP	Autosorb Poremaster mercury porosimeter
IAST	ideal adsorbed solution theory
ISS	International Space Station
LDF	linear driving force
MSA	moisture swing adsorption
N_2	nitrogen
NET	negative emissions technolog
O_2	oxygen
ODEs	ordinary differential equations
ORU	oxygen regeneration unit
PDEs	partial differential equations
PEI	branched poly(ethylenimine)
P&ID	process and instrumentation diagram
ppb	parts per billion

ppm	parts per million
PSA	pressure swing adsorption
R&D	research and development
SSE	sum of squares due to error
TSA	temperature swing adsorption
TVSA	temperature and vacuum swing adsorption
UKCCC	UK Committee on Climate Change
UNFCCC	United Nations Framework Convention on Climate Change
VSA	vacuum swing adsorption

Nomenclature

a	temperature dependent parameter of Toth isotherm	
A_c	column surface area	m^2
A_p	pellet surface area	m^2
$ARE\%$	average relative error	%
b	temperature dependent parameter of Langmuir and/or Toth isotherms	kPa^{-1}
b_0	reference constant at equilibrium of Langmuir and/or Toth isotherms	kPa^{-1}
$b_{0,i}$	pre-exponential adsorption constant of component i of Langmuir and/or Toth isotherms	kPa^{-1}
b_i	adsorption equilibrium constant of component i Langmuir isotherm	kPa^{-1}
$b(T)$	temperature dependent parameter of Langmuir and/or Toth isotherms	kPa^{-1}
c_0	coefficient c_0 defined as the ratio of heat of adsorption $\frac{\Delta H_1}{\Delta H_2}$	
c_i	concentration of component i in the fluid phase	$\mathrm{mol\ m}^{-3}$
c_i^m	concentration of component i in the macropore as described in the adsorption kinetic model	$\mathrm{mol\ m}^{-3}$
c_i^s	concentration of component i at the crystal boundary	$\mathrm{mol\ m}^{-3}$
$\frac{\partial \ln p}{\partial \ln q_\mu}$	thermodynamic correction factor which describes the thermodynamic equilibrium between the two phases	
$\tilde{c}_\mathrm{p}$	molar heat capacity at constant pressure in the fluid phase as described in the adsorption kinetic model	$\mathrm{kJ\ mol}^{-1}\ \mathrm{K}^{-1}$
$\tilde{c}_{\mathrm{p,ads}}$	molar heat capacity at constant pressure in the adsorbed phase as described in the adsorption kinetic model	$\mathrm{kJ\ mol}^{-1}\ \mathrm{K}^{-1}$
$c_{\mathrm{p},i}$	specific heat capacity of component i in the bulk-gas phase	$\mathrm{kJ\ mol}^{-1}\ \mathrm{K}^{-1}$
$c_{\mathrm{p,s}}$	specific heat capacity of adsorbent	$\mathrm{kJ\ kg}^{-1}\ \mathrm{K}^{-1}$
$\hat{c}_{\mathrm{p,sol}}$	specific heat capacity at constant pressure in the solid phase as described in the adsorption kinetic model	$\mathrm{kJ\ kg}^{-1}\ \mathrm{K}^{-1}$
$\hat{c}_{\mathrm{p,w}}$	specific heat capacity of the column wall	$\mathrm{kJ\ mol}^{-1}\ \mathrm{K}^{-1}$
c_T	total concentration in the fluid phase	$\mathrm{mol\ m}^{-3}$
c_T^m	total concentration in the macropore as described in the adsorption kinetic model	$\mathrm{mol\ m}^{-3}$

$\tilde{c}_{\mathrm{v}}$	molar heat capacity at constant volume in the fluid phase as described in the adsorption kinetic model	kJ mol^{-1} K^{-1}
D	diameter of the column	
$d_{\mathrm{c,ext}}$	external diameter of the column	m
$d_{\mathrm{c,int}}$	internal diameter of the column	m
$\Delta\bar{h}_i$	mixture differential enthalpy of adsorption of component i	kJ mol^{-1}
$\Delta\bar{h}_i^0$	pure differential enthalpy of adsorption of component i	kJ mol^{-1}
Δg_{mix}	molar Gibbs energy of mixing	kJ mol^{-1}
ΔH_i	isosteric heat of adsorption of component i at zero coverage	kJ mol^{-1}
ΔH	isosteric heat of adsorption at zero fractional loading	kJ mol^{-1}
ΔH_0	differences in enthalpy between adsorbed and gaseous states	kJ mol^{-1}
$\Delta\check{H}_{\mathrm{ads}}$	total heat of adsorption per unit volume	kJ m^{-3}
$\Delta H_{\mathrm{ads},k}$	enthalpy of adsorption in Bed *k*	kJ
Δh_i^0	pure integral enthalpy of adsorption of component i	kJ mol^{-1}
$\Delta H_{\mathrm{sens},k}$	sensible heat in Bed k	kJ
Δm_{spec}	specific mass change of the sample due to adsorption	kg
D_{ij}	molecular diffusion for the mixture component pair of 'i' and 'j'	m^2 s^{-1}
D_i^{K}	Knudsen diffusion coefficient for the ith component in the macropores of an adsorbent pellet	m^2 s^{-1}
D_i^{L}	axial dispersion coefficient in the fluid phase for the ith component	m^2 s^{-1}
D_i^{m}	bulk or molecular diffusion coefficient for the ith component in the macropores of an adsorbent pellet	m^2 s^{-1}
$D_{\mathrm{m},i}^{\mathrm{e}}$	macropore effective diffusion coefficient for the ith component	m^2 s^{-1}
D_i^{s}	surface diffusion coefficient for the ith component in the macropores of an adsorbent pellet	m^2 s^{-1}
D_i^{v}	viscus diffusion coefficient for the ith component in the macropores of an adsorbent pellet	m^2 s^{-1}
D_{lm}	diameter logarithmic mean	m
D_{m}	molecular diffusivity	m^2 s^{-1}
D_μ	transport diffusivity or else Fickian diffusivity which is referred as the Darken's relation	m^2 s^{-1}
D_μ^0	corrected diffusivity	m^2 s^{-1}
$D_{\mu,\infty}^0$	corrected diffusivity at infinite temperature	m^2 s^{-1}
d_{p}	particle diameter	m
D_{z}	mass axial dispersion coefficient	m^2 s^{-1}
E	heat of adsorption as described in Toth isotherm	kJ mol^{-1}
$E^{(\mathrm{ads})}$	total heat of desorption required for the steps of heating, vacuum, and discharging in the next connected bed	kJ
$E_{j,k}^{(\mathrm{ads})}$	final enthalpy of adsorption/desorption in Bed k at step j	kJ
E_μ	adsorption activation energy	kJ mol^{-1}
$E^{(\mathrm{sens})}$	total sensible heat required for heating up the beds	kJ
$E^{(\mathrm{th})}$	total specific thermal energy use required for heating	kJ mol^{-1}
f	fugacity of the adsorbate in the gas phase	kPa
f_i^0	pure component fugacity in the adsorbed phase	kPa

F	molar flow rate	mol s^{-1}
g	gravity acceleration	m s^{-2}
h_{ext}	external surface heat transfer coefficients	kJ m^{-2} s^{-1} K^{-1}
$\check{H}_{\mathrm{f}}$	enthalpy in the fluid phase per unit volume as described in the adsorption kinetic model	kJ m^{-3}
$\tilde{H}_i$	partial molar enthalpy of component i in the fluid phase as described in the adsorption kinetic model	kJ mol^{-1}
h_{int}	internal surface heat transfer coefficients	kJ m^{-2} s^{-1} K^{-1}
h_{w}	heat transfer coefficients between the bed fluid and the column wall	kJ m^{-2} s^{-1} K^{-1}
J_i	diffusive flux of the ith component in the fluid phase	mol m^{-2} s^{-1}
J_μ	constitute flux inside a micro-particle	mol m^{-2} s^{-1}
K	Henry's law constant	mol kPa^{-1} m^{-3}
K_0	Henry's law reference constant at equilibrium	mol kPa^{-1} m^{-3}
k_{ext}	external air thermal conductivity	kJ m^{-1} s^{-1} K^{-1}
k_{g}	gas/fluid thermal conductivity	kJ m^{-1} s^{-1} K^{-1}
k_{g}	pure gas thermal conductivity	kJ m^{-1} s^{-1} K^{-1}
k_i^{cr}	combined linear driving force coefficient of the ith component in the crystal	m s^{-1}
$k_{i,\mathrm{f}}$	external fluid mass transfer coefficient for the ith component at the macropore	m s^{-1}
k_i^{p}	combined linear driving force coefficient of the ith component in the pellet	m s^{-1}
k_{T}	thermal diffusion ratio	
k_{w}	wall thermal conductivity	kJ m^{-1} s^{-1} K^{-1}
k_{z}	axial thermal dispersion coefficient of the fluid	kJ m^{-1} s^{-1} K^{-1}
L	length of the column	
L_{c}	column/cylinder length	m
L_{m}	mobility coefficient of a molecule	mol m^2 kJ^{-1} s^{-1}
L^{s}	half length of the slab crystal of the radius of the cylindrical and spherical crystals	m
m_{Bal}	balance reading	kg
$m_{\mathrm{Bal,Corr}}$	mass of adsorbate after buoyancy correction	kg
$m_{\mathrm{bed},k}$	mass of the adsorbent in bed *k*	kg
m_i	mass fraction of species i in the adsorbed phase	
m_{s}	mass of reactivated sample as calculated in the loading and reactivation of sample step with an inert gas	kg
m_{sc}	mass of the sample container in vacuum as obtained from black measurement without sample	kg
M_{w}	molecular mass of the gas	kg mol^{-1}
$M_{\mathrm{w},i}$	molecular weight of species i	kg mol^{-1}
N_{B}	number of beds connected in a series	
N_{C}	number of components in the feed stream	
N_{data}	number of pressure steps (observations) at each isotherm	
N_{I}	number of connections of the next independent units as designing in CySim cycle simulator	
n_i^0	pure amount adsorbed of species i	mol kg^{-1}

$n_{\mathrm{ads},i,k}$	moles of component i in the adsorbed phase of Bed k	mol
$n_{\mathrm{bulk},i,k}$	moles of component i in the bulk-gas phase of Bed k	mol
$n_{i,k}$	moles of component i in Bed k	mol
$n_{\mathrm{stored},i}$	moles of the trace impurity i that are stored in both phases of the final/storage bed	mol
$n_{i,\mathrm{tot}}$	total moles of component i at equilibrium between two beds	mol
n_{proc}	number of moles processed at the vacuum step	mol
N_{R}	number of runs of the process	
N_{St}	total number of steps of the process including adsorption, vacuum, heating, and discharging steps of each bed	
n_{t}	total amount adsorbed	mol kg^{-1}
P	pressure	kPa
P_{atm}	atmospheric pressure	kPa
P_{bulk}	bulk-gas phase pressure	kPa
$P_{\mathrm{bulk},k}$	bulk-gas phase pressure in Bed *k*	kPa
p_i	partial pressure of component i in the bulk-gas phase	kPa
P_i^0	surface pressure	kPa
P_{ini}	initial pressure in the bed	kPa
Pr	Prandtl number	
P_{vac}	vacuum pressure	kPa
q	amount adsorbed	mol kg^{-1}
q^{abs}	absolute adsorbed amount	mol kg^{-1}
q^{exc}	excess adsorbed amount	mol kg^{-1}
q_{exp}	ith experimental absolute adsorbed amount	kg kg^{-1}
Q_i	molar concentration of component i in the adsorbent pellet as used in the kinetic model	mol m^{-3}
q_i	adsorbed phase concentration of component i	mol kg^{-1}
q_i^0	pure amount adsorbed of species i	mol kg^{-1}
q_i^*	adsorbed concentration of component i at equilibrium as used in the kinetic model	mol m^{-3}
q_i	molar sorbate concentration of component i as used in the kinetic model	mol m^{-3}
q_μ	concentration of the species in the crystal	mol m^{-3}
q_{s}	monolayer adsorption capacity	mol kg^{-1}
$q_{\mathrm{s},i}$	saturation adsorption capacity of component i	mol kg^{-1}
$q_{\mathrm{st},i}$	isosteric heat of a pure perfect gas i	kJ mol^{-1}
q_{T}	total adsorbed concentration in the micropore	mol m^{-3}
q_{t}	total adsorbed phase concentration	mol kg^{-1}
q_{theor}	ith model-predicted adsorbed amount obtained from the Toth equation	kg kg^{-1}
r	axial coordinate over the radius of the crystal	m
Ra	Rayleigh number	
R_{c}	column radius	m
$RE\%$	relative error	%
Re	Reynolds number	
R_{g}	universal gas constant (equal to 0.008314) that is also illustrated as R	kJ mol^{-1} K^{-1}

R_p	particle radius	m
r_p	microparticle radius	m
S	selection parameter of adsorbent materials	
s	particle shape factor	
Sc	Schimdt number	
$S_{i,j}$	adsorbent selectivity of species i over species j	
T	temperature	K
T_high	regeneration temperature	K
T_∞	temperature of the surrounding environment	K
T_low	adsorption temperature	K
T_vac	vacuum temperature	K
U	heat transfer coefficients between the column wall and the surrounding environment	kJ m^{-2} s^{-1} K^{-1}
$\check{U}_\mathrm{ads}$	internal energy per unit volume in the adsorbed phase as described in the adsorption kinetic model	kJ m^{-3}
$\check{U}_\mathrm{f}$	internal energy in the fluid phase per unit volume as described in the adsorption kinetic model	kJ m^{-3}
$\check{U}_\mathrm{p}$	internal energy in the pellet per unit volume as described in the adsorption kinetic model	kJ m^{-3}
$\check{U}_\mathrm{p,f}$	internal energy in the macropore per unit volume as described in the adsorption kinetic model	kJ m^{-3}
$\check{U}_\mathrm{p,s}$	internal energy in the solid and adsorbed phase per unit volume as described in the adsorption kinetic model	kJ m^{-3}
$\check{U}_\mathrm{sol}$	internal energy per unit volume in the adsorbent as described in the adsorption kinetic model	kJ m^{-3}
V_ads	volume of the adsorbed phase	m^3
V_c	volume of the column	m^3
$\dot{v}_i$	measured volumetric flow rate of species i in the fluid gas	ml min^{-1}
V_macro	volume of the macropores	m^3
V_micro	volume of the micropores or else volume of the adsorbed layer	m^3
V_p	pellet volume	m^3
V_pellet	volume of the pellet	m^3
V_s	specific volume of adsorbent sample displacing the atmosphere	m^3
V_sc	volume of the balance suspended components	m^3
V_sk	skeleton volume	m^3
$V_{\mathrm{void},k}$	volume in the bulk-gas phase	m^3
V_w	volume of the column wall	m^3
w	energy consumption of a feed unit as considered in CySim	kJ
W	working capacity of the adsorbent material	
$W_{\mathrm{el},k}$	adiabatic compression work in Bed k	kJ
w_i	molar fraction of component i in the specific phase considered	
x_i	molar fraction of the ith component in the adsorbed phase	
y_i	molar fraction of the ith component in the bulk-gas phase	

$y_{i,k}$	molar fraction of the ith component in the bulk-gas phase of Bed k	
z	axial coordinate	m

Greek Letters

α	thermal diffusivity	$m^2\ s^{-1}$
β	thermal expansion coefficient	K^{-1}
δ_w	column wall thickness	
ε_b	bed void fraction excluding macropores	
$\varepsilon_{bed,k}$	void fraction of bed k	
ε_p	pellet void fraction	
η_f	fluid viscosity	kPa s
η_i	gas viscosity of the ith component	kPa s
ϑ_f	overall fan efficiency	
μ	chemical potential	$kJ\ mol^{-1}$
μ^0	reference potential which depends only on T and p	$kJ\ mol^{-1}$
ν	air kinematic viscosity	$m^2\ s^{-1}$
ρ	density of the atmosphere surrounding the sample	$kg\ m^{-3}$
ρ_b	bulk density	$kg\ m^{-3}$
$\rho_{bed,k}$	bulk-gas phase density of Bed k	$kg\ m^{-3}$
ρ_{cry}	crystal density of adsorbent material	$kg\ m^{-3}$
ρ_f	fluid density as given in the adsorption kinetic model	$kg\ m^{-3}$
ρ_g	density of the gas phase	$kg\ m^{-3}$
ρ_p	pellet density	$kg\ m^{-3}$
ρ_w	column wall density	$kg\ m^{-3}$
σ	characteristic diameter of the molecule called as collision diameter from Lennard-Jones potential	Å
σ_{12}	collision diameter from the Lennard-Jones potential for the component pair '1' and '2'	Å
τ_p	pellet tortuosity factor which is defined as the ratio between the actual diffusion path length and the radial distance	
υ	interstitial or superficial flow velocity	$m\ s^{-1}$
ϑ_v	overall vacuum system efficiency	
Φ	surface potential	$kJ\ kg^{-1}$
ϕ_i	fugacity coefficient of the ith component	
Φ_{ij}	characteristic Lennard-Jones viscosity parameter (function of the pure gas viscosities and molecular weights) for the component pair 'i' and 'j'	
ϕ_p	non-spherical coefficient that for spherical pellets becomes a unity	
ψ_i	reduced grand potential	$mol\ kg^{-1}$
Ω_{12}	characteristic Lennard-Jones energy parameter for the component pair '1' and '2'	
Ω_μ	characteristic Lennard-Jones viscosity parameters of the ith component	

THE UNIVERSITY of EDINBURGH